

PHASE TRANSFORMATION BEHAVIOUR OF
POLYLACTIDE PROBED BY SMALL ANGLE
LIGHT SCATTERING

Von der Fakultät für Naturwissenschaften
der Universität Paderborn
genehmigte

Dissertation

zur Erlangung des akademischen Grades
Doktor der Naturwissenschaften

— Dr. rer. nat. —

von
Nico Schmidt
aus Castrop-Rauxel

März 2020

Welchen Wert hat all dein Lernen, dein Wissen, wenn es nicht zu Weisheit führt? Und was ist Weisheit anderes als zu wissen, was richtig ist und worin das richtige Handeln besteht?

Iain M. Banks
Das Kultur-Spiel

Die vorliegende Arbeit entstand in der Zeit von August 2014 bis November 2019 im Fachbereich für Physikalische Chemie (Arbeitskreis Prof. Dr. Klaus Huber) der Fakultät für Naturwissenschaften der Universität Paderborn in Kooperation mit dem Fachbereich für Photonik und Materialwissenschaften (Arbeitsgruppe Prof. Dr. Jörg Meyer) der Hochschule Hamm-Lippstadt (HSHL).

1. Gutachter: Prof. Dr. Klaus Huber
2. Gutachter: Prof. Dr. Jörg Meyer

Tag der Einreichung: 06. Dezember 2019

Tag der Disputation: 06. März 2020

Hiermit erkläre ich, die vorliegende Dissertationsschrift selbständig verfasst zu haben. Die dazu genutzte Literatur, zu Hilfeleistungen herangezogene Institutionen sowie Beiträge anderer Personen zu dieser Arbeit sind in der Dissertationsschrift vollständig angegeben bzw. kenntlich gemacht. Teilergebnisse der vorliegenden Arbeit wurden in folgenden Beiträgen vorab publiziert:

Publikationen:

- Nico Schmidt, Susanne Keuker-Baumann, Jörg Meyer, Klaus Huber, J. Polym. Sci. Part B: Polym. Phys. **57**(22), 1483–1495, 2019.

Konferenzbeiträge:

- Nico Schmidt, Jörg Meyer, Klaus Huber, Präsentation: *Phase transformation behaviour of polylactide probed by small angle light scattering*, 9th Young chemists symposium Ruhr, Bochum, 2018.
- Nico Schmidt, Nils Rokossa, Klaus Huber, Jörg Meyer, Poster: *Investigation of the crystallization behaviour of nucleated poly(lactic acid)*, 117th General Assembly of the German Bunsen Society for Physical Chemistry, Hannover, 2018.
- Nico Schmidt, Klaus Huber, Jörg Meyer, Poster: *Investigation of the crystallization behavior of nucleated poly(lactic acid)*, 20th JCF-Frühjahrssymposium, Konstanz, 2018.
- Nico Schmidt, Klaus Huber, Jörg Meyer, Poster: *Investigation of the crystallization behavior of nucleated poly(lactic acid)*, Macromolecular Colloquium Freiburg, Freiburg, 2018.
- Nico Schmidt, Klaus Huber, Jörg Meyer, Poster: *A Small Angle Light Scattering Instrument to Study Crystallization in Poly(lactic acid)*, 6th Young chemists symposium Ruhr, Essen, 2015.

In die Dissertation sind Daten aus folgenden, durch den Autor betreuten, studentischen Arbeiten eingegangen:

[Hem16] Moritz Hemmerich, Bestimmung von Laserstrahlprofilen für den Aufbau und Auslegung einer Kleinwinkellichtstreuapparatur, Bachelorthesis, HSHL, 2016.

[Gra17] Eva Graefenstein, Untersuchung des Kristallisationsverhaltens von Polylactid, Praxissemesterbericht, HSHL, 2017.

[Dzi18] Daniel Dziwisch, Schmelzverhalten von Polylactid in Abhängigkeit der thermischen Vorgeschichte, Projektarbeit, HSHL, 2018.

[Rok18] Nils Rokossa, Differenzkalorimetrische Untersuchungen des isothermen Kristallisationsverhaltens von Polylactid, Bachelorthesis, HSHL, 2018.

[Gro18] Andre Grochowski, Polarisationsmikroskopische Untersuchungen des Kristallisationsverhaltens von Polylactiden, Projektarbeit, HSHL, 2018.

Castrop-Rauxel, März 2020

Nico Schmidt

Danksagung

Es ist mir ein Bedürfnis und es erfüllt mich mit großer Freude, an dieser Stelle all den Menschen zu danken, die auf ihre Weise zum Gelingen dieser Dissertation beigetragen haben.

Mein Dank gilt zunächst Herrn Prof. Dr. Jörg Meyer und Herrn Prof. Dr. Klaus Huber. Beide haben sich auf das für sie neue Format der kooperativen Promotion eingelassen. Herzlich bedanken möchte ich mich für die Themenstellung und ihre kritische Begleitung während der Bearbeitung. Ihrer Bereitschaft zu ausgedehnter Diskussion und Unterstützung in allen Belangen der Promotion konnte ich mir jederzeit sicher sein.

Ich danke Herrn Prof. Dr. Walther Burchard, der mich anhand seines Laboraufbaus in Freiburg persönlich in die Wissenschaft der Kleinwinkellichtstreuung einweihte. Bedanken möchte ich mich bei der Firma Corbion, die die hier untersuchten Polylactid-Proben zu Forschungszwecken bereitgestellt hat.

Den aktuellen und ehemaligen Mitgliedern der Arbeitsgruppen Meyer und Huber danke ich für die freundschaftliche Arbeitsatmosphäre; nicht nur diskutiert, auch gelacht haben wir viel. Bedanken möchte ich mich insbesondere bei Matthias Bürger, der mir mit Begeisterung den Einstieg in die (physikalische) Chemie erleichtert hat.

Weiterhin gilt mein Dank allen Mitarbeiterinnen und Mitarbeitern des Departments Chemie in Paderborn, den Kollegen an der Hochschule Hamm-Lippstadt und den Mitgliedern des L-LABs Lippstadt für die tolle Zusammenarbeit. Susanne Keuker-Baumann und Rita Ties-Bonekamp danke ich für die Unterstützung bei zahlreichen Messungen. Für ihre Bereitschaft, Probleme der abbildenden Optik zu diskutieren, danke ich Prof. Dr. Oliver Sandfuchs, Markus Wahle, Jürgen Schmidtke, Julian Hansen, Markus Giehl und Daniela Karthaus. Bei Anne Büngeler und Lavinia Nimczewski bedanke ich mich herzlich für die Unterstützung bei Messungen im Rahmen dieser Dissertation. Meinen Büronachbarn Florian Bärmann und Frank Tappe danke ich für regen wissenschaftlichen Austausch. Bedanken möchte ich mich weiterhin namentlich bei Prof. Dr. Sabine Fuchs, Michael Luksin, Lukas Pischke, Sebastian Mohr, Marc Kaup, Jürgen Locher und den vielen weiteren Personen, die durch ihre Antworten und Anregungen Impulse zu dieser Dissertation gegeben haben.

Ich danke Andre Da Mota Cardoso, Tibor Dreesen, Daniel Dziwisch, Eva Graefenstein, Andre Grochowski, Moritz Hemmerich, Kevin Kensbock, Tatjana Porwol, Nils Rokossa, Jonas Sichler, Viola Vogt und Dan Zhao, deren Abschlussarbeiten ich betreuen konnte. Ihr Eifer und ihre Wissbegier waren beispielhaft.

Ich danke meinen Freunden und meiner Familie für ihre Unterstützung und ihr Interesse, ausgedrückt durch zahlreiche neugierige Fragen, an meiner Arbeit. Meiner Frau Nadine danke ich von Herzen für ihre uneingeschränkte Unterstützung und ihre Nachsicht.

Ein spezieller Dank gilt Rainer Kurz und Prof. Dr. Jörg Wenz; ohne sie wäre diese Arbeit nicht entstanden.

Kurzfassung

Thermisch induzierte Phasenumwandlungsprozesse in teilkristallinen Kunststoffen wurden am Beispiel von Polylactid (PLA) in Abhängigkeit des Molekulargewichts und der Stereoisomerzusammensetzung des unverzweigten Polymers, sowie in Mischungen der isotaktischen Polymere Poly(L-lactid) und Poly(D-lactid) untersucht. Die betrachteten Umwandlungsprozesse umfassten die isotherme Kristallisation in der unterkühlten Schmelze und die in solchermaßen präparierten Proben ablaufenden Schmelz- und Re-kristallisationsvorgänge während nicht-isothermen Heizens mit konstanter Rate.

Als Untersuchungsmethode wurde die zeitaufgelöste, temperaturabhängige, depolarisierte Kleinwinkellaserlichtstreuung (SALS) genutzt, die durch Messungen mittels thermischer Differenzkalorimetrie (DSC) ergänzt wurde. Für erstere wurde unter Rückgriff auf die Literatur eine Kleinwinkelstreuapparatur des Fourierlinsen-Typs entwickelt. Die korrekte Arbeitsweise des experimentellen Aufbaus wurde durch Größemessung von Kolloiden in Suspension unter Anwendung der Mie-Theorie erfolgreich verifiziert.

Die isotherme Kristallisation von PLA ist gekennzeichnet durch die temperaturabhängige Bildung von Kristallkeimen und deren radialem Wachstum zu Sphärolithen, das bei fortgesetzter Kristallisation zur Ausfüllung des gesamten Probenvolumens mit aneinandergrenzenden Sphärolithen führt. Mittels SALS wurde die temperaturabhängige Sphärolithwachstumsrate über den gesamten Temperaturbereich zwischen Glasübergang und Schmelze ermittelt. Dazu wurde die Tammansche Methode angewendet, mit der für niedrige Unterkühlungen die Sphärolithanzahl soweit erhöht wurde, sodass auch hier ein SALS-Signal erhalten werden konnte. Alle untersuchten PLA-Typen wiesen eine glockenförmige Sphärolithwachstumskurve auf. Für die Homopolymere konnten zwei Maxima identifiziert werden, die auf das Wachstum von α' - bzw. α -Kristalliten zurückzuführen sind.

Während des Aufheizens von kristallisierten Proben mit konstanter Rate bleibt die mittlere Sphärolithgröße unverändert bis zum Erreichen der finalen Schmelztemperatur, bei der die Größe abrupt auf null sinkt. Zugleich sinkt das detektierte Streusignal auf null, was das vollständige Aufschmelzen und die Isotropisierung der vormals kristallinen Polymerketten anzeigt. Dies gilt gleichermaßen für die Schmelz-Rekristallisation der α -Kristallite wie auch für die α'/α -Phasentransformation.

Durch kombinierte SALS-DSC-Messungen konnte gezeigt werden, dass die depolarisierte Streuinvariante direkt mit dem Kristallinitätsgrad der Sphärolithe korreliert und dessen Änderung während der Schmelz-Rekristallisation von α -Kristalliten auch quantitativ widerspiegelt. Das Schmelzen von PLA durch nicht-isothermes Heizen ist gekennzeichnet durch eine Abnahme des Kristallinitätsgrades durch das Schmelzen von kristallinen Domänen innerhalb der Sphärolithe. Wird der Schmelzvorgang unterhalb des finalen Schmelzpunktes pausiert, so führt eine isotherme Wärmebehandlung zu einer erneuten Zunahme des Kristallinitätsgrades. Dabei bleiben die Sphärolithe als kristalline Überstrukturen bis zum Erreichen der finalen Schmelztemperatur erhalten.

Abstract

Phase-transformation processes in semi-crystalline polymers as a function of molecular weight and chain tacticity of the linear polymer were investigated for polylactide (PLA) and mixtures of its isotactic homopolymers poly(L-lactide) and poly(D-lactide), respectively. Three phase transformation processes were analyzed: isothermal crystallization, non-isothermal melting and melt-recrystallization. Melting was analyzed during heating the samples after isothermal crystallization. Analysis also comprised α -phase melt-recrystallization, and polymorphous melt-recrystallization due to the α'/α -transition in the enantio-pure polymer. Studies were performed by combined time- and temperature-resolved depolarized small angle light scattering (SALS) and differential scanning calorimetry (DSC). To this end, a home-built Fourier-lens type SALS device was set up and its operational verification was accomplished by particle-sizing of colloids in suspension by application of Mie-theory.

For the first time a microstructural characterization of morphological changes upon phase-transformation during crystallization and during melting of isothermally crystallized PLA was carried out via SALS. Isothermal crystallization of PLA proceeds via temperature-dependent nucleation and growth of spherulites, which results in a volume-filled morphology on completion of crystallization. Separation of spherulite nucleation and growth by application of Tammann's two stage crystal nuclei development method allowed determining of the spherulite growth rate curve over a temperature interval ranging from the glass transition to the melting point. At an isothermal crystallization temperature high enough, pure α -phase crystals are formed. Exposed to a temperature gradient, the crystals first melt and then recrystallize before they finally melt. With decreasing crystallization temperature, an increasing fraction of PLA is crystallizing in the less stable α' -phase. α' -crystals also melt upon increasing the temperature but recrystallize to the more stable α -phase. A constant spherulite size is revealed by SALS for both processes, the α/α and α'/α melt-recrystallization, until completion of the final melting, thereby supporting integrity of the spherulites throughout the entire processes. Joint DSC and SALS experiments demonstrate that the depolarized scattering invariant correlates with the heat flow recorded by DSC and thus offers an alternative measure for the degree of crystallinity. The following mechanism is identified for both processes: initial melting and recrystallization overlay each other. Crystallinity is not fully recovered upon recrystallization because only part of the original lamellae survives the melt-recrystallization, though with an increased thickness. While lamellae are melting and reforming or simply transforming their phase, the spherulites survive the process until final melting.

Contents

Kurzfassung	VIII
Abstract	IX
Table of contents	X
Glossary	XII
List of abbreviations	XIV
1 Introduction	1
1.1 Motivation and scientific goals	1
1.2 Outline of the thesis	3
2 State of the art	5
2.1 General introduction to light scattering	5
2.1.1 Historical review	5
2.1.2 Structure elucidation via light scattering	6
2.2 Small angle light scattering instruments	7
2.3 Polylactide	9
2.4 Crystallization and melting behaviour of PLA	12
2.5 SALS studies of PLA crystallization	20
3 Small angle light scattering instrument	26
3.1 Light scattering fundamentals	26
3.2 General description of the setup	31
3.3 In-depth description of the SALS instrument	32
3.4 Data acquisition: Performing measurements	42
3.5 Data processing: Preparing data evaluation	44
3.6 Calibration of the scattering angle	50
3.7 Operational verification of the SALS setup	54
3.7.1 Methods and materials	54
3.7.2 Results: Particle sizing of standard latex beads	56
4 Phase transformation behaviour of polylactide	64
4.1 Materials and methods	64
4.2 Light scattering from spherulites	67
4.3 Spherulite linear radial growth rates	72
4.4 Effect of the presence of scPLA	77
4.5 Morphological changes upon heating from the crystalline state	80
4.6 Non-spherulitic crystalline superstructures in compounds of scPLA and PLLA	92

CONTENTS

5 Conclusion and Outlook	98
5.1 Summary of the most relevant results	98
5.2 Perspective	102
Appendix	105
A Polymer characterization of the sample material	105
A.1 Summary of PLA sample properties	105
A.2 Molecular properties	106
A.2.1 Molecular weight	106
A.2.2 Stereochemistry	106
A.3 Thermal properties	109
B Supporting Information	113
C Calculating corrected sums of squares	122
D List of Figures	123
E List of Tables	128
F Bibliography	129

Glossary

In this work widely used and recognized notation of symbols is utilized to provide consistency with literature. However, it is not unusual to find different symbols denoting the same quantity or, vice versa, two completely different quantities denoted by the same symbol even in small well-defined research fields. This is even more true for this interdisciplinary work. For example, G denotes both the Gibbs free enthalpy as well as the radial linear growth rate of spherulites. Therefore, the glossary lists the symbol with both meanings. Hereinafter, it is believed that the correct meaning is apparent for the reader from the context.

α	α crystal modification of PLA polarizability
α'	α' crystal modification of PLA
c	concentration
$\langle D^2 \rangle_z$	z-averaged squared particle diameter
$\delta_{am,s}^0$	intrinsic optical anisotropy of spherulitic amorphous phase
δ_{cr}^0	intrinsic optical anisotropy of a pure crystal
δ^*	relative disorder parameter
D_n	number-averaged particle diameter
D_v	volume-averaged particle diameter
E	(modulus of the) electric field vector
η	viscosity
$f_{cr,s}$	chain orientation factor
F, f	focal distance
G	Gibbs free energy linear radial spherulite growth rate
H	enthalpy
$J_1(x)$	Bessel function of the first kind
K	optical constant, contrast factor
k_i	(modulus of the) incident wave vector
k_s	(modulus of the) scattered wave vector
λ	wavelength in medium
λ_0	vacuum wavelength
m	relative complex refractive index
M_N	number-averaged molecular weight
M_W	weight-averaged molecular weight
ϕ, μ	azimuthal scattering angle
$\phi_{am,s}$	spherulitic amorphous volume fraction
$\phi_{cr,s}$	spherulitic crystalline volume fraction
ϕ_S	volume fraction of spherulites
$P(q)$	form factor
q	(modulus of the) scattering vector

CONTENTS

Q_{HV}	depolarized scattering invariant
R	spherulite size pinhole radius
R_{HV}	Rayleigh ratio
S_i	amplitude scattering matrix element
T	temperature
$t_{1/2}$	crystallization half time
τ_{exp}	detector exposure time
τ_p	crystallization peak time
T_c	crystallization temperature
T_g	glass transition temperature
θ	scattering angle
T_m	melting temperature
T_m^0	equilibrium melting temperature
T_{nuc}	nucleation temperature
U	reduced scattering vector
x	size parameter

List of abbreviations

AR	antireflection (coating)
CCD	charged coupled device
CMOS	complementary metal oxide semiconductor
coPLA	random co-polymer of L-lactide and meso-lactide
D-LA	D-lactic acid
DLS	dynamic light scattering
DSC	differential scanning calorimetry
FDPA	Fraunhofer diffraction pattern analysis
FSC	fast scanning chip calorimetry
FTIR	Fourier transform infrared (spectroscopy)
GUI	graphical user interface
hcPLA	homocrystalline polylactide
HSHL	Hochschule Hamm-Lippstadt
L-LA	L-lactic acid
NMR	nuclear magnetic resonance (spectroscopy)
PDI	polydispersity index
PDLA	poly(D-lactic acid)
PLA	polylactide, poly(lactic acid)
PLLA	poly(L-lactic acid)
PMMA	poly(methyl methacrylate)
POM	polarized optical microscopy
PP	polypropylene
PTFE	poly(tetrafluoroethylene)
PWM	pulse width modulation
RDG	Rayleigh-Debye-Gans theory of light scattering
SAXS	small angle x-ray scattering
scPLA	stereocomplex PLA
SLS	static light scattering
TGA	thermogravimetric analysis
USB	universal serial bus
WALS	wide angle light scattering
WAXD	wide angle x-ray diffraction
XRD	X-ray diffraction

1 Introduction

1.1 Motivation and scientific goals

Poly lactide (PLA) is a semi-crystalline linear aliphatic polyester [1]. Its bulk properties dependent on its molecular weight and the chain architecture [2] as well as on the thermal history of the material [3]. Bulk properties are also influenced by the isomer composition of the chains, both in terms of stereo-isomer ratio and sequence length(s) [4–10].

In order to improve the mechanical properties of products made from PLA with respect to mechanical toughness and thermal stability, crystallization of the material is mandatory [11–13]. Controlling the crystalline morphology of the material is also the key to the fabrication of transparent products from PLA with high melting points [14, 15]. Thus, the crystallization behaviour of PLA has been the subject of intense research [16–22]. The crystallization window of PLA is determined by the glass transition temperature T_g and the melting temperature T_m . Both quantities are functions of the isomer composition of the chain and its molecular weight [23]. X-ray diffraction (XRD) measurements revealed that PLA crystallizes into several (metastable) polymorphs [24–26] and that stereocomplex crystals (scPLA) are formed in racemic as well as in other enantiomeric mixing ratios of PLA [27]. Numerous studies were performed by calorimetry (DSC) to determine crystallization mechanisms and kinetics and by polarized optical microscopy (POM) to follow changes in morphology. PLA with high isomeric purity generates spherulitic morphology upon isothermal [28] and non-isothermal [29] crystallization. Linear radial growth rates $G(T_c)$ of PLA spherulites were determined as a function of the crystallization temperature T_c . Its dependence on molecular weight and on stereoregularity, i. e. mole fraction of the minor repeat-unit was thoroughly characterized in the past [30–34].

Whereas crystallization of PLA spherulites has been intensively investigated, much less is known on the melting of PLA spherulites. DSC [35, 36] and XRD [37–39] clearly show melt-recrystallization phenomena. Melt-recrystallization is caused by the dependence of the melting point of the spherulite-constituting lamellae on crystallization temperature and is not only known for PLA [36, 38] but also for other polymers [40–45]. From the semi-ordered, not yet isotropic melt of lamellae which were crystallized at large undercooling a new population of crystal lamellae can form via rapid recrystallization upon heating [37]. This melt-recrystallization process is accompanied by an increase of the lamellar thickness as evidenced by XRD [37]. Similar findings have been published for syndiotactic polypropylene [46]. A polymorphous α'/α -phase transition due to a change in chain packing during melt-recrystallization, which depends on the thermal history and enantiomeric composition of the polymer, adds to the complexity of the melting behaviour of PLA [37, 39, 47]. DSC experiments on this transition report a weak exothermic peak [37, 39, 48–50]. An increase of D-lactide monomer content lowered the maximum temperature where an α' -phase is still formed during isothermal crystallization [48]. WAXS experiments showed an isosbestic point for the 116 and 203

1. INTRODUCTION

reflections during melt-recrystallization [39]. The isosbestic point [39] together with the short time required for the α'/α -phase transition [49] was used as evidence for the solid-solid nature of the α'/α -phase transition. Combined SAXS-WAXS experiments refined and further confirmed this interpretation [50]. However, knowledge about consequences of melt-recrystallization and α'/α -phase transition on the overall spherulite morphology is still poor. Kishore *et al.* [51] observed spherulite shrinking in size once they got close to the melting point, being in strong contrast to observations made with other polymers [52, 53].

In this work a time-resolved study of the crystallization and the melting behaviour of PLA in terms of changes in spherulite morphology by means of a joint small angle light scattering (SALS) and DSC analysis is presented. SALS is a powerful tool to disclose the supramolecular crystal morphology of semi-crystalline thermoplastics, in particular under conditions where time-resolved structure characterization is a challenge for POM [54–61]. Accordingly, SALS was also used to determine changes in PLA morphology during crystallization [62–64] and in one further case it was applied to characterize the isothermal crystallization of PLA in terms of spherulite growth rates [65]. However, to the best of the author’s knowledge, there is no comprehensive SALS-based characterization available for structure formation during crystallization and for morphological changes during non-isothermal melting of PLA. This lack of information motivated the present work.

The following agenda summarizes the scientific goals of this thesis:

- While there is a range of wide angle light scattering instruments commercially available for the characterization of polymers in dilute solution no instruments are available for the study of phase transformation processes of polymers during crystallization or melting, respectively.
Therefore, the first objective of this thesis shall be the development of a dedicated SALS instrument capable of performing time- and temperature-resolved measurements of structure formation processes in undercooled polymer melts like spherulite growth, and capable of monitoring morphological changes during melting and melt-recrystallization of crystallized polymers.
- Benchmarking of the home-built SALS instrument shall be carried out via particle sizing measurements of colloidal suspensions. To this end Mie scattering theory shall be applied to determine particle sizes of standard latex beads. In particular, these measurements serve in confirming the calibration of the scattering angles of the instrument.
- The isothermal crystallization behaviour of PLA shall be characterized in terms of the temperature-dependent linear radial spherulite growth rate $G(T)$. For the first time, by application of a modified temperature-time protocol SALS mea-

surements shall be extended to the high temperature branch of the growth curve which, so far, was only characterized by microscopy studies.

- The complex phase transformation behaviour of PLA upon heating after isothermal crystallization shall be characterized in terms of changes in spherulite morphology. Investigations shall address the following questions:
 - (i) Does melting or melt-recrystallization affect spherulite size?
 - (ii) Does the degree of crystallinity, as established by calorimetry, change during melting and melt-recrystallization due to a change in the number and size of spherulites or due to a change of spherulitic crystalline domains?
 - (iii) Do spherulitic crystalline domains rearrange during melt-recrystallization, i. e. is the lamellar morphology affected by these processes?
 - (iv) How do spherulite size, degree of crystallinity and lamellar morphology change during the polymorphous α'/α -phase transition?

1.2 Outline of the thesis

The text of this thesis is organized as follows:

CHAPTER 2

provides the context of the present work. Light scattering is introduced as a powerful tool for non-destructive investigation and characterization of polymers in their various states of matter. This is complemented by a short historical review of the development of light scattering theory. Furthermore, state of the art small angle light scattering techniques and instrument setups are reviewed. In the second part of the chapter the protagonist of this work, the polymer PLA, is introduced and the present knowledge of the crystallization and melting behaviour of PLA is presented. In particular, SUBSECTION 2.5 for the first time presents a comprehensive collection of SALS studies of the crystallization behaviour of PLA.

CHAPTER 3

lays the foundations for the investigation of the phase transformation behaviour of PLA by means of the utilized SALS instrument. First, the fundamentals of Rayleigh and Mie scattering theory are introduced. In the following an in-depth description of the SALS instrument, which was built and used for the present work, is given with a focus on data acquisition and processing, and a robust and precise calibration procedure of the instrument. In addition, the home-built sample stage for polymer melts is presented. The chapter concludes with the successful operational verification of the SALS instrument. This was achieved via benchmarking the instrument by particle size measurements of standard latex beads with a commercially available instrument.

1. INTRODUCTION

CHAPTER 4

presents the results from the investigation of the phase transformation behaviour of PLA by a joint DSC and SALS study. The theory of light scattering from polymer spherulites is sketched. It is applied to experiments characterizing the isothermal crystallization behaviour of PLA in terms of the temperature dependent spherulite linear radial growth rate. In this work, for the first time, SALS was applied to the characterization of morphological changes in PLA upon heating from the crystalline state. The results are presented in SUBSECTION 4.5. Also, results from the SALS-based investigations of the crystallization and melting of PLLA homopolymers in the presence of a small amount of scPLA are presented in this chapter.

CHAPTER 5

concludes this thesis by summarizing the findings of this work. Based on questions emerging from the presented results it gives a perspective on future research work.

In the APPENDIX

a comprehensive characterization of the polymers used in this work is given. Furthermore, additional results from DSC and SALS measurements are presented in support of the findings in CHAPTER 4.

2 State of the art

2.1 General introduction to light scattering

2.1.1 Historical review

The theory of light scattering has been under development since the middle of the 19th century. Tyndall was among the first researchers who published studies on the investigation of light scattering phenomena (cf. [66]). In particular he investigated the scattering from aerosols and discovered that scattered light is highly polarized [67, 68]. Only a little later Strutt (3rd Lord Rayleigh) applied Maxwell's theory of electrodynamics to light scattering of particulate matter with size dimensions smaller than the wavelength and demonstrated that the scattered intensity is proportional to the wavelength raised to the fourth power [69]. He thus explained the blue colour of the sky and red sunsets with the preferential scattering of short wavelengths even in the absence of colloidal particles by only the atmospheric gas molecules [70]. Contributions of Debye and Gans added to the theory which by the beginning of the 20th century became known as Rayleigh-Debye-Gans (RDG) theory [71–74]. It explains the scattering of light from particulate matter by emission of secondary radiation from induced dipoles with the same wavelength as the incident radiation (elastic scattering). Prerequisite for application of the theory is a refractive index of the material not too much different from that of the surrounding medium. Only then, the intra-particle electric field can be equated to that of the incident field and the detected intensity can be calculated from superimposing wavelets scattered from all subvolumes of the particle.

A direct solution of the scattering problem for large spherical particles with size dimensions significantly larger than the wavelength and with a refractive index different from the surrounding medium was accomplished by Mie [75] and also by Lorenz [76]. This so-called Lorenz-Mie theory is directly derived from Maxwell's equations and accounts for the spatially dependent electric field inside the particle which now can no longer be approximated by the incident field.

At the same time a fluctuation theory of light scattering was presented by Smoluchowski and Einstein [77, 78]. It attributes light scattering to mean-square fluctuations in density and concentration.

Consequently, light scattering was developed into a powerful tool for non-destructive characterization and probing of soft and condensed matter where characteristic structures have length scales approximately of the order of the wavelength. Zimm, Flory, Pecora [66, 79, 80], to name but a few, laid the foundations for the application of Rayleigh scattering in the field of analysis of colloids and polymers and, in particular, the characterization of polymers in dilute solution. Without claiming completeness, light scattering-based research encompasses colloid flow through porous media [81], fractal colloidal aggregates [82], liquid crystals [83] as well as gas-borne nanoparticles [84] and was applied successfully to the determination of the diffusion constant of dust particles in complex plasmas [85]. Furthermore, light scattering is routinely applied

to the study of the miscibility or phase separation kinetics, respectively, of polymer blends [57, 86–92].

2.1.2 Structure elucidation via light scattering

Knowledge of the characteristics like shape and size of particulate matter is of fundamental importance for numerous technological applications and most relevant to physical phenomena these applications are based on [93, 94].

In parallel with the theory progress was achieved in light scattering instrument technology. A number of wide angle light scattering (WALS) instruments either equipped with a goniometer mounted detector or fixed multi angle detectors are commercially available covering an angular range typically between 20° to 150° [95]. Often, these instruments are capable of dynamic light scattering (DLS) on time-scales from microseconds to several seconds making use of photomultipliers and digital correlators [66]. Particle sizing instruments, which employ either Fraunhofer diffraction pattern analysis (FDPA) or Lorenz-Mie theory, on the other hand have a lower scattering angle limit down to single-digit degrees [96]. In general, they are restricted to static light scattering (SLS) and determine particle sizes in terms of equivalent spheres independent of the actual particle shape. FIGURE 2.1 illustrates the relation between the characteristic

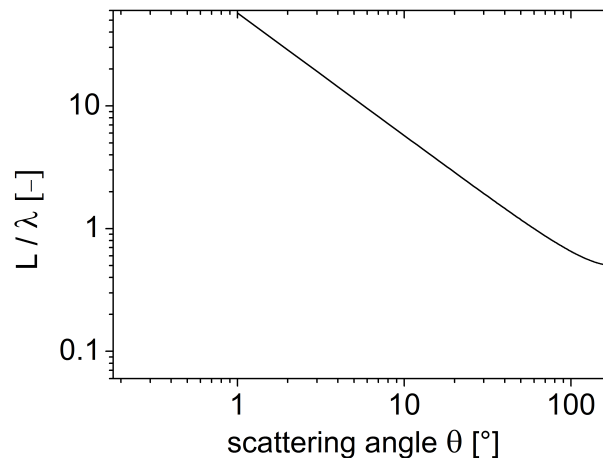


Figure 2.1: Characteristic structure size L normalized by the wavelength λ applied by light scattering as a function of the scattering angle θ .

structure size $L = 2\pi/q$ and the magnitude of the scattering vector $q = 4\pi/\lambda \sin(\theta/2)$ where λ is the wavelength in the ambient medium and θ is the geometrical scattering angle (see SUBSECTION 3.1 for details).

From FIGURE 2.1 it can be realized that characterizing large structures requires investigation of scattering at low angles. To this end dedicated small angle light scattering (SALS) instruments are utilized. Depolarized SALS is particularly suited for the study of morphological features of semi-crystalline polymers [59, 61, 97–99]. Foundations of the research field were laid by Stein and Rhodes in their pioneering work on SALS of

polymer spherulites [52]. The field was advanced rapidly and extended to crystalline aggregates and to the study of the internal ordering of polymer crystals [100–105]. Instrumental details are presented in SUBSECTION 2.2.

2.2 Small angle light scattering instruments

The basic geometry of a small angle light scattering experiment is sketched in FIGURE 2.2. In the setup shown in FIGURE 2.2 the sample is illuminated by polarized light from a laser just as it was done in the present work. This source of high-intensity, monochromatic, collimated light replaced mercury lamps when it became widely available in form of the helium neon gas laser [54, 106]. Either laser tubes inherently providing linearly polarized light are used or polarizing optical components are used to obtain a linearly polarized primary beam [41]. The scattered light passes an analyzer

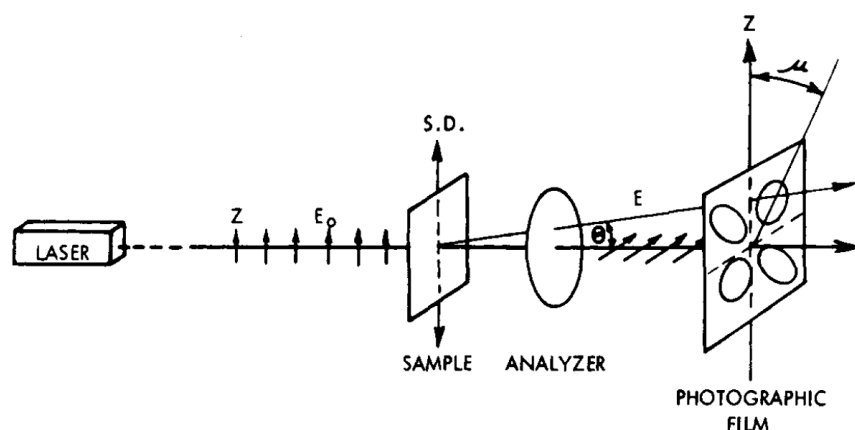


Figure 2.2: Basic geometry of a small angle light scattering experiment. Polarized light of a laser illuminates the sample. The (depolarized) scattered light is either detected directly by a photographic film positioned in forward direction of the sample or the film is replaced by semi-transparent screen. In the latter case the scattering pattern can be recorded by a camera placed behind the screen. Reproduced from [107].

and is recorded subsequently. Historically, the two-dimensional scattering pattern was recorded on a photo-sensitive film which was positioned in forward direction. Thus, the angular range covered by the instrument was determined by the geometrical angle given by the sample to film distance and the size of the film. Much effort was put into the development of photographic detectors for time-resolved measurements [55, 108, 109]. Advances in detector technology allowed replacing photographic films with TV-cameras and, more recently, with photo-sensitive semiconductor detectors like charge coupled devices (CCD) or complementary metal oxide semiconductor (CMOS) sensors [110–112]. The high temporal resolution of these detectors makes real-time monitoring of structure evolution processes feasible [113].

In FIGURE 2.3 the most common designs of SALS detection optics are sketched. Separation of the scattered light from the primary beam is crucial for high-quality SALS

2. STATE OF THE ART

data.

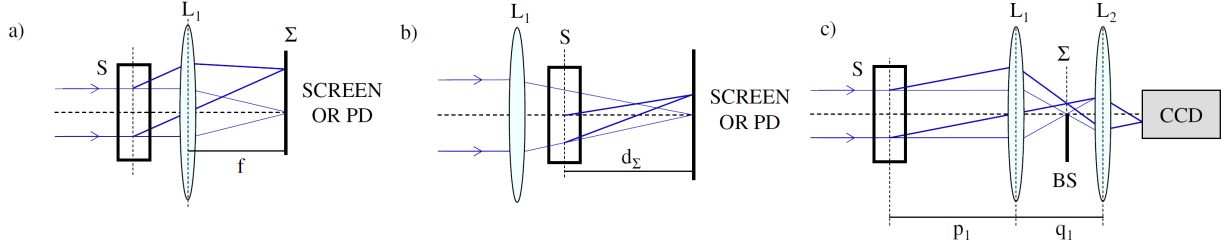


Figure 2.3: Common optical designs for SALS instruments. Here, S denotes the sample, L_1 is the Fourier lens with focal length f , object distance p_1 and image distance q_1 , respectively. Σ is the back focal plane of L_1 . L_2 is an objective lens and d_Σ is the sample to detector distance. BS denotes the beam stop. The scattering pattern is either visualized on a screen or recorded by photodiodes (PD) or semiconductor sensors (CCD), respectively. Adapted from [112].

To this end the Fourier lens design was introduced (FIGURE 2.3a). The Fourier property of a lens implies that any rays entering the lens with angle θ with respect to the optical axis are crossing the back focal plane of that lens, the so-called Fourier plane, on a ring with radius

$$r = f \tan \theta \quad (2.1)$$

where f is the back focal length of the lens. As a consequence smearing of the scattering pattern due to contributions from finite sample thickness and finite beam width are virtually eliminated [114]. Ideally, the primary beam is minimized to a point-like spot in the focus of the lens and scattered intensity can be retrieved at angles close to $\theta \approx 0^\circ$.

The design in (FIGURE 2.3b) is denoted as Reverse Fourier Optics setup. In this setup the lens is positioned in front of the sample. The primary beam now passes the sample in a convergent manner rather than parallel. The maximum scattering angle for a given r can be controlled by the distance d_Σ and is obtained from the above equation by setting $f = d_\Sigma$.

Instruments for particle sizing via static light scattering are based on the optical designs presented in FIGURE 2.3a and 2.3b. Radial symmetry of the scattering pattern is assumed such that only a circular sector-shaped element of the pattern is recorded by a specifically designed detector [115–118]. However, time-resolved imaging of the complete scattering pattern in the Fourier plane is reported only in a limited number of cases. A two-dimensional optical multichannel analyzer with a 50×50 grid was utilized to study the melting and crystallization of LLDPE/LDPE blends [119, 120]. Time-resolved SALS studies on the crystallization of PP were performed with a linear array of 46 photodiodes [121]. More recently the application of large scale x-ray detectors to SALS was demonstrated [122].

The size of the scattering pattern scales with f (FIGURE 2.3a) or d_Σ (FIGURE 2.3b) and

can easily cover a range from tens of millimetres up to centimetres. When the scattering pattern cannot be recorded in the Fourier plane itself the pattern is first visualized on a translucent diffusing screen (see FIGURE 2.3a and 2.3b). Subsequently, the image of the pattern on the screen is recorded by a detector, which is placed at a distance behind the screen [56, 58, 110, 111, 123]. Via optical demagnification with a lens system arbitrary-sized patterns on the screen can be mapped to the detector.

However, a significant drawback of the latter instrument type is the fact that by indirect imaging sensitivity and angular resolution are limited by the screen, which the scattering pattern is visualized on. A problem pertinent to all SALS instruments is the high intensity of the primary beam which is orders of magnitude larger than the scattered intensity and which may thus give rise to detector saturation and diverse stray light issues.

Ferri presented a SALS optics design (FIGURE 2.3c) which allows direct recording of the scattered intensity with widespread ordinary semiconductor sensors [124]. In this setup the Fourier plane is imaged onto the detector plane with an appropriate optical demagnification to suit the detector size. However, the primary beam is prevented from reaching the detector. To this end either a highly absorbing beam stop or a small mirror is positioned in the Fourier plane to remove it from the detection optics. Hence, measurements at very small scattering angles can be achieved. The upper scattering angle limit is given by the numerical aperture of the Fourier lens and the sample to lens distance p_1 . To avoid vignetting, i.e. to avoid artificial loss of intensity with increasing scattering angle, $p_1 > f$ must be fulfilled. This limits the upper scattering angle to $\theta_{max} \approx 15^\circ$.

The Ferri-design (Fourier lens-type SALS instrument) was successfully applied to studies of polymer crystallization mechanisms [125] and investigations of the microstructure of a yield-stress fluid [126]. Application of the instrument design to DLS of colloidal suspensions was demonstrated as well [127].

Due to its superior performance and versatility the Fourier lens-type SALS design presented by Ferri was adopted in this work for the investigation of the phase transformation behaviour of PLA.

2.3 Polylactide

Poly(lactide) (PLA) is a linear aliphatic polyester which can be extracted from non-fossil carbon sources like renewable crops [1]. PLA-based plastics are both bio-compatible as well as bio-degradable. They are among the most promising candidates in the field of eco-sensitive, sustainable bioplastics. As a semi-crystalline thermoplastic compound PLA allows the use of existing processing equipment, e.g. extrusion, injection moulding or fiber spinning [128].

While, in the past, PLA was primarily used for medical applications because of its excellent compatibility with the human metabolism [129, 130], nowadays the material is used in a variety of different applications [9, 131–133]: In the form of films, foams, bot-

2. STATE OF THE ART

ties and hard shells PLA is used in short-lived products in the field of food packaging, as well as disposable tableware. There is also a growing field of application in textile articles. In order to increase added value, various PLA grades have been developed in recent years for use in consumer durables, which includes, for example, the market segment of housings for electrical appliances such as mobile phones and laptops. As a composite material, for example for the air supply in the engine compartment, PLA has also found its way into the automotive sector. In addition, the material properties make PLA a popular material for additive manufacturing in 3D printing. Bio-degradation of PLA can be accomplished by composting at temperatures above the softening temperature of about 60 °C.

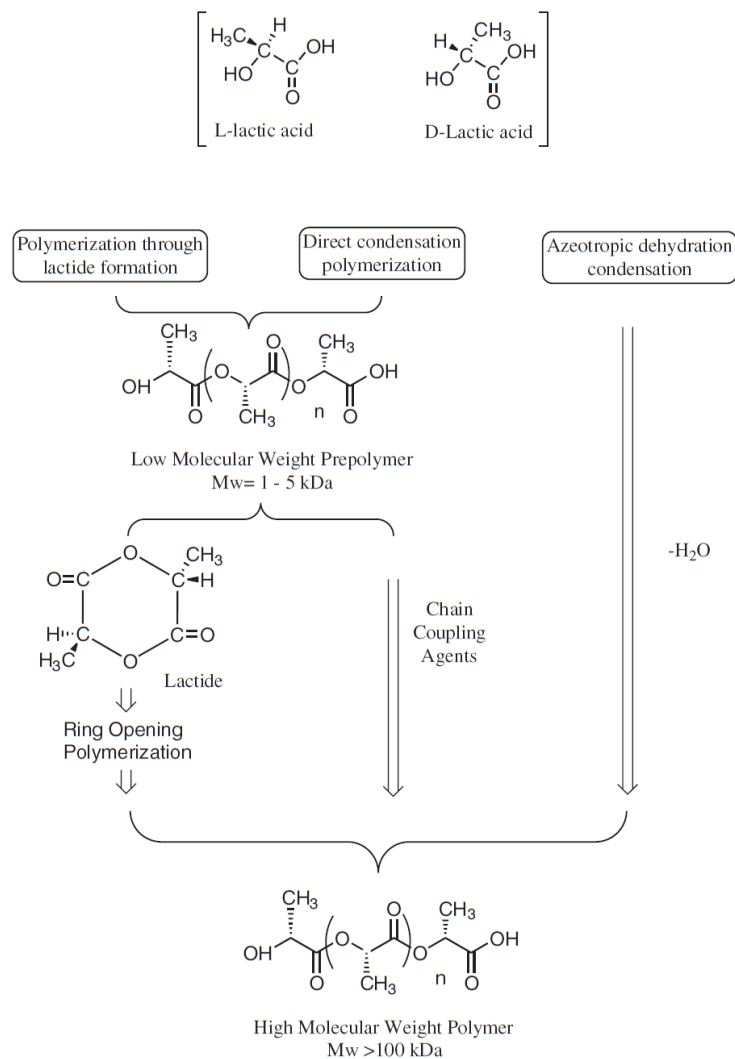


Figure 2.4: Different routes for the synthesis of PLA from the stereoisomers of lactic acid. With amendments reproduced from [9].

2. STATE OF THE ART

Synthesis of PLA was first described by Pelouze in 1845 [134], but commercialization of PLA-based plastics has only been accomplished to a significant extent beyond niche applications since about 2000 [135]. PLA is a bio-based polymer produced by condensation polymerization of lactic acid (LA) or by polymerization of lactide, the cyclic dimer of LA. Lactides can be obtained by oligomerization and cyclization of LA which can be derived from fermentation of corn starch [136]. Due to advantages in process engineering, today PLA is commonly synthesized by ring-opening polymerization (ROP) of the cyclic dimer of lactic acid rather than by a direct polycondensation reaction of the monomeric lactic acid. Synthesis by ROP has been known since the 1930's, but only through the use of efficient catalysts, e. g. on the basis of the (transition) metals zinc or tin ROP can be used industrially [135, 137, 138]. The different routes for synthesis of PLA are shown in FIGURE 2.4. According to widely used nomenclature, the term poly(lactic acid) is used to denote the polycondensation products of LA while the term polylactide is used to stress synthesis by ROP. A detailed description of PLA synthesis can be found in [6].

The properties of PLA depend largely on its stereochemistry [4, 8]. Stereoisomerism results from the chiral carbon center present in LA, the monomeric building block of PLA. LA exists in the two stereoisomeric forms L-LA and D-LA, which yield either pure lactides L,L-lactide and D,D-lactide or D,L-(meso)-lactide. As a consequence, ROP of lactide yields the isomerically pure homopolymers poly(L-lactide) (PLLA) and poly(D-lactide) (PDLA) or poly(L-co-D-lactide) also referred to as poly(meso-lactide). Depending on the feed ratio, block-co-polymers or random co-polymers poly(L-lactide-co-meso-lactide) and poly(D-lactide-co-meso-lactide) can be synthesized. In this work the abbreviation coPLA is used for the random co-polymer. Homopolymers containing less than 1 % of the minor repeat-unit are designated PLLA and PDLA, respectively. Stereochemical pure PLA formulations (PLLA or PDLA homopolymers) show high crystallinity. In contrast, the copolymerization of only small amounts of the stereo partner in the single-digit percentage range significantly reduces the crystallization tendency of the material [33, 34] (see also SUBSECTION 2.4); on further increasing the amount to 12 % crystallization is suppressed completely [18]. Consequently, the biodegradability of the polymer is dependent on its stereochemistry and stereoisomer ratio, as well, because crystalline domains of PLA are less prone to enzymatic attack [139].

Blends of PLA and various other polymers can be made as well as co-polymers of LA with other suitable polymers and, in addition to this, compounds of PLA and certain composites of PLA in conjunction with natural fibres are known [140]. A comprehensive review is presented by Hamad *et al.* [141].

Numerous research reports document the efforts to increase the heat resistance of PLA while maintaining transparency by blending PLA with other transparent polymers [142, 143]. Such results are available, for example, for blends of PLA and PMMA, although it has been shown that both the transparency is reduced and the increased heat resistance is only significant at mixing ratios smaller than 50/50 PLA/PMMA in favour of PMMA [144–146]. Likewise, blending destroys the biodegradability of the

material. By contrast, PLA and PC do not form homogeneous binary blends [147]. In PLA, crystallinity, heat-resistance, and transparency are intimately related [1, 148]. In the present work a deeper understanding is aspired of the crystallization and the melt-recrystallization behaviour of PLA which shall assist tailoring those solid state properties of the material.

2.4 Crystallization and melting behaviour of PLA

From the point of view of fundamental research on polymer phase transitions, PLA is an ideal candidate to study the aspects of polymer crystallization and melting. PLA crystallization proceeds rather slowly and the polymer shows virtually all relevant phenomena with the more sophisticated ones being crystal polymorphism, melt-recrystallization or stereo-complex formation between sterically paired polymers. This SUBSECTION 2.4 is based on an extensive review by Saeidlou *et al.* on the crystallization of PLA [3] and a more recent review by Androsch *et al.* specifically focusing on nucleation and growth of crystals of PLA [149]. In addition, most recent works and developments in the field relevant to this thesis are presented briefly.

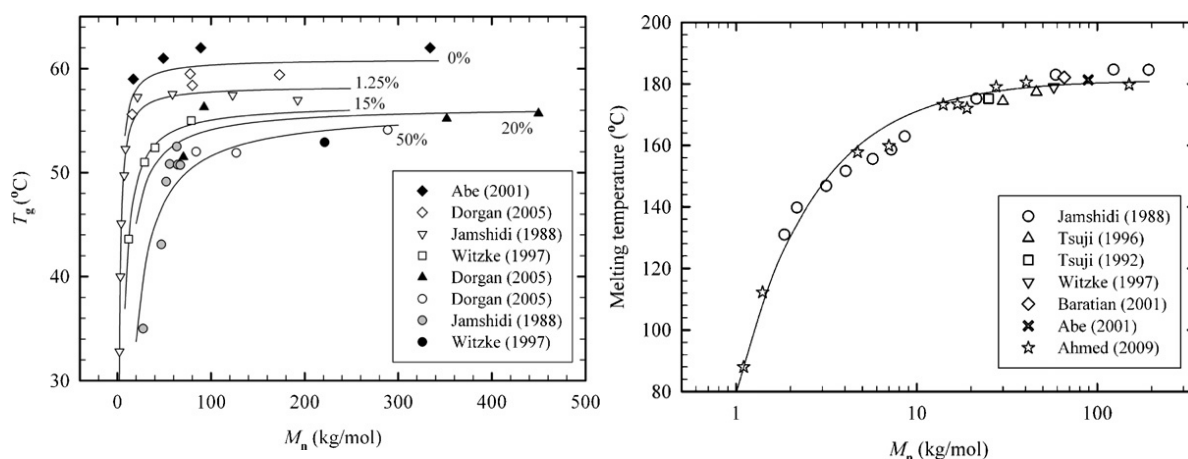


Figure 2.5: Left: Glass transition temperature T_g of linear PLA as a function of molecular weight and isomer composition. Right: Melting temperature T_m of linear PLA with D-LA content less than 1.25 % as a function of molecular weight. Reproduced from [3].

PLA is a semi-crystalline polymer, where crystalline domains are generated in a spherulitic morphology upon unloaded quiescent crystallization [28]. The crystallization and melting behaviour is strongly dependent on the isomer composition of the chains, with respect to isomer ratio and sequence length(s), on the molecular weight, on the temperature history of the bulk material [3] and on the chain architecture [2]. The crystallization window of linear PLA is determined by the glass transition temperature T_g and the melting temperature T_m . Both quantities are functions of the isomeric composition of the chain and its molecular weight. FIGURE 2.5 illustrates these relationships.

2. STATE OF THE ART

At molecular weights $M_n \geq 100$ kg/mol the two quantities attain their asymptotic values. The glass transition shows a certain sensitivity to the isomeric composition. Poly(meso-lactide) has an asymptotic T_g which is lower than that of the homopolymer by 10 K at the most. However, poly(meso-lactide) is crystallizable on processing-relevant time scales only at about $\leq 10\%$ content of the minor repeat unit.

Depending on processing conditions different crystal structures result which strongly affect thermal [10, 148, 150], mechanical [151–154] and barrier [152] properties of the material. The polymorphs of PLA are denoted α' , α , β and γ . In addition to the homocrystalline (hc) phases a stereocomplex crystal [155], so-called scPLA [27], can be formed between PLLA and PDLA chains by heterocrystallization. The melting temperature of scPLA is at around 230°C which is significantly higher than that of hcPLA [156]. Epitaxial crystallization of PLLA on a hexamethylbenzene substrate results in formation of the orthorhombic γ -phase [25]. Recently, observation of the metastable γ -PLLA in racemic mixtures of PLLA and PDLA was reported [26]. Upon fiber drawing from the melt [24] or solution [157] or crystallization from the melt under shear and pressure fields [158] the metastable, frustrated β -phase with trigonal unit cell is formed [159]. Evidence was presented that quiescent crystallization of PLLA at 90°C proceeds in a transient manner via the β -phase, which is converted rapidly into α' -PLLA [160].

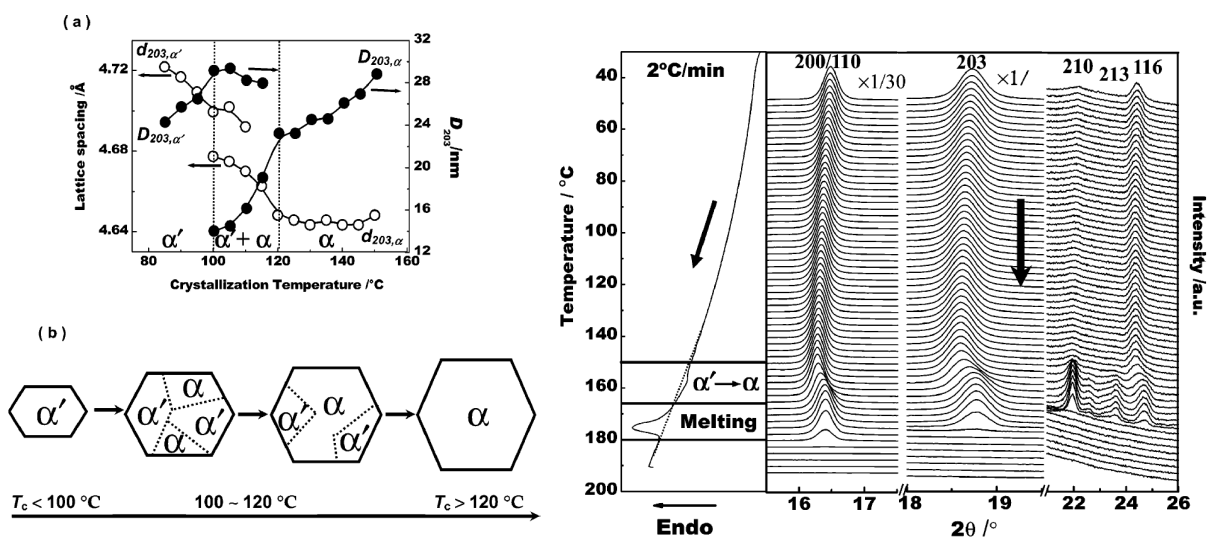


Figure 2.6: Isothermal crystallization temperature-dependent lattice spacing (○) and crystal size (●) based on XRD measurements (a), and crystalline volume fractions (b) of α' -phases and α -phases. Right: Changes in crystalline morphology of PLLA upon heating simultaneously monitored via DSC and WAXD. The sample was isothermally melt-crystallized at 90°C . Reproduced from [39].

Together with the α -phase [161], the α' -phase [47] is most relevant to crystallization from solution or melt crystallization commonly applied in industrial injection molding, blow molding or extrusion processing. The pseudo-orthorhombic α' -phase is formed in PLLA crystallized at temperatures below 120°C , the orthorhombic α -phase is formed

2. STATE OF THE ART

at temperatures above 100 °C. This leads to exclusive crystallization in the one form or the other at high supercooling or low supercooling, respectively, and a crystallization window between 100 °C and 120 °C where both polymorphs in PLLA are formed [39, 49]. This situation is visualized in FIGURES 2.6a and b. Based on XRD measurements α -phase crystals are first observed at an isothermal crystallization temperature of 100 °C. At the expense of the α' -phase crystals their volume fraction increases with increasing isothermal crystallization temperature. At around 120 °C α' -phase crystals are no longer detected. Research of the phenomena described above and in the following is almost exclusively based on studies of the homo-polymer PLLA. It is assumed, however, that those findings hold for enantio-pure PDLA as well.

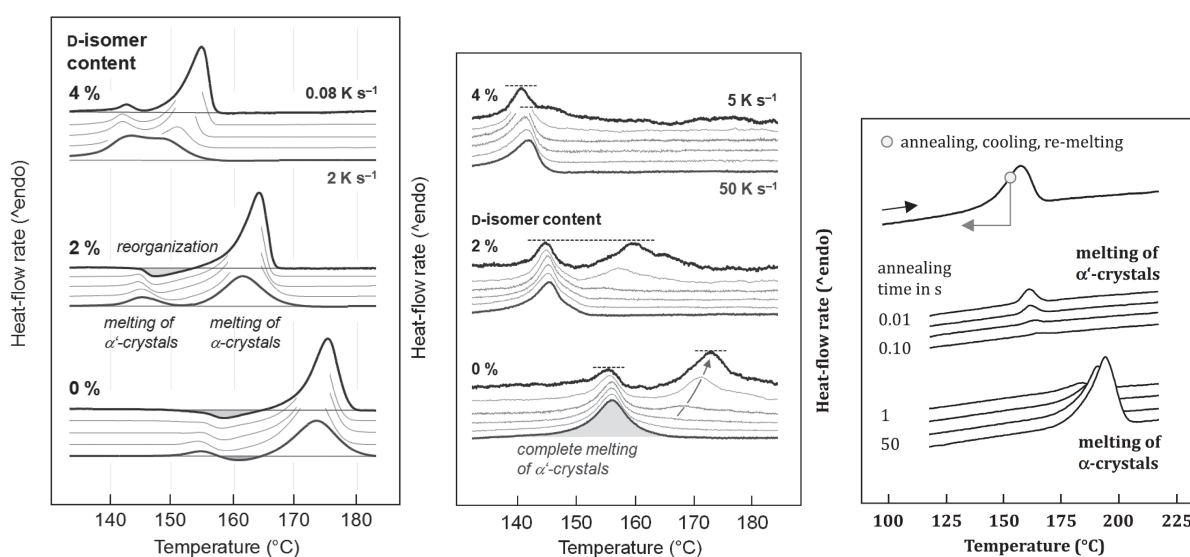


Figure 2.7: Left and middle: Effect of the heating rate on the melting of α' -crystals and reorganization into α -crystals of PLA ($M_W = 120 \text{ kg mol}^{-1}$) with varying D-lactide fraction. Samples were isothermally crystallized at 90 °C for 80 min. Reproduced from [162]. Right: Kinetics of melt-recrystallization of α' -crystals of PLLA ($M_W = 100 \text{ kg mol}^{-1}$) at 150 °C after isothermal crystallization at 90 °C for 80 min. Heating rates were 1000 K/s⁻¹. Reproduced from [163].

Conformational disorder (condis) in the α' -phase leads to an increased lattice spacing and a lower packing density of the helical chain segments as compared to the α -phase crystals (see FIGURE 2.6a) [39, 154]. The enthalpy of melting is significantly lower than that of the stable α -phase [164]. As a consequence, the mesophase condis-crystals are metastable with a stability limit at around 150 °C for the homopolymer and reduced stability limit depending on the isomer-ratio in case of random-co-polymers of PLA [162]. Upon heating an α'/α -transition is observed [165]. The phenomenon is illustrated in FIGURES 2.7 and 2.6 (right side), respectively. Reorganization of the α' -phase into the α -phase proceeds via melting within $\approx 0.1 \text{ s}$ and subsequent rapid recrystallization from the crystal remnants upon annealing. α -phase crystals can be observed after only 1 s of annealing and these domains quickly grow upon further annealing. This so-called melt-recrystallization proceeds faster by about two orders of magnitude than

2. STATE OF THE ART

quiescent crystallization from the isotropic melt at identical temperature [163, 166]. A critical heating rate exists leading to the suppression of the melt-recrystallization of α' -phase crystals into α -phase crystals (see FIGURE 2.7). It decreases with increasing D-lactide content due to the required segregation of chain defects. The critical heating rate to suppress the α'/α -transition also decreases with increasing molecular weight [167]. The dependence of the melting temperature of α' -crystals on the molecular weight seems to be negligible for weights larger than several tens of kg mol^{-1} [167]. There are, however, indications for an increase in melting temperature with crystallization temperature [167]. At low heating rates like in conventional DSC analysis α'/α -transition gives rise to a complex melting behaviour of α -crystals formed at $T_c \geq 100^\circ\text{C}$ and α -crystals formed by melt-recrystallization from α' -remnants [39, 168].

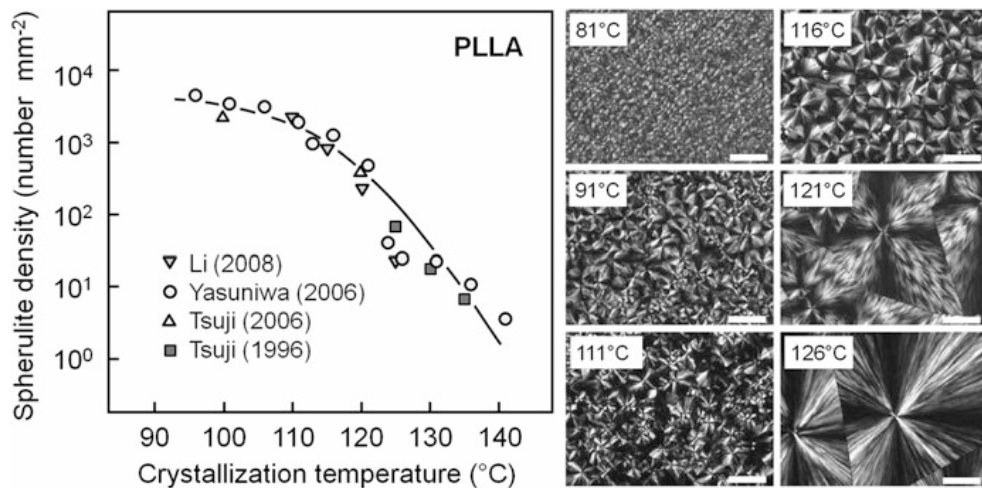


Figure 2.8: Left: Primary crystal nuclei density as assessed from spherulite density as a function of the isothermal crystallization temperature for PLLA ($M_W \in (91, 202) \text{ kg mol}^{-1}$, D-lactide $< 0.7\%$). Right: POM images of isothermally crystallized PLLA ($M_W = 91 \text{ kg mol}^{-1}$). Scale bars represent 50 μm distance. Reproduced from [169].

Overall crystallization behaviour of PLA has been the subject of numerous investigations [16, 17, 19, 20, 22, 28, 36]. Studies were performed predominantly by calorimetry (DSC) to follow overall crystallization and by POM to follow changes in morphology, namely spherulite growth. The density of primary crystal nuclei was assessed from POM images by counting of spherulites in isothermally crystallized PLA samples. As is shown in FIGURE 2.8 the nuclei density is a function of crystallization temperature. The number of spherulites increases with the extend of undercooling of the melt in parallel with the decreased energy required to form a nucleus of critical size in the melt. At large supercooling near the glass transition the diffusion controlled primary nucleation is assumed to decrease again due to increased viscosity of the melt. No data on nuclei densities in this temperature regime is given in the figure nor is it to the best of knowledge of the author reported elsewhere in literature. Again, crystal

2. STATE OF THE ART

nucleation is strongly dependent on the isomeric composition of the polymer chain. In the presence of the enantiomeric partner in the polymer chain the resultant nuclei density due to isothermal crystallization is significantly decreased [170]. The minor repeat-units act as defects in the chain architecture and, thus, hamper crystallization. Crystal nucleation, i.e. formation of primary nuclei, in PLA was extensively studied via fast scanning chip calorimetry (FSC) by Androsch *et al.* [29, 171–173]. The key findings are summarized in FIGURE 2.9. Primary nucleation is a function of the respective crystallization temperature. It can also be observed below the glass transition temperature, however, with a largely increased induction time. Three different regimes of crystallization are observed with respect to the cooling rate of the melt to below the glass transition temperature. At small cooling rates crystal growth and nuclei formation are observed. When the cooling rate is increased nuclei can be formed but can no longer grow. At even higher cooling rates nuclei formation ceases as well.

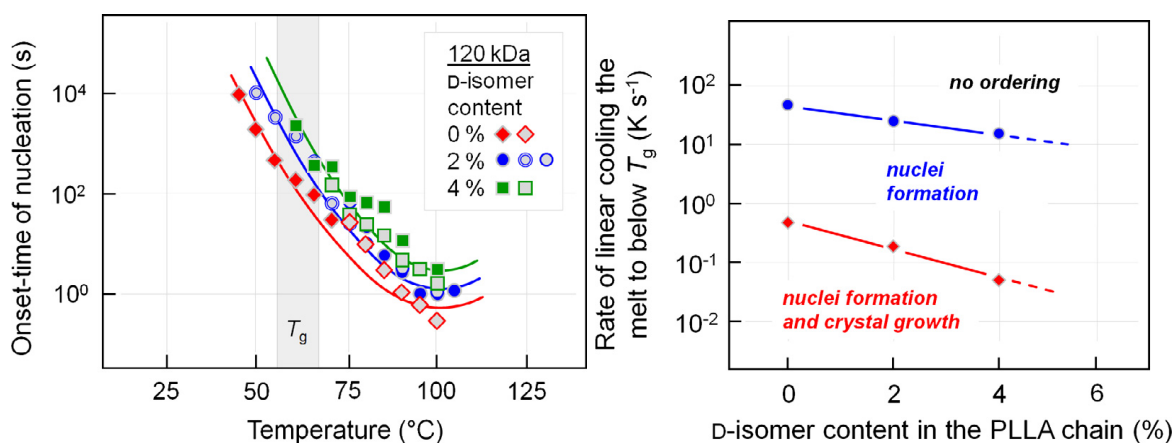


Figure 2.9: Left: Dependence of the onset time of isothermal nuclei formation in PLA ($M_W = 120 \text{ kg mol}^{-1}$) on crystallization temperature and stereo-regularity. Right: Lower critical cooling rates from the PLA melt to below T_g depending on stereo-regularity for either suppression of crystal growth (red diamonds) or suppression of nuclei formation (blue circles). Reproduced from [170].

Minor repeat-units, introduced into the chain via co-polymerization, act as chain defects. An increased onset time of primary crystal formation and reduced critical cooling rate to suppress growth or crystal formation, respectively, indicate exclusion of these chain segments from the crystalline structure at a crystallization stage as early as primary nucleation.

Spherulite linear radial growth rates $G(T_c)$ of PLA were determined in isothermal experiments as a function of the crystallization temperature T_c at variable molecular weight M_W and at variable stereoregularity, i.e. mole fraction of the minor repeat-unit. Typical results are depicted in FIGURE 2.10 and FIGURE 2.11.

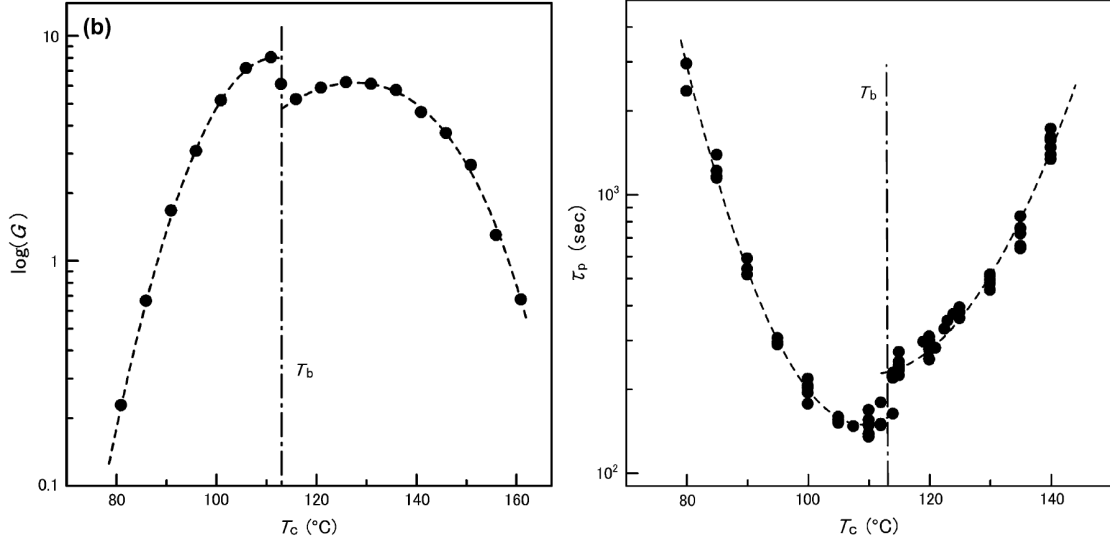


Figure 2.10: Left: Linear radial growth rate $G(T_c)$ of spherulites of PLLA ($M_W = 91 \text{ kg mol}^{-1}$) as a function of crystallization temperature T_c . Right: Time of maximum endothermic heat flux during isothermal crystallization (peak crystallization time τ_p) as a function of the crystallization temperature. Reproduced from [32].

The temperature dependent spherulite growth rate of PLA basically follows a bell-shaped curve. Growth rates are lowest near the glass transition temperature and the melting temperature, respectively, and increase towards intermediate temperatures. Close inspection reveals the existence of a discontinuity in the growth rate at around 120°C dividing the curve into two temperature regions each showing a local maximum in the growth rate curve. The discontinuity in the growth rate curve is close to the temperature designating the transition to an exclusive α -phase crystallization, and it is shifted to lower temperatures with increasing content of the minor repeat-unit (see also the phase-diagram in FIGURE 2.12). The growth rate maxima are ascribed to the growth rate maxima of the α' -phase crystals and the α -phase crystals, respectively. Kinetics of overall isothermal crystallization, i. e. phase transformation of the melt into the solid state via combined nucleation and growth of spherulites, are routinely studied by determination of the crystallization half-time $t_{1/2}$. It denotes the time when half of the amorphous melt has transformed into the crystalline phase. Due to experimental convenience the crystallization half-time is often approximated by the time of maximum endothermic heat flux (peak crystallization time τ_p) in isothermal heat flux measurements. The plot of τ_p versus the crystallization temperature is U-shaped with large peak crystallization times at large and low undercooling, respectively, and a minimum at intermediate temperatures. The plot, thus, reflects the combined effects of crystal nucleation and spherulite growth on the overall crystallization kinetics and shows a discontinuity as well. While a local minimum can be identified on the side of large undercooling, no local minimum can be observed at low undercooling. Here, an increase in the spherulite growth rate is overcompensated by a decreasing spherulite

density (cf. FIGURE 2.8).

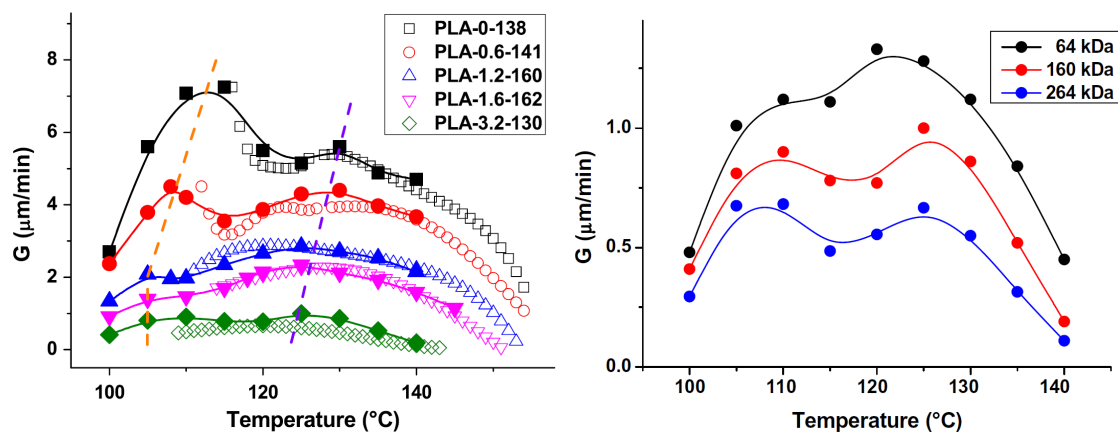


Figure 2.11: Spherulite linear radial growth rates as a function of the crystallization temperature. Left: Effect of chain stereoregularity (wt% of D-lactic acid units, point-separated number in the sample designator) and molecular weight (kg mol^{-1} , three last digits in the sample designator). Right: Effect of molecular weight on the growth rate of PLA with ≈ 3 wt% D-lactic acid units. Reproduced from [33, 34].

Di Lorenzo *et al.* determined the effect of molecular weight and stereoregularity on temperature-dependent spherulite growth rates of PLA (see FIGURE 2.11). To this end classical isothermal procedures (filled symbols) were applied. Spherulite growth rates were determined from the derivative of the spherulite radius with respect to time. In addition, a non-isothermal procedure (open symbols) was developed to determine temperature-dependent spherulite growth rates [30, 31]. In that process the sample was cooled with a constant cooling rate from the melt and spherulite radii were monitored as a function of temperature. Then, the derivative of the spherulite radius with respect to temperature was calculated and multiplied with the cooling rate to obtain the linear radial spherulite growth rate. Results from both methods show good agreement as can be seen in FIGURE 2.11.

At fixed isomer-ratio the growth rates decreased with increasing molecular weight. While the temperature of the discontinuity in the growth rate curve was constant the relative height of the local maxima shifted to lower undercooling with decreasing molecular weight.

At constant molecular weight the growth rates decreased with increasing amount of the minor repeat-unit in the chain reflecting the defect-nature of these units. While the local maximum at large undercooling is strongest in case of the homopolymer it decreases with decreasing optical purity in favour of the maximum at low undercooling. Both the temperature of the discontinuity and the peak temperatures of the maxima are shifted towards lower absolute temperatures. This trend is in parallel with a decrease in the melting temperature (see FIGURE 2.12).

Complementing the above investigations Song *et al.* [48] demonstrated that while the

2. STATE OF THE ART

transition temperature of exclusive α' -phase crystallization and α -phase crystallization, respectively, decreases with decreasing optical purity, i. e. stereoregularity, the temperature for the transition from growth regime II to regime III of Lauritzen-Hoffman theory [174–176] seems to be unaffected (see FIGURE 2.12).

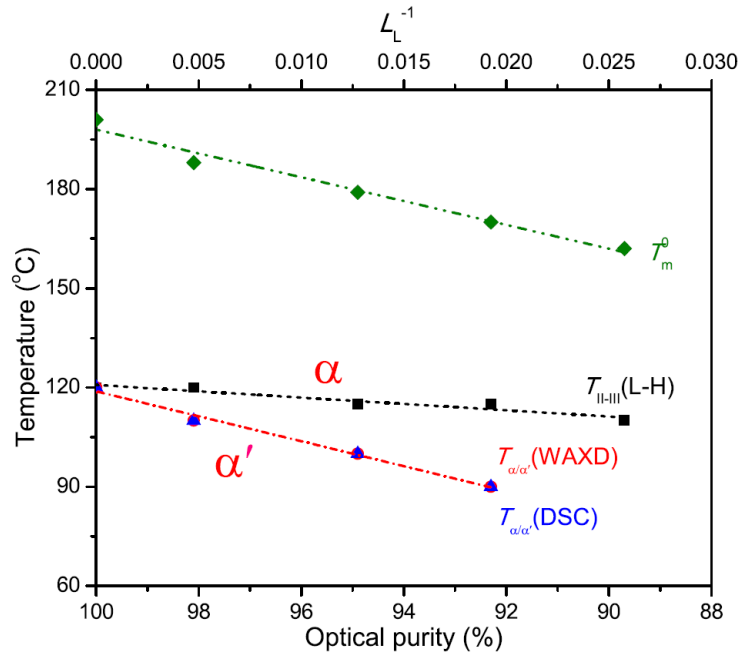


Figure 2.12: Temperature-dependent crystal polymorphism of PLA ($M_W \in (140 - 180) \text{ kg mol}^{-1}$) as a function of the optical purity (i. e. stereoregularity or isotactic sequence length L_L of the chain, respectively). T_m^0 denotes the equilibrium melting temperature, $T_{||-|||}$ (L-H) denotes the temperature of change of gross crystallization behaviour from growth regime II to growth regime III of Lauritzen-Hoffman theory, $T_{\alpha'/\alpha}$ (WAXD) and $T_{\alpha'/\alpha}$ (DSC) denote the temperature limit of α' -phase crystallization only and α -phase crystallization only, respectively, as determined by WAXD and DSC. Reproduced from [48].

Overall crystallization kinetics of PLA are rather slow. This becomes apparent immediately when considering the crystallization half-times or peak crystallization times, respectively, which are of the order of minutes (see FIGURE 2.10) and, thus, are rather large compared to other thermoplastic polymers. Consequently, much effort was put into the study of heterogeneous nucleation of PLA [177]. It was reported that addition of 1 wt% talc as nucleating agent and 5 wt% polyethylene glycol (PEG) as plasticizer greatly reduced crystallization half-times and increased overall relative crystallinity up to 40% of injection molded PLA (2% D-LA) [178]. Addition of micro-sized talc particles to PLA (4.5% D-LA) was superior to addition of nano-sized nucleating agents like nanoclay in terms of crystallization half-times while no effect was found on overall relative crystallinity [179]. Poly(ethylene glycol) grafted graphene oxide was utilized as a simultaneous heterogeneous nucleation agent and chain mobility promoter in solution-cast PLLA films [180].

Another approach to speed up overall crystallization of PLA is the blending of PLLA and PDLA. In equimolar mixtures (rac-PLA) crystallization from the melt leads to formation and growth of sc-spherulites [18, 181]. Spherulite growth rates of sc-spherulites are larger than those of hc-spherulites at the same isothermal crystallization temperature and an increased spherulite density is observed. An increased spherulite nucleation is also observed in PLLA blended with small amounts of up to 10 wt% of PDLA [182, 183]. As the melting point of sc-PLA is much larger than that of hc-PLA stereo-complex crystals can act as heterogeneous nucleation sites in the molten PLLA matrix at temperatures below 200 °C.

2.5 SALS studies of PLA crystallization

In this subsection a comprehensive review of works applying depolarized SALS to the study of the crystalline morphology of PLA is presented. For a description of the theory of light scattering from spherulites and the interpretation of specific scattering patterns the reader is referred to SUBSECTION 4.2.

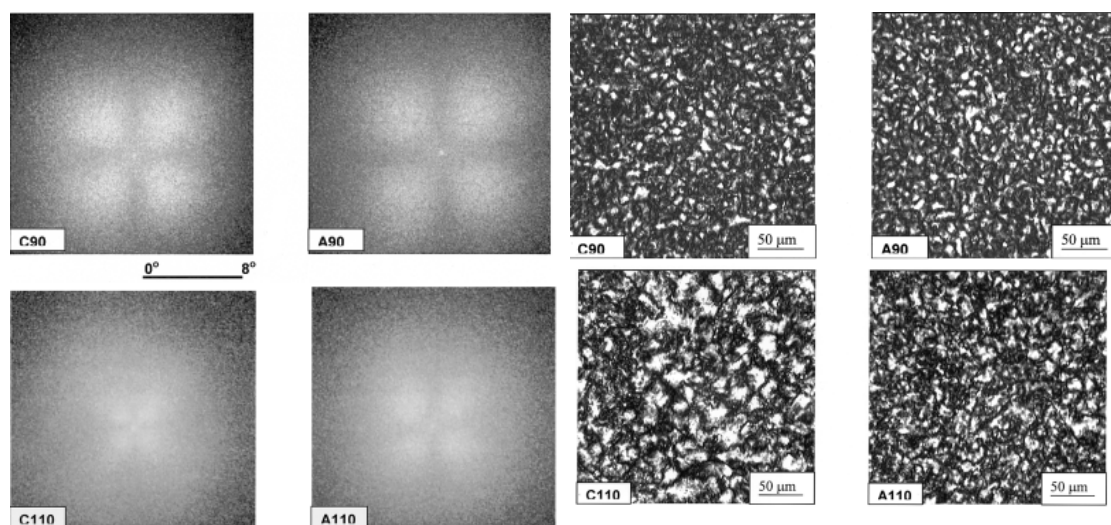


Figure 2.13: Depolarized SALS scattering patterns (left) and corresponding polarized light microscopy images (right) of isothermally crystallized PLA. The sample names designate the thermal history and crystallization temperature. Samples were either melt-quenched (C) or re-heated to the crystallization temperature after melt-quenching to the glassy state (A). Modified reproduction from [62].

The application of depolarized SALS to the study of isothermal crystallization of PLA ($M_W = 166 \text{ kg mol}^{-1}$, 4.1 % D-isomer content) either directly quenched from the melt (process C) to the respective temperature or re-heated from the glassy state after quenching from the melt to the amorphous state (process A), respectively, was reported in [62]. Selected results are depicted in FIGURE 2.13. Re-heated samples showed

2. STATE OF THE ART

a higher spherulite density compared to melt-quenched samples due to activation of crystal nuclei which were formed prior to isothermal crystallization during quenching to room-temperature. The difference in spherulite density was accompanied by a difference in average spherulite size. As evidenced from static depolarized SALS measurements the average spherulite size was larger in case of isothermally crystallized samples quenched directly from the melt state. Static SALS patterns were recorded on photographic film for evaluation. Small angle x-ray scattering (SAXS) measurements showed that the long period signal was independent of the thermal history of the sample but was determined by the crystallization temperature only. As the long period signal reflects the lamellar thickness of PLA crystals this suggests invariance of the crystallization process in terms of the lamellar morphology with respect to sample preparation by either process A or B.

The isothermal crystallization behaviour of PLLA ($M_W = 117 \text{ kg mol}^{-1}$) at 75°C , 85°C and 90°C was investigated by simultaneous dielectric relaxation spectroscopy (DRS) and depolarized SALS [63]. Results are illustrated in FIGURE 2.14. Scattering patterns were recorded on photographic film at various times of the crystallization process. While the average spherulite size was examined at discrete times radial spherulite growth rates were not determined. Instead temporal evolution of overall relative crystallinity was investigated and correlated with the sample morphology. It was shown

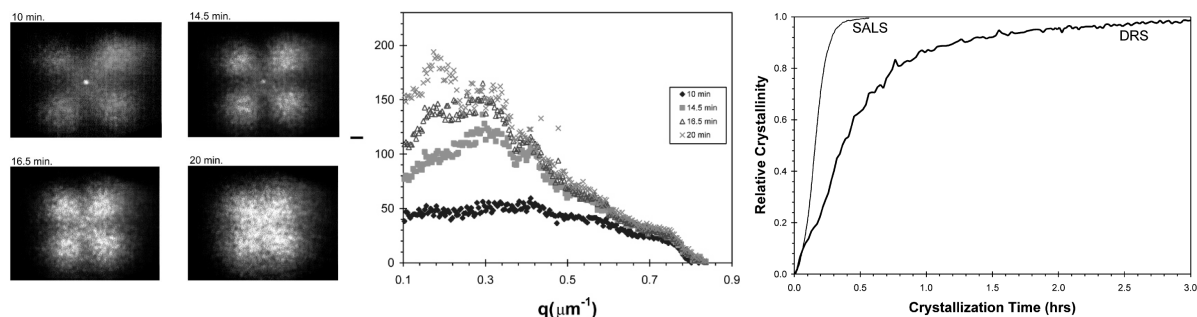


Figure 2.14: Evolution of spherulite size in PLLA crystallized at 90°C after quenching from the melt as determined by depolarized SALS (left, middle). Right: Temporal evolution of the overall relative crystallinity determined from the normalized reduction in light transmission of the primary beam (SALS) and normalized reduction in the dielectric permittivity (DRS). Reproduced from [63].

that SALS was more sensitive to the onset of crystallization than DRS. Detection of the characteristic four-lobed depolarized scattering pattern preceded the respective signals from DRS. According to the authors, on the other hand, DRS was more sensitive for following overall crystallization kinetics in PLLA. SALS showed that at volume filling by spherulites transmission of the primary beam reached its minimum. At that stage overall crystallinity of the sample was 30% as determined by WAXS and 60% as measured by DRS, respectively. A further decrease in relaxed low frequency permittivity was attributed to continued crystallization of the remaining amorphous fraction.

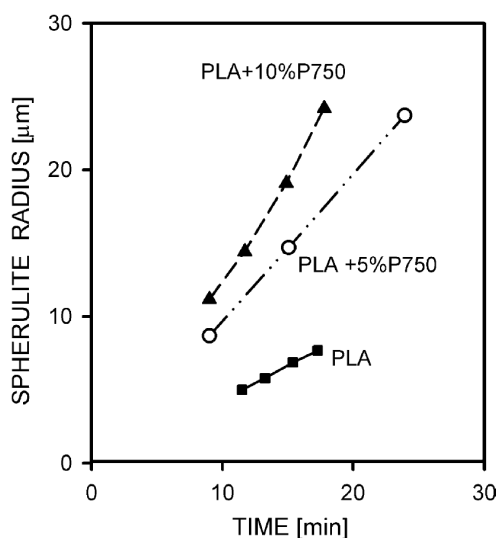


Figure 2.15: Spherulite size determined by depolarized SALS versus time for neat and plasticized PLA ($M_W = 166 \text{ kg mol}^{-1}$, 4.1 % D-isomer content) isothermally crystallized at 130°C after quenching from the melt. P750 denotes a monomethyl ether of poly(ethylene glycol) terminated with a hydroxyl and a methyl group at opposite chain ends ($M_W = 0.750 \text{ kg mol}^{-1}$). Reproduced from [64].

The effect of plasticization of PLA ($M_W = 166 \text{ kg mol}^{-1}$, 4.1 % D-isomer content) with poly(ethylene glycol)s (PEG) ($M_W = 0.400 - 0.750 \text{ kg mol}^{-1}$) which were terminated with different end groups was studied in [64]. Isothermal radial spherulite growth rates were determined via depolarized SALS at 130°C after quenching from the melt (see FIGURE 2.15). To this end scattering patterns were recorded on photographic film. Time-dependence of spherulite radii yielded the growth rates. Plasticization lead to a significant increase in the growth rates. Non-linear time-dependence of spherulite size at addition of 10 % plasticizer indicates accelerated spherulite growth. No effect of differently terminated PEGs on the growth rates was detected.

Recently, application of time-resolved depolarized SALS to the study of spherulite growth rates of PLA was reported [65]. A PLLA homopolymer ($M_W = 144 \text{ kg mol}^{-1}$), a PLA random copolymer ($M_W = 184 \text{ kg mol}^{-1}$, 5 % D-isomer content) and a mixture of PLLA with 1 wt% of a PDLA homopolymer ($M_W = 112 \text{ kg mol}^{-1}$) were isothermally crystallized on a dual hot stage. Near instantaneous quenching to the crystallization temperature was achieved by pneumatically moving the sample from one hot stage which was kept at melting temperature to the other one kept at the respective crystallization temperature. For measurements of spherulite radii at high supercooling ($T_c < 120^\circ\text{C}$) depolarized SALS patterns were projected onto a screen and recorded by a digital camera at an acquisition rate of 1 Hz. At low supercooling ($T_c > 120^\circ\text{C}$) spherulite radii were determined by POM. Selected results are depicted in FIGURE 2.16. Derivation of the average spherulite radius with respect to time yielded the isothermal linear radial spherulite growth rate G dependent on crystallization temperature.

2. STATE OF THE ART

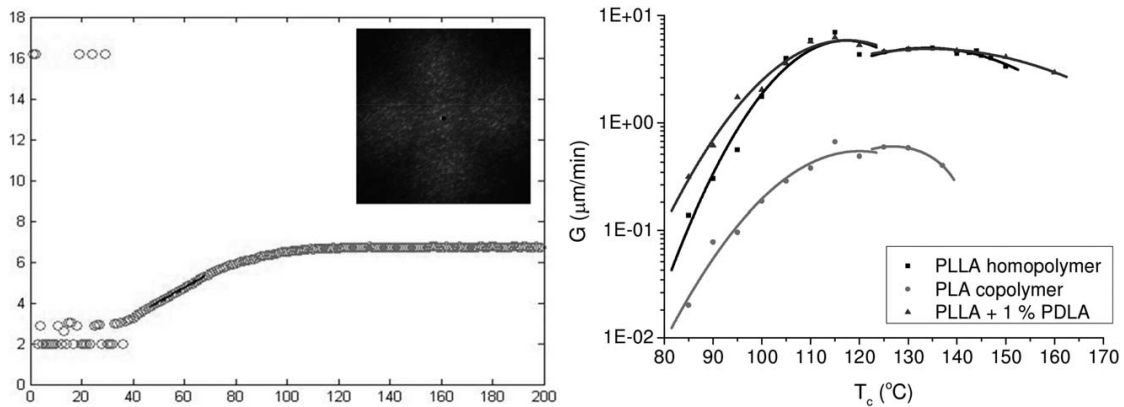


Figure 2.16: Left: Average spherulite radius (vertical axis [μm]) as a function of isothermal crystallization time (horizontal axis [s]) of a PLLA/1%PDLA mixture crystallized at $100\text{ }^\circ\text{C}$. The inset shows a typical four-lobed depolarized scattering pattern. Right: Radial spherulite growth rates as a function of crystallization temperature T_c determined from SALS measurements ($T_c < 120\text{ }^\circ\text{C}$) and POM measurements ($T_c > 120\text{ }^\circ\text{C}$). Reproduced from [65].

SALS measurements yielded the discontinuity in the crystal growth curve of PLA at $T_c = 120\text{ }^\circ\text{C}$ [32–34] and available crystal growth data allowed assessment of the dependency of crystal nuclei density on crystallization temperature also showing the discontinuity. It was proposed that α' and α crystals might grow from different nuclei. Static depolarized SALS was applied to the study of the crystal morphology of a 1:1 poly(L-lactide)/poly(D-lactide) blend (PLLA: $M_W = 210\text{ kg mol}^{-1}$. PDLA: $M_W = 212\text{ kg mol}^{-1}$) [184]. Amorphous films were prepared by hot-pressing of blend sediments and quenching into ice water. Those blend sediments were obtained by solution-precipitation of a 1:1 PLLA/PDLA chloroform solution into methanol, which is a non-solvent for PLA. The films were annealed (cold crystallized) at $80\text{ }^\circ\text{C}$ for 5 h and at $120\text{ }^\circ\text{C}$ for 1 h to yield fully crystallized samples in the α' -phase and the α -phase, respectively. The annealed films did not contain stereocomplex crystals. Instead, PLLA and PDLA separately formed homocrystals as evidenced by XRD and FTIR measurements.

Subsequently, the films were heated to $190\text{ }^\circ\text{C}$ and $200\text{ }^\circ\text{C}$, respectively, which is above the melting temperature of the α' -phase crystals and the α -phase crystals, and the formation of stereocomplex crystals from the melt was studied. The results are depicted in FIGURE 2.17.

The SALS scattering patterns are indicative for a qualitative difference in the morphology of sc-crystals depending on the thermal history of the sample. From the characteristic four-lobed scattering patterns (c, d) it was concluded that crystallization of samples annealed at $120\text{ }^\circ\text{C}$ leads to spherulitic aggregates of sc-crystals. On the other hand, a so-called + -type scattering pattern (a, b) was observed for samples annealed at $80\text{ }^\circ\text{C}$ and melt-recrystallized at either $190\text{ }^\circ\text{C}$ or $200\text{ }^\circ\text{C}$. The authors concluded, that such scattering patterns, along with results from DSC, suggest formation and one-

2. STATE OF THE ART

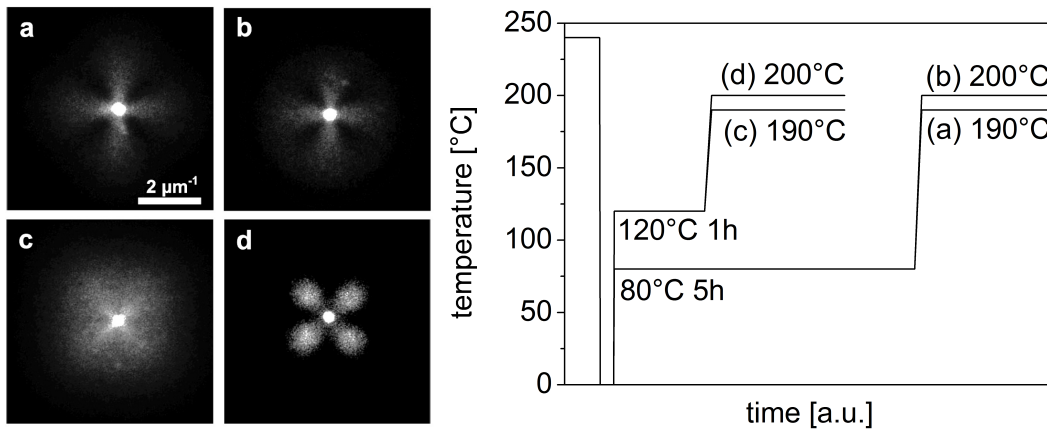


Figure 2.17: Left: Depolarized SALS patterns of racemic PLLA/PDLA blends crystallized at 190 $^{\circ}\text{C}$ (a,c) and 200 $^{\circ}\text{C}$ (b,d) for 2 h after prior annealing at 80 $^{\circ}\text{C}$ (a,b) and 120 $^{\circ}\text{C}$ (c,d). Reproduced from [184]. Right: Corresponding temperature-time protocols to the scattering patterns a-d.

dimensional growth of rod-like sc-crystals.

The effect of high-pressure CO_2 treatment on the temperature-dependent development of crystalline morphology in transparent melt-pressed films of PLLA ($M_W = 320 \text{ kg mol}^{-1}$) was investigated in [185]. The findings by depolarized SALS are depicted in FIGURE 2.18. The untreated samples show the familiar four-lobed scattering pattern indicative for spherulitic crystalline morphology. A transition towards the +-type scattering pattern can be observed under high-pressure CO_2 treatment at low annealing temperatures which is ascribed to the transition to a rod-like crystalline superstructure.

2. STATE OF THE ART

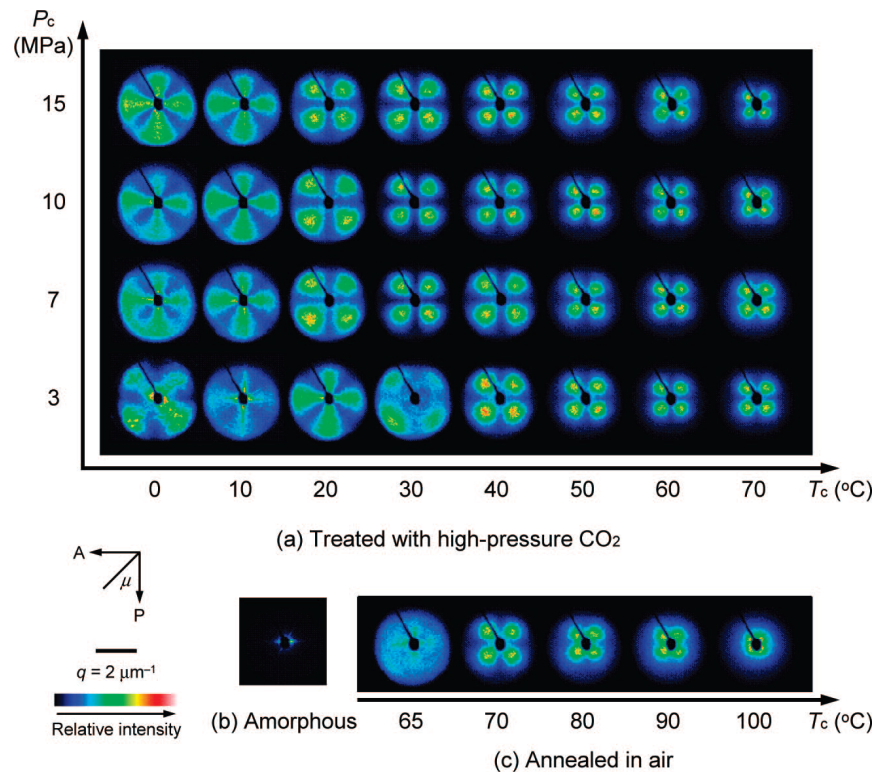


Figure 2.18: Depolarized SALS patterns of films annealed at various temperatures under high-pressure CO₂ treatment (a) and annealed under ambient conditions at the indicated temperatures (c). Reproduced from [185].

3 Small angle light scattering instrument

3.1 Light scattering fundamentals

Extensive monographs on the theory of light scattering are available [96, 186, 187]. Hence, only the most vital aspects of the theory as well as the most important equations are reviewed in the following section.

Whenever matter like an ensemble of single molecules or larger particles is irradiated by light the oscillating electric field sets the electric charges of those entities into motion, thus, inducing dipoles in that matter. These dipoles oscillate synchronously with the incident wave and subsequently emit secondary radiation. This process is called elastic scattering. There is no frequency change from the incident to the scattered light, accordingly wavelengths remain constant.

FIGURE 3.1 depicts the geometry of the general scattering problem. An arbitrary particle in the center of which the origin of a Cartesian coordinate system is located is illuminated by a linearly polarized, monochromatic, harmonic plane wave with its electric field vector parallel to the x-axis and propagating in z-direction with wavevector

$$\vec{k} = \frac{2\pi n}{\lambda_0} \vec{e}_k \quad (3.1)$$

where λ_0 is the vacuum wavelength of the incident light and n is the refractive index of the medium surrounding the particle. Since only elastic scattering is considered the moduli of incident and scattered wave vector are equal in magnitude $|\vec{k}_i| = |\vec{k}_s| = k$. The scattering angle is defined as the angle enclosed by the (forward) direction of the incident beam \hat{e}_z and the scattering direction \hat{e}_r . Both directions define the scattering plane which makes the azimuthal angle ϕ with the \hat{e}_x -direction¹. By a rigorous treatment of the scattering problem it can be shown that in the far-field approximation the incident and the scattered electric fields are related via

$$\begin{pmatrix} E_{\parallel s} \\ E_{\perp s} \end{pmatrix} = \frac{\exp\{ik(r-z)\}}{-ikr} \begin{pmatrix} S_2 & S_3 \\ S_4 & S_1 \end{pmatrix} \begin{pmatrix} E_{\parallel i} \\ E_{\perp i} \end{pmatrix} \quad (3.2)$$

where the elements $S_i(\theta, \phi)$ are functions of the particle polarizability and in general depend on scattering angle θ and azimuthal angle ϕ . The elements S_i form the amplitude scattering matrix \mathbf{S} . The distance z is the projection of \vec{r} , the vector to the point of observation, onto the propagation direction of the incident beam. The components of the incident and scattered electric fields are defined parallel E_{\parallel} and perpendicular E_{\perp} with respect to the plane of scattering.

For any spherical particle with isotropic polarizability the amplitude scattering matrix reduces to

$$\begin{pmatrix} S_2 & S_3 \\ S_4 & S_1 \end{pmatrix} = \begin{pmatrix} S_2(\theta) & 0 \\ 0 & S_1(\theta) \end{pmatrix} \quad (3.3)$$

¹In the literature on SALS of polymer spherulites the angle ϕ is usually denoted μ [52].

3. SMALL ANGLE LIGHT SCATTERING INSTRUMENT

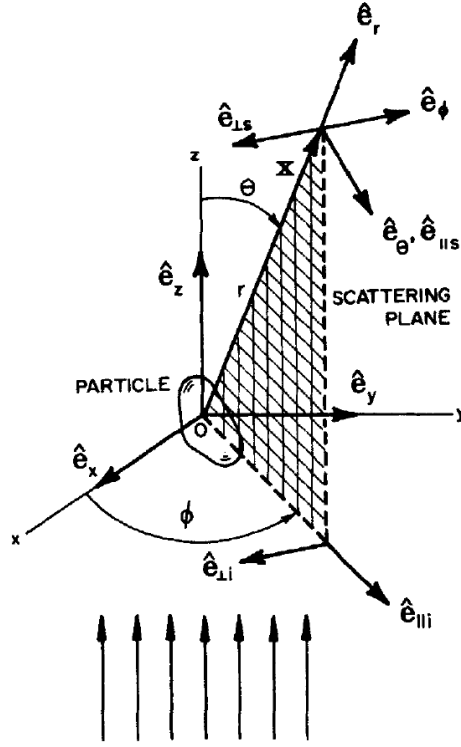


Figure 3.1: Geometry of the scattering problem. The incident radiation indicated by the arrows in the lower part of the figure is propagating in z-direction. Reproduced from [187].

since the cross-polarization elements $S_3 = S_4 = 0$ and the co-polarization elements S_1 and S_2 depend on the scattering angle θ only [186].

Exact expressions for the elements of the amplitude scattering matrix exist only for a limited number of cases the most important of which is a single homogeneous dielectric isotropic sphere of arbitrary radius R and arbitrary refractive index dispersed in a non-absorbing medium.

This system is described in terms of the the relative complex refractive index $m = m' + im''$ given by the ratio of the refractive indices of the particle n_p and the ambient medium n , respectively, and the size parameter $x = kR$ with wave number k in the ambient medium and radius of the sphere R .

Mie Scattering. Derived from first principles of electrodynamic theory Mie presented a general solution now referred to as Lorenz-Mie theory recognizing previous work of Lorenz to the scattering problem of an isotropic sphere [75, 76]. The elements of the amplitude scattering matrix are given by

$$S_1(\theta) = \sum_{n=1}^{\infty} \frac{2n+1}{n(n+1)} (a_n \tau_n(\cos \theta) + b_n \tau_n(\cos \theta)) \quad (3.4)$$

$$S_2(\theta) = \sum_{n=1}^{\infty} \frac{2n+1}{n(n+1)} (a_n \tau_n(\cos \theta) + b_n \tau_n(\cos \theta)) \quad (3.5)$$

3. SMALL ANGLE LIGHT SCATTERING INSTRUMENT

where coefficients a_n and b_n are functions of spherical Bessel functions, which take the relative refractive index m and size parameter x as arguments. The functions $\pi_n(\cos \theta)$ and $\tau_n(\cos \theta)$ are expressed in terms of Legendre polynomials. To attain convergence of the infinite series summation in EQUATIONS (3.4) and (3.5) a finite number N of terms given by

$$N = x + 4x^{1/3} + 2 \quad (3.6)$$

is required [187]. In numerical calculations N is used to truncate the series [188, 189]. Subsequently, the transverse components of the scattered electric field are obtained from EQUATION (3.2) as

$$-E_{\perp s} = -E_{\phi} = \frac{\exp\{ik(r-z)\}}{-ikr} S_1(\theta) \sin \phi \quad (3.7)$$

$$E_{\parallel s} = E_{\theta} = \frac{\exp\{ik(r-z)\}}{-ikr} S_2(\theta) \cos \phi \quad (3.8)$$

leading to the intensity of the scattered light in an arbitrary direction

$$I_s(\theta, \phi) = \frac{i_1}{k^2 r^2} \sin^2 \phi + \frac{i_2}{k^2 r^2} \cos^2 \phi = I_{\phi} + I_{\theta} \quad (3.9)$$

with

$$i_1 = |S_1(\theta)|^2 \text{ and } i_2 = |S_2(\theta)|^2. \quad (3.10)$$

In EQUATION (3.9) I_{ϕ} and I_{θ} arise from the incident electric field perpendicular and parallel to the plane of scattering (see FIGURE 3.1). The scattered fields are out of phase by

$$\tan \delta = \frac{\text{Re}S_1 \text{Im}S_2 - \text{Re}S_2 \text{Im}S_1}{\text{Re}S_1 \text{Re}S_2 + \text{Im}S_1 \text{Im}S_2}. \quad (3.11)$$

The scattering amplitude functions for an opaque sphere are given by

$$S_1(\theta) = S_2(\theta) = x^2 \frac{2J_1(x \sin \theta)}{x \sin \theta}. \quad (3.12)$$

Employing Babinet's principle the same holds for the diffraction of light by a circular aperture (Fraunhofer diffraction limit). Consequently, from EQUATION (3.9) the Airy pattern

$$I(\theta) = \frac{I_0 R^4 k^2}{r^2} \left(\frac{2J_1(x \sin \theta)}{x \sin \theta} \right)^2 \quad (3.13)$$

is obtained, where J_1 is a first order Bessel function of the first kind.

Rayleigh Scattering. When scattering entities are small compared to the wavelength²

$$2kR \ll 1 \quad (3.14)$$

²"say $\lambda/20$ " [186, p. 395]

3. SMALL ANGLE LIGHT SCATTERING INSTRUMENT

$$2kR|m| \ll 1 \quad (3.15)$$

the electric field is homogeneous over the whole particle and the polarization is established quasi-instantaneously in the whole volume.

Then, in analogy to EQUATION (3.3), the amplitude scattering matrix is given by

$$\begin{pmatrix} S_2(\theta) & 0 \\ 0 & S_1 \end{pmatrix} = ik^3\alpha \begin{pmatrix} \cos\theta & 0 \\ 0 & 1 \end{pmatrix} \quad (3.16)$$

where α is the polarizability of the particle [186]. In general, α is a tensor. However, it reduces to a scalar for particles with isotropic polarizability.

By inserting EQUATION (3.16) into EQUATION (3.9) the famous result of Rayleigh for the angular distribution of the scattered light of a particle much smaller than the wavelength is retrieved

$$\frac{I_s}{I_0} = \frac{k^4\alpha^2}{r^2} (\sin^2\phi + \cos^2\theta \cos^2\phi) = \frac{k^4\alpha^2}{r^2} \sin^2\Psi \quad (3.17)$$

where Ψ is the angle enclosed between the direction of scattering \vec{e}_r and the dipole parallel to the x-axis. Here, the identity

$$\sin^2\Psi = 1 - \sin^2\theta \cos^2\phi \quad (3.18)$$

was used which can be derived from geometric considerations.

In incident natural light all orientations of the electric field vector are present in equal shares such that

$$\langle \sin^2\phi \rangle = \langle \cos^2\phi \rangle = \frac{1}{2} \quad (3.19)$$

and from EQUATION (3.9) follows

$$I = \frac{i_1 + i_2}{2} \frac{I_0}{k^2 r^2} = \frac{k^4 \alpha^2}{r^2} I_0 \frac{1 + \cos^2\theta}{2}. \quad (3.20)$$

EQUATION (3.17) accounts for the features of Rayleigh scattering, i. e. the proportionality to λ^{-4} , equi-intensity and full linear polarization when observed under an angle of $\Psi = 90^\circ$. Also the proportionality of the scattered intensity to the square of the particle volume is given since the polarizability α is a volume-based quantity. In FIGURE 3.2 the angular intensity distribution is depicted for the three different polarization states of incident light.

Rayleigh-Deybe-Gans theory. In RDG theory the boundary conditions EQUATIONS (3.14) and (3.15) are relaxed such that

$$|m - 1| \ll 1 \quad (3.21)$$

$$2kR|m - 1| \ll 1 \quad (3.22)$$

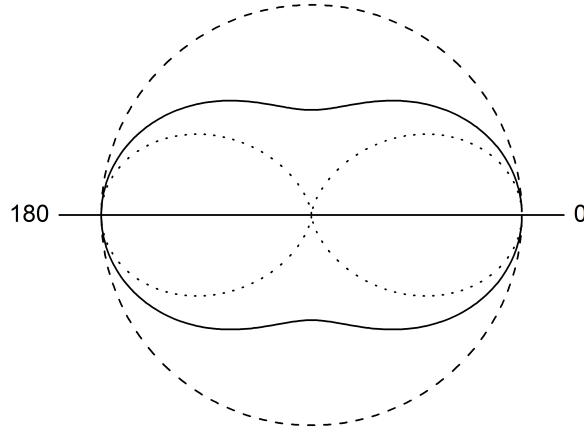


Figure 3.2: Polar diagram of the angular intensity distribution in the scattering plane for Rayleigh scattering. The incident light is vertically polarized (- - -), horizontally polarized ($\cdot \cdot \cdot$) or unpolarized (—).

the refractive index of the particle is close the refractive index of the ambient medium and the field inside the particle can be approximated by the incident field. In particular, phase and amplitude of the traversing incident ray (and the scattered ray) are unaffected by the particle. As a consequence intra-particle subvolumes are in a fixed phase-relation to each other. Thus, the angular intensity distribution is given by an interference pattern of scattered wavelets from all subvolumes of the particle.

This scattering behaviour is universal to all electromagnetic radiation. Therefore, introduction of the scattering vector

$$\vec{q} = \vec{k}_s - \vec{k}_i = \frac{4\pi n}{\lambda_0} \sin\left(\frac{\theta}{2}\right) \quad (3.23)$$

which relates the incident and scattered wave via their wave vectors \vec{k}_i and \vec{k}_s , respectively, represents a convenient way for comparing scattering experiments carried out with different light sources or in different media since q normalizes the scattering angle to the wavelength.

Also, the collective scattering from all subvolumes from all particles in the illuminated sample volume then yields an angular intensity distribution which is characteristic for the geometry of the scattering particles, e. g. spherical, rod-like, coil-like etc. It is expressed as the so-called form factor

$$P(\vec{q}) = \frac{I_s(\vec{q})}{I_s(0)} \quad (3.24)$$

which is a function of q and is normalized to the forward scattering at $\theta = 0$ and which is $P(\theta \neq 0) < 1$ for any particle shape.

3.2 General description of the setup

A general overview of the home-built small angle light scattering apparatus is given with special emphasis on the interplay of the various components and the working principle of the device. A more detailed description of the components, data-acquisition and -processing as well as calibration procedures is given in SUBSECTION 3.3.

FIGURE 3.3 depicts the setup. The attenuated beam of a linearly polarized laser passes through a hole in the thermally-controlled stage and transmits the sample. A first lens collects the scattered light and focuses the primary beam onto a beam stop in its back focal plane thus effectively eliminating it from the detection optics. Subsequently, a second lens images the scattering pattern onto the detector of a digital camera. The camera is connected to a personal computer for data transfer and storage. An analyzer is utilized for measurements of scattered light at a selected state of polarization. A dedicated software supplied with the camera is used to control data acquisition and to set the respective imaging parameters.

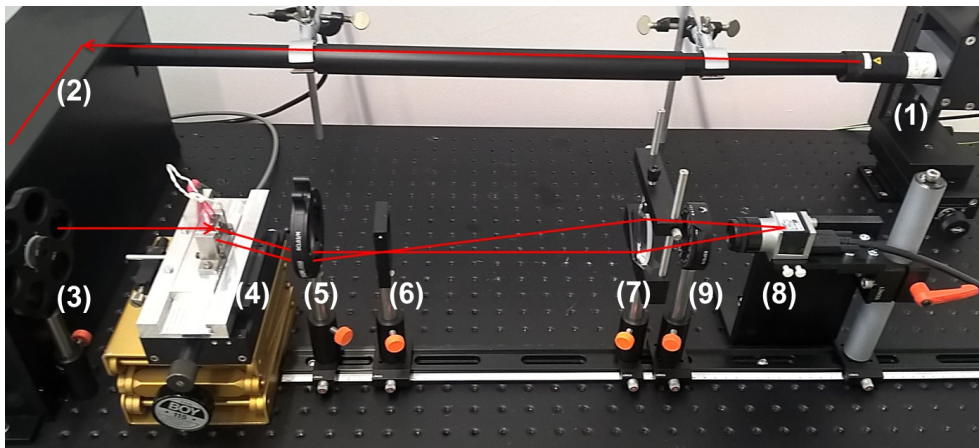


Figure 3.3: Overview of the home-built small angle light scattering instrument. The linearly polarized beam of a He-Ne laser (1) was deflected by two mirrors (2), attenuated (3) and transmitted the sample through a hole in the temperature-controlled stage (4). A Fourier lens (5) collected the scattered intensity and focused the primary beam in its back focal plane onto a beam stop (6). Subsequently, the objective lens (7) imaged the scattering pattern onto the detector (8). An analyzer (9) was utilized for measurements of depolarized scattering.

Two different sample stages were developed in-house. The first (colloid suspension stage) could accommodate up to five scattering cells for measurements of colloidal suspensions. Its temperature could be varied from room temperature up to several tens of degrees by a water-thermostat. The second sample stage (polymer melt stage) was used for measurements of polymer melts in the temperature range from 30 °C to 250 °C. It was equipped with electrical resistive heaters, respectively, and featured a passive convective cooling. The temperature was controlled by an electronic interface

which was connected to a personal computer. In this way, user defined temperature-time profiles, both isothermal and dynamic, could be realized via specifically developed software routines.

3.3 In-depth description of the SALS instrument

Light source. A continuous wave He-Ne laser (G040804000, Qioptiq Photonics GmbH & Co. KG, Göttingen, Germany) with a vacuum wavelength $\lambda_0 = 632.8$ nm was used as the light source for the small angle scattering instrument. The 2 mW laser was operated in single-mode (TEM00) and was linearly polarized. TEM00 denotes the fundamental, i. e. single-lobed, transverse electromagnetic mode (TEM) of the laser resonator [190]. The beam diameter was 0.75 mm and the beam divergence was only 1.2 mrad. Both, the beam profile (near-Gaussian across the beam cross section) and the linear polarization of the laser (polarization $> 500:1 = 99.8\%$) were verified by standard laser characterization techniques to ensure highest quality of the scattering experiments [Hem16].

A He-Ne (gas) laser was deliberately preferred over a (semiconductor) laser diode. While both lasers are widespread sources for high-intensity coherent radiation and reasonably priced the latter requires substantial measures to achieve the same laser beam quality as a He-Ne laser [95]. He-Ne lasers have a long average lifetime of over 10000 hours while meticulous heat-management is required in case of laser diodes to prevent early hardware failure. Above all, semiconductor laser diodes come with an asymmetric, highly divergent beam profile by design necessitating complex secondary optics for collimation and beam shaping while the opposite is true for He-Ne lasers [190, 191].

Sample stages. Depending on the system under investigation, i. e. for either characterizing colloidal suspensions or polymer melts, appropriate sample environments could be realized by choosing from two different sample stages, which were developed in the course of this thesis. A specifically designed rail system allowed a quick exchange of the stages. The stages were mounted on carriages. Mounting was exercised in such a way that the sample position was unchanged with respect to laser beam and detection optics. Thus, there was no need for recalibration of the scattering vector. The sample stages were held in place by an interlock-system.

Colloid suspension stage. FIGURE 3.4 depicts the sample stage for liquid colloidal suspensions. The stage consisted of a metal rack with five slots to accommodate rectangular flat-cells with up to 2 mm optical path length (110-OS-2-20, Hellma GmbH & Co. KG, Müllheim, Germany). The rack was made of copper because of its high heat conductivity (compare TABLE 3.1) to allow fast thermal equilibration. It could be moved on a guide rail perpendicular to the primary beam to select the sample for measurement. At each sample position a bore with 2 mm diameter allowed the beam to pass through the rack. The rack was thermally isolated by a plastics cladding.

3. SMALL ANGLE LIGHT SCATTERING INSTRUMENT

Poly(tetrafluoroethylene) (PTFE) was used because of its high temperature-stability and low thermal conductivity [192]. To minimize stray light the cladding in forward direction was made of a non-transparent black-dyed plastic because it was noticed that the bright-white PTFE front cladding used previously contributed to low-angle scattering. The copper block was anodized to obtain a low-reflective black surface finish. The five circular apertures in the cladding in forward direction had a diameter of 8 mm to facilitate unaffected passage of the scattered light to the detection optics. For temperature control water could be circulated through channels in the rack. To this end, two connections were installed on the side of the block. Its temperature could be varied from room temperature up to several tens of degrees by a water thermostat (HAAKE Fisons S/F3, Thermo Haake GmbH, Karlsruhe, Germany).



Figure 3.4: Stage for liquid samples to enable SALS measurements of colloidal systems hosting up to five flat-cells for investigation of colloidal suspensions. The (attenuated) laser beam enters the stage from the upper left of the image and leaves it together with the forward scattered light to the lower right towards the detection optics. Temperature-control was realized by a water thermostat.

Polymer melt stage. An aluminium metal block was heated by two electrical resistive cartridge heaters (HT15W, Thorlabs GmbH, Dachau, Germany), which were placed inside of two bores in the block and held in position by set screws. Another bore accommodated the temperature sensor (PT1000 W-EYK 6, Heraeus Sensor Technology GmbH, Kleinostheim, Germany), which was also held in position by a set screw. For optimum thermal contact a heat sink compound was applied to increase the thermal conductivity at the interface of the electrical components and the metal block. The aluminium block was black anodized to minimize stray light from reflections from the metal surface. FIGURE 3.5 depicts the stage. The aluminium block was L-shaped in cross-section and had a flat front face of 22 mm \times 22 mm to accommodate the samples. The heaters were inserted from the top into the 6 mm thick part. The temperature

3. SMALL ANGLE LIGHT SCATTERING INSTRUMENT

sensor was inserted from the side into the 10 mm thick lower part. The block was fixed in an iron frame and thermally isolated by a PTFE liner. The frame was mounted on a carriage for readily positioning it in the beam path via the guide rail system. Polymer films were placed between two microscopy cover glasses. The sample thus prepared was pressed to the front face of the aluminium block by two flat springs for optimal thermal contact.

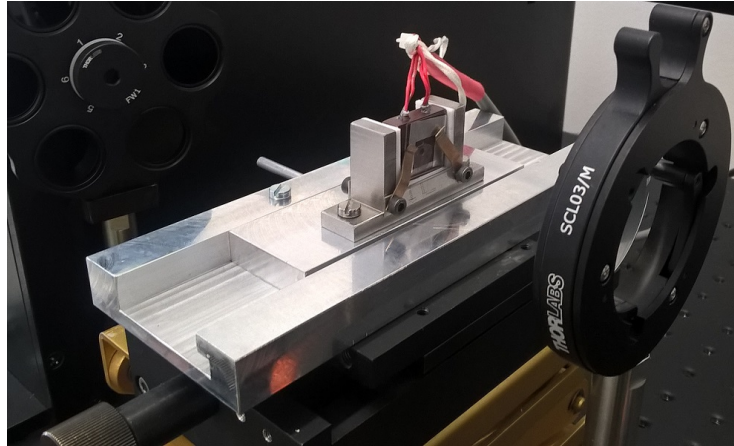


Figure 3.5: High temperature sample stage for SALS measurements of polymer melts. The (attenuated) laser beam enters the stage from the upper left of the image and leaves it together with the forward scattered light to the lower right towards the detection optics. User defined temperature-time profiles could be realized by a specifically developed electronic control interface.

Temperature-control of the stage was realized by an electronic controller board (Arduino UNO, an open-source electronics platform, www.arduino.cc), which uses the ATmega328 8 bit micro-controller (Atmel Corp., San José, USA). A PI-control cycle was implemented via a software script, which was executed on the device. PI is short for *proportional* and *integral* and denotes a special kind of control loop feedback mechanism [193]. The full source code is provided by the digital copy of this thesis. It continuously processed the data from the temperature sensor T_{sensor} and controlled the power supply for the electrical heaters in order to attain the user-defined target temperature T_{set} . The cycle time was $\Delta t = 0.1$ s, which was appropriate due to the thermodynamic inertia of the system. In FIGURE 3.6 a chart depicts the interconnection of components involved in the temperature-control of the polymer melt stage.

More precisely, the temperature-dependent voltage signal of the PT1000 sensor was fed via a Wheatstone bridge to an operational amplifier (OPAMP), filtered and translated into an actual temperature. Due to digitization the uncertainty in temperature was $\Delta T \pm 0.3$ K. The difference of the process variable T_{sensor} to the set point T_{set} at time t yielded the deviation, the so-called error value, $e(t) = T_{set} - T_{sensor}(t)$. This value was

3. SMALL ANGLE LIGHT SCATTERING INSTRUMENT

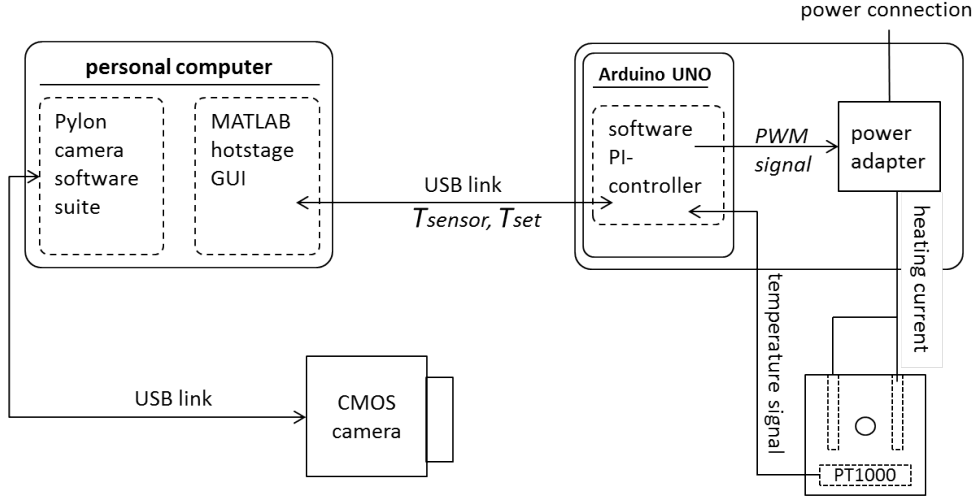


Figure 3.6: Sketch of the polymer melt stage and the components involved in the temperature-control of the device. An Arduino UNO serves as an electronic interface running a software PI-controller for temperature control.

used for the calculation of the control variable

$$Y(t) = K_P \cdot e(t) + K_I \sum_{n=1}^N (e(n \cdot \Delta t) \cdot \Delta t), \quad (3.25)$$

where $t = N \cdot \Delta t$. The control variable is comprised of two terms. In the first (proportional) term the instantaneous error value is multiplied with the proportionality constant K_P , which determines the magnitude of the response. The second term is an integral term and reflects the accumulated deviation by summing the instantaneous error values over time. It is multiplied with the integral gain constant K_I . The integral term eliminates oscillations from a system which is proportionally-controlled (P-controlled) only. Based on Y via a pulse width modulated (PWM) signal the device controlled the power supply to the resistive heaters from a separate power adapter which was connected to mains. Note that no measures were taken for active cooling. In case of negative Y simply no heating was prompted. The device provided an electronic interface for setting the temperature of the stage. More complex time-temperature protocols could be realized by a timed MATLAB³ script (cf. FIGURE 3.6).

The internal temperature scale of the device was verified by melting of standards with known melting points (VWR International GmbH, Darmstadt, Germany). The standards were vanillin ($T_m = 81 - 83^\circ\text{C}$), benzoic acid ($T_m = 121 - 123^\circ\text{C}$), sulphanilamide ($T_m = 164 - 166^\circ\text{C}$) and caffeine ($T_m = 234 - 236^\circ\text{C}$, $\leq 99.7\%$). Small quantities of the powdery materials were molten, pressed between microscopy cover glasses

³MATrix LABoratory

3. SMALL ANGLE LIGHT SCATTERING INSTRUMENT

and cooled down. The samples were mounted on the stage and the temperature was gradually increased. Upon melting the samples turned from opaque to transparent. In FIGURE 3.7 melting points T_{sensor} which were determined in the previously described way are plotted versus the mid-temperature T_m of the nominal melting point temperature range. As can be seen the temperature was correctly determined by the device within experimental uncertainty over its operational range from near room temperature up to 250 °C. In addition the temperature dynamics of the device was assessed by

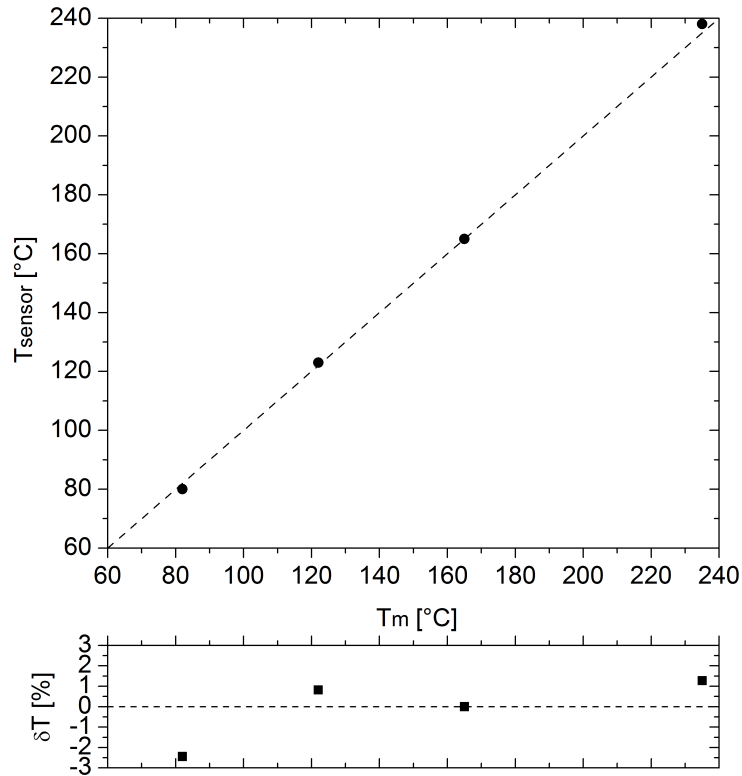


Figure 3.7: Temperature scale verification of the home-built hotstage. Melting points as determined by the device versus nominal melting points. The dashed line in the upper graph with slope 1 is the equi-temperature line $T_{sensor} = T_m$.

temperature-jump experiments (see FIGURE 3.8). The dynamics is determined by the heat capacity of the metal block and the power dQ_{el}/dt supplied by the resistive heaters to the block and the heat loss dQ_{loss}/dt to the surrounding, respectively, according to

$$\frac{dQ}{dt} = \frac{dQ_{el}}{dt} - \frac{dQ_{loss}}{dt} = c_p \cdot m \cdot \frac{dT}{dt} \quad (3.26)$$

where dQ/dt is the heat flux of the metal block, c_p the specific heat capacity, m the mass of the metal block and dT/dt is the rate of temperature change. In equilibrium, the heat supply to the stage by the resistive heaters and loss due to convective and conductive transport to ambient air and stage mount, respectively, balance. Estimation

3. SMALL ANGLE LIGHT SCATTERING INSTRUMENT

of the loss at the maximum operation temperature of 250° to ambient air yields

$$\frac{dQ_{loss}}{dt} = \alpha \cdot A \cdot \Delta T \quad (3.27)$$

where α is the heat transfer coefficient (here 35 W/(m² K) [194]), A is the surface area and ΔT is the temperature difference to the surrounding medium. The calculation yields $dQ_{loss}/dt \leq 10$ W, which was easily compensated for by the resistive heaters supplying $dQ_{el}/dt = 15$ W each. Excess power allowed rapid heating rates as depicted in FIGURE 3.8. The instrument quickly responds to a change of the set point temperature with heating rates well above 50 K/min. Upon reaching the set point temperature the typical decaying temperature oscillations due to PI-control can be recognized in the left-hand graph. Passive cooling resulted in a rather slow decrease in temperature with an additional decrease of the cooling rate with temperature difference ΔT .

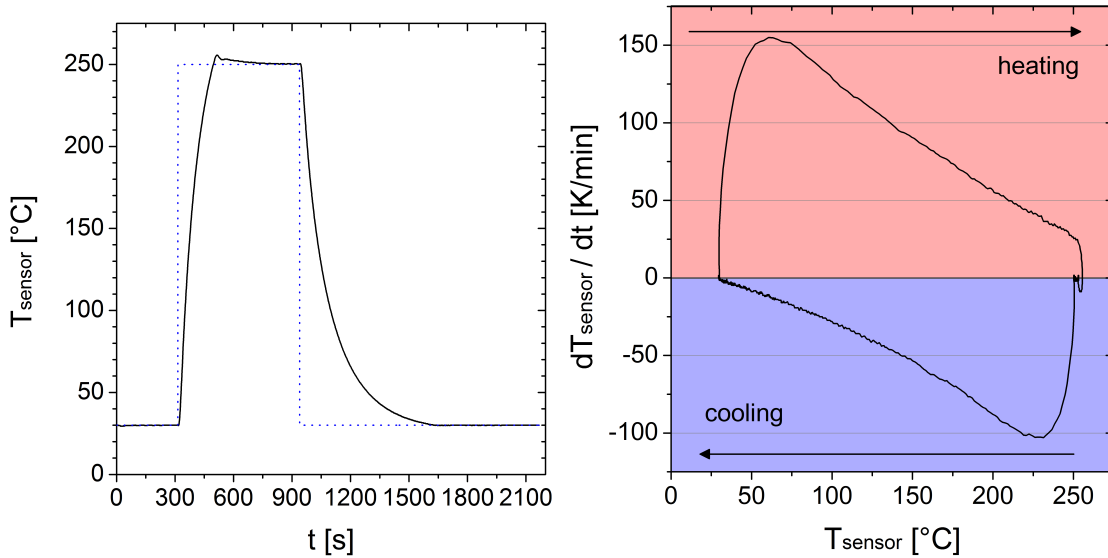


Figure 3.8: Temperature dynamics of the home-built polymer melt hotstage ($K_P = 10$, $K_I = 0.1$). Left: Heating and cooling (—) in response to an instantaneous change of the set point temperature (· · ·). Right: Temperature dependent heating and cooling rates for the temperature jump shown in the left figure.

According to EQUATION (3.26) the heat capacity determines the maximum attainable changes in temperature of the stage. TABLE 3.1 lists a number of qualified materials for the metal block. Since the volume of the block was constant the material selection was based on volume based material properties rather than on mass based quantities. To this end, the heat capacity was estimated as a per-volume quantity by multiplication with density. Neglect of the temperature-dependence of the quantities introduced a small negligible error in the calculations. While gold and silver show suitable thermodynamic properties, choosing this materials was no option due to prices. Eventually, aluminium was chosen due to its significantly lower heat capacity compared to copper

3. SMALL ANGLE LIGHT SCATTERING INSTRUMENT

although heat conductivity was lower too. For completeness the properties of PLA are reproduced as well as the material properties of borosilicate glass from which the microscopy cover glasses are typically made of. Sapphire represents an alternative substrate material for polymer melts. However, suitable components were not readily available and sapphire birefringence can cause problems especially in the experiments with polarized laser light.

Table 3.1: Thermal properties of materials used for temperature-dependent experiments.

	density $\rho[\text{g}/\text{cm}^3]$	heat capacity $c_p[\text{J}/(\text{kg} \cdot \text{K})]$ $c[\text{J}/(\text{cm}^3 \cdot \text{K})]$		conductivity $\lambda[\text{W}/(\text{m} \cdot \text{K})]$	Ref.
copper	8.92	385	3.43	400	[195]
aluminium	2.70	897	2.42	235	[195]
silver	10.49	235	2.47	430	[195]
gold	19.32	128	2.47	320	[195]
borosilicate glass	2.23	850	1.9	1.2	[196]
sapphire	≈ 4	≈ 418	≈ 1.7	42	[195]
polylactide	≈ 1.2	≈ 2000	≈ 2.5	≈ 0.2	[130]

Optical train. The instrument was mounted horizontally on a 60 cm by 120 cm optical breadboard (G437511912, Qioptiq Photonics GmbH & Co. KG, Göttingen, Germany) which was, in turn, positioned on a vibration isolating cushion placed on a free-standing laboratory bench (FIGURE 3.3). For details on the alignment procedure of the optical components see FIGURE B.1 in APPENDIX B.

The linearly polarized HeNe laser (G040804000, Qioptiq Photonics GmbH & Co. KG, Göttingen, Germany) was mounted on a laser adjustment stage (LJ 80-D54-XY, OWIS GmbH, Staufen i. Br., Germany) in such a way that its polarization direction was perpendicular to the plane defined by the surface of the laboratory bench. Subsequently, the laser beam was deflected by two mirrors (so-called dogleg configuration). Thus, the beam path between laser head and detector was U-shaped which maximized the path length in the second leg for more precise beam alignment and left plenty of space for the detection optics. Silver mirrors (PF05-03-P01, Thorlabs GmbH, Dachau, Germany) were used as they offer the highest reflectance in the spectrum of visible light of any metallic mirror (e. g. aluminum, gold) [197]. The mirrors had a durable SiO_2 overcoat with a thickness of approximately 100 nm in order to protect them from oxidation [198]. For precise alignment of the laser beam the mirrors were fixed to kinematic mirror mounts on optical posts (KM05/M, KCP05/M, PH75/M, TR100/M, Thorlabs GmbH, Dachau, Germany). A box with one small entry and one small exit slit protected the mirrors from dust. Tubing between the laser head and the first mirror shielded the non-attenuated laser beam. On exiting the box the laser beam passed an attenuator which included three absorptive antireflection coated neutral density filters mounted on a filter wheel (G065063000, Qioptiq Photonics GmbH & Co. KG, Göttingen).

3. SMALL ANGLE LIGHT SCATTERING INSTRUMENT

gen, Germany). Optical densities were OD1.0 (NE10B-A, Thorlabs), OD1.3 (NE13B-A, Thorlabs) and OD2.0 (NE20B-A, Thorlabs), respectively, which allowed attenuation of the beam to $T = 1/10^{OD} = 10\%$, 5% and 1% of its nominal power.

Next the beam passed the sample holder through a small hole for illuminating the specimen. The two home-built sample holders were mounted on a specifically designed rail system for easy exchange of the sample environments. An interlock system held the respective sample holder in place. The rail system was mounted on a linear stage which, in turn, was mounted on another linear stage for both lateral and vertical alignment with respect to the laser beam.

The detection optics was mounted on a 1 m long profiled optical rail (G061361000, Quioptiq). The individual optical components were mounted on a carrier-post system (carrier G061372000, carrier G061374000, mounting column G023041000, rod G024232000, Quioptiq) which could be moved on the rail along the beam direction and allowed vertical positioning of optical elements. For minimization of stray light all optical surfaces had an antireflection (AR) coating. In addition, the surfaces of the sample holders were black anodized. Only the surfaces of the flat-cells for suspensions and the coverglasses enclosing the polymer melts lacked AR coating. A self-centering mount (SCL03/M, Thorlabs) kept the double-convex Fourier lens (#48-255-INK, Edmund Optics Ltd., Nether Poppleton, UK; $F = f_1 = 60$ mm, $\varnothing = 40$ mm) in position, which collected the scattered light and focussed the primary beam onto the beam stop. The latter was made from matt black paper and had a width of 1 mm (compare FIGURE 3.18). A second double-convex objective lens (LB1309-A, Thorlabs; $F = f_2 = 75$ mm, $\varnothing = 50$ mm) was mounted on an adjustable-height optics clamp (VG100/M, Thorlabs) for large-diameter lenses and imaged the scattered light onto the detector.

In FIGURE 3.9 the working principle of the detection optics is illustrated in detail. The Fourier property of a lens ensures that any rays entering the lens with angle θ with respect to the optical axis will intersect the back focal plane of the lens on a ring with radius

$$G_2 = f_1 \tan \theta \quad (3.28)$$

where f_1 is the focal length of the lens. Consequently, the primary beam with $\theta \ll 1$ was focussed in the back focal point of the lens L1 where it could be prevented from progressing to the detector by placing a beam stop at this position. Via the objective lens L2 the Fourier plane was demagnified and imaged onto the detector.

The following boundary conditions guided the design of the optical train. First, the minimum size of the beam stop was set to 0.5 mm in radius. This was done to ensure ease of manual alignment of the beam stop and its fabrication by the mechanical workshop. The beam stop was set to block scattering in an angular range from $\theta = 0^\circ$ to a maximum of $\theta = 0.5^\circ$. With EQUATION (3.28) this yielded

$$f_1 \geq \frac{0.5 \text{ mm}}{\tan(0.5^\circ)} = 57 \text{ mm} \approx 60 \text{ mm} \quad (3.29)$$

for the focal length of the Fourier lens L1. Second, the maximum scattering angle,

3. SMALL ANGLE LIGHT SCATTERING INSTRUMENT

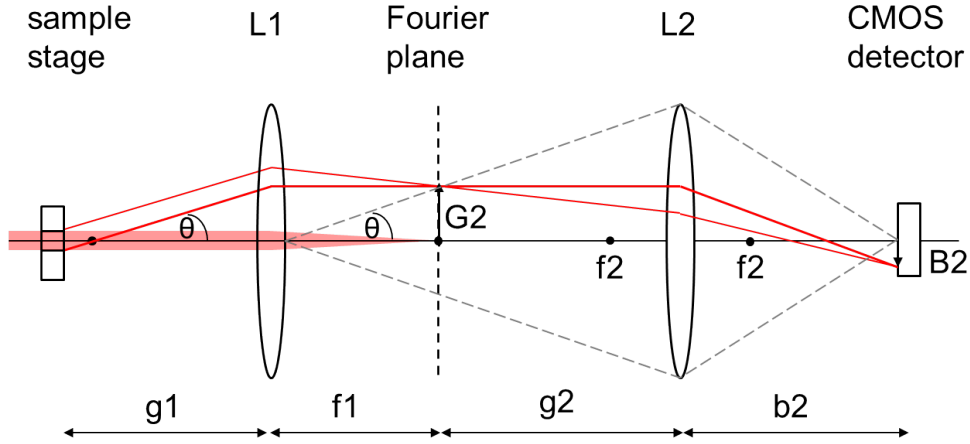


Figure 3.9: Fourier lens-type detection optics of the SALS instrument. The back focal plane of the Fourier lens L1 was mapped by the objective lens L2 onto the camera sensor. A beam stop positioned in the back focal point of L1 could be used to remove the primary beam from the detection optics. Distances are not to scale. The distance g_1 corresponds to Q_1 in [124].

which could be captured by the corners of the quadratic detector chip in centrosymmetric imaging (i.e. primary beam centered in the image frame), was set to $\theta_{max} = 15^\circ$, yielding $G_{2,max} = 60 \text{ mm} \cdot \tan(\theta_{max}) = 16 \text{ mm}$. Then, via demagnification of $M = B_2/G_{2,max} = -1/2$ the Fourier plane was imaged by the objective lens L2 to the detection plane where $B_2 = \sqrt{2} \cdot 5.65 \text{ mm} \approx 8 \text{ mm}$ is the maximum image size of L2, which was given by half of the diagonal of the detector chip (which was $11.3 \text{ mm} \times 11.3 \text{ mm}$ in size). With these parameters set, from the definition of the magnification

$$M := \frac{B_2}{G_2} = -\frac{b_2}{g_2} \stackrel{!}{=} -\frac{1}{2} \quad (3.30)$$

and the lens equation

$$\frac{1}{f_2} = \frac{1}{b_2} + \frac{1}{g_2} \quad (3.31)$$

where f_2 is the focal length of lens L2, the distances b_2 (L2-detector distance; image distance of L2) and g_2 (L2-Fourier plane distance; object distance of L2) were defined:

$$\frac{b_2}{g_2} = \frac{3/2 f_2}{3 f_2} \simeq \frac{112 \text{ mm}}{225 \text{ mm}} \quad (3.32)$$

By convention the magnification is negative for an inverted, real image. Correct recording of the scattering pattern in the Fourier plane by the detector with the correct magnification was ensured by imaging a test target of known size, which was positioned in the back focal plane of L1. The image is shown in FIGURE 3.10. The target showed three concentric circles corresponding to specific scattering angles with respect to the

3. SMALL ANGLE LIGHT SCATTERING INSTRUMENT

Fourier lens. It was placed in the Fourier plane and illuminated with a small lamp. Objective lens L2 and camera were moved until a sharp, format filling image of the outer ring was attained indicating correct adjustment of magnification and focus. Note that the test target was imaged distortion-free by objective lens L2. Inhomogeneous image brightness was due to imperfect illumination conditions by the small lamp. Subsequent calibration (see SUBSECTION 3.6) yielded the exact scattering angles. The sample

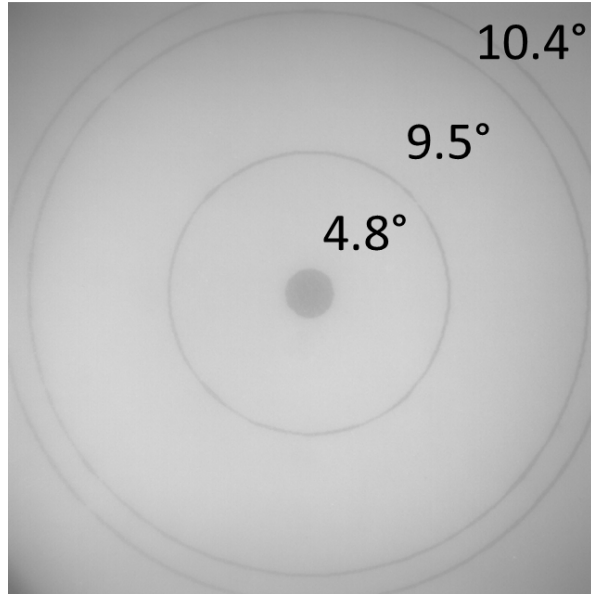


Figure 3.10: Image of the test target placed in the Fourier plane of L1 for adjusting magnification and focus of the detector by setting the distances g_2 and b_2 . Inhomogeneous image brightness was due to imperfect illumination conditions of the target.

stage, i. e. the scattering volume, was positioned just outside of the front focal point f_1 of L1 such that $g_1 > f_1$, and without measurable vignetting (see SUBSECTION 3.7).

An analyzer (LPVISE100-A, Thorlabs) was positioned in the optical path. It was mounted on a rotation mount (RSP1D/M, Thorlabs) and had a graduated angle scale for alignment of the analyzer in vertical or horizontal position, respectively, for measurements of the polarized or depolarized components of the scattered light. Positioning the analyzer directly in front of the camera aperture rather than between sample and Fourier lens helped to reduce stray light and improved data quality.

The scattered light was detected by a digital machine-vision camera (acA2040-90um, Basler AG, Ahrensburg, Germany). It was mounted adjustable in height (G061200000, G061325000, Quioptiq). Additionally, a narrowband band pass filter (#65-166, Edmund Optics) with a transmission window with a width of 10 nm centered at 632 nm matching the laser wavelength was attached to the camera. It further reduced unwanted parasitic light and shielded the sensor surface from omnipresent dust particles.

Detector. A digital machine-vision camera (acA2040-90um, Basler) was used as the light sensitive area detector (cf. the user's manual [199] for full documentation). The camera was equipped with a quadratic CMOS-type image sensor (CMV4000, ams Sensors Germany GmbH, Nürnberg, Germany) with dimensions of $11.3 \text{ mm} \times 11.3 \text{ mm}$. Sensors fabricated in complementary metal-oxide-semiconductor (CMOS) technology do not show the phenomenon of so-called blooming which is often observed with charge-coupled device (CCD) cameras when electrical charges of saturated pixels migrate to adjacent pixels thus distorting the signal [197]. The monochromatic sensor chip had a spatial resolution of 2048×2048 pixels with a size of $5.5 \mu\text{m} \times 5.5 \mu\text{m}$ for each pixel, and a 12 bit intensity resolution, respectively, equivalent to 4095 intensity levels at constant detector exposure time. In addition, the chip featured an electronic global shutter which ensured uniform image brightness by synchronous start and end of exposure of all of the pixels. At full spatial resolution the camera provided 90 frames per second maximum while the exposure time could be varied between $28 \cdot 10^0$ and $10 \cdot 10^6 \mu\text{s}$ in $1 \mu\text{s}$ increments.

The camera was connected to a computer via a USB 3.0 device link⁴ for data transfer as well as power supply. Data acquisition was controlled via the Basler pylon camera software suite which was installed on the same computer.

3.4 Data acquisition: Performing measurements

Prior to experiments the components of the SALS instrument had to be set up for measurement. For temperature-control either the thermostat had to be set to the target temperature or the corresponding parameters T_{set} for the target temperature and T_{dot} for the temperature change per minute had to be entered in the software interface for the polymer melt stage, respectively. The electronic controls of the latter were initialized with standard parameters $T_{set} = 30^\circ\text{C}$ and $T_{dot} = 10 \text{ K/min}$ as soon as the device was powered up by connecting to the computer via the USB link or by switching on the power supply.

The detector was operated via the Basler pylon camera software suite. As soon as the camera was powered up it was initialised with default parameters. In FIGURE 3.11 the graphical user interface of the software is shown. The reader is referred to FIGURE 3.6 for details on the interconnection of the instrument components.

The parameters for IMAGE FORMAT CONTROL were set as follows: Resolution 2048×2048 , binning *off*, offset *off*, pixel format *mono12*. In particular, setting the last parameter is important to utilize the maximum dynamic range of the detector.

The parameters for ANALOG CONTROL were set as follows in order to ensure linear response behaviour of the detector electronics: Gain *off*, black level *off*, Gamma 1.

In the ACQUISITION CONTROL panel the shutter mode was set to *global*. The exposure

⁴Universal Serial Bus (USB), specified in [200].

3. SMALL ANGLE LIGHT SCATTERING INSTRUMENT

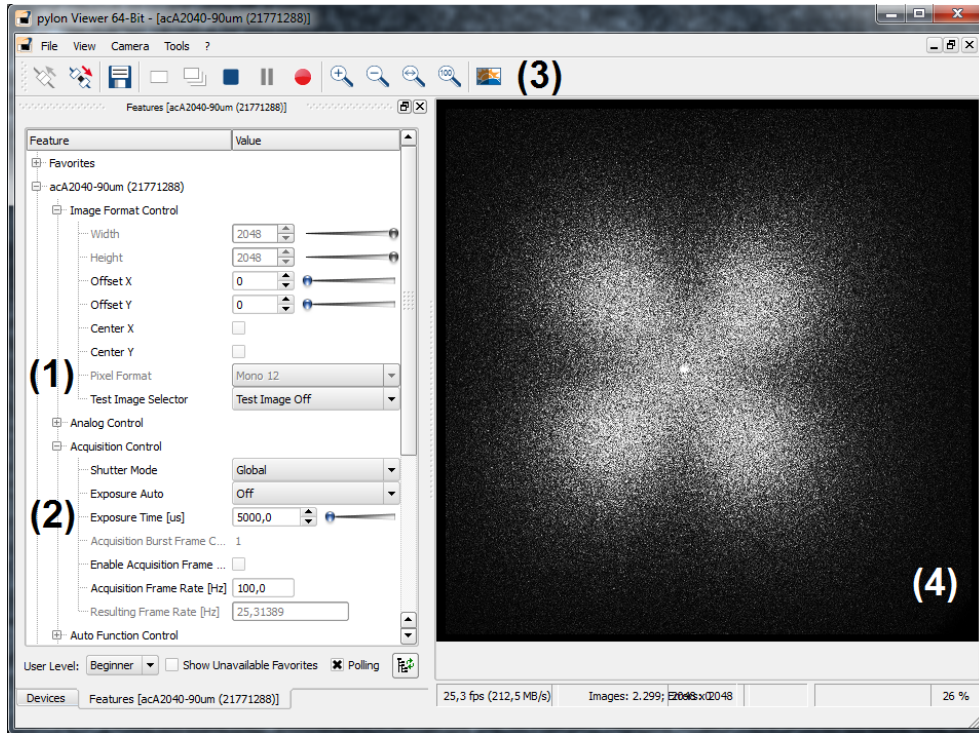


Figure 3.11: Graphical user interface (GUI) of the Basler Pylon camera software suite. Parameters like PIXEL FORMAT (1) and EXPOSURE TIME (2) were set in the control panel on the left. Data acquisition was controlled with the buttons at the top (3). A real-time image was presented on the right (4) (here, H_V scattering pattern of spherulites, see SUBSECTION 4.2).

time τ_{exp} was chosen to match the experimental conditions. In a time series the parameter could be corrected manually without interrupting data-taking to adjust image acquisition to the scattering behaviour of the sample.

Actual data acquisition was commenced by either clicking the SINGLE-SHOT button of the software or by using the RECORD FUNCTION. In the first case the scattering pattern was recorded immediately and the image file was saved on the hard-drive. In the latter case a time series was acquired according to the parameters for timed exposure, namely NUMBER OF EXPOSURES and INTERVAL. The interval time could be set from seconds to hours. The duration of data acquisition resulted from the number of exposures multiplied by the interval, which included the exposure time.

A correlation of temperature and image data was only possible by comparing the temperature log of the high-temperature stage with the acquisition time of the images or by manually logging temperature and acquired image frame which was appropriate for slow temperature ramps.

3.5 Data processing: Preparing data evaluation

Processing of the raw data comprised (1) data correction and (2) data reduction. Processing via these two steps is well separated from (3) data analysis [201]. Data correction and reduction were carried out with a single integrated MATLAB script whereas dedicated routines were used for data analysis as explained below.

A rigorous treatment of processing of raw intensity data from small angle scattering experiments is presented by Pauw *et al.* [202] who describe a comprehensive schema, which was adopted in this work for data correction and reduction albeit a full implementation of all of the various routines was neither carried out nor necessary. In the following the steps for data correction and reduction are described. The reader is referred to the documentation given in the MATLAB code for details on the actual implementation of the routines.

- (i) data read-in (DS): Acquired frames were saved by the Pylon software suite as separate files in the TIFF⁵ file-format with 16bit resolution per pixel. In this process the 12 bits of the camera pixel intensity data were shifted to the right by 4 bits and the lower 4 bits were set to zero thus increasing the stored entry to values up to 65535. Note that this was an undocumented specific peculiarity of the software⁶. The data read-in routine in the MATLAB script cancelled the bitshift to obtain the correct intensity data with entries ranging from 0 to 4095.
- (ii) masking (MK): In order to exclude pixels from further processing their position could be marked in a mask file. The mask had to be generated manually. However, this could conveniently be accomplished with standard office image processing software which in general offers appropriate tools for image manipulation. For all measurements with inserted beam stop a mask was generated and applied to subsequent data post-processing. Note that in principle complex masks are conceivable which could relay additional information to the post-processing algorithm like statistical weights for intensity data. Here, the implemented masking mechanism was binary in nature, i. e. pixel data was either processed with its full value or the data was excluded completely implying that the pixel was not counted for later intensity averaging. In addition, saturated pixels could optionally be excluded from further processing by setting the respective parameter in the script.
- (iii) solid angle correction (SP): In FIGURE 3.12 a simplified scattering geometry without detection optics is depicted with the scattering sample A, and the detector aligned at right angle with respect to the primary beam. As can be seen the solid angle subtended by an arbitrary pixel at position (x, y) depends on its radial distance

$$R_d = \sqrt{(x - x_c)^2 + (y - y_c)^2} \quad (3.33)$$

⁵Tagged Image File Format (TIFF), specified in [203].

⁶Private communication Uli Kleffel (Rauscher GmbH, Olching, Germany), Mai, 19th 2017.

3. SMALL ANGLE LIGHT SCATTERING INSTRUMENT

to the beam center at position (x_c, y_c) on the detector. The solid angle can be

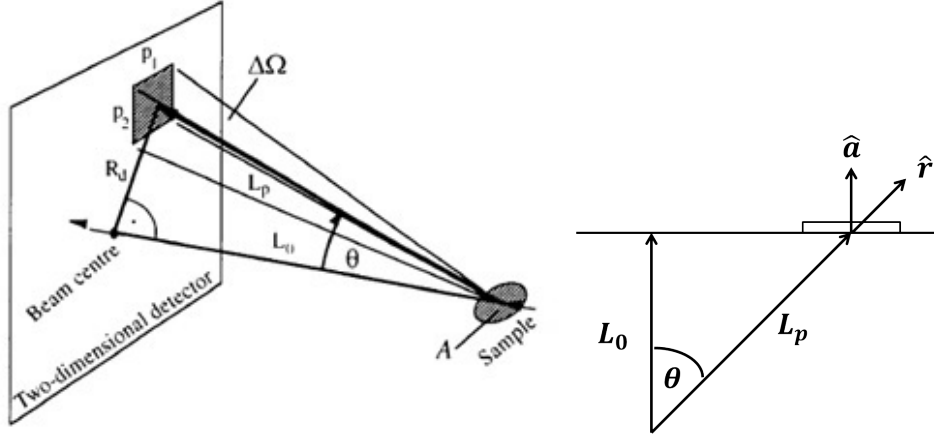


Figure 3.12: Left: Solid angle $\Delta\Omega$ subtended by a pixel of a two-dimensional detector with respect to the sample position. L_0 is the distance of detector and sample, L_p is the distance between sample and pixel and R_d is the pixel position with respect to the beam center. p_1 and p_2 are the pixel dimensions. Modified reproduction from [204]. Right: Sketch illustrating calculation of the solid angle.

calculated from the surface integral over a pixel with surface area S

$$\Delta\Omega \approx \int_S \frac{\hat{r} \cdot \hat{a} dS}{L_p^2} = \frac{p_1 p_2 \cos \theta}{L_p^2} \quad (3.34)$$

where \hat{r} is the unit vector of the position vector \hat{L}_p , which points from the scattering volume to the incremental pixel surface element dS , and \hat{a} is the surface normal vector to dS . Edge lengths of the pixel are denoted with p_1 and p_2 . In FIGURE 3.12 the situation is illustrated. Obviously, $\cos \theta = L_0/L_p$ such that

$$\Delta\Omega = \frac{p_1 p_2 L_0}{L_p^2 L_p}. \quad (3.35)$$

Normalization of the solid angle of a pixel at R_d and with distance L_p to the solid angle of the central pixel with $R_d = 0$ and distance L_0 yields

$$\frac{\Delta\Omega(R_d)}{\Delta\Omega(0)} = \frac{L_0^3}{L_p^3} = \cos^3 \theta. \quad (3.36)$$

The above derivation⁷ also holds for the setup with detection optics when aberrations can be neglected since the throughput (geometrical étendue) of an ideal optical system is invariant [207].

⁷Not to be confused with the \cos^4 law of illumination which describes the natural decrease in luminosity towards the edges of an image created by an objective lens of a laterally extended object with uniform brightness [205, 206].

- (iv) averaging (AV): Two consecutive processes were applied for data reduction. Radial symmetry or symmetry of the scattering pattern with respect to certain radial directions allowed reduction of the two-dimensional scattering data to one-dimensional data by azimuthal averaging. To this end, all data on a ring or on ring elements, respectively, with a width of one pixel was averaged. FIGURE 3.13 illustrates the two different choices for azimuthal averaging. As a result the scattered intensity as a function of the radial distance R_d to the beam center on the detector was obtained. For further data-reduction data of adjacent rings could be merged. This process is known as binning. In general rings / bins with a

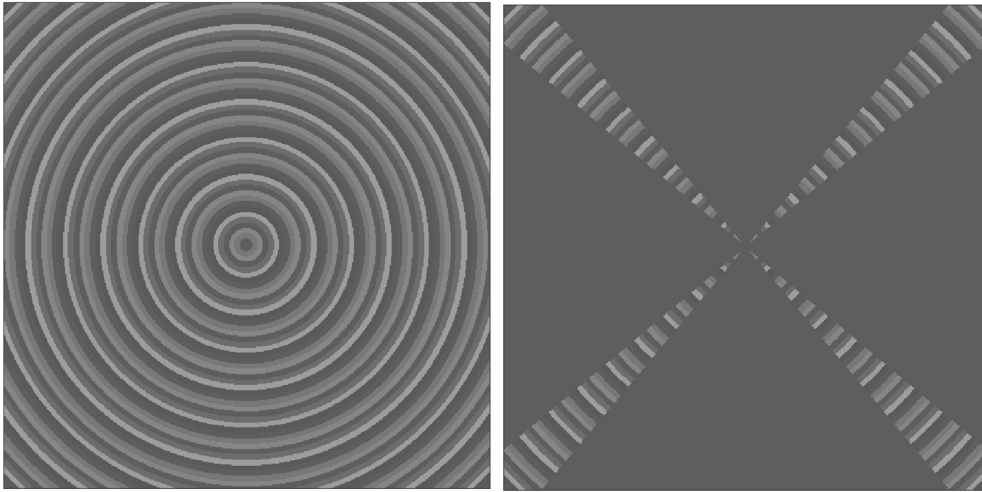


Figure 3.13: Visualization of the averaging process of scattered intensity in azimuthal direction. Left: Ring-wise 2π azimuthal average. Right: Averaging along the diagonals with azimuthal angle restricted to $\phi = 45^\circ \pm 2.5^\circ$ in the four image quadrants. Gray scales indicate rings or arches, respectively, belonging to the same scattering angle θ . For better clarity images are displayed with reduced pixel resolution.

constant q -spacing are desirable. However, in the small angle scattering regime

$$\Delta q = q_2 - q_1 \approx \frac{4\pi}{\lambda} \left[\frac{\theta_2}{2} - \frac{\theta_1}{2} \right] = \frac{4\pi}{\lambda} \frac{\Delta\theta}{2} \quad (3.37)$$

and it makes no difference if spacing is chosen with respect to q or to the scattering angle θ when θ is a linear function of R_d . The latter assumption was justified by the results of the scattering angle calibration (see SUBSECTION 3.6).

- (v) background subtraction (BG): All of the above explained data correction and reduction processes were applied to the background data as well. As the final step in data processing the background data calculated for each ring / bin was subtracted from the respective scattering data to yield the net scattering intensity. Background data was obtained from measurement of the scattering from pure solvent or the amorphous polymer melt in the respective experimental settings.

3. SMALL ANGLE LIGHT SCATTERING INSTRUMENT

Note that the above schema was applied to the two-dimensional detector data in order to obtain one-dimensional scattering curves for further evaluation (see SUBSECTIONS 3.6 and 3.7, and SECTION 4). For the presented two-dimensional detector data (e. g. FIGURES 4.5 and 4.22) data-processing was limited to background correction by pixel-wise subtraction of the background signal from the sample signal.

In the above schema no measures were taken to correct for misalignment, i. e. tilting, of the detector with respect to the primary beam. Prerequisite for high data quality was a near-orthogonal detector beam-configuration which could be verified by the calibration measurement as described in SECTION 3.6.

For pixel detectors an additional three corrections had to be considered to compensate for detector imperfections.

- dark current correction (DC): Dark current arises from thermally induced random generation of electrons in the photo-sensitive electronics of the detector and leads to non-zero intensity data even in unexposed pixels. The effect is an increase in the average intensity. FIGURE 3.14 depicts the average intensities taken over image frames which were recorded with the detector aperture closed and at various exposure times. Over five orders of magnitude in exposure time the dark signal is quasi-constant. The DC signal showed a slight dependence on camera temperature which increased noticeable after switching it on. Data shown in the figure was recorded 4 h after starting the device, hence, it could be assumed that thermal equilibrium of the sensor electronics was reached. The background signal reading, recorded in the dark laboratory room with closed laser, is hardly higher. In processing DC signals are removed from the scattering data by background subtraction when the exposure times are the same.
- flat-field correction (FF): This correction accounts for pixel to pixel variation in light sensitivity of the sensor elements. Here, the correction was not part of data processing. Instead, it was carried out online by the sensor chip electronics based on a calibration pre-performed by the camera manufacturer. Details on the calibration of sensor sensitivity were not available⁸.
- angular efficiency correction (AE): Conversion of incident photons into an electronic signal is in general dependent on the angle of incidence onto the photo-sensitive element. The more obliquely photons impinge onto the detector, i. e. the larger the angle of incidence, the less is the resulting signal output. Here, incidence angles were smaller than 10° by design. Micro-lenses installed on the detector chip for better signal yield further alleviated this problem. Hence, AE was not explicitly taken into account during data post-processing [208].

Multi frame averaging is an interesting option to reduce experimental uncertainties of scattered intensities, especially in static scattering experiments. Here, this was not

⁸Private communication Uli Kleffel (Rauscher GmbH, Olching, Germany).

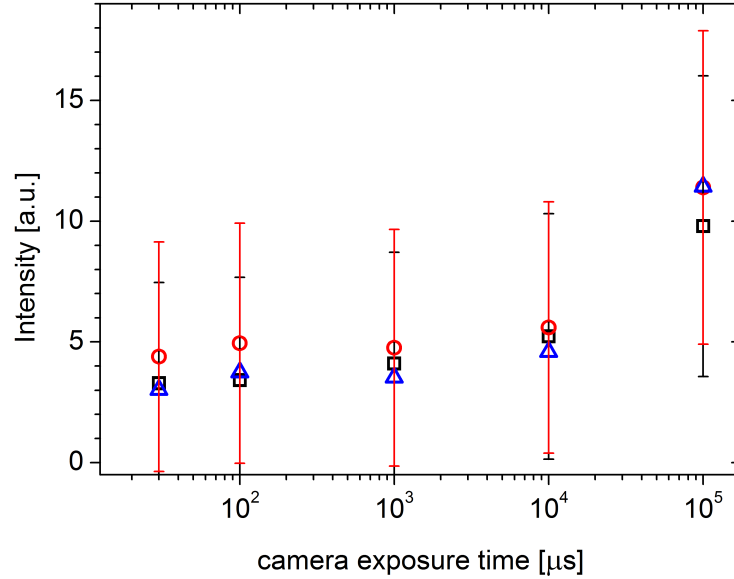


Figure 3.14: Average dark current and background signals taken over the full image frame of the detector at various exposure times. DC signals (mean: □) were recorded with closed camera aperture. Background signals (mean: ○, median: △) were recorded with the laser off. Recordings were carried out 4 h after the camera was started to allow thermal equilibration of the sensor electronics.

used, but could easily be implemented into the data processing routines in the future. Data processing described above did not include normalization to (attenuated) primary beam intensity, which would have required recording of the primary beam intensities.

FIGURE 3.15 depicts a flow chart of the steps involved in data processing. Input to the data processing algorithms were the image files generated by the camera software. Subtraction of background data (BG) or masking (MK) were optional. Mandatory inputs were the beam center position x_c , y_c on the detector and the number of rings to be merged to a bin including the value 0, where no binning would be performed. In all cases a report file was generated summarizing the input processing parameters. Depending on the choice full azimuthal averages and/or azimuthal averages with a restricted angular range were generated. Also, reduced data sets were generated from those averages by further merging (binning) scattering intensities in radial direction. In general, four rings were merged. By default, an additional data set was generated which yielded average scattering intensities and the intensity variances of single pixel-wide rings. No background subtraction was applied to this data set such that it gave access to the raw scattered intensities. For obtaining the variances as a measure for experimental uncertainties a so-called running statistics approach was applied.

The latter proceeding is described briefly in the following. The running statistics approach was employed to compute for each ring indexed R and comprising n pixels the

3. SMALL ANGLE LIGHT SCATTERING INSTRUMENT

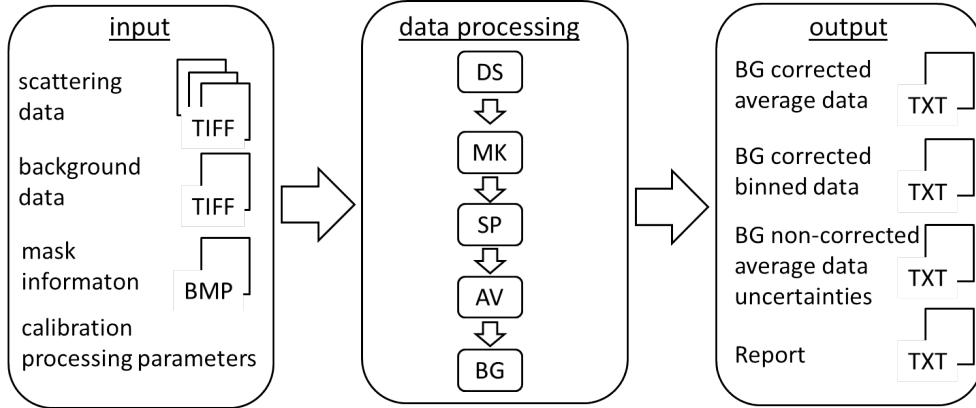


Figure 3.15: Chart depicting data processing. Inputs to the algorithms are image files of scattering data, background and the mask information, scattering angle calibration and processing parameters like beam center position x_c, y_c . Processing comprised data read-in (DS), masking (MK), data averaging and binning (AV) and background subtraction (BG). Solid angle correction (SP) was skipped (see SUBSECTION 3.6). Depending on processing parameters different data sets are obtained: averaged intensities and binned intensities with background subtraction, averaged intensities without background subtraction and associated uncertainties. In all cases a report file is generated summarizing the input parameters.

statistical mean

$$\bar{x}_{R,n} = \frac{1}{n} \sum_{i=1}^n x_{R,i} \quad (3.38)$$

and the unbiased sample variance

$$s_{R,n}^2 = \frac{1}{n-1} \sum_{i=1}^n (x_{R,i} - \bar{x}_{R,n})^2 \quad (3.39)$$

in a single pass, inspecting each datum $x_{R,i}$ only once, thus saving computational time. Here, $x_{R,i}$ is the intensity data of a pixel on ring R . When processing the two-dimensional detector data the algorithm first determines from the coordinates of a pixel the corresponding ring. It then takes the intensity data of that pixel $x_{R,i}$ and updates the intensity mean and variance of that ring. As the image data is processed pixel-wise starting at the upper left corner and stopping in the bottom right corner of the two-dimensional data set the mean intensities and variances of the rings build up only incrementally. For such a scenario Knuth [209] presents an online algorithm based on Welford's method [210] (cf. APPENDIX C) for computing the incremental update of the mean via

$$\bar{x}_{R,k} = \bar{x}_{R,k-1} + \frac{x_{R,k} - \bar{x}_{R,k-1}}{k} \quad (3.40)$$

and computing the incremental update of the variance via

$$S_{R,k} = (k-1)s_{R,k}^2 = \sum_{i=1}^k (x_{R,i} - \bar{x}_{R,k})^2 \quad (3.41)$$

$$= S_{R,k-1} + (x_{R,k} - \bar{x}_{R,k-1})(x_{R,k} - \bar{x}_{R,k}) \quad (3.42)$$

such that

$$s_{R,k} = \sqrt{\frac{S_{R,k}}{k-1}} \quad (3.43)$$

with high numerical precision and high numerical stability [211–213].

3.6 Calibration of the scattering angle

As described in SUBSECTION 3.3 matching of the scattering angle and detector pixel was given by the specific design of the detection optics. However, the scattering angle at the position of a pixel was not readily available as geometric distances were not available at the required precision, especially in view of the lack of knowledge of the exact position of the sensor chip in the camera housing. Above all, the detector position within the camera housing was not documented at all. Therefore, a convenient way for calibrating the pixel-scattering angle assignment was to measure the diffraction pattern of a circular aperture and to fit the mathematically exact solution [124].

First, the beam center (x_c, y_c) was determined from a measurement with removed beam stop. Beam intensity was reduced with the strongest attenuator (here, OD2) and camera exposure time was reduced to $t_{exp} = 100 \mu s$. This allowed direct imaging of the laser beam with the detector as is depicted in FIGURE 3.16. The false-colour image of the pattern generated by the primary beam on the detector shows a regular arrangement of spots rather than a single bright spot from the laser beam. It can be explained as an interference pattern caused by repeated reflections of light from the regularly structured sensor chip surface and a protective cover glass which was mounted on top of the chip. The primary beam is identical with the white-ringed black spot in the image center. Due to the so-called Black-Sun phenomenon zero intensity is assigned to highly saturated pixels which, thus, appear black in the resulting image data⁹.

Second, the diffraction pattern of the circular aperture was recorded. Two apertures with different sizes were available (G000-619-215, $100 \mu m$, G000-619-216, $50 \mu m$, Quiop-tiq). These were obtained as unmounted molybdenum substrates into which the apertures had been laser-etched. FIGURE 3.17 depicts the smaller aperture as viewed in light microscopy. Prior to use, the apertures were checked for their size and circularity. To position them in the laser beam a specifically designed holder was used, which was placed into one of the slots of the colloid suspension stage. Thus, the aperture could be placed exactly at the place corresponding the center of a 2 mm flat-cell cuvette. In FIGURE 3.17 the holder is compared to such a cuvette. Since the sample positions with

⁹CMV2000-AN2-v2.1, Image artifacts application note, CMOSIS NV, 2010.

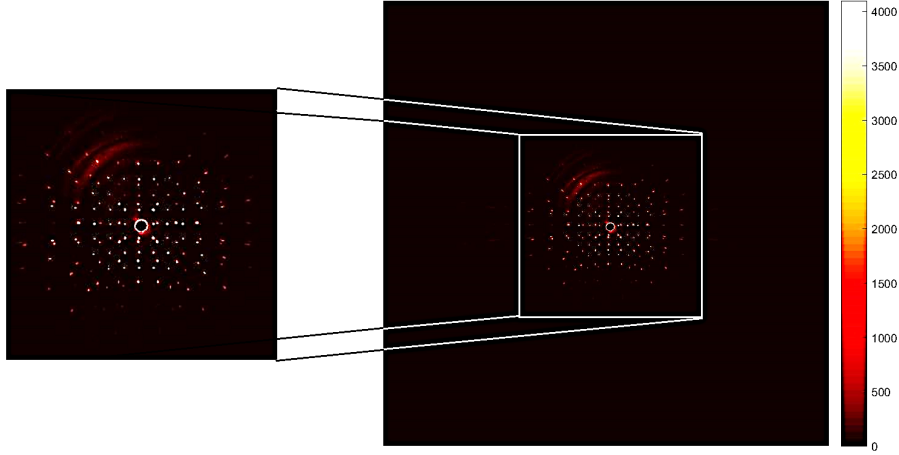


Figure 3.16: False-colour image of the pattern generated by the primary beam on the detector imaged at high attenuation and short exposure time with removed beam stop. The regular spot pattern is caused by repeated reflections of light from the regularly structured sensor chip surface and a protective cover glass on the chip giving rise to a diffraction pattern. Due to the so-called Black-Sun phenomenon the primary beam appears as a black spot in the image center. With the beam stop in place no interference pattern is detected. This also applies to depolarized measurements with the beam stop removed. In both cases the primary beam is effectively removed from the detection optics.

respect to the Fourier lens were identical for the polymer melt stage and the colloid suspension stage the calibration was valid for both sample environments.

FIGURE 3.18 shows the recorded diffraction pattern of the $50\ \mu\text{m}$ aperture. The data were averaged azimuthally totally and within a small sector along the diagonals outward from the center at multiples of $\mu = 45^\circ$, respectively. The results of the two averaging processes yielded the two curves which are depicted in the right graph of FIGURE 3.18. Obviously, these two curves overlay, i. e. the scattering pattern is highly symmetric about the beam center, which proves that the the detector surface was oriented perpendicularly to the laser beam axis and the components of the detection optics were precisely aligned.

As shown in SECTION 3.1 the diffraction pattern of a circular aperture is exactly described by the Airy pattern

$$I(\chi) = I_0 \left(\frac{2J_1(\chi)}{\chi} \right)^2 \quad (3.44)$$

where $J_1(\chi)$ is the Bessel function of the first kind of order one and

$$\chi = kR \sin \theta \quad (3.45)$$

with wave number k , scattering angle θ and radius of the aperture R . Direct curve fitting of EQUATION (3.44) to the data was not possible due to clipping of data upon

3. SMALL ANGLE LIGHT SCATTERING INSTRUMENT

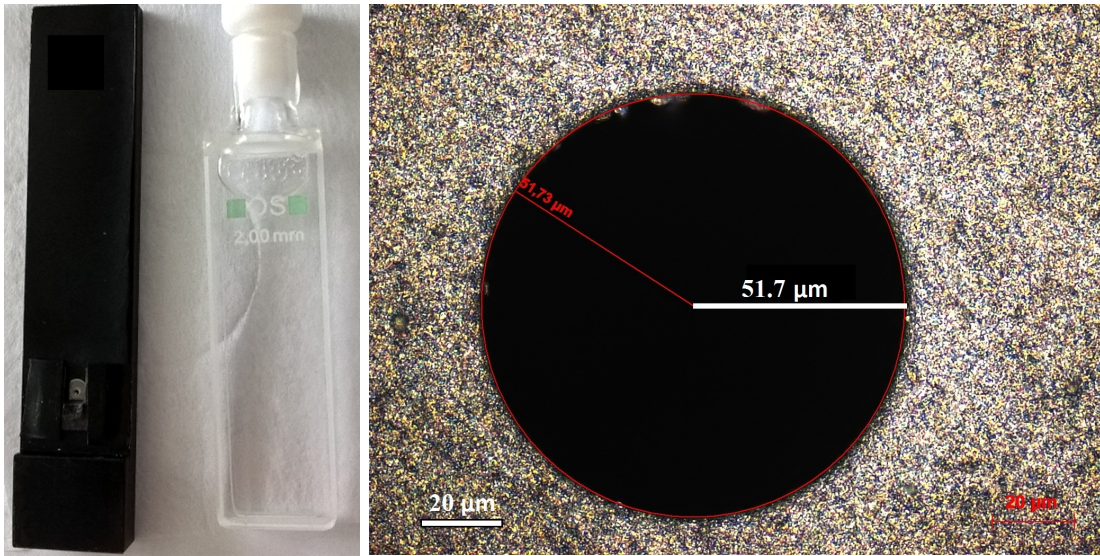


Figure 3.17: Left: Holder mimicking the geometry of a flat-cell cuvette for positioning the apertures in the laser beam. The aperture was mounted to a recess in the lower part of the holder. Thus, the aperture position was identical to the center of the optical path of the flat-cell cuvettes or the position of the polymer melt. Right: $50\ \mu\text{m}$ aperture viewed by light microscopy.

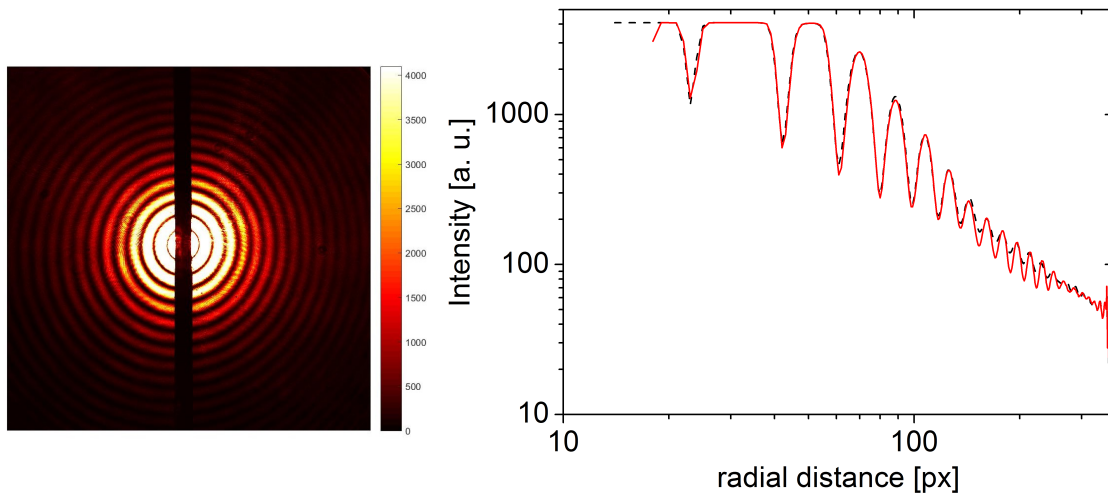


Figure 3.18: Left: False-colour image of the diffraction pattern of the $50\ \mu\text{m}$ aperture recorded at an exposure time of $t_{exp} = 0.1\ \text{s}$ with beam stop in place and laser attenuated to 10% of the primary power. Right: Processed diffraction pattern. The curves from azimuthal averaging (---) and averaging along diagonal sections at $\mu = 45^\circ$ (—) overlay proving precise alignment of the detection optics.

pixel saturation at low scattering angles. Further reducing the primary intensity, on the other hand, would have reduced the data range for fitting as well. Instead, calibration of the scattering angle was carried out based on the positions of the local minima of the experimental data. As will be explained below this had the additional benefit of

3. SMALL ANGLE LIGHT SCATTERING INSTRUMENT

taking into account image distortions due to lens aberrations.

The scattering pattern has minima whenever $J_1(x) = 0$. The zeros of the Bessel function are tabulated or can easily be generated by MATLAB or by other common data processing software [214]. In FIGURE 3.19 the assignment of scattering angles to the local minima of the experimental intensity data is shown. With known wave vector and aperture radius R determined by light microscopy, the diffraction angle (= scattering angle) could be obtained from EQUATION (3.45). By interpolation the scattering angle of each pixel ring could be determined.

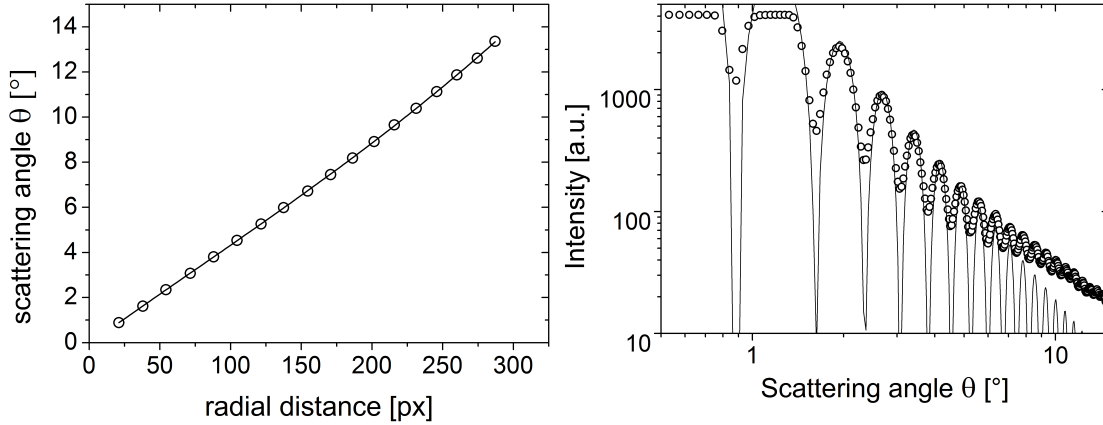


Figure 3.19: Left: Calibration (—) of scattering angles θ via assignment of radial distances R_d of intensity minima (o) to the respective known angles θ . Right: Measured intensity distribution (o) of the aperture with $R = 50 \mu\text{m}$ as a function of diffraction angle compared to the theoretical curve (—).

Obviously, the θ did not exactly follow a linear trend with $R_d[\text{px}]$. This was due to aberrations of the detection optics [112]. While chromatic aberration was of no relevance to the single-wavelength SALS instrument, geometric lens aberrations had to be considered. Five types of geometric aberrations are known [197]. Coma, field curvature and distortion are effects of off-axis rays entering the optical system. These aberrations were of minor relevance to the SALS instrument and could be neglected since all scattered light emerged from the illuminated sample volume close to the optical axis. The aberrations left were spherical aberration which is an axial effect and astigmatism which is both an off-axis and axial effect. To account for these aberrations the data $\theta_{\text{Airy}}(R_d)$ was fitted empirically with a polynomial of 3rd order.

Comparison of the measured intensity plotted versus the calibrated diffraction angle with the theoretical curve given by EQUATION (3.44) shows that the positions of minima and maxima are in very good agreement. A deviation of the experimental and theoretical intensities is observed at larger angles. Here, the experimental intensity is higher than predicted. This can be ascribed to spherical aberrations introduced by the Fourier lens. Note that this effect surpassed intensity reduction by solid angle effects. Hence, the SP-correction in data processing was switched off as it would further increase the intensity at large angles, thus adding to the mismatch of experimental and theoretical

intensity. In FIGURE 3.19 the experimental curve is shown without solid angle (SP) correction.

Calibration with the 100 μm aperture was carried out as well and the coefficients for the interpolation were obtained. Calibration of the scattering angle with the two different-sized apertures did overlay. Relative deviations were no more than 5%.

3.7 Operational verification of the SALS setup

Operational verification and check of the scattering angle calibration of the home-built SALS instrument were performed by particle size measurements of standard latex beads.

3.7.1 Methods and materials

Scanning electron microscopy. Particle sizes of standard latex beads were verified by means of scanning electron microscopy (NEON 40 EsB CrossBeam, Carl Zeiss AG, Oberkochen, Germany). From each suspension of the standard latex beads a single drop was dried at ambient conditions on a freshly prepared flat mica sheet, which was fixed onto the specimen stub by double sided carbon adhesive discs (Science Services GmbH, Munich, Germany). After sputter-coating (3 nm Au/Pd 80/20 wt%/wt%, BAL-TEC SCD 500 sputter coater) pictures of the samples with high topographic contrast were obtained by applying the SE2-detector at an acceleration voltage of 2 kV.

Malvern Mastersizer S. As a benchmark for the home-built SALS instrument particle sizing was performed on a commercial instrument (Malvern Mastersizer S, Malvern Instruments GmbH, Herrenberg, Germany). The instrument was equipped with an unpolarized 5 mW continuous wave HeNe Laser ($\lambda_0 = 632.8 \text{ nm}$) which was expanded up to 18 mm in diameter prior to illuminating the sample. The circular sector detector comprised 42 elements, which covered a range of scattering angles of $0.01^\circ - 135^\circ$ with a resolution of the scattered intensity of 14 bit.

The instrument could be equipped with two alternative lens-cell configurations for measurements of the particle size: (a) a 300F Fourier lens and MS7 cell which featured a magnetic stirrer and which had a path length of 14.3 mm was recommended for a size range of 0.5 - 880 μm and (b) a 300RF reverse-Fourier lens and MS1 flow-through cell which had a path length of 2.4 mm was recommended for an extended size range of 0.05 - 880 μm . The configurations are depicted in FIGURE 3.20. For measurements with the MS7 cell the sample cell was filled with purified water (Milli-Q, Millipore Sigma Burlington, MA, USA). To this end the sample compartment of the instrument was opened and the liquid was injected into the cell with a syringe. The sample compartment was closed and a measurement of the background was performed. Subsequently, with sample compartment open, the magnetic stirrer was switched on and a drop of the particle standard suspension was added. If sample turbidity was too high, as indicated by the instrument software, the suspension was diluted by removing some of the liquid and adding more solvent. For measurements the sample compartment was

3. SMALL ANGLE LIGHT SCATTERING INSTRUMENT

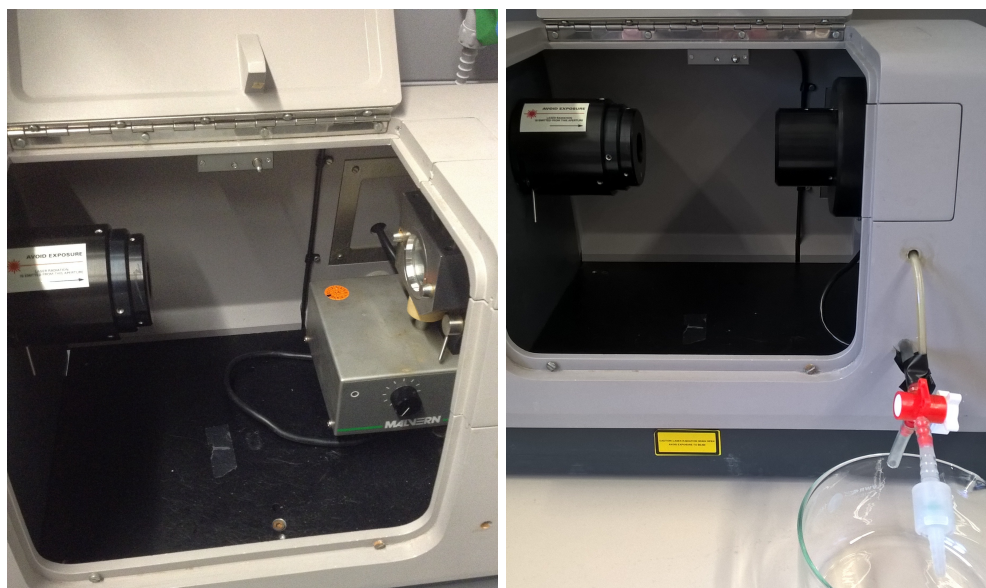


Figure 3.20: Lens-cell combinations of the Mastersizer S. In the open sample compartment the laser is on the left. The detector is to the right outside the picture. Note the different order of components for the two configurations. Left: MS7 cell and 300F Fourier lens. Right: 300RF reverse-Fourier lens and MS1 cell with flexible piping for emptying and filling the cell from the outside of the instrument.

closed.

For measurements with the MS1 cell the particle suspension was diluted first with purified water in a freshly-cleaned beaker. Via flexible tubes, which were connected to the inlet and outlet of the cell, the liquids could be injected from the outside of the instrument. Again, a background measurement of the solvent was performed followed by measurement of the sample suspension.

The scattering data were evaluated with the software of the instrument applying a full Mie theory model. Parameters were selected for a monomodal system of polystyrene particles (with complex refractive index $m = 1.6000 + 0.000i$) dispersed in water ($m = 1.3300 + 0.0000i$).

Particle sizing with the SALS instrument. Particle size measurements were carried out utilizing the colloidal suspension stage. Experiments were performed at room temperature without further thermo-control of the device. Particle suspensions in purified water were measured in flat-cells with 2 mm optical path. Prior to data recording optimum acquisition parameters were determined by test measurements of the suspensions. The background scattering was acquired only after sample measurements utilizing the same set of acquisition parameters.

UV/vis spectrometry. Transmission of the sample suspensions at the laser wavelength was determined by spectrometry (Lambda-19, PerkinElmer, Waltham, USA). The UV/vis/NIR spectrophotometer was a double-beam ratio-recording instrument featuring a double-monochromator. Relative transmission τ with respect to the sol-

vent, i. e. a cuvette filled with purified water, was determined in a small spectral range of 625 - 641 nm.

Standard latex beads. Three different-sized standard latex beads were utilized for benchmarking the home-built SALS instrument. The standards were obtained from BS-Partikel GmbH (Wiesbaden, Germany). The particles were provided in the form of stabilized aqueous suspensions and had a certified nominal size of $5.15 \pm 0.05 \mu\text{m}$ (HS0500-20, charge HS312.513), $2.06 \pm 0.07 \mu\text{m}$ (HS0200-20, charge HS012.157) and $519 \pm 14 \text{ nm}$ (HS0050-20, charge HS425.161), respectively. The number mean diameter and volume mean diameter stated on the certificates were identical since the polydispersity of the particles was low enough.

Preparation of particle suspensions. Prior to measurement particle suspensions were prepared by dispersing the standard latex beads in purified water (Milli-Q, Millipore Sigma Burlington, MA, USA). To this end a single drop of the $5 \mu\text{m}$ and the $2 \mu\text{m}$ particles stock suspensions, respectively, was added to 20 ml water in freshly cleaned graduated flasks. Two separate samples each were prepared in this way. Dispersion was aided by manually shaking the flasks. As suggested by the manufacturer the first drop from the dispensers was discarded. A dilution series of the 500 nm particles was prepared. 2 drops were added to 25 ml purified water. From this suspension 10 ml were diluted with a further 15 ml purified water. This process was applied once more to the diluted suspension yielding the third one. For measurement the suspensions were injected into flat-cell cuvettes and the relative transmission with respect to purified water was determined by vis spectroscopy. Except for the non-diluted dispersion of 500 nm particles all suspension had a relative transmission of well above 90 %.

3.7.2 Results: Particle sizing of standard latex beads

Reference measurements. Prior to benchmarking the home-built small angle light scattering instrument described above with standard latex beads, these particles were characterized both by direct imaging via scanning electron microscopy and light scattering-based particle sizing with the Malvern Mastersizer S (Malvern Instruments GmbH, Herrenberg, Germany). The results are summarized in FIGURES 3.21 - 3.23. SEM micrographs revealed spherical particles with a very narrow size distribution. Solvent evaporation as part of the sample preparation left the particles regularly-spaced in a hexagonal close-packed (hcp) lattice, which extended over several layers. For all samples the particle diameters determined by SEM coincided with the nominal sizes within experimental uncertainty. Measured values for the diameter were $5.1 \mu\text{m}$, $2.0 \mu\text{m}$ and 510 nm , respectively. Measurements with the Malvern Mastersizer S yielded the volume-based particle size distribution. The peaks of the distributions were identical to the nominal sizes within experimental uncertainty. Additionally, the volume mean diameter $D[4,3]$ (D_v) and z-averaged squared diameter $D[8,6]^2$ ($\langle D^2 \rangle_z$) were calculated,

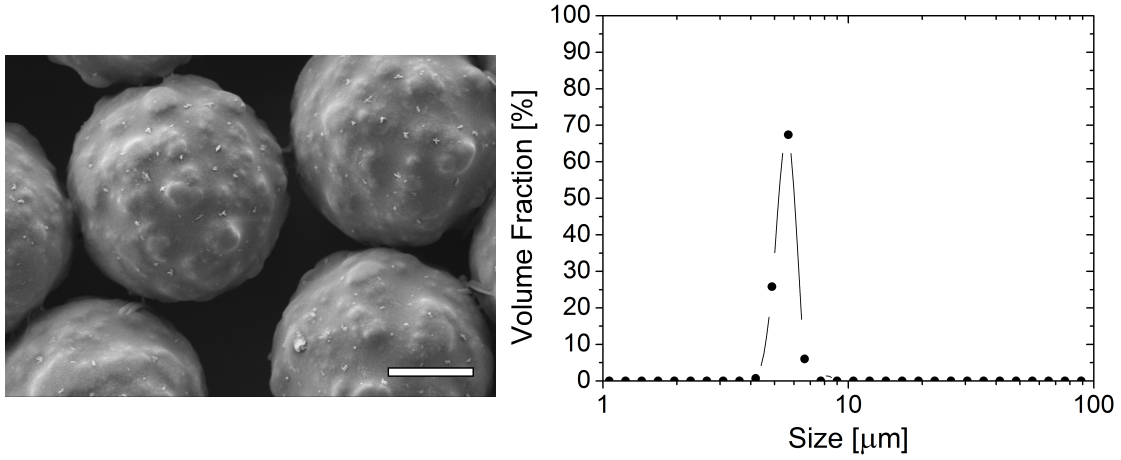


Figure 3.21: Left: Scanning electron micrograph of 5 μm standard latex beads. The scale bar represents 2 μm . Right: Results of particle sizing with the Malvern Mastersizer S. The distribution of the volume fraction shows a peak at $5.19 \pm 0.10 \mu\text{m}$.

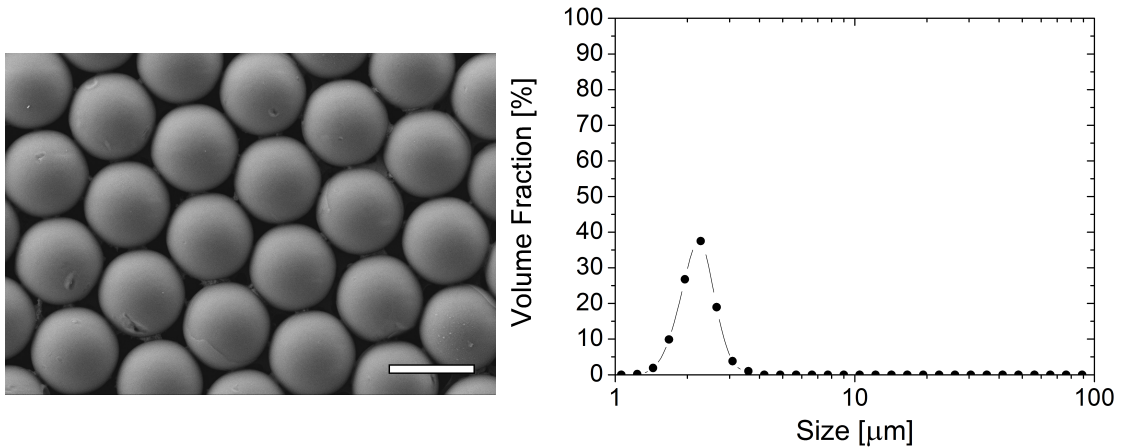


Figure 3.22: Left: Scanning electron micrograph of 2 μm standard latex beads. The scale bar represents 2 μm . Right: Results of particle sizing with the Malvern Mastersizer S. The distribution of the volume fraction shows a peak at $1.99 \pm 0.04 \mu\text{m}$.

where

$$D[p, q]^{(p-q)} = \frac{\sum D_i^{p-3} v_i}{\sum D_i^{q-3} v_i}. \quad (3.46)$$

with the geometric mean diameter $D_i = \sqrt{D_{i,lower} D_{i,upper}}$ given by the square root of the product of the lower and upper diameter limit of the discrete size class i and with v_i the volume fraction of particles within the size class i . Note that calculations of derived quantities is best performed using the geometric mean diameter rather than the arithmetic mean because the former one more appropriately represents the logarithmic spacing of the size class limits. Size classes defined in such a way yield the

3. SMALL ANGLE LIGHT SCATTERING INSTRUMENT

optimum resolution in terms of the particle size distribution for the given detector geometry and optical configuration of the instrument¹⁰. TABLE 3.2 summarizes the results of the measurements and calculations. Peak values and D_v coincided with the nominal specifications within experimental uncertainty except for the 500 nm particles the peak value of which was slightly smaller than the nominal size. The diameters agree, however, within 2% relative error. Results for z-averaged squared diameters are larger by definition. However, no comparative data was provided by the certificates of the standard latex beads.

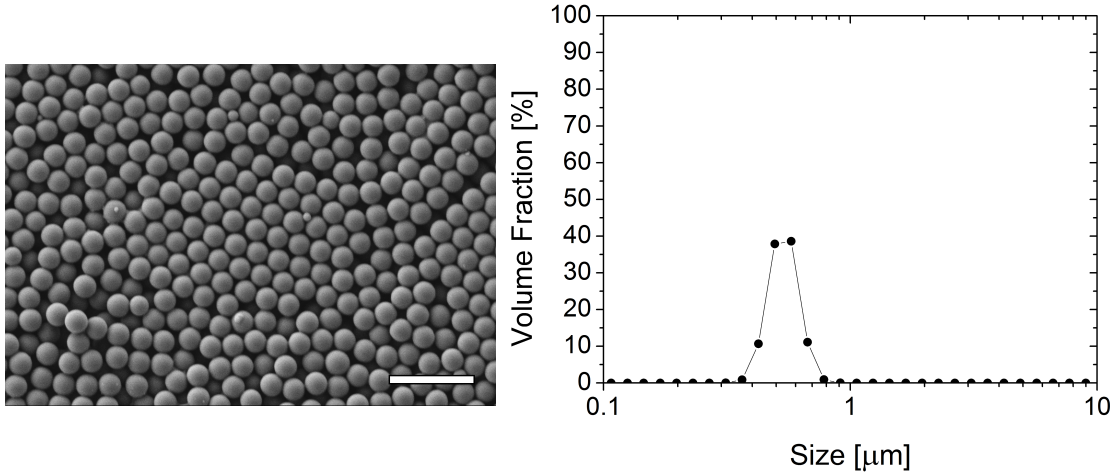


Figure 3.23: Left: Scanning electron micrograph of 500 nm standard latex beads. The scale bar represents $2\ \mu\text{m}$. Right: Results of particle sizing with the Malvern Mastersizer S. The distribution of the volume fraction shows a peak at 500 nm.

Table 3.2: Particle size values of the standard latex beads utilized for benchmarking the home-built SALS instrument as verified by various methods. All entries are in μm .

<u>nominal size</u>	<u>SEM</u>	<u>Mastersizer S</u>		
$D_n = D_v$		peak	D_v	$\langle D^2 \rangle_z$
5.15 ± 0.05	5.1	5.19 ± 0.10	5.14 ± 0.12	5.31 ± 0.30
2.06 ± 0.07	2.0	1.99 ± 0.04	1.99 ± 0.04	2.25 ± 0.02
0.519 ± 0.014	0.510	0.500	0.500	0.533

Small angle light scattering of standard latex beads. Experimental SALS curves for the $5\ \mu\text{m}$ and $2\ \mu\text{m}$ standard latex beads, respectively, are depicted in FIGURE 3.24 and FIGURE 3.25. Scattered intensities could be measured in an angular range $0.5^\circ < \theta < 11.5^\circ$. The scattering angle θ in the medium was derived by Snell's law from the calibrated scattering angle θ_{calib} in air ($n = 1.000$) via $\sin \theta = \sin(\theta_{calib})/n_m$ where $n_m = 1.333$ is the refractive index of water. The corresponding q -range was $0.12\ \mu\text{m}^{-1} < q <$

¹⁰Mastersizer S manual, MAN0101 Issue 1.3 August 1997.

3. SMALL ANGLE LIGHT SCATTERING INSTRUMENT

$2.65 \mu\text{m}^{-1}$. The lower limit was determined by the finite size of the beam stop (cf. FIGURE 3.18), the upper limit of the scattering angle was determined by the sample to Fourier lens distance. As discussed in SECTION 3.6 processing of experimental SALS data was carried out without solid angle correction (SP). In the figures the experimental results are compared to calculated scattering curves. Theoretical scattering curves of

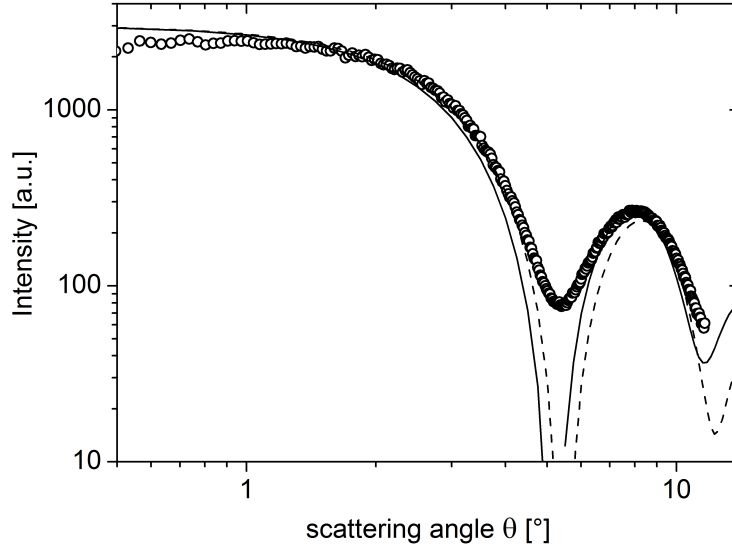


Figure 3.24: SALS scattering curve (o) of $5 \mu\text{m}$ standard latex beads dispersed in water compared to theoretical scattering curves based on Lorenz-Mie theory with $R = 2.575 \mu\text{m}$ (—) and $R = 2.5 \mu\text{m}$ (- - -). Calculations were performed with algorithms from [188]. Exposure time was $\tau_{exp} = 2000 \mu\text{s}$, acquisition was performed with OD2 attenuation, sample transmission was $\tau = 96\%$.

monodisperse model systems were calculated according to Lorenz-Mie theory utilizing the MATLAB algorithm `MIE_TETASCAN(M, x, NSTEPS)` given in [188]. The calculations yielded the Mie scattering intensities $|S_1(\theta)|^2$ and $|S_2(\theta)|^2$, respectively, as tabulated data intensities $|S_i(\theta)|^2$ versus scattering angle θ . The scattering curves are symmetric with respect to the forward direction. The data set, subsequently, contained $|S_1(\theta)|^2$ in the angular range $0 < \theta < \pi$ and $|S_2(\theta)|^2$ in the angular range $\pi < \theta < 2\pi$ in an angular spacing of π/NSTEPS , where the number of data points `NSTEPS` corresponded to one of the input parameters of the program. The other two input parameters were the relative refractive index

$$m = \frac{n_p}{n_s} = \frac{1.5960}{1.333} = 1.1973 \quad (3.47)$$

where n_p was the refractive index of polystyrene and n_s of water, respectively, and the size parameter $x = kR$ (see SUBSECTION 3.1) where

$$k = \frac{2\pi n_s}{\lambda_0} = \frac{2\pi \cdot 1.333}{0.6328 \mu\text{m}} = 13.2356 \mu\text{m}^{-1} \quad (3.48)$$

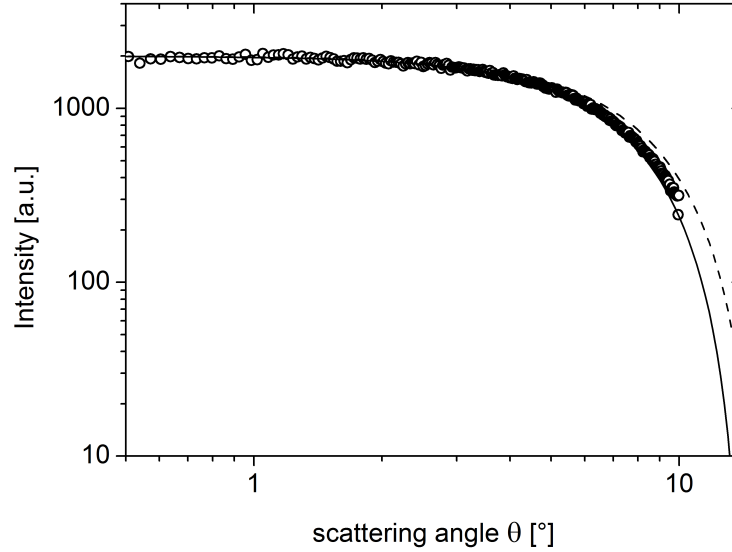


Figure 3.25: SALS scattering curve (o) of $2\ \mu\text{m}$ standard latex beads dispersed in water compared to theoretical scattering curves based on Lorenz-Mie theory with $R = 1.03\ \mu\text{m}$ (—) and $R = 0.95\ \mu\text{m}$ (- - -). Calculations were performed with algorithms from [188]. Exposure time was $\tau_{exp} = 4000\ \mu\text{s}$, acquisition was performed with OD2 attenuation, sample transmission was $\tau = 92\ \%$.

with the laser vacuum wavelength $\lambda_0 = 632.8\ \text{nm}$. Results of the calculations are depicted in FIGURE 3.26. All particles show a strong scattering in forward direction. It is the stronger the larger the particle gets. The overall scattered intensity increases with particle size. A distribution of local maxima in the perpendicular and parallel component of the scattered intensity can be observed being more pronounced with increasing particle radius.

The total scattered intensity was calculated according to EQUATION (3.9) as

$$I_s(\theta) = \frac{1}{k^2 r^2} \frac{i_1 + i_2}{2} I_0 = I'_0 (|S_1(\theta)|^2 + |S_2(\theta)|^2) \quad (3.49)$$

where $\langle \sin^2 \phi \rangle = \langle \cos^2 \phi \rangle = 1/2$ was applied. Taking the averages over ϕ is identical to the azimuthal averaging of the experimental SALS data. The latter yields the total scattered intensity into a ring as a function of θ and represents a sampling of all scattering planes with angles $0 \leq \phi < 2\pi$ for a given scattering angle. Ultimately comparison of theoretical and experimental scattering curves allowed direct comparison of the particle size values obtained from SALS and other techniques. The quantity I'_0 in EQUATION (3.49) was treated as a parameter and was varied until the experimental curve and the theoretical curve matched best.

Good agreement of experimental and calculated scattering intensities was achieved in case of the $5\ \mu\text{m}$ particles. Deviations were caused by the small but finite polydispersity of the system. The measurements just missed the second minimum due to scattering angle limitations. The depicted angular range is increased beyond the experimental

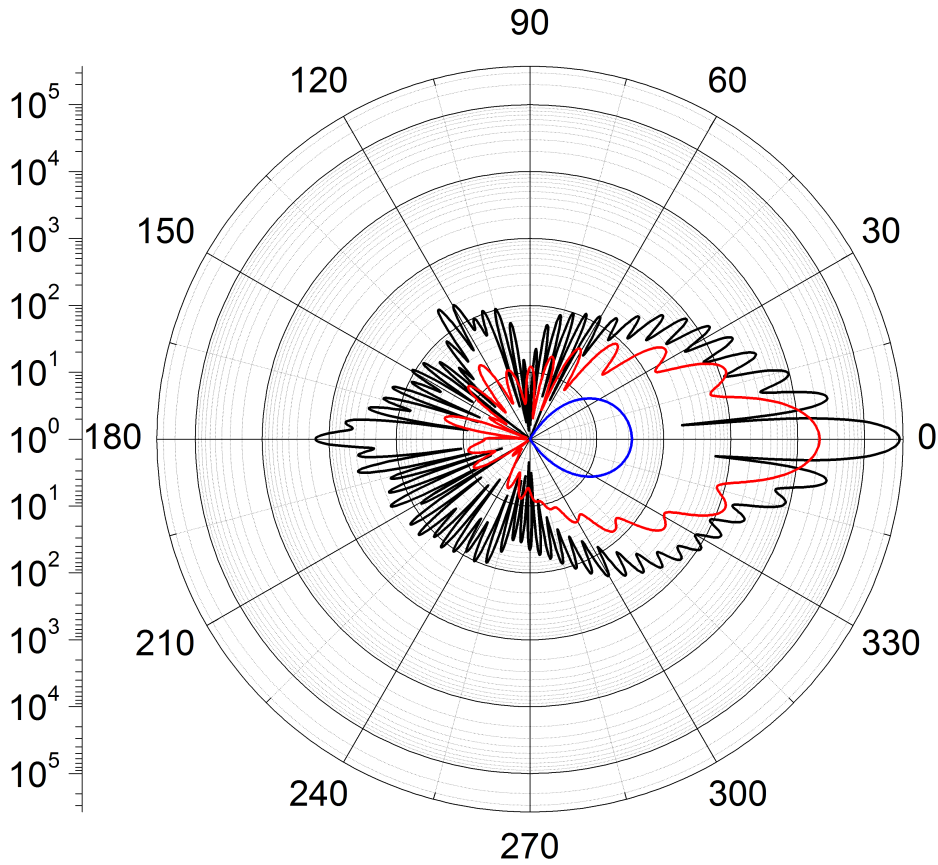


Figure 3.26: Polar diagram of the intensities scattered by the standard particles based on Lorenz-Mie theory. Numerical calculations were carried out with MATLAB algorithms from [188]. In the upper half circle ($0^\circ < \theta < 180^\circ$) the perpendicular intensity $|S_1(\theta)|^2$ is plotted. In the lower half ($180^\circ < \theta < 360^\circ$) the parallel component $|S_2(\theta)|^2$ is plotted. The curves are symmetric with respect to the half circles. Particle radii are $2.575 \mu\text{m}$ (black, outermost curve), $1.03 \mu\text{m}$ (red) and $0.26 \mu\text{m}$ (blue, innermost curve). Parameters of the calculations were $m = 1.1973$, $k = 13.2356 \mu\text{m}^{-1}$ and $\text{NSTEPS} = 720$.

range to visualize the location of the second minimum. In case of the $2 \mu\text{m}$ particles experimental and calculated scattering curves also show very good agreement. However, going to smaller particles with a diameter of 500 nm revealed strong deviations between experimental and calculated scattering intensities. FIGURE 3.27 shows three different experimental curves corresponding to decreasing particle concentration leading to increased transmitted intensity as determined prior to the SALS measurements by spectrometry. The measurements show a comparable trend of an initial decrease in scattering intensity changing into an upward slope at large scattering angles in contradiction to the theoretical Mie-scattering calculations which are plotted as well in the figure. In FIGURE 3.28a the signals of the dilution series uncorrected for the background signal are compared to the corresponding background measurements.

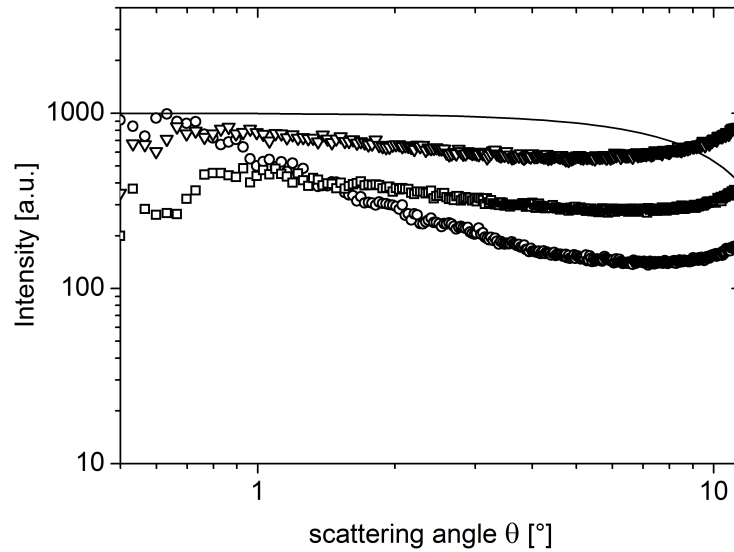


Figure 3.27: SALS scattering curve of 500 nm standard latex beads dispersed in water compared to theoretical scattering curves based on Lorenz-Mie theory with $R = 260$ nm (—). Sample transmissions τ were 96% (o), 92% (\square) and 76% (∇). Calculations were performed with algorithms from [188]. Exposure time was $\tau_{exp} = 5000 \mu s$, recordings were performed with OD2 attenuation.

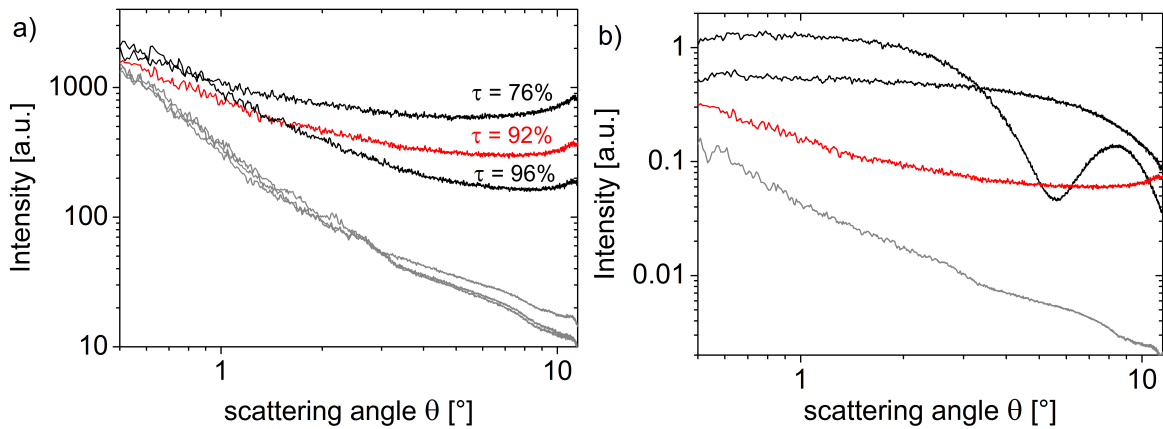


Figure 3.28: Uncorrected (non-processed) SALS intensities of particle suspensions compared to the respective background signal (lower, gray curves). a) Signals of the dilution series of 500 nm suspensions. Recordings were carried out with the same acquisition parameters. b) Typical SALS signals of all three standard suspensions normalized to exposure times. The red curve in a) and b) corresponds to the same measurement of the 500 nm-sized standard beads.

Background measurements were recorded for each experiment separately and show very good agreement. For scattering angles larger than 2° the background signal contributes less than 3% to the overall scattering signal. The background signal quickly drops in magnitude to the magnitude of the detector dark signal.

As can be seen, sample intensities approach the background signal with increasing di-

3. SMALL ANGLE LIGHT SCATTERING INSTRUMENT

lution. However, the upturn remains at large angles. The effect was already discussed in SECTION 3.6 and ascribed to spherical aberration of the Fourier lens L_1 . The effect is not visible in case of the larger particles (see FIGURE 3.28b), because it is compensated for by the strong angular dependence of the scattered intensity of the larger particles. We conclude by stating that the lower size limit of the home built SALS instrument for reliable particle size measurements must lie between $2\ \mu\text{m}$ and $0.5\ \mu\text{m}$. For particles smaller than this limit the angular scattered intensity distribution could not be determined accurately due to imaging limitations of the detection optics.

4 Phase transformation behaviour of polylactide

4.1 Materials and methods

Materials. Poly(L-lactide) (designated PLLA1 in this work) and poly(D-lactide) (PDLA) homopolymers were provided by Corbion (Total Corbion PLA bv, Gorinchem, The Netherlands) as well as a random co-polymer grade poly(L-co-D-lactide) (coPLA) with 4 % D-isomer content. Additionally, a high-molecular weight poly(L-lactide) (PLLA2) (Evonik Industries AG, Essen, Germany) was used in this work. Polymers were delivered as pellets or flakes, respectively, and used as-received without further purification. The properties of the polymers are summarized in TABLE 4.1. The polydispersity ($PDI = M_W/M_N$, where M_W is the weight average and M_N is the number average molecular weight) of the samples was between 1.5 and 1.8. The reader is referred to APPENDIX A for a comprehensive characterization of the PLA samples used in this work.

Table 4.1: Properties of the polylactide samples used in the studies of the phase transformation behaviour of PLA.

designation	D-units [%]	M_W [kg mol ⁻¹]	T_m^0 [°C] ^c
PLLA1	0	143	186 ± 2
PLLA2	0	406	199 ± 6
PDLA	100	153	181 ± 5
coPLA	4	163	171 ± 4
nPLLA1	2 ^a	143 / 153 ^b	189 ± 4 ^d
nPLLA2	2 ^a	406 / 153 ^b	201 ± 7 ^d

a) weight fraction of PDLA chains in the blend in %

b) M_W of the PLLA and PDLA components

c) equilibrium melting point determined by Hoffman-Weeks extrapolation

d) see FIGURES B.3 and B.4 in APPENDIX B

In addition, stereocomplex nucleated PLLA samples (nPLLA1 and nPLLA2) were prepared by solution casting of PLLA1 or PLLA2, respectively, mixed with 2 wt% of PDLA from dichloromethane (DCM, 99.8 %, AnalaR Normapur, VWR International GmbH, Langenfeld, Germany). The presence of scPLA crystals is known to accelerate overall crystallization of polylactide as the stereocomplexes act as heterogeneous nucleation sites [156]. Stock solutions were prepared and mixed in the respective ratios. In order to obtain films 5 ml solution were placed on petri dishes (diameter 50 mm). The solvent was allowed to evaporate for at least 24 h. The petri dishes were covered with lids to avoid rapid evaporation. Films with a thickness of 30 - 40 μ m were obtained and dried in a vacuum oven at 100 mbar and 30 °C overnight to remove residual solvent. Due to enhanced interaction PLLA and PDLA form scPLA with a much higher melting point of around 230 °C than the homocrystals of PLLA or PDLA (hcPLA) [215]. The presence of stereocomplex crystals in the films was verified by DSC, which showed the

4. PHASE TRANSFORMATION BEHAVIOUR OF POLYLACTIDE

characteristic endothermic melting of scPLA at 225 °C (see FIGURE B.2 in APPENDIX B).

Small Angle Light Scattering (SALS). Depolarized SALS was carried out with the home-built device described in detail in SECTION 3. For all experiments the high temperature sample stage for studying polymer melts was used.

Specimens were prepared by melting polymer samples on a laboratory hotplate (MR Hei-Standard, Heidolph Instruments, Schwabach, Germany) at 200 °C pressed between two microscopy cover glasses (18 mm × 18 mm cover glass, thickness no. 1 = 130 μm, borosilicate glass, VWR Chemicals). Spacers made from laboratory aluminum sheets were used to keep the sample thickness constant at 50 μm.

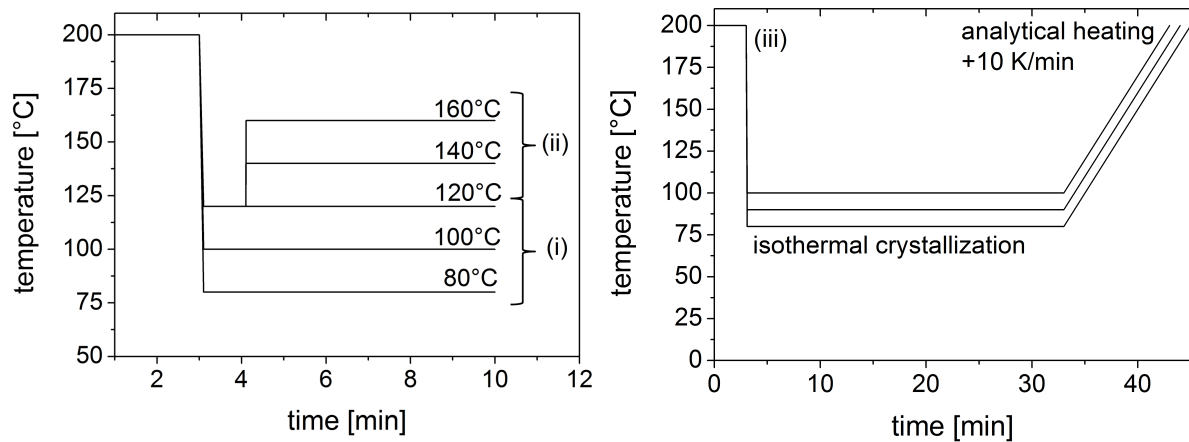


Figure 4.1: Temperature-time protocols for SALS measurements of the isothermal spherulite growth rate (left) and SALS characterization of the melting behaviour of PLA after isothermal crystallization (right).

Three different temperature-time protocols were applied in the SALS experiments. They are sketched in FIGURE 4.1. In isothermal crystallization experiments the thermal history of a specimen was erased by melting at 200 °C on the laboratory hotplate for 3 min. Subsequently, the sample was either (i) quenched to the respective isothermal crystallization temperature when experiments were carried out below approximately 120 °C, i. e. at large undercooling, or (ii) an intermediate nucleation step was introduced when experiments were carried out at low undercooling, i. e. at temperatures larger than approximately 120 °C. In the first case (i), the sample was quickly transferred with a vacuum pick-up tool to the SALS hotstage, which was kept at the isothermal crystallization temperature, and recording of scattering intensity was started immediately. Manual transfer of the sample from the hotplate to the hotstage took place in less than 10 s. In the second case (ii) when the undercooling was low the number density of spherulites was too low to give an adequate scattering signal for SALS measurements due to the decrease of several orders of magnitude in primary nucleation rate. This problem first and foremost affected experiments with the neat polymers, but also experiments with the nucleated polymers were affected, though at higher crystal-

lization temperatures, i. e. lower undercooling. The problem was bypassed by application of Tammann's two-stage crystal nuclei development method [173, 216]. After melting, the sample was first transferred to a second hotplate (MR Hei-Tec, Heidolph Instruments, Schwabach, Germany) at the respective nucleation temperature and kept there for 1 min allowing formation and initial growth of spherulites. A nucleation temperature of $T_{nuc} = 120^\circ\text{C}$ seemed to fit best to the procedure. Only then, the sample was transferred with a vacuum pick-up tool to the SALS hotstage, which was kept at the isothermal crystallization temperature, and recording of the scattering pattern was started. This made possible determination of spherulite growth rates solely by means of SALS over the whole temperature interval from near the glass transition temperature to near the melting temperature.

Note, that using (different) laboratory hotplates for preparing the polymer melt and performing isothermal crystallization of the sample material, and manual transfer thereof is an established technique for polymers with slow to moderate crystallization kinetics like PLA [217, 218].

In experiments on the phase transformation behaviour during melting of polylactide (iii), first the thermal history of the sample was erased by melting at 200°C on a laboratory hotplate for 3 min. The sample was quickly transferred to the SALS hotstage and isothermally crystallized for 30 min directly followed by heating to the melting temperature at 10 K/min and synchronous recording of the scattering pattern.

Scattering patterns were recorded at a maximum rate of 1 Hz and saved as sequences of separate image files on a personal computer via the Basler pylon camera software suite, which was provided with the digital camera. The image files were 2048×2048 pixels in size, corresponding to the maximum resolution of the camera detector chip. Data-reduction and data-evaluation were carried out with dedicated MATLAB scripts. The two-dimensional data sets were reduced to one-dimensional data sets by taking the azimuthal average over pixels belonging to the same ring centered on the position of the primary beam on the detector. The thickness of the rings was one pixel to yield maximum angular resolution with the given detector chip. This procedure is valid in the small-angle approximation. For processing of radially non-symmetric scattering patterns which did show azimuthal periodicity the averaging process was altered by considering only pixels fulfilling the appropriate constraints on the azimuthal angle μ . The details of the data processing and calibration of the respective scattering angle θ to each pixel ring are presented in SUBSECTIONS 3.5 and 3.6. For background subtraction the signal of the amorphous sample was used, which either corresponded to the first image of the sequence in isothermal crystallization experiments or the last image of the sequence in melting experiments. All data sets were normalized to the applied detector exposure times.

In the experiments the sample volume V , which was illuminated by the laser, was kept constant and the sample-detector distance r was identical for all measurements. The intensity of the primary beam I_0 was not recorded. However, the stability of the laser was verified periodically with a power meter (PM160, Thorlabs). Therefore, any recorded scattering signal was proportional to the angle-dependent Rayleigh ratio for

depolarized scattering

$$R_{H_V}(\theta, \mu) = \frac{i_{H_V}(\theta, \mu)r^2}{I_0V} \quad (4.1)$$

where $i_{H_V}(\theta, \mu)$ is the scattering intensity.

4.2 Light scattering from spherulites

Phase transformation of a number of high polymers from the non-ordered amorphous state¹¹ into the ordered crystalline state proceeds via nucleation and growth of spherulites [220–224]. These structures have been known for a long time from inorganic matter but extensive studies on polymer spherulites started only with the works of Bunn and Alcock [225] and Bryant [226] in the 1940s. Spherulites (Greek $\sigma\phi\alpha\acute{\iota}\rho\alpha$) are spherically symmetric supramolecular structures which form in the viscous polymer bulk when temperatures are between the glass transition and the melting temperature. Their size increases linearly with time until they impinge on each other and the whole volume is filled by spherulites with sizes ranging from several 100 nm up to several 10 mm.

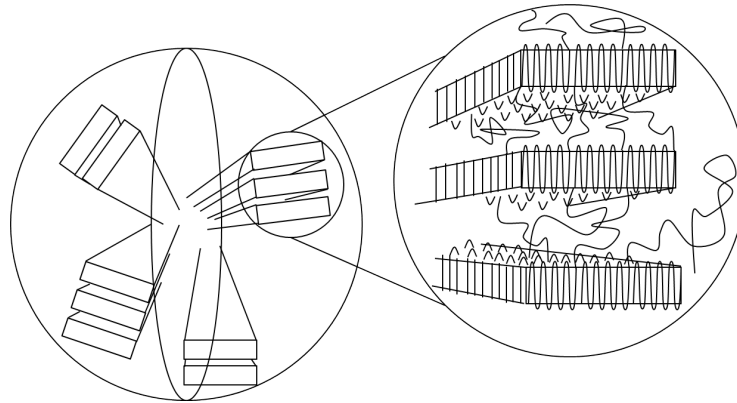


Figure 4.2: Sketch of the internal structure of polymeric spherulites. These consist of crystalline domains made up of radially directed lamellar stacks and inter-lamellar amorphous domains. After Boyd *et al.* in [227]. Lamellae are interconnected by so-called tie-molecules. The reader is referred to [218] for a discussion of the lamellar chain-folding structure in terms of the successive adjacent re-entry number of PLA chains.

Polymeric spherulites are two-phase structures with crystalline and amorphous domains. In FIGURE 4.2 the internal structure of a polymer spherulite is sketched. Radially directed fibrils, so-called lamellae, originating from the spherulite nucleus present

¹¹The interested reader is referred to the account by G. D. Wignall [219] on the discovery of the random coil chain conformation of linear polymers in the melt state by small angle neutron scattering in the 1970s.

the crystalline phase. The lamellae are made up of layers of chain-folded polymers giving rise to tangential orientation of the chains with respect to the spherulite radius vector [228]. Their thickness is of the order of 10 nm. Non-crystallizable material like entangled chains and chain ends are segregated during crystallization from the lamellae thus forming the inter-lamellar amorphous domains.

Spherulitic crystallization is comprised of formation / activation of the spherulite cores, denoted as primary nucleation, and subsequent deposition of further chains on the crystal growth faces of the lamellae, which is denoted as secondary or surface nucleation. The latter determines the growth of those lamellae and, in turn, determines the radial growth rate of spherulites. As the cross-section of the lamellae is constant during isothermal crystallization multiplication of lamellae (by mechanisms which are still under debate) is a necessary requirement to keep the growing spherulite volume uniformly filled with lamellae.

Due to their internal structure spherulites are optically anisotropic objects. In POM they can easily be distinguished from the optically isotropic melt (see FIGURE 4.3). Light extinction along the directions of the polarizer and the analyzer point at a specific alignment of the optical indicatrices.

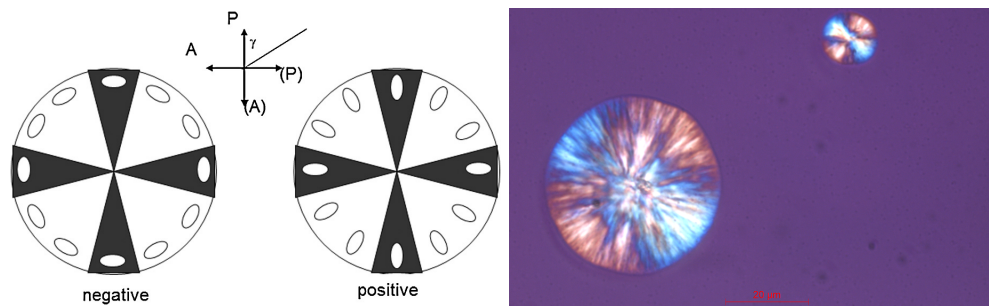


Figure 4.3: Left: Two possible orientations of the indicatrix with respect to the spherulite radius direction giving rise to the Maltese cross when viewed under crossed polarizers. Reproduced from [224]. Right: PDLA spherulites crystallized at 140 °C viewed in POM with additional full wave sensitive tint plate. The spherulite shows negative birefringence as indicated by the colouring of the quadrants (first and third one red, second and fourth quadrant blue).

A theory of light scattering from spherulites was first presented by Stein and co-workers, who treated the scattering problem in the RDG-approximation and modelled spherulites as spherical, optically anisotropic entities [52]. In the following the depolarized scattering from spherulites and its application to the characterization of spherulite morphology is given based on the formulation of the theory presented in [229]. The interested reader is referred to the work of Champion *et al.* [230] for a derivation in the amplitude scattering matrix formalism presented in SUBSECTION 3.1.

The Rayleigh ratio R_{HV} (defined in EQUATION 4.1) of depolarized scattering, with the analyzer oriented perpendicular to the polarization direction of the primary beam, from a single optically anisotropic spherulite which is embedded in an isotropic ma-

trix is given by

$$R_{H_V} = \frac{16\pi^4}{\lambda_0^4} V_S^2 \cos^2(\rho_2) (\alpha_r - \alpha_t)^2 \sin^2(2\mu) \left(\frac{\cos^2(\theta/2)}{\cos(\theta)} \right)^2 \times \left(\frac{3}{U^3} \right)^2 (4 \sin U - U \cos U - 3SiU)^2 \quad (4.2)$$

with polarizabilities of the spherulite α_r in radial direction and α_t in tangential direction and with vacuum wavelength λ_0 [52, 229]. The formula yields a four-lobed scattering pattern (see FIGURE 4.4) with intensity maxima on the diagonals (odd multiples of $\mu = 45^\circ$) of each image quadrant. The scattering intensity is a function of the scattering angle θ , which is defined with respect to the direction of the primary beam, and of the azimuthal angle μ , which is defined with respect to the polarization direction of the incident field. $V_S = 4/3\pi R^3$ is the volume of the spherulite. A geometric polarization correction is introduced by the term

$$\cos \rho_2 = \frac{\cos \theta}{(\cos^2 \theta + \sin^2 \theta \sin^2 \mu)^{1/2}}. \quad (4.3)$$

In the small angle regime the correction can be neglected since $\cos \rho_2 \approx 1$. The reduced

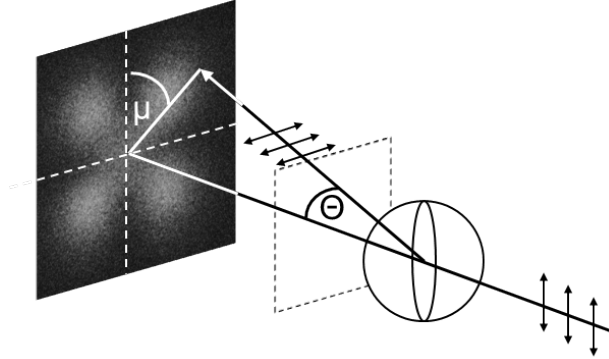


Figure 4.4: Typical four-lobed H_V pattern from an optically anisotropic spherulite in a depolarized SALS experiment. The scattering angle θ is defined with respect to the primary beam. The azimuthal angle μ is defined with respect to the polarization direction of the incident field.

scattering vector

$$U = R \cdot q = R \cdot \frac{4\pi n_m}{\lambda_0} \sin \left(\frac{\theta}{2} \right), \quad (4.4)$$

where n_m is the refractive index of the matrix surrounding the spherulites, presents the variable used in EQUATION (4.2). The refractive index of the polymer melt corresponding to the matrix is $n_m = 1.45$ at the wavelength of the laser and is independent of the enantiomeric composition of the polylactide under investigation [231]. It is apparent

that via U the H_V scattering pattern is sensitive to the spherulite radius R . From the intensity maximum at θ_{max} on the diagonals defined by odd multiples of $\mu = 45^\circ$ the average spherulite radius can readily be obtained from the peak position

$$\frac{d}{dU} \left(\frac{3}{U^3} \right)^2 (4 \sin U - U \cos U - 3SiU)^2 \stackrel{!}{=} 0 \quad (4.5)$$

where

$$SiU = \int_0^U \frac{\sin t}{t} dt \quad (4.6)$$

is the sine integral. The relation between the spherulite radius and the magnitude of the scattering vector q_{max} associated with the peak in scattering intensity, thus, is

$$R = \frac{4.10}{q_{max}}. \quad (4.7)$$

In experiment, in general, the recorded scattering signal is a result of the collective scattering of an array of spherulites which may, in addition, deviate from the model spherical entities with strictly defined optical anisotropy. Stein *et al.* showed that the Rayleigh ratio then can be expressed as

$$R_{H_V} = \frac{16\pi^4}{\lambda_0^4} V_S \phi_S \cos^2(\rho_2) (\alpha_r - \alpha_t)^2 \sin^2(2\mu) \left(\frac{\cos^2(\theta/2)}{\cos(\theta)} \right)^2 \times \left(\frac{3}{U^3} \right)^2 (4 \sin U - U \cos U - 3SiU)^2 [\kappa(\theta, \mu)F(\theta, \mu)]^{-1} \quad (4.8)$$

where V_S is an averaged volume of a spherulite and ϕ_S is the volume fraction of spherulites in the illuminated sample volume, respectively [229]. The function $\kappa(\theta, \mu)$ is a correction for multiple scattering. $F(\theta, \mu)$ introduces corrections for so-called external and internal disorder referring to two kinds of imperfections, micro-scale intra-spherulitical and macro-scale extra-spherulitical morphological imperfections. Both functions account for experimentally observed deviations from the ideal scattering behaviour given in EQUATION (4.2) in terms of non-zero scattering at low q and a slower decay in scattering intensity at large q .

Internal disorder is related to density fluctuations within spherulites. The lamellar structure is not aligned perfectly about the radius vector. Instead, due to random arrangement of spherulite lamellae and lamellar branching, fluctuations in the lamellar orientation are caused. Hence, also the polarizabilities show local fluctuations. As a consequence the peak maximum is decreased while excess scattering is observed at all other scattering angles q .

External disorder describes three more aspects of deviation from the ideal scattering of an ideal model spherulite. First, it is generally accepted that spherulites evolve via successive growth stages from the primary nucleus into rod-like and sheaf-like precursor structures and finally into spherical entities [221]. These incompletely developed

spherulites cause excess scattering at low and large q , however, the position of the scattering peak is not affected [100].

The second aspect of external disorder is spherulite truncation after impingement [53, 232, 233]. This is the case at the end of the crystallization process, but may even happen before due to random placement of the spherulite nuclei. Note that this is irrespective of the nature of the nucleation process being either homogeneous or heterogeneous. Truncated spherulites are no longer spherical in appearance but are rather polygonal shaped crystalline entities. Under these circumstances the meaning of the spherulite radius R is lost but it rather defines an average distance r from the nucleus to the spherulite boundary.

Intimately related with the spherulite nucleation process is the distribution of spherulite sizes, which is the third aspect of external morphological disorder. The resulting scattering signal from an array of spherulites is dominated by the larger spherulites because of their much greater scattering power which scales with the square of the volume. Hence, any size information obtained from the scattering curve is heavily weighted towards the larger spherulites in the distribution.

It was demonstrated by Wissler *et al.* that an effective radius

$$\langle R \rangle = \frac{\langle r^{n+1} \rangle}{\langle r^n \rangle} \quad (4.9)$$

can be extracted from the peak of the H_V scattering pattern from a collection of (truncated) spherulites with various sizes. It is given by the ratio of the higher moments

$$\langle r^n \rangle = \int_0^\infty r^n N(r) dr \quad (4.10)$$

of the distribution where $N(r)$ is the distribution function and n is the order of the moment, with the moments depending on whether spherulites are two- or three-dimensional [234]. They also stated that determining $N(r)$ is fruitless due to additional effects like internal disorder affecting the scattering curve and the insensitivity of the scattering signal to all but the largest spherulites.

The effect of the spherulite nucleation process and the resulting size distribution of truncated spherulites on the characterization of the effective radius from the scattering maximum was discussed in detail by Bartczak and Galeski who, thus, brought together the above mentioned considerations on external disorder in one model [235]. They concluded that the relation between the average spherulite size and the magnitude of the scattering vector q_{max} associated with the peak of the H_V scattering intensity is given by

$$\langle R \rangle = \frac{\langle r^5 \rangle}{\langle r^4 \rangle} = \frac{4.10}{q_{max}}. \quad (4.11)$$

This result is valid for an assembly of truncated spherulites irrespective of their nucleation mechanism being either sporadic, yielding a broad size distribution, or instantaneous (athermal) primary nucleation, yielding a narrow size distribution, respectively.

Note again that the spherulite radius is known to increase linearly with time during isothermal crystallization and so the effective spherulite size determined from EQUATION (4.11) is a linear function of time, as well.

4.3 Spherulite linear radial growth rates

Spherulite growth was monitored in terms of the scattering vector q_{max} associated with the intensity maximum of the depolarized scattering pattern as a function of time during isothermal crystallization. In FIGURE 4.5 a typical four-lobed H_V scattering pattern from depolarized SALS experiments is depicted along with the time-dependent one-dimensional scattering curves obtained from data-reduction of the two-dimensional data-sets. Depolarized SALS measurements were performed without placing a beam

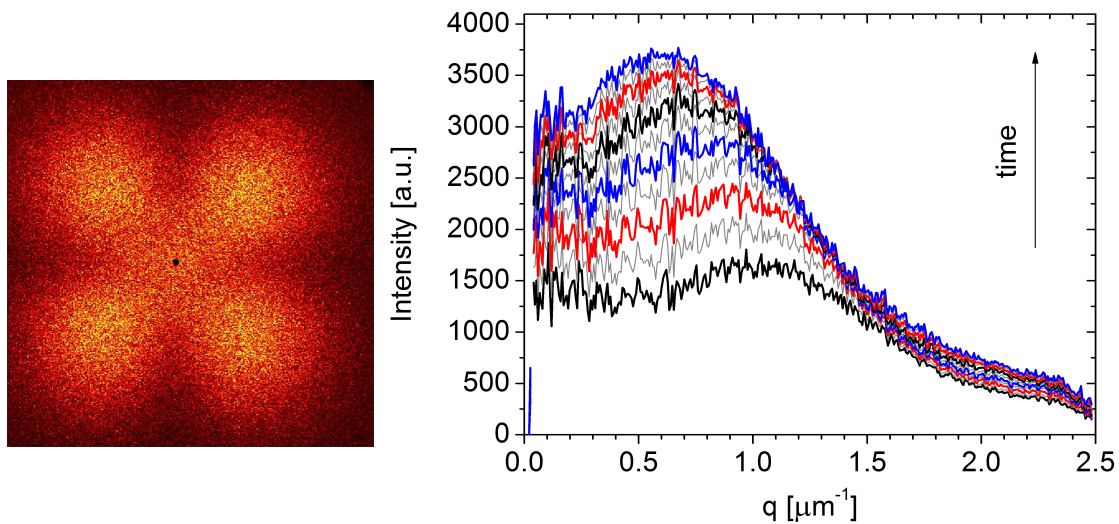


Figure 4.5: Typical four-lobed H_V scattering pattern of spherulites (left) during isothermal crystallization experiments and scattering curves (right) along the diagonals (odd multiples of $\mu = 45^\circ$). Some of the curves are coloured to aid the eye. Data from PLLA1, $T_c = 85^\circ\text{C}$.

stop in the detection optics of the SALS instrument. This approach fully utilized the very small cross-section of the primary beam on the detector which is a beneficial feature of the Fourier-type SALS instrument. Thus, the angular range of the instrument was limited towards low q by the image of the primary beam only. Detrimental effects of a physical beam stop were avoided. Most of the intensity of the primary beam was blocked by the analyzer. However, residual intensity reached the detector due to the finite extinction ratio of the utilized analyzer. Although desirable, it was not possible to quantitatively record the intensities of the scattered light and the primary beam simultaneously with the camera. Under experimental conditions for recording of the scattering pattern, at a given sensor exposure time and due to the limited range in sensitivity of the sensor chip the residual intensity from the transmitted primary beam caused saturation of the respective detector pixels. After background subtraction the

primary beam is marked by the black pixels in the center of the detector image.

Furthermore, the recorded scattering pattern shows two more characteristics. First, the scattered intensity is non-zero at low q due to intra-spherulitic disorder and spherulite-impingement as was discussed already in the preceding SUBSECTION 4.2. Second, the scattered intensity is not a continuous distribution but the scattering pattern displays a fine granular structure. This phenomenon is also reflected in the appearance of the one-dimensional scattering curves which could easily be mistaken for noise. This so-called speckling is a result from interference of the highly coherent laser light scattered from different spherulites [103, 236–238]. Speckling becomes the less pronounced for assemblies of spherulites the larger their size and their number, i. e. the larger the illuminated sample volume [232].

From the plot in FIGURE 4.5 it can be seen that with time during isothermal crystallization the scattering peak at q_{max} increases in magnitude and shifts to lower scattering angles due to the growth of spherulites in the sample. For calculation of the average spherulite radius the peak position was determined from an empirical polynomial fit of 4th order to the scattering curve [239].

Exemplary results of average spherulite radii $\langle R \rangle$ as a function of time for various isothermal crystallization temperatures are plotted in FIGURE 4.6. The lower limit of

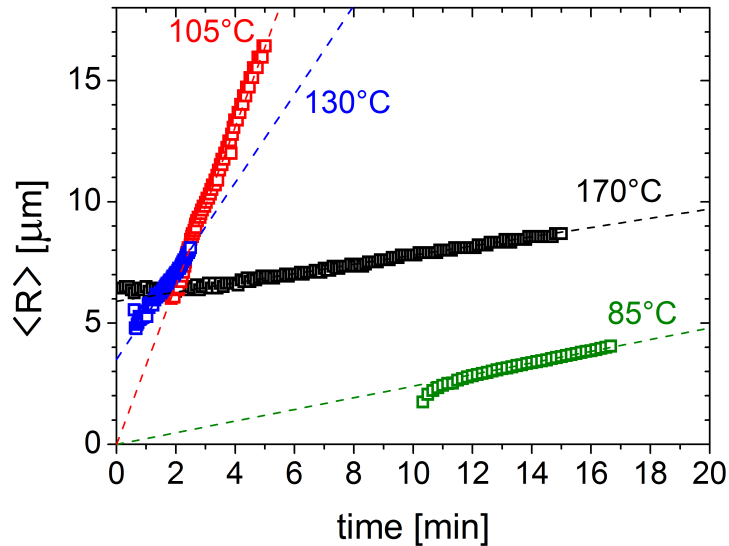


Figure 4.6: Exemplary average spherulite radii $\langle R \rangle$ as a function of time at the indicated isothermal crystallization temperatures T_c . Data-sets are from PLLA2. The dashed lines represent extrapolations of the radii to time zero. For experiments at $T_c = 170^\circ\text{C}$ (\square) and $T_c = 130^\circ\text{C}$ (\square) the initial radius was non-zero due to pre-formation of spherulites at larger undercooling (Tammann method). For experiments carried out at $T_c = 105^\circ\text{C}$ (\square) and $T_c = 85^\circ\text{C}$ (\square) the initial radii were zero indicating negligible nucleation induction time.

spherulite radii which could be determined with the home-built SALS instrument was $2\ \mu\text{m}$ due to upper limitations of the scattering angle by the detection optics. As can be seen, the linear growth stage of the spherulites prior to impingement of neighbouring

spherulites was captured by the measurements. Extrapolation of the spherulite radii to size zero revealed zero induction time of spherulite growth in case of large undercooling at crystallization temperatures $T_c = 85^\circ\text{C}$ and $T_c = 105^\circ\text{C}$. This is in good agreement with literature data on the onset of crystal nucleation, which is of the order of only seconds in the respective temperature interval [149]. Non-zero radii at time zero in experiments carried out at lower undercooling resulted from spherulites which were formed prior to the isothermal experiment by application of Tammann's two-stage crystal nuclei development method [173, 216]. Tammann's method made possible SALS measurements also at low undercooling. This method separated growth from nucleation. Spherulites were nucleated at large undercooling where the nucleation rate is high and growth is negligible. Then, spherulite growth was monitored at lower undercooling where the spherulite nucleation rate is negligible. Linear fitting of the time-dependent radii yielded the spherulite linear radial growth rates

$$G(T_c) = \frac{d\langle R \rangle}{dt} \quad (4.12)$$

as a function of the isothermal crystallization temperature. The variation of the growth rate with crystallization temperature T_c is depicted in FIGURE 4.7 for PLLA1. Data could be obtained via SALS in the regime of $T_g < T_c < T_m$ with T_g the glass transition temperature and T_m the melting temperature. In addition, growth rate data obtained from POM measurements [Gra17, Gro18] in a temperature regime of $115^\circ\text{C} \leq T_c \leq 150^\circ\text{C}$ is plotted. Samples were cooled from the melt at -30K/min , which was the maximum rate for the POM device [Gra17]. At $T_c < 115^\circ\text{C}$ the spherulite density was too large and their size was too small, at $T_c > 150^\circ\text{C}$ spherulite nucleation was too low for efficient POM measurements.

The two data sets from the different methods are congruent with each other. The growth rate curve shows the typical temperature-dependence for semi-crystalline polymers. Growth rates are small at low undercooling and at large undercooling, respectively, due to increased critical nucleus size in the first case and increased viscosity inhibiting segmental diffusion in the latter case. The obtained growth rate curve is in good agreement with previous works which applied polarized optical microscopy only [22, 30, 48, 240] or SALS and POM for different temperature intervals [65]. Also, the characteristic local maximum of the growth rate, being located on the low-temperature flank of the curve, was observed [33, 34, 65]. Note, that the SALS-based growth rate curve presented in this thesis for the first time covers the entire temperature range of T_c including the branch with low undercooling.

FIGURE 4.8 summarizes the results of the SALS studies of the crystallization behaviour of polylactide in terms of the crystallization temperature-dependent spherulite linear radial growth rate. In addition to PLLA1 presented above data from PLLA2, PDLA and coPLA is depicted which means that the effects of stereoisomer composition and molecular weight on the growth rate can be scrutinized.

As expected all polymers show a bell-shaped growth rate curve falling off towards the glass transition and large undercooling, and towards the melting temperature at low

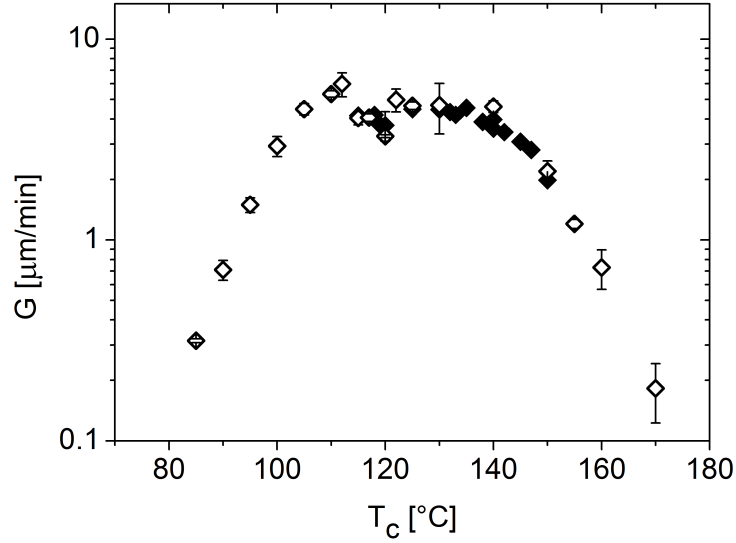


Figure 4.7: Temperature dependent linear radial growth rates $G(T_c)$ of PLLA1 spherulites determined from the derivative of the spherulite radii with respect to time as established by isothermal SALS experiments (\diamond) and POM (\blacklozenge). POM data is from [Gra17, Gro18].

undercooling. In the limits of experimental uncertainty the growth rate curves of the two PLLA homopolymers PLLA1 and PLLA2 overlay. Although both polymers differed in molecular weight by a factor of almost three an effect of molecular weight on the growth rate could not be established unambiguously from the data in contrast to other studies [34]. The investigated PDLA sample showed spherulitic growth at rates comparable to that of the PLLA polymers. The coPLA sample, however, showed a significant decrease in the growth rate over the whole temperature range as compared to the homopolymers with similar molecular weight.

Within experimental uncertainty the discontinuity of growth rate curves of the PLLA and PDLA homopolymers, respectively, at around 115 °C due to the polymorphic transition from α' -phase crystallites to α -phase crystallites is clearly noticeable in the SALS-based data.

With growth rate data exclusively from SALS spanning almost the full crystallization temperature window of polylactide it was possible to analyse the crystallization behaviour of polylactide in terms of the Lauritzen-Hoffman (LH) theory [174–176]. This shall be demonstrated in the following for the PLLA2 sample.

The LH theory is a kinetic model which describes the spherulite linear radial growth rate G in the scheme of secondary nucleation of chain segments via

$$G(T_c) = G_0 \exp\left(-\frac{U^*}{R(T_c - T_\infty)}\right) \exp\left(-\frac{K_g}{T_c \Delta T f}\right) \quad (4.13)$$

where T_c is the crystallization temperature, G_0 is a molecular weight-dependent pre-factor and R is the universal gas constant. The first exponential term accounts for

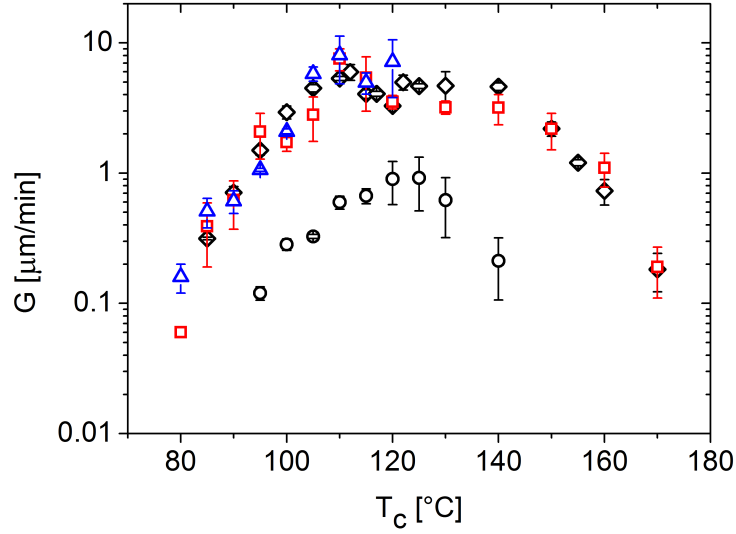


Figure 4.8: Temperature dependent linear radial growth rates $G(T_c)$ of PLLA1 spherulites (\diamond), PLLA2 (\square), PDLA (\triangle) and coPLA (\circ) determined by isothermal SALS measurements. Data of PLLA1 correspond to those shown in FIGURE 4.7.

transport of chain segments to the growing crystal face where U^* is the energy required for passing the interface between the melt and crystal phase and $T_\infty = T_g - C$ is the limiting temperature where all chain motions associated with viscous flow cease. For polylactide $C = 30$ K was used [28]. The second term models the thermodynamic driving force of the crystallization process where K_g is the nucleation parameter associated with the energy required for the formation of a critically-sized surface nucleus (so-called stem), $\Delta T = T_m^0 - T_c$ is the undercooling with respect to the equilibrium melting temperature $T_m^0 = 200$ °C as determined via Hoffman-Weeks analysis [241] from DSC measurements (see APPENDIX A.3) and $f = (2T_c)/(T_c + T_m^0)$ is a correction factor accounting for the change in enthalpy of fusion with temperature. The LH theory discusses three different temperature-dependent regimes of the growth rate G , denoted as I, II, III. These regimes are characterized by the relative magnitude of the rate of secondary surface nucleation i of chain segments and the rate of lateral covering of the growth face g by the ensuing addition of further chain segments (stems). Transitions between regimes arise from the strong change in i while g shows only a weak dependence on temperature [242]. Equation (4.13) can conveniently be rewritten to obtain the resulting nucleation rate constants K_g via

$$\ln G + \frac{U^*}{R(T_c - T_\infty)} = \ln G_0 - \frac{K_g}{T_c \Delta T f}. \quad (4.14)$$

In FIGURE 4.9 the resulting Lauritzen-Hoffman plot is depicted. Separate fitting was carried out to account for the two different slopes in the data-set. The nucleation parameters obtained in this way were $K_g(\text{III}) = 3.57 \cdot 10^5 \text{ K}^2$ at large undercooling and $K_g(\text{II}) = 1.7 \cdot 10^5 \text{ K}^2$ at low undercooling, respectively. The ratio of the two nucleation

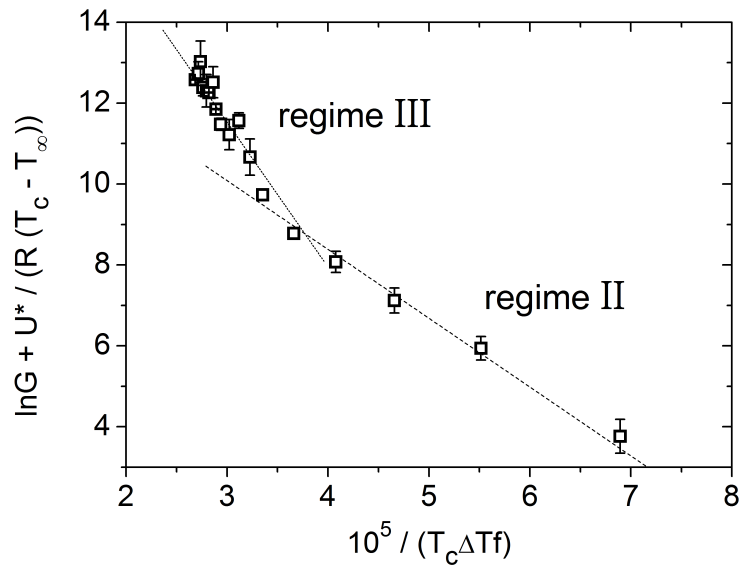


Figure 4.9: Lauritzen-Hoffman analysis of the spherulite growth rate data of PLLA2. The constants used in Equation (4.14) were $U^* = 6.27 \cdot 10^3 \text{ J mol}^{-1}$ and $T_\infty = T_g - 30 \text{ K}$.

parameters is 2.1, which is close to the theoretical value of 2 indicating a transition from growth regime III to II within the LH model. Data suggests a regime transition at around 130°C , which is slightly higher than reported in literature [31, 48]. At very low undercooling the LH theory predicts regime I growth. This was not observed in our experiments in agreement with literature [31, 48].

For the sake of completeness, the reader shall be made aware of criticism on the application of LH theory to the full growth rate data set of PLA spanning homogeneous as well as mixed phases of α' -phase and α -phase crystals. The major arguments of the ongoing discussion are summarized in [31]. In particular, the causal relation between the α'/α -phase transition and the LH regime transition is under debate. It is not yet clarified whether one of the transitions is the consequence of the other or if the two phenomena are mutually related to each other, at all.

4.4 Effect of the presence of scPLA

The effect of nucleating polylactide via blending of PLLA with small amounts of PDLA on the crystallization behaviour was studied with the two blends nPLLA1 and nPLLA2, respectively. First, the overall crystallization behaviour of the materials was characterized by DSC measurements (see APPENDIX A.3 for experimental details). Second, spherulite linear radial growth rates were determined via SALS measurements.

FIGURE 4.10 depicts the thermograms of the isothermal crystallization segment after cooling from the melt to various crystallization temperatures at a rate of -50 K/min . Melting of the samples was carried out at 200°C which was below the melting temperature of the stereocomplex crystals. Since the spherulite growth rate of polylactide has

4. PHASE TRANSFORMATION BEHAVIOUR OF POLYLACTIDE

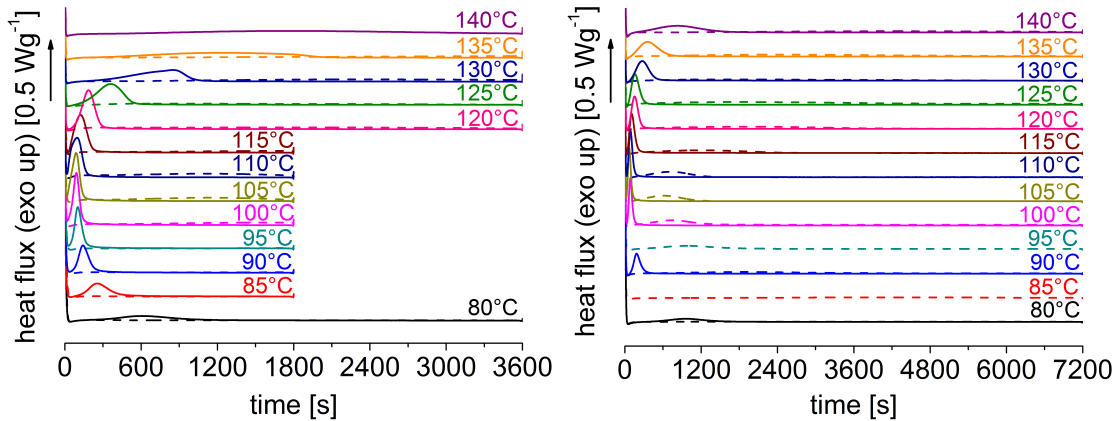


Figure 4.10: DSC thermograms of the isothermal crystallization of the nucleated samples (—) nPLLA1 and nPLLA2 in comparison to the neat polymers (- - -) PLLA1 and PLLA2, respectively, at the indicated crystallization temperatures. Samples were cooled from the melt at a rate of -50 K/min. The data-set for PLLA2 is from [Rok18].

its maximum at around 110°C , as was demonstrated in SUBSECTION 4.3, and spherulite nucleation increases with undercooling, DSC measurements of PLLA1 and nPLLA1, respectively, were optimized with respect to the duration of the isothermal crystallization segment. In case of PLLA2 and nPLLA2, respectively, the segment length was set to 2 h irrespective of the crystallization temperature which yielded straight baselines when, after completion of isothermal crystallization, the signal dropped to a constant value with the steady-state heat-flux of the instrument. Note, however, that crystallization of nPLLA2 was completed within 20 min of the isothermal experiments. The same holds for all measurements of nPLLA1 but those two measurements at lowest undercooling. The thermograms of the stereocomplex-assisted nucleated polymers show distinctive exothermic peaks indicative for isothermal crystallization. At the given scale the exotherms of the neat polymers are hardly noticeable in case of PLLA1 while they can be discerned better in case of PLLA2. For the neat polymers the crystallization exotherms not only occur later in the process but are also much broader and lower in magnitude than in case of the nucleated polymers. In analogy to [32] the times τ_p associated with the peak of the crystallization exotherms were determined as a function of the crystallization temperature. For symmetric peaks τ_p is identical to the half-time of crystallization $t_{1/2}$ which is the characteristic time for reaching half of the final sample crystallinity. The results are shown in FIGURE 4.11. The τ_p of the nucleated polymers are compared to those of the neat polymers. For the neat polymers the local minimum of τ_p at around 105°C coincides with the maximum in the spherulite growth rate (compare FIGURE 4.8). No distinct minimum in τ_p can be observed for the nucleated materials. Obviously, stereocomplex assisted nucleation speeds up the overall isothermal crystallization of polylactide by a factor of up to 20 in the presence of 2 wt% of scPLA. The data suggests that this heterogeneous nucleation is most effective at large undercooling and decreases with decreasing undercooling.

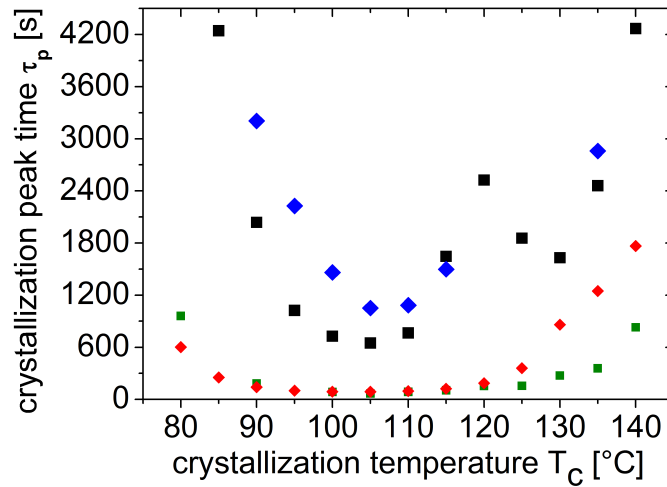


Figure 4.11: Crystallization peak times τ_p during isothermal crystallization of the nucleated samples nPLLA1 (♦) and nPLLA2 (■) in comparison to the neat polymers PLLA1 (♦) and PLLA2 (■), respectively, as a function of the indicated crystallization temperatures. Samples were cooled from the melt at -50 K/min.

In FIGURE 4.12 SALS measurements of the effect of the presence of scPLA in nPLLA1 and nPLLA2 on the spherulite linear radial growth rate are depicted. It should be pointed out again that measurements were carried out after melting of the samples at 200 °C which is below the melting point of the stereocomplex crystals present in the material. As is evidenced from the graphs the growth rate curve of nPLLA1 overlays well with the growth rate data of PLLA1 over a temperature interval ranging from 90 °C to 170 °C. Hence, stereocomplex assisted nucleation did not have a measurable effect on spherulite linear radial growth rates. Compared to the neat polymer the lowest temperature accessible for size-determination of spherulites was, however, shifted to slightly higher temperatures. At isothermal crystallization temperatures below 90 °C an increase of scattering intensity was noticed at large q . While this indicated spherulitic growth the scattering intensity maximum was out of range of the angular range of the detector, thus, preventing size-determination. This observation indicates enhanced spherulite number density with impingement stopping spherulite growth at small radii $\langle R \rangle \leq 2$ μm . Furthermore, due to increased spherulite number density, growth rates could easily be obtained up to temperatures ≤ 140 °C without application of Tamman's method. The drop in the curve at around 120 °C is indicative for the discontinuity of the growth rate reported in literature associated with the transition of the crystal lattice from the conformationally disordered α' -form to the ordered α -form [32].

The results obtained for nPLLA2 were very similar to those obtained for nPLLA1. The spherulite growth rate curves of the nucleated and non-nucleated samples were congruent within experimental uncertainty. The temperature range accessible for SALS measurements was 90 °C to 135 °C without application of Tamman's method. Inter-

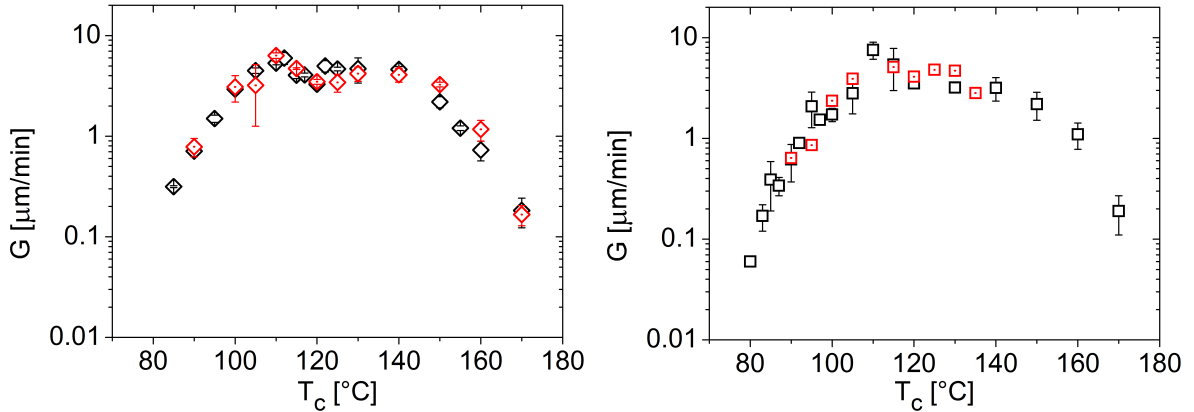


Figure 4.12: Temperature dependent linear radial growth rates $G(T_c)$ of PLLA1 spherulites (\diamond), stereocomplex nucleated nPLLA1 (\diamond), PLLA2 (\square) and stereocomplex nucleated nPLLA2 (\square) determined by isothermal SALS measurements. Data of PLLA1 and PLLA2 correspond to those shown in FIGURE 4.7 and FIGURE 4.8, respectively.

estingly, in contrast to observations made for nPLLA1, the depolarized SALS scattering patterns of nPLLA2 at large undercoolings not only showed the characteristic clover-leaf scattering pattern of spherulites. Significant scattering was observed along the azimuthal directions defined by $\mu = 0^\circ$ and $\mu = 90^\circ$ (+-type pattern). This peculiar scattering pattern is indicative for the co-formation and growth of an additional type of crystalline superstructure in the scPLA-PLLA2-compound in parallel to the well-characterized spherulitic superstructures unequivocally present in the samples. The findings are presented along with a discussion in SUBSECTION 4.6.

4.5 Morphological changes upon heating from the crystalline state

Samples of coPLA and PDLA were isothermally crystallized from the melt at various temperatures for 30 min and the melting behaviour during subsequent heating runs was characterized in terms of changes in morphology. All samples reached a plateau of the average spherulite size during the isothermal crystallization interval of the applied temperature-time protocol (see FIGURE 4.13). In parallel with the size the total integrated scattering intensity (invariant Q_{HV} , see below) reached a plateau. Hence, the sample morphology was fully developed and the total sample volume was populated with space-filling spherulites after isothermal crystallization. This result enabled attributing all observations made in the subsequent heating run to temperature-induced effects and not to completion of an otherwise ill-developed sample morphology.

In FIGURE 4.14 a typical evolution of the radial R_{HV} scattering intensity profile of coPLA with temperature during a heating run is shown. For better illustration the number of curves was reduced by showing only every tenth scattering curve, thus, leaving an interval of 5 K between successive curves. All curves show the maximum in scattering intensity characteristic of the respective average spherulite size in the sample.

4. PHASE TRANSFORMATION BEHAVIOUR OF POLYLACTIDE

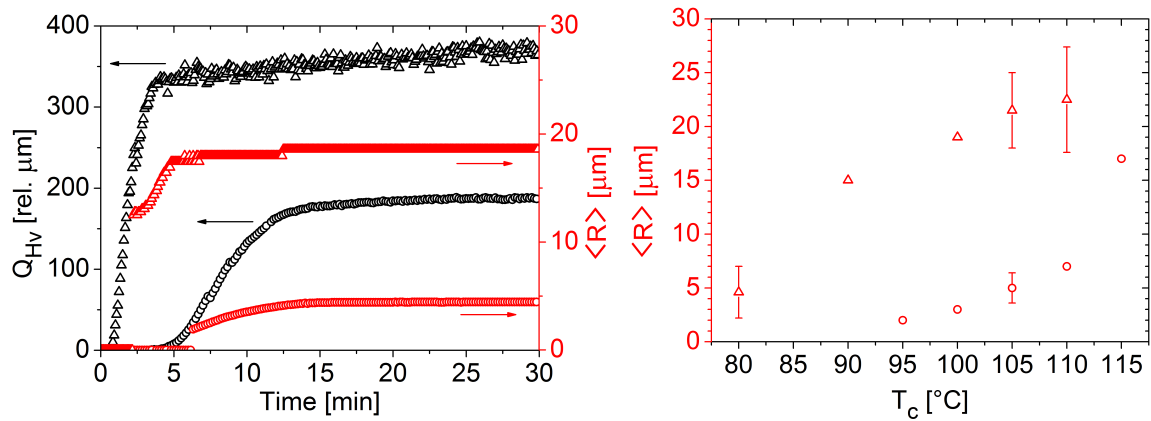


Figure 4.13: Left: Average spherulite size of coPLA (\circ) and PDLA (Δ), and total integrated scattering intensity (invariant Q_{H_V} , black symbols) during isothermal crystallization at 105°C. Right: Final average spherulite size as a function of isothermal crystallization temperature.

Interestingly, the position of the peak maximum remained unchanged upon heating, which implies that the spherulite size remained unchanged until the melting point was reached. Crystal melting is only reflected in the decreasing magnitude of the scattering

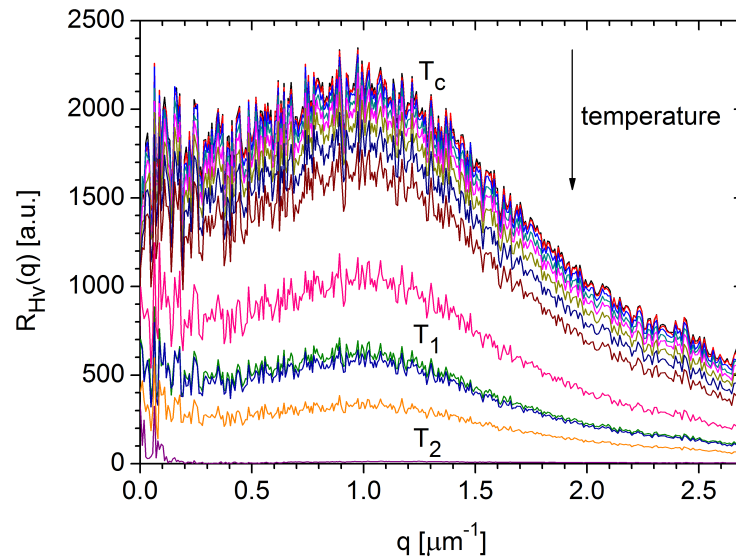


Figure 4.14: Radial H_V scattering intensity profiles of coPLA during the analytical heating run at a rate of 10 K/min after isothermal crystallization at $T_c = 105^\circ\text{C}$ for 30 min. Curves are separated by a 5 K interval corresponding to an elapsed time of 30 s between successive curves. Intensity decreases with increasing time/temperature with a brief halt at T_1 . Final melting with zero scattered intensity occurs at T_2 .

curves. This proceeded in a non-linear manner as indicated by the non-uniform spacing of the scattering curves in the plot. Increasing the temperature from T_c onwards

caused first a gradual decrease in the scattering intensity followed by an accelerated decrease which came to a brief halt at a temperature denoted T_1 prior to final melting at temperature T_2 where the scattering intensity dropped to zero.

For a more elaborate analysis the depolarized scattering invariant

$$Q_{H_V} = \int_0^\infty R_{H_V}(q)q^2 dq \quad (4.15)$$

was calculated. In analogy to the Porod invariant in X-ray scattering it yields the total integrated depolarized light scattering intensity [243]. From FIGURE 4.14 it is obvious that Q_{H_V} is a temperature-dependent quantity. In case of depolarized scattering from spherulites the invariant is related to the mean square anisotropy $\langle \delta^2 \rangle$ of the spherulites via

$$Q_{H_V} = \frac{K}{15} \langle \delta^2 \rangle \quad (4.16)$$

where K is a constant [107]. The anisotropy term

$$\langle \delta^2 \rangle = \phi_s (\alpha_r - \alpha_t)_s^2 \quad (4.17)$$

includes the volume fraction ϕ_s of spherulites in the illuminated sample volume and a quadratic term taking into account the spherulite polarizabilities in radial and tangential direction, respectively

$$(\alpha_r - \alpha_t)_s = \delta_{cr}^0 \phi_{cr,s} f_{cr,s} + \delta_{am,s}^0 \phi_{am,s} f_{am,s} + \delta_F \quad (4.18)$$

where $\delta_{cr}^0 = (\alpha_r - \alpha_t)_{cr}^0$ is the intrinsic anisotropy of a pure crystal and $\delta_{am,s}^0$ is the intrinsic anisotropy of an inter-lamellar amorphous volume element, respectively. The intra-spherulitic crystalline volume fraction is denoted $\phi_{cr,s}$. The intra-spherulitic amorphous volume fraction is given by $\phi_{am,s} = (1 - \phi_{cr,s})$. The orientation of the polymer chains inside the crystals ($p = cr$) and in the inter-lamellar amorphous volume ($p = am$) with respect to the spherulite radial direction is given by a Hermans-type orientation factor

$$f_{p,s} = \frac{3 \langle \cos^2 \psi \rangle - 1}{2} \quad (4.19)$$

where ψ is the angle between the direction of the chain segments defined by the crystallographic c axis for chain segments inside crystalline lamellae, and the spherulite radius direction. The orientation factor is 1 for chains parallel to the radius vector, $-1/2$ for perpendicularly aligned chain segments and 0 for an isotropic distribution of chain segments [244]. Contributions from the amorphous inter-lamellar phases are considered to be small compared to the crystalline birefringence. In case of polylactide, this assumption is justified by birefringence measurements of polylactide melt-spun fibers. It was found that the chain orientation in the amorphous inter-crystalline volume is low and, thus, does not contribute significantly to the overall optical anisotropy [245–247]. The last term δ_F is the form birefringence of the crystalline lamellae within the

spherulites [107]. In general, it is assumed to be negligible [97].

FIGURE 4.15 depicts a representative plot (see also FIGURES B.7 and B.8 in APPENDIX B) of the temperature-dependent invariant and average spherulite size during the melting of coPLA while heating after isothermal crystallization for 30 min. The trend of Q_{HV} is compared with the DSC trace of the analytical heating run with a temperature-time protocol corresponding to that of the SALS measurement (see APPENDIX A.3 for instrumental details). As already indicated by FIGURE 4.14, the average spherulite size

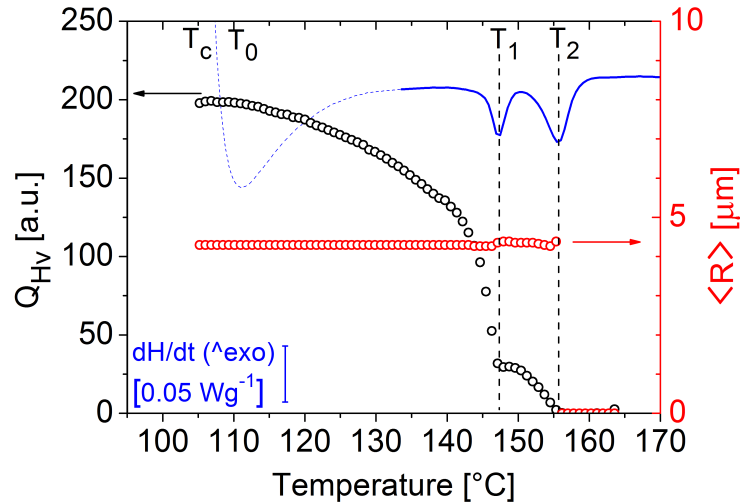


Figure 4.15: Average spherulite size (\circ), depolarized scattering invariant Q_{HV} (\circ) and corresponding DSC thermogram (—) of coPLA as a function of temperature in the analytical heating run at a rate of 10 K/min after isothermal crystallization at $T_c = 105^{\circ}\text{C}$ for 30 min. Exothermic heat flow is in positive ordinate direction. The endothermic signal at around $T = 115^{\circ}\text{C}$ is an artefact due to the transient behaviour of the DSC instrument when switching mode of operation from isothermal crystallization to non-isothermal analytical heating.

virtually remained constant until completion of melting, where it abruptly dropped to zero. The scattering invariant started to gradually decrease at temperature T_0 only a few degrees above the isothermal crystallization temperature T_c . This decrease accelerated and turned into an intermediate plateau at temperature T_1 prior to final melting at temperature T_2 where the invariant dropped to zero. DSC heat flux data of the analytical heating run was acquired immediately after finishing of the isothermal crystallization segment. The endothermic DSC signal at around $T = 115^{\circ}\text{C}$ is an artefact due to the transient behaviour of the DSC instrument when switching mode of operation from isothermal crystallization to non-isothermal analytical heating. The interfering effect on the heat flux measurement of this DSC peak close to the isothermal crystallization temperature occurring after starting to increase the temperature could be alleviated by a modified temperature-time protocol: heating was performed at a rate of 20 K/min and started at room temperature after quenching the sample at a rate of -50 K/min from the isothermal crystallization segment. The applied cooling rate minimized unwanted sample annealing during cooling. Fortunately, this procedure

yielded DSC thermograms closely matching those from the temperature-time protocol which were adjusted to the SALS experiments (see FIGURE B.5 in APPENDIX B). In Figure 4.15 the analytical DSC heating run shows two sharp melting endotherms with peak temperatures T_1 and T_2 , respectively. The double melting-peak behaviour is well known for polylactide and a number of other polymers [36, 40–42, 165, 248]. It is a process involving melting, recrystallization and remelting of the polymer. The first endothermic peak at T_1 is associated with the melting of crystals formed at T_c . Their melting temperature increases with crystallization temperature (see FIGURE A.5 in APPENDIX A.3 and FIGURE B.6 in APPENDIX B) due to the temperature-dependence of the thickness of the crystal lamellae. The second endothermic signal results from the melting of a new crystal population. It is formed via rapid (melt-)recrystallization from the semi-ordered, not yet isotropic melt of the former crystal population melted at T_1 [37, 46]. As the temperature interval for recrystallization is narrow, the melting peak temperature T_2 of this population is quasi-stationary and shows only a marginal dependence on T_c .

As suggested further by the coincidence of the two endothermic peaks at T_1 and T_2 with the two step-like drops of Q_{H_V} , the parameter Q_{H_V} is directly related to the degree of crystallinity. The depolarized scattering invariant, with the assumptions introduced above, reads as

$$Q_{H_V} = \frac{K}{15} \phi_s (\delta_{cr}^0 \phi_{cr,s} f_{cr,s})^2. \quad (4.20)$$

With their size unchanged so is the volume fraction ϕ_s of the spherulites, and utilizing the additional assumptions that the intrinsic crystalline birefringence δ_{cr}^0 and the crystalline orientation $f_{cr,s}$ do not change upon heating the square root of the invariant is a measure for relative spherulitic crystallinity

$$(Q_{H_V})^{1/2} \propto \phi_{cr,s} \quad (4.21)$$

and its derivative

$$\frac{d(Q_{H_V})^{1/2}}{dT} \propto \frac{d\phi_{cr,s}}{dT} \quad (4.22)$$

is a measure of the change in crystallinity - just like the DSC heat flow signal. Applied to the data in FIGURE 4.15 Equations (4.21) and (4.22) yield FIGURE 4.16. The normalized square root of the invariant dropped to approximately one half of its initial magnitude, which is indicative for a corresponding decrease in sample crystallinity due to melt-recrystallization. During this process the initial population of spherulitic lamellae undergoes melting and by recrystallization is replaced by a new population of thicker lamellae [39]. In the non-isothermal heating run melt-recrystallization does not re-establish the initial degree of crystallinity. The normalized derivative of the crystallinity according to EQUATION (4.22) is in good agreement with the normalized DSC heat flow and even the peak ratio is reproduced (see also FIGURES B.9 and B.10 in APPENDIX B). Hence, SALS measurements and DSC measurements confirm each other. It is concluded that for the process of melting, recrystallization and remelting in case

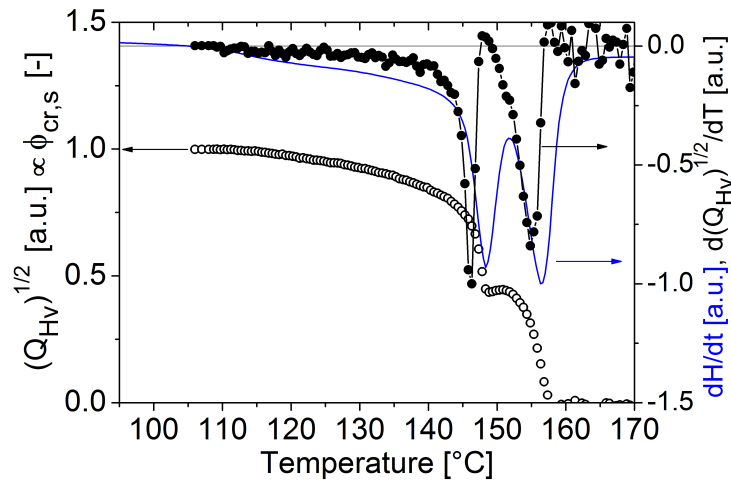


Figure 4.16: Normalized square root of the depolarized scattering invariant Q_{HV} (o) of coPLA and its first derivative (●) as a function of temperature in the analytical heating run at a rate of 10 K/min after isothermal crystallization at $T_c = 105^\circ\text{C}$ for 30 min. The DSC thermogram (—) was recorded at a rate of 20 K/min. Exothermic heat flow is in positive ordinate direction.

of coPLA the endothermic heat flow in DSC and the change in the scattering invariant Q_{HV} are indeed both proportional to a change in the spherulitic crystallinity associated with the lamellar crystalline domains.

Close inspection shows a constant offset of the peak temperatures of a SALS signal compared to the corresponding DSC signal. Although differences in sample masses and differences in the heat transfer properties of the two techniques have to be considered, this is attributed mainly to the fact that in non-isothermal SALS experiments with the home-built polymer sample stage the sensor temperature lagged behind the sample temperature.

In the following the mechanism of spherulite melting shall be addressed. Any considerations of this process have to take into account the invariance of the spherulite size throughout the entire melting process. It might be hypothesized that the endothermic heat flow determined by DSC measurements indicates the melting of whole spherulites. Would a fraction of spherulites vanish from a monodisperse population by melting the average size would remain unchanged, which is also compatible with the experimental observations. However, upon annealing the remaining spherulites then could grow at the expense of the freshly created amorphous volume thereby increasing $\langle R \rangle$. To test this hypothesis coPLA was isothermally crystallized at 105°C for 30 min and subjected to a temperature increase to 145°C at 10 K/min. The final temperature of 145°C was close to the peak of the first endotherm, where the sample was annealed subsequently for several minutes. The results are shown in FIGURE 4.17. As can be seen the average spherulite size remained unchanged upon annealing after partial melting. Interestingly, the scattering invariant regained in magnitude within a few minutes and grew asymptotically to a limiting value, which was, however, be-

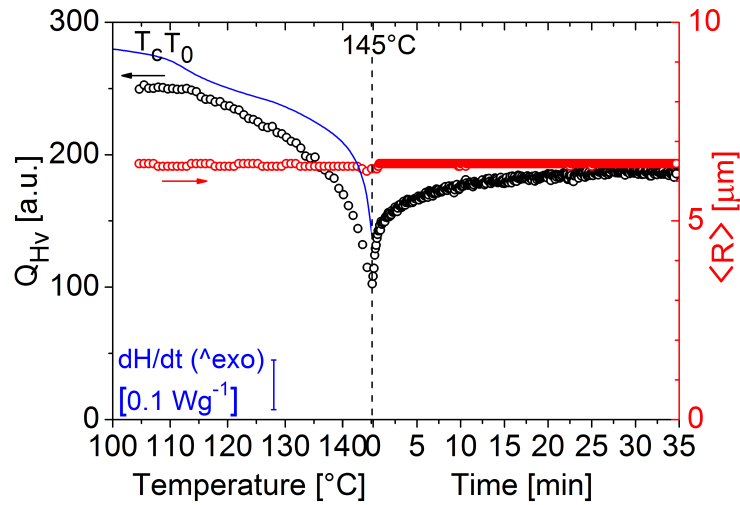


Figure 4.17: Average spherulite size (\circ) and depolarized scattering invariant Q_{H_V} (\circ) of coPLA as a function of temperature in the analytical heating run at a rate of 10 K/min after isothermal crystallization at $T_c = 105^{\circ}\text{C}$ for 30 min and during annealing at 145°C for 35 min. In addition, the DSC thermogram of the analytical heating run is shown ($-$). Exothermic heat flow is in positive ordinate direction.

low the value at T_c . It is well established that melting of spherulitic polymer crystals induced by a temperature gradient proceeds via a three-step process, melting of the crystalline lamellae succeeded by a partial recrystallization of the melted domains and finally followed by a melting of the recrystallized domains [42, 249]. The process of α -phase melt-recrystallization has to obey a mechanism where melting of lamellae runs parallel, i.e. simultaneously, to recrystallization, because distinct DSC peaks signifying the two different processes would appear otherwise. The presented combined SALS/DSC analysis clearly demonstrated that the integrity of the spherulites is conserved throughout the entire process and that melt-recrystallization does not lead to a full recovery of the original degree of crystallinity under non-isothermal conditions. The discussion shall now be focused on the feature of polymorphism of crystalline PLA which can particularly well be analyzed with the pure homopolymers. Crystallization of the homopolymers of polylactide PDLA and PLLA at temperatures below 100°C leads to exclusive formation of metastable α' -phase crystals [39, 47, 163]. At temperatures above 120°C exclusive formation of α -phase crystals occurs. At crystallization temperatures between 100°C and 120°C mixed crystal phases are observed [49]. Upon heating, the metastable α' -crystals undergo rapid melt-recrystallization into the stable α -form (α'/α -transition) at their stability limit of approximately 155°C . As a consequence, an exothermic heat flow signal is observed whenever the crystallization enthalpy of the newly formed α -phase exceeds the total melting enthalpy referring to the metastable α' -phase or, in case of a mixed crystalline phase, exceeds the melting of α' -phase and α -phase crystals formed at T_c , respectively. This shall be outlined with experiments on pure PDLA, presented in FIGURE 4.18.

4. PHASE TRANSFORMATION BEHAVIOUR OF POLYLACTIDE

FIGURE 4.18A is a representative plot (see also FIGURE 4.18B, and FIGURES B.11 and B.12 in APPENDIX B) of the melting behaviour of PDLA upon heating after isothermal crystallization at 105°C as monitored by SALS and DSC. The average spherulite size remained constant until completion of melting. The apparent increase of the size in the final melting step was an artefact from the fitting routine for the scattering peak position. The invariant Q_{H_V} first remained constant and decreased only at temperatures above 150°C . It dropped to zero at the melting temperature T_2 , which is close to the peak temperature of the melting endotherm in the DSC thermogram. At temperature T_1 the scattering invariant dropped to an intermediate plateau.

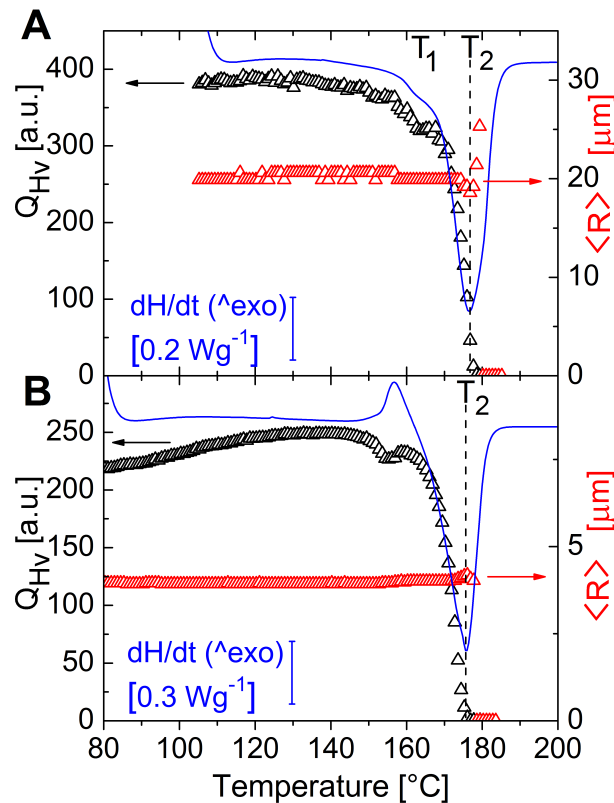


Figure 4.18: Average spherulite size (Δ), depolarized scattering invariant Q_{H_V} (Δ) and corresponding DSC thermogram ($—$) of PDLA as a function of temperature in the analytical heating run at a rate of 10 K/min after isothermal crystallization at (A) $T_c = 105^\circ\text{C}$ and (B) $T_c = 80^\circ\text{C}$ for 30 min. Exothermic heat flow is in positive ordinate direction.

In contrast to the coPLA sample discussed above, this drop in the scattering invariant was not accompanied by a corresponding marked endothermic peak in the DSC thermogram but rather by a small endothermic shoulder preceding the main melting endotherm. This can be attributed to a transformation of metastable α' -crystals, which were formed during isothermal crystallization at T_c , into more stable α -phase crystals with the exothermic heat flow from α -crystallization being just strong enough to compensate for the endothermic heat flow of α' -melting. Taken together, FIGURES 4.18A,

4. PHASE TRANSFORMATION BEHAVIOUR OF POLYLACTIDE

4.18B, and FIGURES B.11 and B.12 in APPENDIX B, show an amplification of the exothermic recrystallization peak as the crystallization temperature decreases from 110 °C to 80 °C, fully in line with the accompanying increase of the tendency to form α' -crystals. Recent studies demonstrated that the upper limiting temperature for the growth of α' -crystals shows a strong dependence on isomer composition of polylactide [48]. While in case of enantio-pure homopolymers the growth of α' -crystals is observed up to temperatures of 120 °C, α' -growth ceases already at a temperature of 90 °C in case of a random-copolymer with a fraction of 4% of the minor repeat unit [48]. Hence, in case of the coPLA discussed in FIGURES 4.15 - 4.17 only α -phase crystals were involved in melt-recrystallization. The PDLA sample crystallized at 105 °C in FIGURE 4.18A, however, formed α' and α crystals and showed an α'/α -transition via melt-recrystallization. However, in case of the α'/α -transition phenomenon great caution has to be exercised in correlating the scattering invariant to the square of the intra-spherulitic crystalline volume fraction $\phi_{cr,s}$ as given by EQUATION (4.20), because changes in $\delta_{cr,s}^0$ and $f_{cr,s}$ cannot be ruled out. The intrinsic birefringence $\delta_{cr,s}^0$ and the chain orientation factor $f_{cr,s}$ of α' -phase crystals likely differ from those of the α -phase crystals, which may, together with $\phi_{cr,s}$ influence Q_{H_V} .

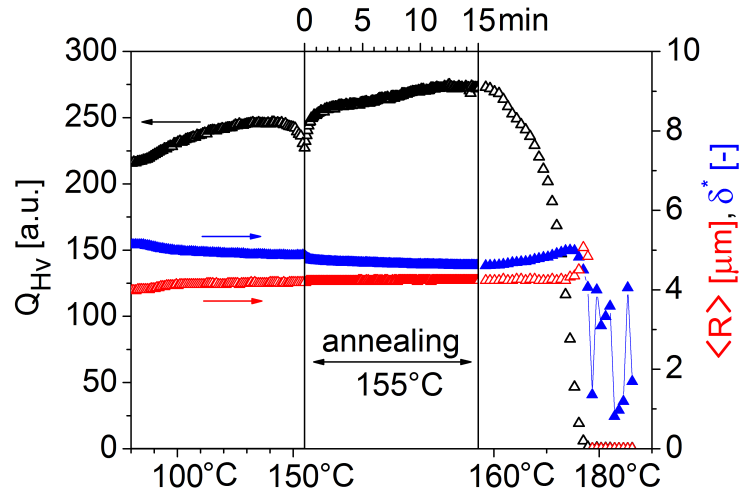


Figure 4.19: Average spherulite size (Δ) and depolarized scattering invariant Q_{H_V} (Δ) of PDLA as a function of temperature and time in the analytical heating run at a rate of 10 K/min after isothermal crystallization at $T_c = 80$ °C for 30 min and during annealing at 155 °C for 15 min. In addition, the relative disorder parameter δ^* (\blacktriangle) defined by EQUATION (4.23) is plotted.

In order to elucidate the recrystallization process of enantio-pure polylactide during the α'/α -transition, two different temperature-time protocols were applied to the melting of PDLA. In both protocols a PDLA sample was crystallized at 80 °C for 30 min. The choice of $T_c = 80$ °C for the isothermal crystallization assured that pure α' -phase was formed during the isothermal crystallization. In a first experiment the melting

behaviour was characterized in a continuous analytical heating run (FIGURE 4.18B). In a second experiment with the same parameters the heating run was interrupted at 155 °C and the sample was annealed at that temperature for 15 min before the analytical heating run was resumed and completed (FIGURE 4.19).

The continuous heating run (FIGURE 4.18B) was characterized by a constant spherulite size up to the final melting point. At temperature T_2 the size dropped to zero simultaneously with the scattering invariant and the dominant melting endotherm reached its peak. The scattering invariant first slightly increased upon heating. This is attributed to the stabilization/perfection of conformationally disordered α' -phase crystals [166]. However, it is difficult to attribute the increase of the scattering invariant to one of its constituting parameters as stabilization due to crystal perfection might involve changes in intrinsic crystal birefringence $\delta_{cr,s}^0$, crystal orientation $f_{cr,s}$ or crystalline volume fraction $\phi_{cr,s}$, respectively. At around 155 °C, which is identical to the thermal stability limit of α' -crystals, the scattering invariant reached a local minimum and, upon further heating, recovered slightly in magnitude paralleled by the DSC recrystallization exotherm signalling the α'/α -transition.

In case of the annealing experiment (FIGURE 4.19) the scattering invariant was identical to the curve in the continuous heating experiment up to the annealing temperature. At that temperature it significantly increased during annealing while the average spherulite size again remained unchanged (see also FIGURE 4.20).

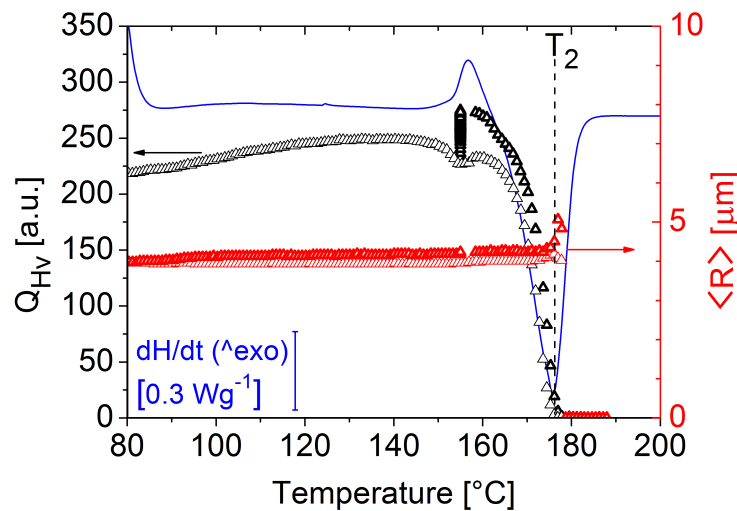


Figure 4.20: Average spherulite size (Δ) and depolarized scattering invariant Q_{H_V} (Δ) of PDLA as a function of temperature in the analytical heating run at a rate of 10 K/min after isothermal crystallization at 80 °C for 30 min and during an analogous experiment with added annealing segment (bold symbols) at 155 °C for 15 min. The DSC thermogram of the continuous heating run (—) was obtained in analogy to the SALS experiment at a rate of 10 K/min. Exothermic heat flow is in positive ordinate direction. Data indicated by regular open symbols are identical to those in FIGURE 4.18B

In order to correlate results from SALS and DSC the relative increase in the scattering

4. PHASE TRANSFORMATION BEHAVIOUR OF POLYLACTIDE

invariant was determined from the maximum values of Q_{H_V} located at 160°C for the annealed and non-annealed sample, respectively. At that temperature melting of the metastable α' -phase was completed and the scattering signal resulted from the recrystallized α -phase only. The relative increase in crystallinity as determined by SALS from the magnitudes of the scattering invariant taken at 160°C of the non-annealed (1) and the annealed (2) sample was $(Q_{H_V}(2)/Q_{H_V}(1))^{1/2} = 1.1$ (see FIGURE 4.20). The relative increase in the sample crystallinity was determined by DSC from integration of the melting peak centred at T_2 . This is depicted in FIGURE 4.21. In the continuous experiment (1) and in the annealing experiment (2) the enthalpies (ΔH_{ic}) due to isothermal crystallization at 80°C were $\Delta H_{ic}(1) = -27\text{J/g}$ and $\Delta H_{ic}(2) = -30\text{J/g}$, respectively. Consequently, sample preparation yielded nearly identical initial crystallinity and the difference in the enthalpies of fusion could be attributed to the differences in the applied heating protocols. The calculated enthalpies of fusion for the ensuing two different experiments, were $\Delta H_m(1) = 62\text{J/g}$ and $\Delta H_m(2) = 75\text{J/g}$, respectively. Hence, annealing resulted in an increase in relative crystallinity by $\Delta H_m(2)/\Delta H_m(1) = 1.2$ as determined by calorimetry, which is closely matching the results obtained from SALS.

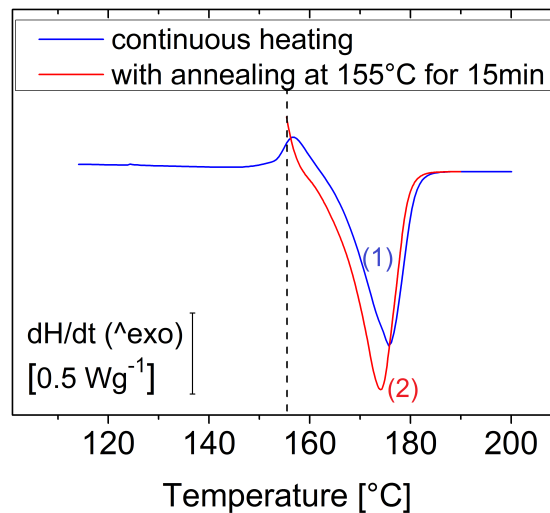


Figure 4.21: DSC thermograms of the analytical heating after isothermal crystallization of PDLA at 80°C for 30 min. In analogy to the SALS experiments, heating was started at 80°C directly after isothermal crystallization and carried out at 10K/min until 200°C . The graph shows (1) a continuous analytical heating run (—) and (2) a run, which was interrupted at 155°C for 15 min (—) for sample annealing before completion of heating. The exothermic event at around 160°C (—) indicates recrystallization due to the α'/α -transition which is followed by complete melting of the α -phase crystals at 175°C . Exothermic heat flow is in positive ordinate direction.

The kinetics of recrystallization of PDLA during annealing shall be addressed in more detail in FIGURE 4.19, where the evolution of the scattering invariant of PDLA as a function of time during the annealing step at 155°C for 15 min is depicted. When heated to the annealing temperature the invariant showed a drop in magnitude indicative

for the transformation of the crystalline domains. It, however, recovered within only one minute to its previous magnitude. As discussed above, this is indicative for the rapid melt-recrystallization process during the α'/α -phase transition of the crystalline lamellae. Upon further annealing crystal perfection set in and a further increase in the scattering invariant was observed. This process was significantly slower than the melt-recrystallization during the α'/α -phase transition. On the other hand it substantially contributed to the final magnitude of the scattering invariant attained at the end of annealing. As discussed above ideal spherulite scattering is perturbed by so-called internal and external disorder. External disorder is caused by incomplete spherulite development, e. g. due to impingement. It causes excess scattering at low and large q while the position of the scattering peak is not affected [100]. Internal disorder refers to morphological imperfections caused by density fluctuations within spherulites. The lamellar structure is not aligned perfectly along the radius vector. Instead, due to random arrangement of spherulite lamellae and lamellar branching fluctuations in the lamellar orientation are caused, also showing local fluctuations of the polarizabilities. As a consequence the peak maximum on the $\mu = 45^\circ$ diagonals is reduced and simultaneously excess scattering is observed at all other scattering angles. Interestingly, the form of the scattering curve was invariant during melting and melt-recrystallization, which strongly suggests that the spherulite morphology is invariant during these processes (see FIGURE 4.14). Accordingly, the relative disorder parameter

$$\delta^* = \frac{Q_{H_V}(\mu = 45^\circ)}{Q_{H_V}(\mu = 0^\circ | 90^\circ)} \quad (4.23)$$

given by the ratio of the scattering invariants along the $\mu = 45^\circ$ diagonals, comprising the spherulite scattering maximum, and the invariant along the principal directions with $\mu = 0^\circ$ and $\mu = 90^\circ$, with zero scattering in the ideal model, is a convenient measure of spherulite internal disorder [58]. This ratio showed only an insignificant decrease during heating and a discontinuity accompanied by a slight displacement at 155°C before annealing. Only when the final melting set in the disorder parameter slightly increased before it dropped to unity (or rather fluctuated when scattering intensities were dominated by background fluctuations) when the melting point was reached. Interestingly, neither (polymorphous) melt-recrystallization during α'/α -phase transition in PDLA (see also FIGURE B.13 and B.14 in APPENDIX B) nor melt-recrystallization of α -phase crystals in coPLA (see also FIGURES B.15 and B.16 in APPENDIX B) caused substantial changes in spherulitic crystalline order, which implies that also the lamellar orientation was preserved during that process.

4.6 Non-spherulitic crystalline superstructures in compounds of scPLA and PLLA

In SUBSECTION 4.4 the effect of the presence of a small amount of scPLA, by mixing PLLA with 2 wt% PDLA, on the crystallization behaviour of polylactide homopolymers is presented. It was shown by DSC measurements that the overall crystallization process is significantly accelerated by scPLA crystallites which acted as heterogeneous nucleation sites. The formation of spherulites was monitored via depolarized SALS measurements and the linear radial growth rate curve was determined over a wide range of crystallization temperatures. From comparing growth rate curves of nucleated polylactide with the pure PLLA it can be seen that the spherulite growth rate is unaffected in the compounds containing a small amount of scPLA. In the investigated temperature range the morphology of the crystallized PLA samples is of the spherulite type.

However, as already mentioned, close inspection of the H_V scattering patterns of nPLLA2 at large undercooling yields the interesting observation of a pattern qualitatively different from the typical four-lobed scattering pattern of spherulites. In analogy to the works of Marubayashi *et al.* [185] and Na *et al.* [184] the newly observed scattering pattern shall be denoted a +-type pattern in clear contrast to the four-lobed clover leaf-type pattern shown in FIGURE 4.5 in SECTION 4.3. In FIGURE 4.22 these scattering patterns are depicted as they were observed at the end of isothermal crystallization in the temperature interval from 85 °C to 100 °C. Note that the indicated crystallization times t_c agree well with the end of the crystallization endotherms as observed in DSC measurements (compare FIGURE 4.10).

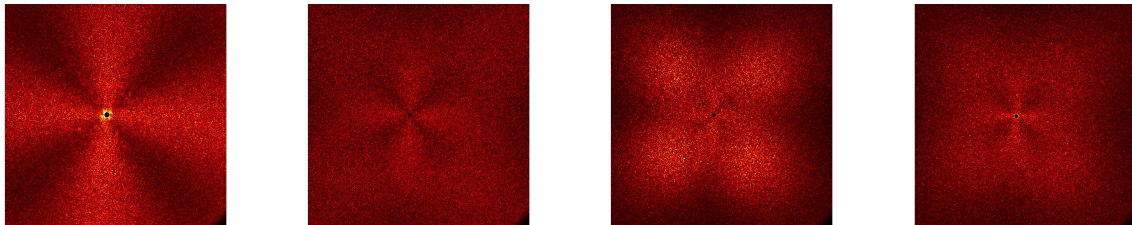


Figure 4.22: Depolarized SALS patterns of nPLLA2 after isothermal crystallization during t_c at temperatures T_c . To aid the eye intensities R_{H_V} were adjusted. From left to right: $T_c = 85^\circ\text{C}$ ($t_c = 20$ min, $R_{H_V} \times 1$), $T_c = 90^\circ\text{C}$ ($t_c = 10$ min, $R_{H_V} \times 0.05$), $T_c = 95^\circ\text{C}$ ($t_c = 6.7$ min, $R_{H_V} \times 0.1$), $T_c = 100^\circ\text{C}$ ($t_c = 4$ min, $R_{H_V} \times 2$).

The +-type pattern is not observable in scattering experiments carried out at crystallization temperatures $T_c > 100^\circ\text{C}$. Neither was the +-type scattering pattern observed for the stereocomplex nucleated nPLLA1 nor was it observed for the pure polymers PLLA2 or PLLA1 although measurement conditions were comparable in terms of laser attenuation and sensor exposure times. Hence, the occurrence of the +-type scattering pattern is related to the presence of scPLA in PLLA2. At this point it is not clear why the pattern could not be observed in experiments with nPLLA1. The two samples had

a different molecular weight which might give a hint to a possible cause.

With increasing crystallization temperature in addition to the $+$ -type pattern the typical four-lobed clover leaf-type pattern becomes noticeable in the recorded data of nPLLA2 which allowed measurements of the spherulite growth rates. Since the spherulite growth rates of the pure polymer sample PLLA2 and the nPLLA2 samples with added scPLA are identical it can be concluded that indeed the clover leaf-type pattern observed in nPLLA2 is due to the growth of the same type of crystalline superstructure, namely spherulites as observed with pure PLLA2. In FIGURE 4.22 it can also be seen that the peak position of the scattering maxima of the lobes shifts to lower q with increasing crystallization temperature. As the data represent the sample morphology at the end of isothermal crystallization it can safely be concluded that the average spherulite size increased, i. e. their number density decreased, in parallel with the crystallization temperature. It might be speculated that in case of the sample crystallized at $T_c = 85^\circ\text{C}$ the superposition of the $+$ -type pattern and the clover leaf-type pattern could not be observed because the lobes of the clover leaf-type pattern were outside of the detector range, i. e. average spherulite size was too small for detection.

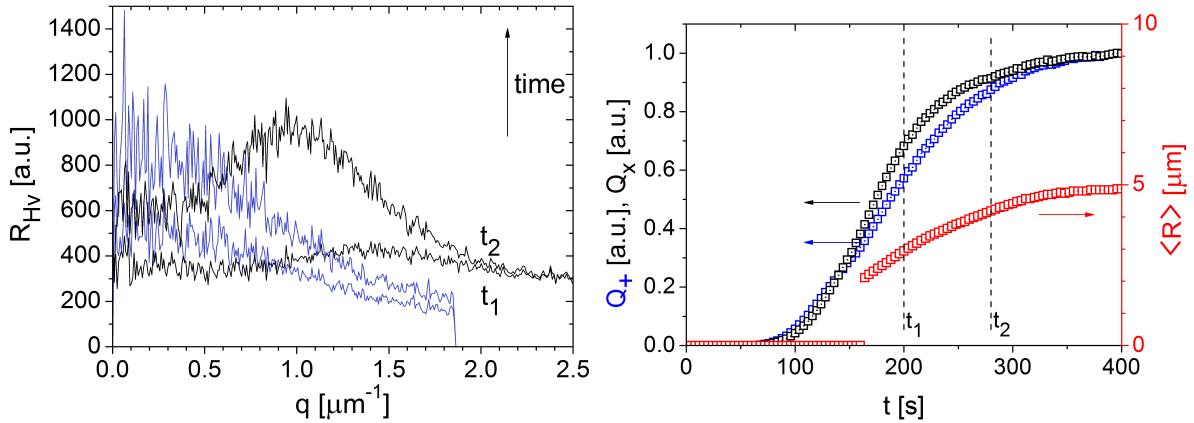


Figure 4.23: Left: Scattering curves of the $+$ -pattern (—) and the (four-lobed) clover leaf-pattern (—) at times t_1 and t_2 . Right: Average spherulite radius (\square) of nPLLA2 and normalized integrated scattering intensities Q_+ of the $+$ -pattern (\square) and Q_x of the (four-lobed) clover leaf-pattern (\square) as a function of time during isothermal crystallization at $T_c = 95^\circ\text{C}$.

The temporal evolution of a complex combined $+$ -type and clover leaf-type scattering pattern is depicted in FIGURE 4.23 for nPLLA2 isothermally crystallized at $T_c = 95^\circ\text{C}$. Averaged scattering intensity profiles were calculated for the clover leaf-type pattern along $\mu = 45^\circ$ and its odd multiples, and the $+$ -type pattern along the principal directions $\mu = 90^\circ$ and its multiples. Scattering profiles at times $t_1 = 200\text{ s}$ and $t_2 = 280\text{ s}$ during isothermal crystallization are compared. At t_1 formation of the typical maximum in the profile of the clover leaf-type pattern can be identified. In the course of isothermal crystallization at t_2 the maximum becomes more pronounced and shifts to lower scattering angles q (compare FIGURE 4.5). This allowed monitoring of the growth of spherulites starting at $\langle R \rangle = 2\ \mu\text{m}$ and levelling off at $\langle R \rangle \approx 5\ \mu\text{m}$.

The scattering profile of the $+$ -type pattern does not show a maximum but rather shows a monotonic decay with q . The profile is truncated at $q \approx 1.9 \mu\text{m}^{-1}$ due to the geometric constraints of the detector which covered a smaller q -range on the vertical and horizontal axis than along its diagonals where the clover leaf-type pattern was located. The two types of scattering patterns suggest formation and growth of two different kinds of crystalline superstructures, which differ in optical anisotropy resulting from specific orientation of the crystalline domains.

For comparison of the kinetics of the crystallization process of the two structures in analogy to the scattering invariant Q_{HV} the invariants Q_+ and Q_\times for the $+$ -pattern and the clover leaf-pattern, respectively, were calculated from the respective scattering curves.¹² In FIGURE 4.23 evolution of the invariants is depicted as a function of the isothermal crystallization time. Interestingly, when normalized, the invariants of the different types of patterns show nearly the same time-dependence, which is indicative for a similar mechanism of the formation and growth of the two types of crystalline superstructures. Also, the invariants reach a plateau simultaneously with the spherulites reaching their final average size marking the end of the crystal growth stage.

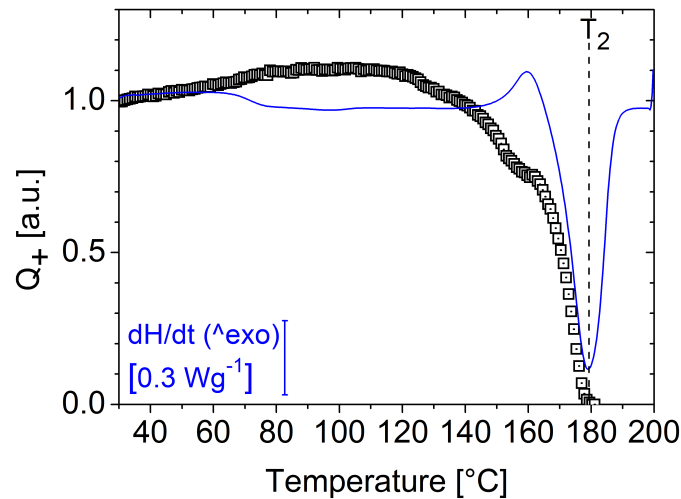


Figure 4.24: Normalized depolarized scattering invariant Q_+ (\square) of nPLLA2 as a function of temperature in the analytical heating run at a rate of 10 K/min after isothermal crystallization at $T_c = 85^\circ\text{C}$ for 20 min. In addition, the DSC thermogram of the analytical heating run is shown ($—$), which was performed at a rate of 20 K/min after isothermal crystallization at 80°C for 2 h. Exothermic heat flow is in positive ordinate direction.

In analogy to the SALS experiments presented in SUBSECTION 4.5 the melting behaviour of nPLLA2 after isothermal crystallization at $T_c = 85^\circ\text{C}$ was investigated. The sample

¹²In this thesis the indices $+$ and \times for the invariants visualize the sections (range in μ) of the two-dimensional scattering pattern which were considered in data evaluation. However, note that in [185] the term “ \times -type scattering pattern” is used to denote a rotated $+$ -type pattern, thus forming an \times -like scattering intensity distribution in the detection plane.

was crystallized for 20 min on a laboratory hotplate and quenched to room temperature. Subsequently, the sample was positioned in the SALS stage and acquisition parameters were optimized before commencing the heating at a rate of 10 K/min from 30 °C to 200 °C. The findings are discussed in FIGURE 4.24 in terms of the depolarized scattering invariant Q_+ as a function of temperature during the analytical heating run. Since the scattering pattern changed only in intensity and the angular distribution was not affected by melting the invariant defined in EQUATION (4.15) was used to characterize the melting behaviour. In addition the DSC thermogram of nPLLA2 is plotted. Note, however, that the DSC trace is from a sample crystallized at $T_c = 80$ °C for 2 h because the particular data set of the sample crystallized at $T_c = 85$ °C was corrupted. The procedure is legitimate as can be seen from comparison of the DSC thermograms of the analytical heating of nPLLA2 in FIGURE B.4 in APPENDIX B. The DSC heating curves of samples crystallized at $T_c = 80$ °C and $T_c = 90$ °C do not show a significant difference. Hence, either of the thermograms might serve as a substitute for the corrupted data set.

As discussed already above from the DSC traces of isothermal crystallization it can be safely concluded that isothermal crystallization was completed within 20 min. Hence, the sample morphology was fully developed and observations made by SALS during the subsequent heating run were due to temperature-induced effects and not related to completion or to otherwise ill-developed sample morphology. The scattering invariant was normalized to the initial value. A slight increase was monitored resembling observations made with the homopolymer PDLA crystallized at $T_c = 80$ °C (see FIGURE 4.20). Also the drop of the integrated intensity to a plateau at around 160 °C in parallel with the DSC exothermic peak associated with the α'/α -transition preceding the final decrease of Q_+ to zero is familiar from previous measurements.

Vanishing of the scattering invariant coincides with the peak of the final melting endotherm of α -phase crystals determined by calorimetry. Hence, the +-type scattering pattern is induced by the presence of scPLA during isothermal crystallization, however, it is not indicative for the formation and growth of a supramolecular structure purely made of stereocomplex crystals, because melting is observed at much lower temperatures than expected for scPLA which is stable up to 230 °C.

To conclude this subsection on non-spherulitic crystalline superstructures in PLLA in the presence of a small amount of scPLA in the following the above reported results shall be summarized and be discussed against the background of findings reported in literature.

- (i) Isothermal crystallization experiments of nPLLA2 by SALS at large undercooling revealed a scattering pattern (+-type) which qualitatively differed from that of polymer spherulites (clover leaf-type). This is indicative for the formation of non-spherulitic crystalline superstructures.
- (ii) With increasing crystallization temperature coexistence of the +-type and the clover leaf-type scattering pattern was observed for $T_c \leq 100$ °C. From the spherulitic

rulite scattering pattern the growth rate curve was obtained as demonstrated in SUBSECTION 4.4. Due to the congruence of the growth rate curves of the nucleated and non-nucleated polymer the observed new type of crystalline superstructure in nPLLA2 does not affect the spherulite growth.

- (iii) When normalized to their final magnitude the scattering invariants Q_+ and Q_x overlay, they show nearly identical isothermal crystallization kinetics.
- (iv) During melting from the crystalline state prepared at $T_c = 85^\circ\text{C}$ the Q_+ invariant shows the same qualitative behaviour as the invariant of the pure polymer. In particular, temperature-dependent changes in the invariant are indicative for the α'/α -transition and the temperature where the invariant decays to zero is identical to the peak melting temperature of α -phase crystals as observed by DSC measurements.

Indeed, the +-type SALS scattering pattern was reported for a racemic PLLA/PDLA blend [184]. Also, crystallization of pure PLLA under high-pressure CO_2 treatment can lead to observation of the +-type SALS scattering pattern [185]. In both works the implications for the type of crystalline superstructure yielding the +-type SALS scattering pattern are discussed in detail. It is concluded that the scattering pattern is explained best by a crystalline sample morphology which is comprised of a random assembly of optically anisotropic rod-like crystals. In order to yield the +-type scattering pattern the principal axis of polarizability of those rod-like crystals must be tilted at 45° with respect to the rod-axis.

Note, however, that the situation reported in this thesis is different from that reported in [184] in two vital aspects. First, in this thesis the sample composition was highly asymmetric, PDLA content was only 2 wt%. Second, sample preparation and thermal history, respectively, was different. In this thesis film preparation by solvent casting resulted in the formation of sc-crystallites prior to isothermal crystallization experiments. This fact has a remarkable consequence for the structural and, thus, thermal properties of the emerging crystalline superstructure as will be described in the following. In [184] (compare FIGURE 2.17) an amorphous sample was cold-crystallized at 80°C yielding space-filling α' -phase spherulites as evidenced by a four-lobed SALS scattering pattern. In particular, this sample preparation yielded separate homocrystalline phases of PLLA and PDLA, respectively, as demonstrated by XRD and FTIR measurements. Only then via melt-recrystallization [250] the sc-phase displaying the +-type scattering pattern was formed at annealing temperatures above the melting temperature of the α -phase.

In this thesis, however, it is demonstrated that the +-type SALS scattering pattern associated with rod-like crystals vanishes at $T_m = 180^\circ\text{C}$ the melting temperature of α -phase crystals. In other words, the newly observed crystalline superstructures show the same temperature characteristics as the PLLA homopolymer. Since the latter is the dominant phase in the sample it can be safely concluded that the superstructure indeed is comprised of crystalline PLLA with its lamellar orientation being severely

modified by the presence of scPLA.

While the details of the modification of the lamellar ordering are not yet understood, literature reports the occasional observation of crystalline domains with lamellae oriented in tangential rather than radial direction in stereocomplex spherulites [251]. This is in support of the idea that stereocomplex crystallites, which are homogeneously dispersed in the sample [252], can modify the lamellar morphology of the adjacent homopolymer phase during crystallization. Also, Marubayashi *et al.* clearly demonstrated the ability of PLLA to crystallize in a non-spherulitic, namely rod-like, morphology [185]. A number of publications report on the formation of fibrillar or gel-like structures in blends of the two different PLA homopolymers [183, 215]. More recently, the formation of a dual crystalline morphology, comprising network-like and spherulite-type crystalline domains, in melt-mixed asymmetric blends of PLLA with up to 5 wt% PDLA was observed by POM [253]. Most importantly, growth of stereocomplex spherulites exhibiting the common radial lamellar substructure, and which had a melting point of around 218 °C, was witnessed in parallel with formation of an extra-spherulitic crystalline network. The transition from the +-type scattering pattern to a dominantly four-lobed clover leaf-type scattering pattern depicted in FIGURE 4.22 is in agreement with a transition of the dual crystalline morphology towards a spherulite dominated sample morphology with increasing crystallization temperature. In addition, the network is described as being a less organized worm-like crystalline structure with a melting temperature significantly lower than that of the stereocomplex spherulites. This is also in agreement with the above presented experimental data. Still, more research is needed to characterize this newly observed non-spherulitic crystalline superstructures in terms of the details of the lamellar orientation and with respect to homopolymer ratios and sample thermal history.

5 Conclusion and Outlook

5.1 Summary of the most relevant results

In this work the phase transformation behaviour of polylactide (PLA) in terms of spherulite growth and melting was investigated by means of a joint study via small angle light scattering (SALS) and differential scanning calorimetry (DSC). Three phase transformation processes were analyzed: isothermal crystallization, non-isothermal melting and melt-recrystallization. Melting was analysed during heating the samples after isothermal crystallization. Analysis also comprised α' -phase melt-recrystallization, and polymorphous melt-recrystallization due to the α'/α -transition in the enantio-pure polymer. The SALS and DSC techniques allowed determining the crystallization kinetics of PLA and characterization of the melting behaviour. Via SALS changes in the sample crystalline morphology could readily be monitored. Both methods confirmed each other. The complementary results added to the understanding of the crystallization and melting of PLA.

The DSC technique is an established method in polymer analytics and a variety of instruments is commercially available from a number of companies. Also SALS instruments are commercially available. However, these instruments, in general, are dedicated to the task of particle sizing. The highly integrated devices hardly allow any customization for a specific type of measurement task other than the dedicated one. Hence, the first goal of this work was developing and setting up of a home-built SALS instrument capable of temperature- and time-resolved measurements of the depolarized scattering of polymer crystalline superstructures like spherulites:

- The home-built SALS instrument was of the Fourier-lens type. This design was chosen for its superior performance in terms of separation of the primary beam and the scattered light. The instrument was equipped with a linearly polarized HeNe laser as the light source and the scattered light was detected by a two-dimensional CMOS sensor of a digital camera. The angular scattering range accessible was 0.7° to 15.4° corresponding to $0.5^\circ < \theta < 11.5^\circ$ in water. Depolarized measurements of PLA could be performed in an angular range $0.1 \mu\text{m}^{-1} < q < 2.65 \mu\text{m}^{-1}$. The maximum temporal resolution of the detector was 40 ms, i. e. 25 frames per second.

Two different sample environments were made available: One for measurements of colloidal suspensions in rectangular flat cuvettes and one for measurements of thin polymer films. In the first case the temperature could be set by a water thermostat, in the latter a home-built high-temperature stage allowed measurements of polymer systems in the solid or melt state, i. e. in the range from room temperature up to 250°C . Temperature control was realized by a home-built electronic controller featuring a digital interface for connection to a personal computer. In this way customized temperature-time protocols could be realized. The temperature scale of the stage was calibrated with melting point standards.

5. CONCLUSION AND OUTLOOK

Operational verification of the SALS instrument and the data-processing routines was carried out via sizing of monodisperse latex beads in aqueous dispersion. The obtained scattering data was treated with Mie-scattering theory and the derived sizes of the particle standards were compared to results from a commercial particle sizing instrument and the nominal sizes provided by the supplier. The results confirmed the accurate performance of the home-built instrument down to a lower limit of the particle radius of $2\ \mu\text{m}$.

The key findings of the studies presented in this work on the phase transformation behaviour of PLA during isothermal crystallization and melting from the crystalline state are as follows:

- **Linear radial spherulite growth rate curves** were determined for two enantiopure samples of PLLA with different molecular weights, one PDLA and a random co-polymer containing 4% of the minor repeat unit. All polymers showed the bell-shaped growth rate curve falling off towards large and low undercooling, respectively. In case of the homopolymers a discontinuity in the growth rate curve associated with the growth of α' - and α -phase crystals was observed. The homopolymers showed comparable growth rates whereas the presence of 4% of an enantiomeric repeat unit, i. e. partial randomization of tacticity, in coPLA significantly reduced the growth rate.

Due to temperature-dependent homogeneous spherulite nucleation the number of growing spherulites decreases with decreasing undercooling. This excludes SALS measurements at low-enough undercooling where spherulite nucleation is negligible. Spherulite nucleation, therefore, was stimulated by quenching the polymer melt to large undercooling where primary nucleation is strong and crystal growth is insignificant. Subsequently, the sample was brought to the isothermal crystallization temperature of interest and SALS measurements were performed. This so-called Tamman method [173, 216] extended the temperature range for SALS measurements to the full interval between the glass transition temperature and the melting temperature, where undercooling is low.

- **Invariance of the spherulite size up to final melting temperature.** The non-isothermal melting and (polymorphous) melt-recrystallization of PLA after isothermal crystallization was investigated for PDLA and coPLA. The sample morphology after isothermal crystallization for 30 min was characterized by space-filling (truncated) spherulites. Final average spherulite size was a function of the crystallization temperature, increasing with decreasing undercooling. Accordingly, the number of spherulite nuclei, i. e. the spherulite number density decreased with decreasing undercooling.

It was found for coPLA and PDLA, that the average spherulite size was unaffected by melting and melting-recrystallization processes. When compared to DSC measurements, it was found that in all cases the peak temperature of the final melting endotherm coincided with the abrupt drop of the average spherulite

size to zero and with the disappearance of the depolarized scattering from spherulites, marking their complete disintegration and the randomization of the polymer chains. From the invariance of the average spherulite radius during heat induced melting it was concluded that the same invariance holds for the number of spherulites. Hence, phase transformations affected neither the number nor the size of spherulites. This is valid for the melt-recrystallization of the α -phase as well as for the α'/α -phase transformation. Neither a melting or melt-recrystallization mechanism involving spherulite shrinking nor complete melting of spherulites accompanied by a change in their number is compatible with these observations.

- **Spherulitic crystallinity during melting.** Changes in the depolarized scattering intensity from spherulites during melting and melt-recrystallization were expressed in terms of changes in the depolarized scattering invariant. As the size and number of the spherulites remained constant, those variations of the invariant are associated via the spherulite optical anisotropy with the spherulitic crystallinity.

In case of the α -phase melt-recrystallization of coPLA the double endothermic DSC event could unambiguously be attributed to a decrease in spherulite crystallinity by temperature- and time-resolved monitoring of the depolarized scattering invariant via SALS. Full recovery of the original degree of crystallinity can be excluded because the second drop of the depolarized scattering invariant started from an intermediate level which was significantly lower than the original level observed directly after completing isothermal crystallization. Melt-recrystallization of polylactide with spherulitic morphology proceeds via melting of the spherulite constituting lamellae. A new population of lamellae can form rapidly via recrystallization from those freshly created locally disentangled (spherulitic) domains with both processes running concomitantly [249]. Macroscopically, the spherulitic superstructure, thereby, is preserved as inferred from a constant spherulite size. The decrease in crystallinity is attributed to kinetic effects when new lamellae with larger thickness [37, 44, 221, 228, 254] have to be formed from the remnants of the former structure. During non-isothermal melt-recrystallization, the critical size of nuclei continuously increases along with temperature and the orientation of the chain segments from freshly molten crystals is randomized by thermal diffusion and reptation, thus antagonizing recrystallization. Referring to the model suggested by Strobl *et al.* [221] which suggests that melt-recrystallization occurs via a melting zone running through a lamella, some of the originally existing lamellae may not recover anymore.

An analogous joint SALS and DSC treatment of the melt-recrystallization behaviour of PDLA was not as straight-forward because the endothermic melting of α' -phase and α -phase crystals was obscured by the exotherm of the recrystallization of α -phase from α' -phase in the investigated range of isothermal crystallization temperatures. The lack of the first endothermic melting peak in

5. CONCLUSION AND OUTLOOK

combination with a first exothermic peak, emerging with increasing intensity as the crystallization temperature decreases, is nicely compatible with the fact that the α -phase crystallizing in an α'/α -phase transition is thermodynamically more stable than the α' -phase, and that melting of α' -phase is running parallel to the recrystallization of α -phase, however, with the simultaneity of the two processes not necessarily taking place at the same lamellae, respectively. Stopping the temperature increase at the temperature where melted α' -phase material recrystallizes to α -phase material shed further light onto the process. While the spherulite size remained unchanged during annealing of the sample at that given temperature, a partial regain in the depolarized scattering invariant was observed. The regain in the scattering invariant is associated with an increasing spherulitic crystallinity. However, quantifying the change in the degree of crystallinity due to the α'/α -transition in PDLA via the depolarized scattering invariant remains a challenge for SALS because the optical constants of the α' -phase crystals are not known yet and changes in the scattering invariant, thus, might either stem from changes in crystallinity or from birefringence of the material.

- **The effect of the presence of scPLA** in low amounts in a homopolymer matrix was investigated for two PLLA samples with different molecular weights mixed in solution with 2 wt% of PDLA. The presence of scPLA in transparent film samples, which were obtained via film-casting from solution, was verified by DSC measurements, which showed the characteristic melting-endotherm of scPLA at a temperature at around 230 °C. In isothermal DSC experiments the stereocomplex-assisted nucleation leads to faster overall crystallization. Peak crystallization times as defined by the maxima of the symmetric crystallization exotherms were significantly shorter than those of pure polylactide. The data suggests that this heterogeneous nucleation is most effective at large undercooling where scPLA crystallites act as heterogeneous seeds for spherulite nucleation. SALS measurements confirmed the increase in spherulite number density in the presence of scPLA, measured average spherulite sizes in fully crystallized samples were smaller than in samples of the pure polymer. On the other hand, the stereocomplex-assisted nucleation of PLLA by mixing with 2 wt% of PDLA did not alter the temperature-dependent spherulite growth rate. Characterization via SALS showed that the spherulite growth rate curves of the nucleated and the pure samples overlaid within experimental uncertainty. These findings agree well with results which were published by another group [65] during the term of this thesis and which were also obtained by depolarized SALS.

In this thesis, however, for the first time evidence for the (co-)formation and growth of non-spherulitic superstructures in scPLA-nucleated polylactide in isothermal experiments at large undercoolings were obtained from depolarized SALS measurements. Scattering was no longer characterized by the four-lobed intensity distribution of spherulites but rather scattering was observed along the principal directions of $\mu = 0^\circ$ and $\mu = 90^\circ$ indicating the presence of a completely dif-

ferent kind of crystalline aggregate. These newly observed superstructures show temperature characteristics which are comparable to those of the PLA homopolymers. The behaviour of the scattering invariant during melting is highly indicative for the α'/α -phase transition, final melting as indicated by the dropping of the scattering signal to zero occurs at around 180 °C, which is the melting point of α -phase crystals. These findings sustainably suggest that the presence of scPLA induces non-spherulitic crystallization of the homopolymer. While the crystalline lattice seems to be unaffected, the lamellar orientation in the crystalline aggregates is severely modified by the presence of scPLA crystallites. However, more research is needed to elucidate the morphological nature of these newly observed crystalline non-spherulitic superstructures.

The presented findings may aid in defining an agenda for future research work. Therefore, in the following perspective some topics are addressed serving as a concluding remark of this thesis.

5.2 Perspective

The SALS instrument described in detail in CHAPTER 3 can be improved in several ways covering aspects from both the software routines as well as the mechanical and optics setup:

- Improvements to the instrument can be achieved regarding the optics of the device. So far simple bi-convex lenses were used. However, it is expected that using an asphere as Fourier lens, which corrects for image distortions due to spherical aberration, and a proper camera objective will further increase the data-quality. The present device lacks a monitor for the intensity of the primary beam. Such a device would enable monitoring of the stability of the source intensity and the transmitted intensity. Knowledge of these quantities is a prerequisite for determining absolute Rayleigh ratios.

In addition, a motorized stage for the analyzer would allow quasi-simultaneous measurements of the polarized V_V and depolarized H_V scattering of the same sample. To this end, successive measurements would be carried out in alternating analyzer directions yielding an alternating sequence of polarized and depolarized scattering records. To realize such a feature improvements to the software routines for data acquisition and evaluation are necessary along with the synchronization of the timed data acquisition from the camera and intensity monitors with the temperature-time protocol applied to the sample and the alteration of the analyzer position.

- Improvements to the software can be achieved by an integration of functionalities and routines for data acquisition in one application and data evaluation in another application or even merging into one single application.

For the present setup a graphical user interface (GUI) integrating data-acquisition

and temperature-control seems most desirable. To this point a MATLAB script interface and the Pylon camera software suite were used in parallel without mutual synchronization. Here, an integrated software application unifying data-acquisition and temperature-control would be of great help and may create opportunities for more complex time- and temperature-dependent experiments.

More sophisticated software routines would also enable data-acquisition in high dynamic range mode by setting multiple exposure times, thus extending the sensitivity range both to higher and lower scattering intensities in a single measurement run. Dedicated software could also mitigate the problem of detector saturation by automated adjustment of camera exposure times.

While the instrument proved its capacity of acquiring static time series, in principle, dynamic light scattering could be realized with the instrument as well for investigation of slow dynamics. With the detector operating at 90 frames per second a minimum lag time of $\tau = 12$ ms seems feasible.

The results presented in CHAPTER 4 might serve as a starting point for future research work on the phase transformation behaviour of PLA. In addition, the home-built SALS instrument presents a platform for further research in fields related to the study of soft and condensed matter. New insights are expected from addressing the following topics:

- In this work the change in crystallinity during melting, phase α/α melt-recrystallization and the polymorphous melt-recrystallization due to α'/α -transition was monitored by SALS. It seems worthwhile to complement or even combine these findings with time- and temperature-resolved x-ray scattering measurements thus gaining access to the arrangement of crystallites and to the morphology of the crystallites [255]. Some information on the evolution of lamellar thickness and long spacing during non-isothermal melting-recrystallization processes is available. However, of particular interest are the changes in the orientation of chain segments and the fluctuation of density in the crystalline domains during the phase transformation processes, which have not been revealed in detail so far.
- It is well known that the crystalline morphology and, in particular, the size and number of spherulites largely affects the optical and mechanical properties of semi-crystalline polymers. This also holds for PLA. With the finding of a constant spherulite size but lamellar reorganisation during (polymorphous) melt-recrystallization the question arising immediately is whether this process has an effect on the mechanical properties of the material. Such studies might as well look into the effect of the annealing time after recrystallization.
- In this work the effect of the presence of a small amount of scPLA in the homopolymer on crystallization and melting was investigated and comparisons to the behaviour of the pure polymers were made. Further research is necessary to scrutinize the effect of the ratio of scPLA and pure polymer on the spherulite

5. CONCLUSION AND OUTLOOK

growth rate. From these studies also new insights are expected on the modification of the spherulitic morphology in the presence of scPLA. Results presented in this thesis indicate an additional molecular-weight dependent effect on the crystalline superstructure of scPLA-homopolymer-composites which presents a field for further research on its own.

- Chain architecture of PLA [7, 8, 256–258] and co-polymerization with other polymers [140, 259] presents a further, vast research field. The reviews cited in the state of the art of this work might serve as a starting point for identifying candidates for promising materials.
- The presented methodology might be applied to the study of the crystallization and melting behaviour of blends of PLA with other polymers by means of combined SALS and DSC. Of course, the range of other polymeric systems worth considering is huge and investigations might well be extended to other semi-crystalline polymers and their blends.
- The SALS instrument developed in this work might be applied to the study of phase separation processes in polymer blends [141, 260, 261]. Literature reports on investigations of the miscibility of various polymers via SALS [87, 91, 92]. Also kinetics of phase separation were analysed for the spinodal decomposition of two-component systems [90, 98].

The points addressed above cannot cover all issues of the present and emerging field of studies of the structure of polymeric systems. The author is confident that this work helps scattering light on aspects of polymer morphology. Still, there is more exciting research ahead.

Appendix

A Polymer characterization of the sample material

A.1 Summary of PLA sample properties

Poly lactide sample material was provided by Total Corbion PLA bv¹³. As part of the cooperation between HSHL and Corbion the poly(L-lactide) injection grade Purapol¹⁴ L130 and poly(L-co-D-lactide) thermoforming grade Purapol LX175, a random co-polymer with 4% D-isomer content, as well as poly(D-lactide) Luminy D120 were provided for research purposes. In addition, a high-molecular weight medical grade poly(L-lactide) Resomer L210S (Evonik Industries AG, Essen, Germany) was used in this work. The polymers were delivered as pellets or flakes, respectively, and used as-received without further purification.

TABLE A.1 summarizes the properties of the polymers in terms of isomer content, weight-averaged molecular weight M_W (see SUBSECTION A.2.1), polydispersity index ($PDI = M_W/M_N$, where M_N is the number average molecular weight) and glass transition temperature T_g , and melting temperature T_m , respectively.

Table A.1: Polymer properties of the polylactide samples used in this work.

name	D-isomer [%]	M_W [kg mol ⁻¹]	PDI	T_g [°C] ^a	T_m^0 [°C]	tradename
PLLA1	0	143	1.6	62	186 ± 2	Purapol L130
PLLA2	0	406	1.5	63	199 ± 6	Resomer L210S
PDLA	100	153	1.6	62	181 ± 5	Luminy D120
coPLA	4	163	1.8	59	171 ± 4	Purapol LX175

a) ISO-midpoint according to DIN EN ISO 11357-2

The stereochemical composition of the PLA samples was determined via polarimetry and nuclear magnetic resonance (NMR) spectroscopy, and the manufacturers' specifications were validated. The details are described in SUBSECTION A.2.2. Thermal characterization was carried out via DSC. The experimental details are given in SUBSECTION A.3. In addition via thermogravimetric analysis (TGA) the thermal (oxidative) degradation of the polymers was investigated.

Thermal oxidative degradation and hydrolysis play a major role for the degradation of PLA in terms of molecular weight at elevated temperatures [262–264]. However, degradation in the undercooled melt is sufficiently slow to allow measurements over the course of several minutes [265]. Also, in order to minimize degradation PLA was

¹³Total Corbion PLA bv is a 50/50 joint venture of the Dutch company Corbion N.V. and the French company Total S.A. founded in 2017.

¹⁴The product family name Purapol was changed into the registered trademark name Luminy[®] when Total Corbion formally started up operations in March 2017.

kept in the melt-state as short as possible. In addition, experiments were conducted with freshly prepared samples.

Another degradation mechanism which had to be considered was photodegradation. Photodegradation of PLA, which is accompanied by a decrease in molecular weight [266] and racemization of the polymer [267], when irradiated by UV light, was reported in literature [268]. Bulk erosion of the material irrespective of the degree of crystallinity was observed [269]. However, no photodegradation of PLA by laser light on experiment-relevant time scales was expected during SALS measurements, because the energy of the photons of the utilized HeNe laser was much lower than that of short-wavelength UV radiation.

A.2 Molecular properties

A.2.1 Molecular weight

Molecular weights were determined by size exclusion chromatography (GPC, Shimadzu Co., Kyoto, Japan) performed in chloroform (TCM) (HPLC grade $\geq 99.8\%$ stabilized, HiPerSolv CHROMANORM®, VWR International GmbH, Langenfeld, Germany) at 40 °C. TABLE A.1 summarizes the properties of the polymers in terms of isomer content, weight-averaged molecular weight M_W and polydispersity index (PDI = M_W/M_N , where M_N is the number average molecular weight), respectively. Solutions were prepared with a concentration of 6 g/l and filtered (Chromafil PTFE 0.45 μm , Macherey-Nagel, Düren, Germany) into vials. A sample volume of 50 μl was injected and eluted with TCM at a flow rate of 1 ml/min for 40 min. A refractive index detector (RID-20A, Shimadzu Co.) was used to determine the elution times of the respective sample constituents. The instrument was equipped with one precolumn (8x50 mm) and two analytical columns (8x300 mm) (PSS Polymer Standards Service GmbH, Mainz, Germany). The columns were filled with particles of 5 μm diameter and made from a styrene-divinylbenzene copolymer network. Porosity of the analytical column fillings was 10³ Å and 10⁵ Å, respectively. The instrument was calibrated with a polystyrene standard kit (DIN kit polystyrene, 1.4k, 9k, 18k, 100k und 560k, Polymer Standard Service, Mainz, Germany).

A.2.2 Stereochemistry

Polarimetry. Specific optical rotation $[\alpha_D^{25}]$ of PLA samples was determined via polarimetry (241MC polarimeter, PerkinElmer, Waltham, USA) for the sodium D-line ($\lambda = 589 \text{ nm}$) in TCM (reagent grade $> 99.8\%$, Honeywell International Inc., Morristown, NJ, USA) at a temperature of 25 °C. Polymer concentration was $c = 10 \text{ g/l}$. From the rotatory power $[\alpha_D^{25}]$ the optical purity OP of the polymers was calculated via

$$OP = \frac{[\alpha_D^{25}]}{[\alpha_D^{25}]_0} \quad (\text{A.1})$$

A. POLYMER CHARACTERIZATION OF THE SAMPLE MATERIAL

where $[\alpha_D^{25}]_0 = -156^\circ$ is the specific optical rotation of enantio-pure PLLA and $[\alpha_D^{25}]_0 = +156^\circ$ of enantio-pure PDLA, respectively [3]. Derived parameters were the molar fraction of D-LA in the chain

$$X_D = \frac{[\alpha_D^{25}] + 156}{312} \quad (\text{A.2})$$

and the isotactic sequence length of a L-LA rich *random* co-poly lactide

$$\bar{\xi} = \frac{a}{X_D} \quad (\text{A.3})$$

where the coefficient $a \in [1,2]$ reflects polymerization incorporation of D-LA from meso-lactide (D,L-lactide, $a = 1$) or from the enantio-pure lactide (D,D-lactide, $a = 2$) [18]. If the polymerization feed contains both types of dimers the parameter a depends on their ratio.

The results are summarized in TABLE A.2. The manufacturers' specifications which were provided with the polymers were verified within experimental uncertainty. Note, that based on the results from NMR measurements (see below) for coPLA $a = 2$ was used for determining the isotactic sequence length.

Table A.2: Stereo-isomer composition of the polylactide samples as determined by polarimetry.

	$[\alpha_D^{25}]$ [$^\circ \text{ ml g}^{-1} \text{ dm}^{-1}$]	OP [-]	X_D [-]	$\bar{\xi}$ [-]
PLLA1	-158 ± 5	1.01 ± 0.03	-0.01 ± 0.02	-
PLLA2	-162 ± 8	1.04 ± 0.05	-0.02 ± 0.03	-
PDLA	$+161 \pm 5$	1.03 ± 0.03	1.02 ± 0.02	-
coPLA	-147 ± 4	0.94 ± 0.03	0.03 ± 0.01	67 ± 22

Nuclear Magnetic Resonance Spectroscopy. Proton decoupled ^{13}C NMR spectra were acquired on a Bruker Avance 500 NMR spectrometer at 500 MHz. Measurements were performed in CDCl_3 (Chloroform D1 for nmr spectroscopy, Merck Uvasol, Deuterium degree $> 99.8\%$ stabilized with silver) at 30°C . Sample concentration was around 20 mg/ml. The chemical shift was calibrated with the deuterium resonance of the solvent (lock signal). A total of 65536 data points were acquired at a spectral width of 10 kHz and an acquisition time of 3.2 s. Signal averaging over up to 2048 scans was performed to enhance the signal to noise-ratio.

On the molecular level PLA is composed of lactic acid monomers yielding either isotactic (i) pairs -LL- and -DD-, respectively, or syndiotactic (s) pairs -DL- and -LD-. Bero *et al.* [270], Thakur *et al.* [271] and Zell *et al.* [272] demonstrated the stereosensitivity of the methine and the carbonyl ^{13}C NMR resonances and also presented an assignment of the tetrad and hexad resonances to the stereosequence.

The spectra obtained from the sample material are depicted in FIGURE A.1. As can be seen the homopolymers show only one unique peak in the methine and carbonyl region which is indicative for isotacticity of the chains. This finding is also in line with results from polarimetry (see above). Only in case of coPLA additional resonances

A. POLYMER CHARACTERIZATION OF THE SAMPLE MATERIAL

can clearly be identified. Evaluation of the spectra was carried out in analogy to [48]. Compared to data from literature all peaks are displaced by 0.1 ppm to higher chemical shifts. However, based on the strong isotactic peak assignment of the resonances could be accomplished. The tetrads *iss*, *ssi* and *sss* are absent in the spectrum of coPLA

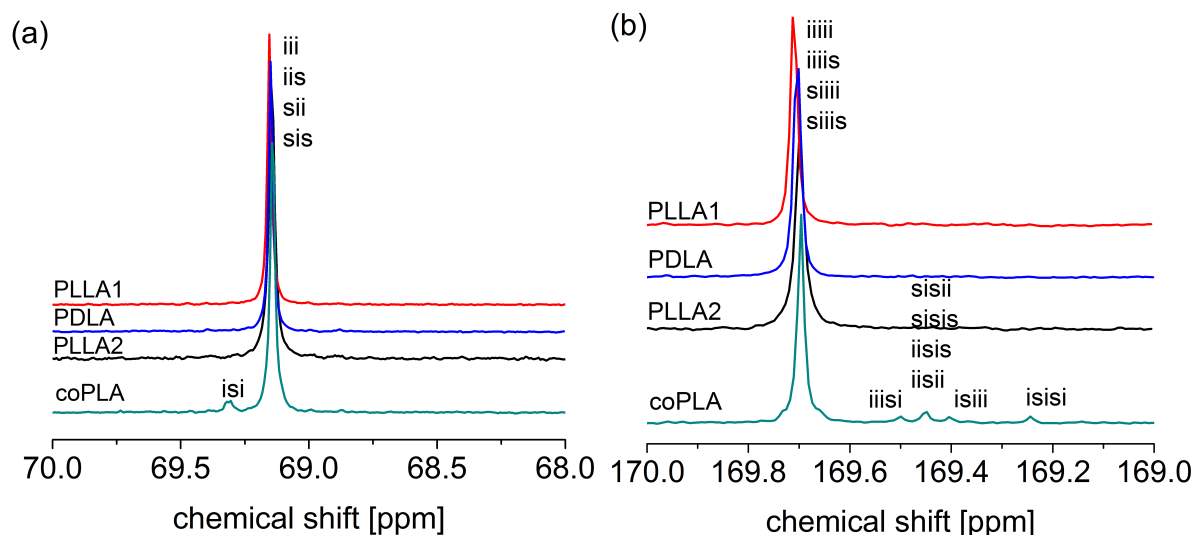


Figure A.1: ^{13}C NMR spectra of the methine region (a) and carbonyl region (b) of the polylactide samples.

which is indicative for a polymerization of coPLA from L-lactide in excess and D-lactide as the minor component rather than Meso-lactide [271, 273]. As a consequence, signal intensities could be compared to theoretical calculations given by [270]. The results are given in TABLE A.3. For coPLA measured signal intensities could best be matched by calculated intensities based on a copolymer composed of 95/5 wt/wt L-lactide and D-lactide. This ratio agrees well with the manufacturer's specifications stating a content of 4% of the minor, i. e. D-lactide, isomer unit.

A. POLYMER CHARACTERIZATION OF THE SAMPLE MATERIAL

Table A.3: Stereo-isomer composition of the polylactide samples as determined by NMR spectroscopy. The entries represent the integrated signal intensities of the stereo-sequence tetrads and hexads of isotactic (i) or syndiotactic (s) lactic acid monomer pairs.

	Tetrads [%]		Hexads [%]				
	iii	isi	iiii	iiisi	iisii	isiii	isisi
	+iis		+iiii		+iisis		
	+sii		+siii		+sisii		
	+sis		+siii		+sisis		
PLLA1	100	0	100	0	0	0	0
PLLA2	100	0	100	0	0	0	0
PDLA	100	0	100	0	0	0	0
coPLA	95.0 (95.3) ^a	5.0 (4.8)	87.0 (86.0)	3.0 (2.4)	5 (4.8)	2.7 (2.4)	2.2 (2.4)

a) numbers in brackets: theoretical signal intensities for a copolymer with 95/5 wt/wt

L-lactide / D-lactide composition [270]

A.3 Thermal properties

Differential Scanning Calorimetry. Thermal analysis was performed on a DSC1 (Star System DSC1, Mettler Toledo, Gießen, Germany), which was equipped with an intracooler and an autosampler in closed aluminium crucibles with a volume of 40 μ l (ME-00026763, Mettler Toledo). A second instrument used was a DSC 204 F1 Phoenix (Netzsch GmbH & Co. KG, Selb, Germany). Sample weights were close to 10 mg. Measurements were performed in nitrogen atmosphere at a flow rate of 50 ml/min. The temperature scale and the enthalpy scale of the instruments were calibrated with indium and zinc standards.

The standard procedure for polymer characterization was a double heating-cooling cycle from 25 °C to 250 °C at a heating rate of +10 K/min and a cooling rate of -10 K/min. The obtained glass transition temperatures were \approx 60 °C. They are listed in TABLE A.1. In isothermal crystallization experiments the thermal history of the samples was erased by melting at 200 °C for 3 min. Subsequently, the sample was cooled at a rate of 50 K/min to the respective crystallization temperature T_c and crystallized for 30 min ($85^\circ\text{C} \leq T_c \leq 115^\circ\text{C}$) or 60 min ($T_c = 80^\circ\text{C}$, $T_c \geq 120^\circ\text{C}$), respectively, before being cooled to room temperature at 50 K/min. After equilibrating for 2 min the analytical heating was carried out at 20 K/min.

Linear Hoffman-Weeks analysis [241] (see FIGURES A.2 to A.5) was utilized for determining the equilibrium melting temperature T_m^0 via extrapolation of the peak temperatures $T_m(T_c)$ of the final melting endotherms to $T_m = T_c$ (see also [Dzi18, Rok18]). The results are listed in TABLE A.1.

A. POLYMER CHARACTERIZATION OF THE SAMPLE MATERIAL

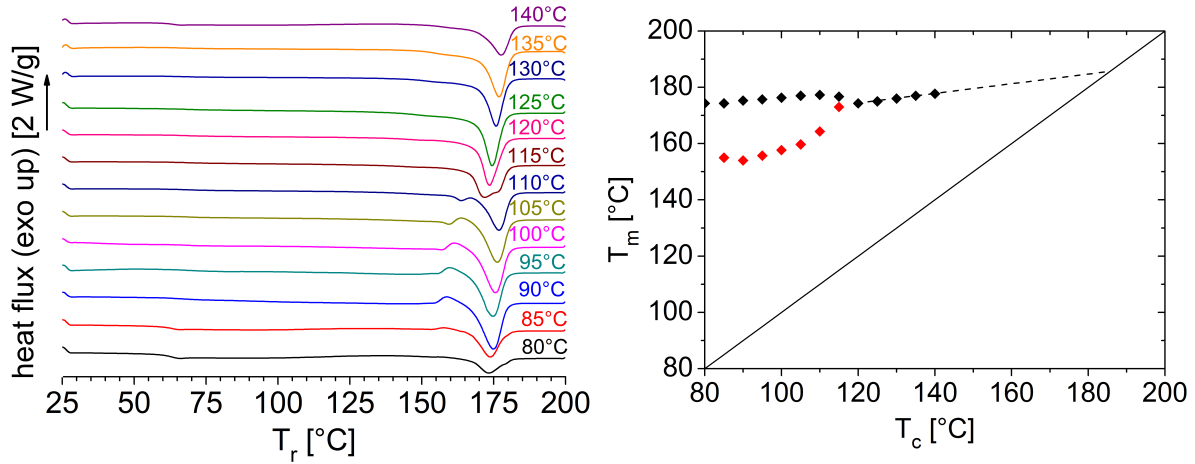


Figure A.2: Left: DSC thermograms of PLLA1 of the analytical heating run at 20 K/min after isothermal crystallization at the indicated temperatures. Right: Determination of the equilibrium melting temperature T_m^0 of PLLA1 via Hoffman-Weeks analysis of the peak temperatures (◆) of the final melting endotherm with $T_c > 120^\circ\text{C}$. The endothermic signal (◆) preceding the final melting endotherm was due to the α'/α -transition and was not used for extrapolation. At $T_c = 115^\circ\text{C}$ the transition causes a double-peaked melting endotherm, at lower T_c a recrystallization exotherm can be identified separating the lower endothermic signal (◆) and the final melting endotherm (◆).

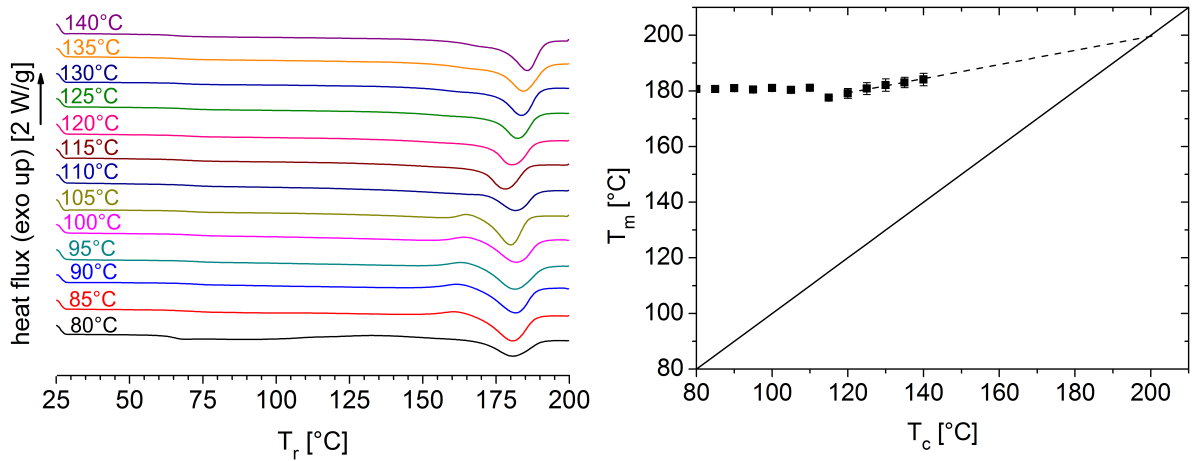


Figure A.3: Left: DSC thermograms of PLLA2 of the analytical heating run at 20 K/min after isothermal crystallization at the indicated temperatures. Right: Determination of the equilibrium melting temperature T_m^0 of PLLA2 via Hoffman-Weeks analysis of the peak temperatures (■) of the final melting endotherm with $T_c > 120^\circ\text{C}$.

A. POLYMER CHARACTERIZATION OF THE SAMPLE MATERIAL

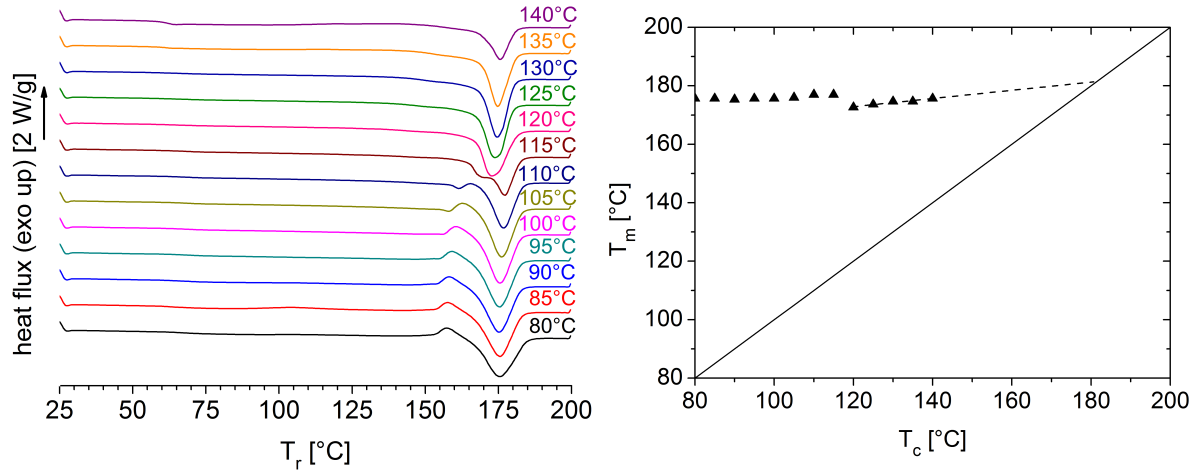


Figure A.4: Left: DSC thermograms of PDLA of the analytical heating run at 20 K/min after isothermal crystallization at the indicated temperatures. Data-set based on [Rok18]. Right: Determination of the equilibrium melting temperature T_m^0 of PDLA via Hoffman-Weeks analysis of the peak temperatures (\blacktriangle) of the final melting endotherm with $T_c > 120^\circ\text{C}$.

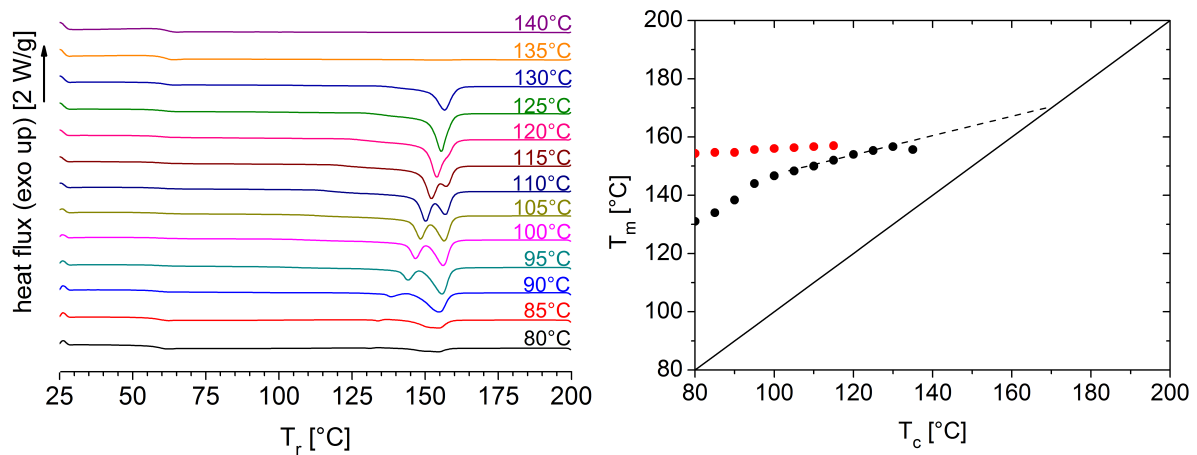


Figure A.5: Left: DSC thermograms of coPLA of the analytical heating run at 20 K/min after isothermal crystallization at the indicated temperatures. Right: Determination of the equilibrium melting temperature T_m^0 of coPLA via Hoffman-Weeks analysis of the peak temperatures (\bullet) of the T_c -sensitive melting endotherm with $T_c > 100^\circ\text{C}$. The quasi-stationary melting endotherm (\bullet) was due to melt-recrystallization signalling final melting of the recrystallized phase, and was not used for extrapolation.

Thermogravimetric analysis. Isothermal and non-isothermal thermogravimetric analysis (TGA) were performed on a TGA/SDTA851 (Mettler Toledo, Gießen, Germany) with open aluminium oxide crucibles with a volume of $150\ \mu\text{l}$ (ME-24124, Mettler Toledo). The instrument was calibrated with indium and aluminium standards. Sample mass was between 20 and 80 mg. In order to analyze the thermal stability (pyrolysis kinetics) of PLA in an inert atmosphere, non-isothermal TGA was carried out at a heating rate of $5\ \text{K}/\text{min}$ and with purge gas argon at a flow rate of $55\ \text{ml}/\text{min}$. In order to mimic conditions in isothermal SALS experiments, isothermal TGA was performed in synthetic air at a flow rate of $85\ \text{ml}/\text{min}$. Samples were heated at a rate of up to $100\ \text{K}/\text{min}$ to the respective isothermal temperature, which subsequently was kept for 120 min.

Results of the measurements are depicted in FIGURE A.6. The weight loss curves (FIGURE A.6a) are sigmoidal in shape with a sharp decrease in a narrow temperature range. Complete decomposition with residual char content $< 1\%$ was observed in inert atmosphere. Temperatures of thermal stability T_5 indicating a weight loss of

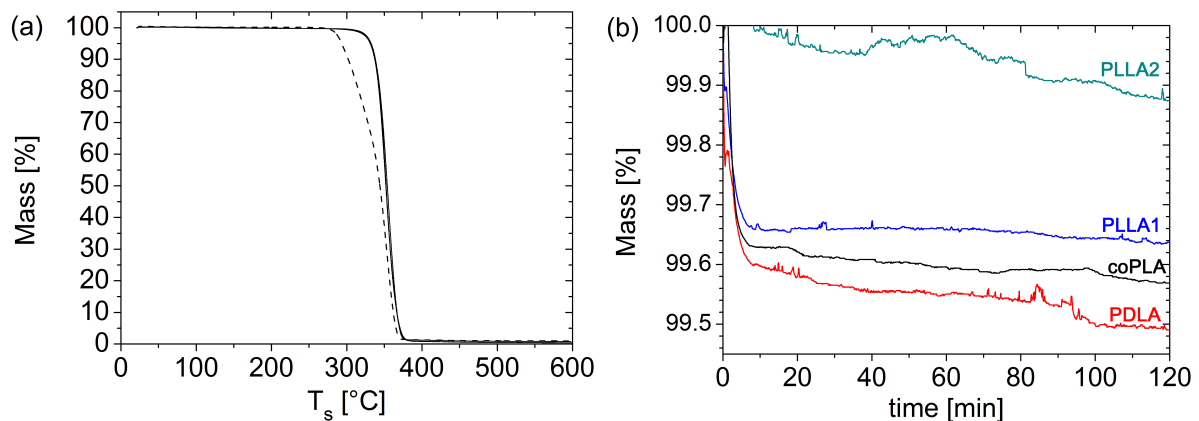


Figure A.6: a) Non-isothermal TGA in argon at a heating rate of $5\ \text{K}/\text{min}$ (PLLA1: —, PLLA2: ---, PDLA: —, coPLA: —). b) Isothermal TGA in synthetic air at various temperatures (PLLA1: 110°C , PLLA2: 140°C , PDLA: 130°C , coPLA: 150°C).

5% were $T_5 = 332^\circ\text{C}$ for PLLA1, PDLA and coPLA, and $T_5 = 293^\circ\text{C}$ in case of PLLA2, respectively. These findings are in good agreement with literature [274].

In order to determine thermal stability under conditions more closely resembling experimental conditions of SALS measurements isothermal TGA (FIGURE A.6b) was conducted in synthetic air. The rapid change in mass in the first five minutes of the measurement is attributed to the transient behaviour of the instrument. As measurements were conducted above 100°C this might also indicate the loss of water from the sample pellets. The mass loss curves then show a plateau of the sample mass with a very small loss of only $\approx 0.1\%$ over the course of two hours.

B Supporting Information

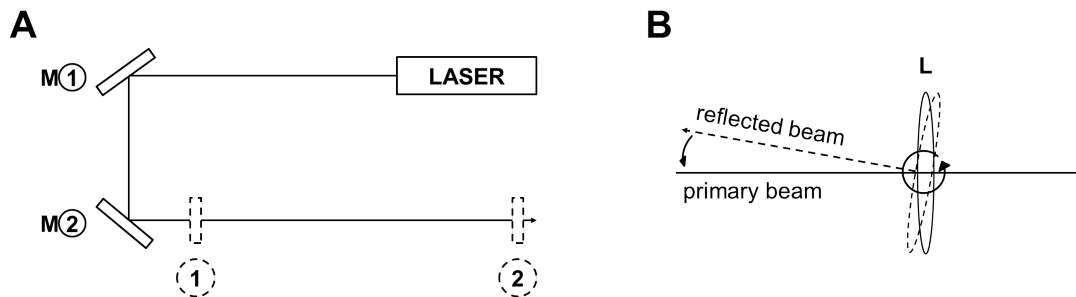


Figure B.1: Alignment of the optical components of the SALS device. A) Alignment of the primary beam is carried out by repeatedly positioning a target at positions 1 and 2 in the detection leg and adjusting the beam position with the corresponding mirrors M1 and M2, respectively. B) Orthogonal orientation of the lenses with respect to the primary beam is achieved by closely aligning the back reflection of the primary beam from the lens surface with the incident beam. Exact co-alignment of the two beams should be avoided, however, to avoid back reflection of the reflected beam into the laser tube, which could be harmful to the laser.

B. SUPPORTING INFORMATION

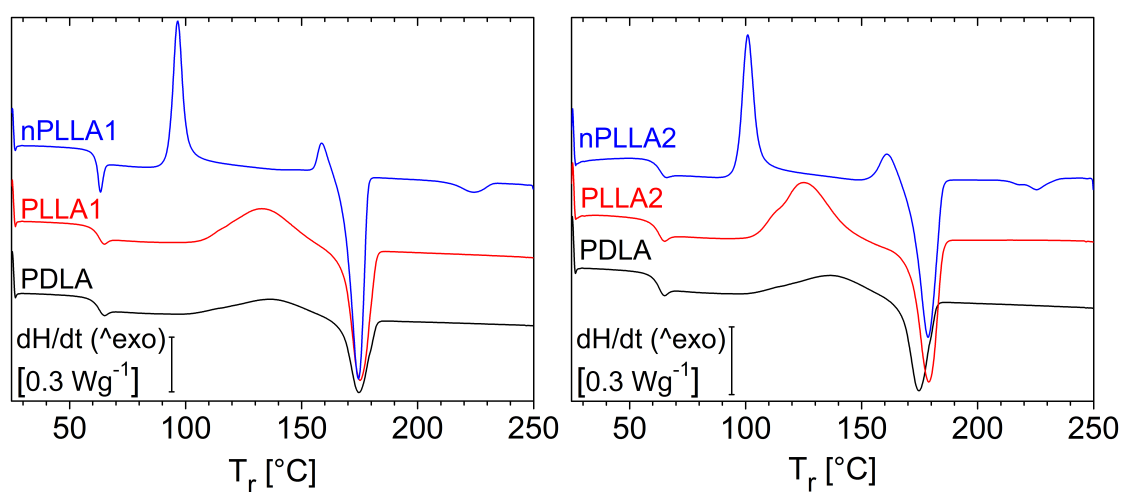


Figure B.2: DSC thermograms of the first heating from 25 °C to 250 °C at a rate of 10 K/min of nPLLA1 (left) and nPLLA2 (right) compared to the pure PLLA1 and PLLA2, respectively, and PDLA polymers. Exothermic heat flow is in positive ordinate direction. The glass transition at 60 °C is followed by a cold crystallization peak at around 100 °C. The second exothermic event at around 160 °C indicates recrystallization due to the α'/α -transition which is followed by complete melting of the α -phase crystals at 175 °C. Cold crystallization of the pure polymers takes place at temperatures above 110 °C and no substantial α' -phase is formed and, thus, there is no second exothermic peak. For nucleated materials the endothermic event at 225 °C is indicative for the melting of scPLA, thus, confirming successful nucleation by film-casting of solution-mixed PLLA and PDLA. No such signal can be observed in the pure polymers.

B. SUPPORTING INFORMATION

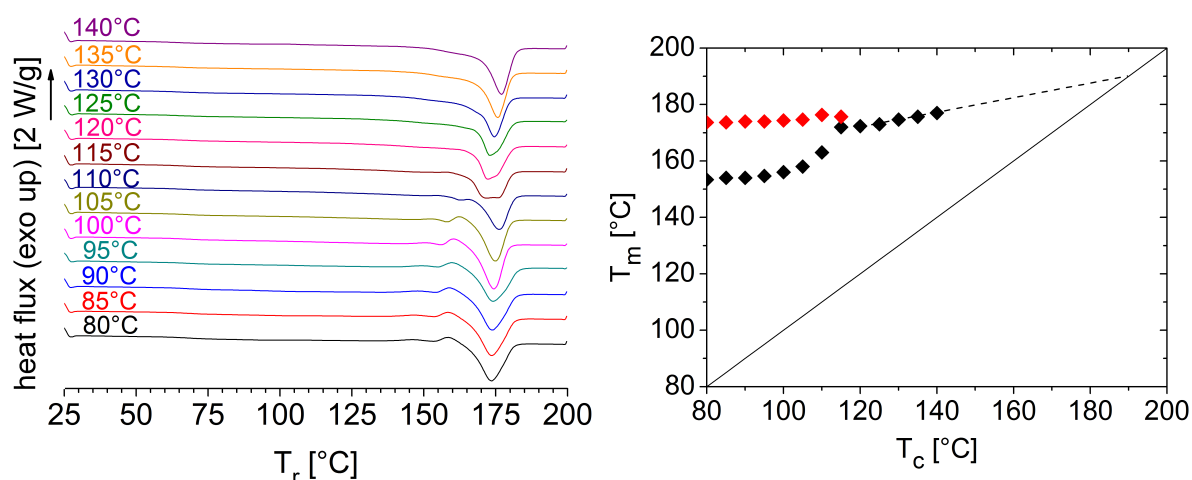


Figure B.3: Left: DSC thermograms of nPLLA1 of the analytical heating run at 20 K/min after isothermal crystallization at the indicated temperatures. Exothermic heat flow is in positive ordinate direction. Right: Determination of the equilibrium melting temperature T_m^0 of nPLLA1 via Hoffman-Weeks analysis of the peak temperatures (◆) of the final melting endotherm with $T_c > 120^\circ\text{C}$. The quasi-stationary melting endotherm (◆) for $T_c > 120^\circ\text{C}$ was due to melt-recrystallization signalling final melting of the recrystallized phase, and was not used for extrapolation.

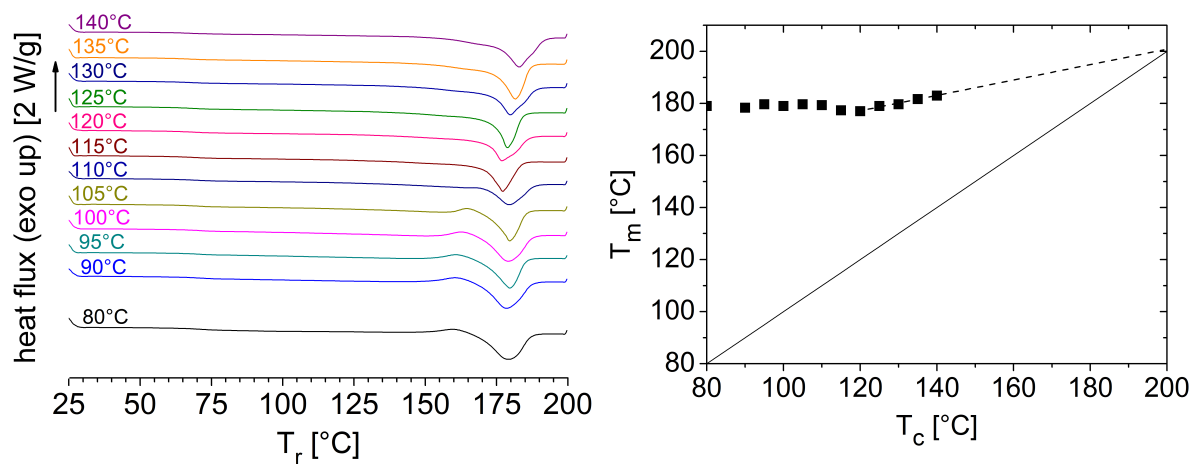


Figure B.4: Left: DSC thermograms of nPLLA2 of the analytical heating run at 20 K/min after isothermal crystallization at the indicated temperatures. Exothermic heat flow is in positive ordinate direction. Right: Determination of the equilibrium melting temperature T_m^0 of nPLLA2 via Hoffman-Weeks analysis of the peak temperatures (◼) of the final melting endotherm with $T_c < 120^\circ\text{C}$.

B. SUPPORTING INFORMATION

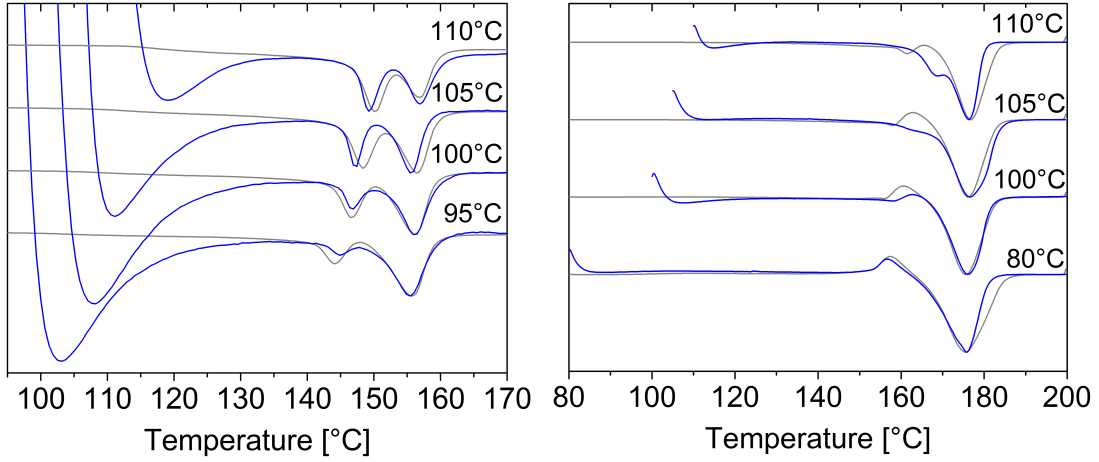


Figure B.5: DSC thermograms of coPLA (left) and PDLA (right) of the analytical heating runs after isothermal crystallization for 30 min at the indicated crystallization temperatures. Exothermic heat flow is in positive ordinate direction. For a given crystallization temperature the depicted DSC traces differ in the applied temperature-time protocol. Signal acquisition was performed either (i) immediately following the crystallization segment at a heating rate of 10 K/min (blue, compare SUBSECTION 4.1) or (ii) after quenching to room temperature subsequent to isothermal crystallization and at a rate of 20 K/min (gray, see APPENDIX A.3). For coPLA, in case (i) DSC data is severely distorted by a transient-signal of the DSC apparatus when switching from isothermal to non-isothermal measurement mode. With respect to the positions of the melting endotherms the DSC traces acquired by the two methods are identical.

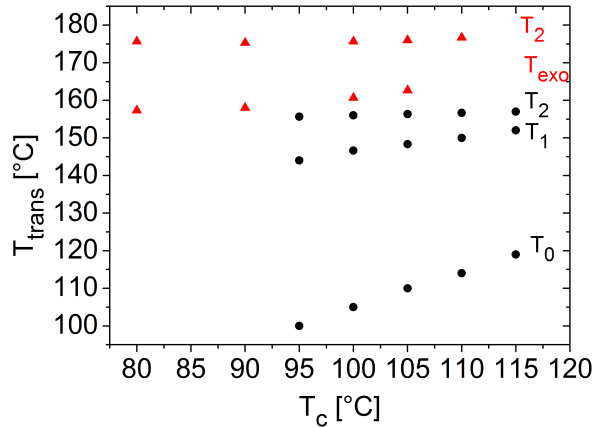


Figure B.6: Melting peak temperatures T_1 and T_2 of coPLA (●) and PDLA (▲), respectively. DSC traces were acquired after quenching to room temperature subsequent to isothermal crystallization for 30 min and at an analytical heating rate of 20 K/min (see APPENDIX A.3). The temperature T_{exo} denotes the peak temperature of the exothermic signal preceding the dominant melting peak of PDLA. The temperature T_0 denotes the onset of an endothermic heat flow associated with the melting of a fraction of the crystal population, which was formed at the isothermal crystallization temperature T_c observed in the analytical heating of coPLA.

B. SUPPORTING INFORMATION

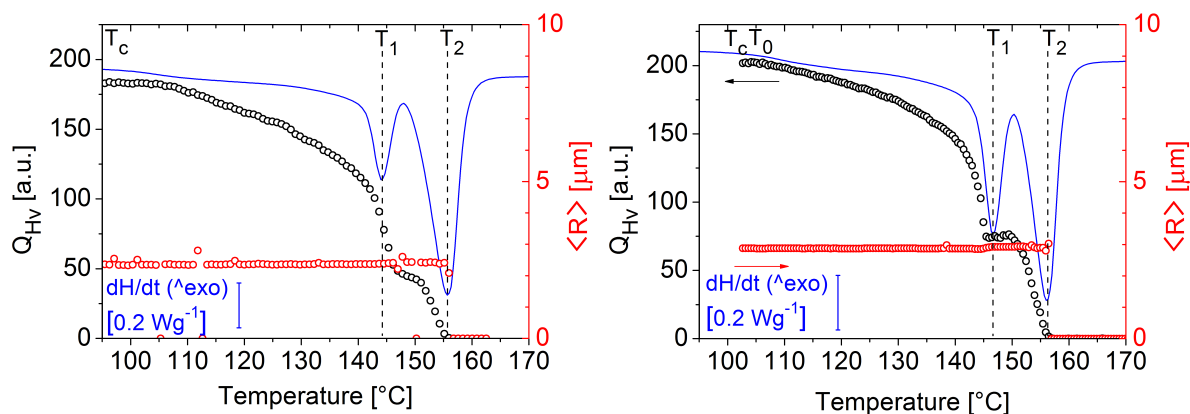


Figure B.7: Average spherulite size (\circ) and depolarized scattering invariant Q_{HV} (\circ) of coPLA as a function of temperature in the analytical heating run at a rate of 10 K/min after isothermal crystallization for 30 min at $T_c = 95^\circ\text{C}$ (left) and $T_c = 100^\circ\text{C}$ (right). DSC thermograms ($—$) were recorded at a rate of 20 K/min after quenching to room temperature (compare FIGURE B.5, see discussion in SUBSECTION 4.5). Exothermic heat flow is in positive ordinate direction.

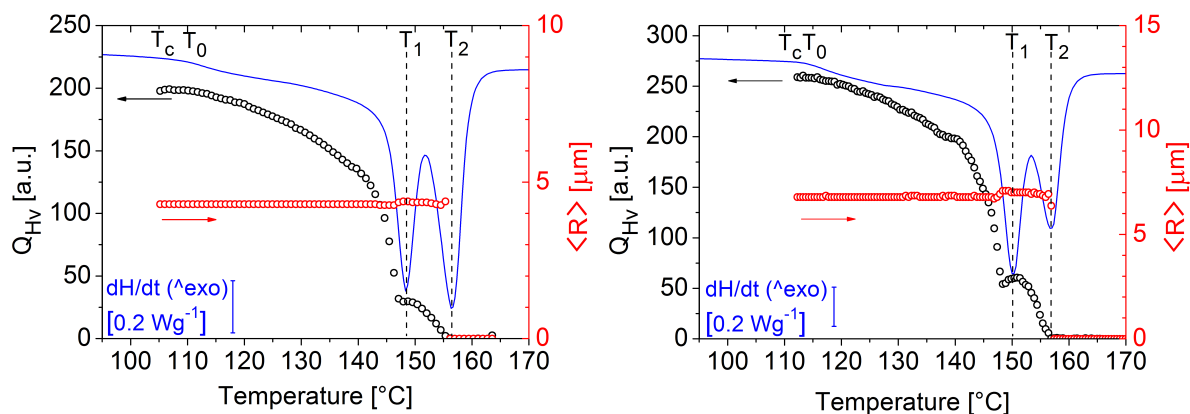


Figure B.8: Average spherulite size (\circ) and depolarized scattering invariant Q_{HV} (\circ) of coPLA as a function of temperature in the analytical heating run at a rate of 10 K/min after isothermal crystallization for 30 min at $T_c = 105^\circ\text{C}$ (left) and $T_c = 110^\circ\text{C}$ (right). DSC thermograms ($—$) were recorded at a rate of 20 K/min after quenching to room temperature (compare FIGURE B.5, see discussion in SUBSECTION 4.5). Exothermic heat flow is in positive ordinate direction.

B. SUPPORTING INFORMATION

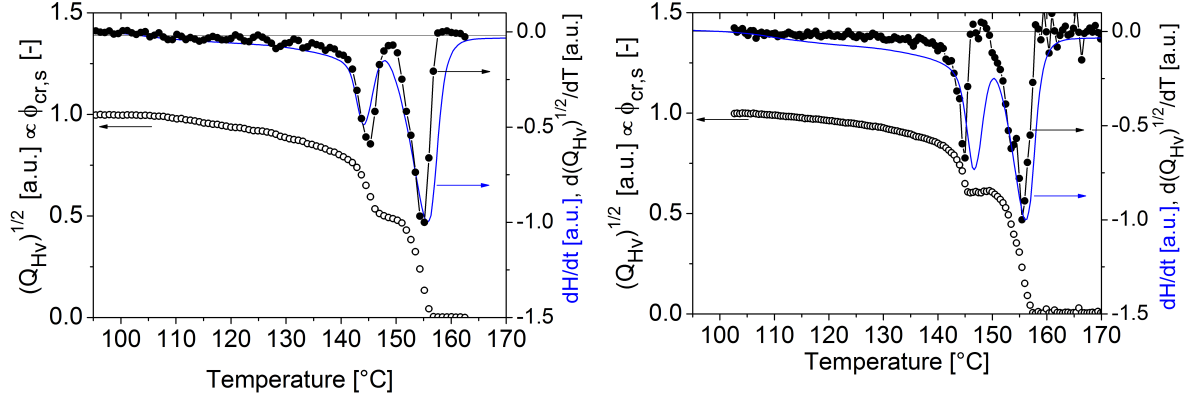


Figure B.9: Normalized square root of the depolarized scattering invariant Q_{HV} (○) of coPLA and its first derivative (●) as a function of temperature in the analytical heating run at a rate of 10 K/min after isothermal crystallization at 95 °C (left) and 100 °C (right) for 30 min. The DSC thermogram (—) was recorded at a rate of 20 K/min after quenching to room temperature (compare FIGURE B.5, see discussion in SUBSECTION 4.5). Exothermic heat flow is in positive ordinate direction.

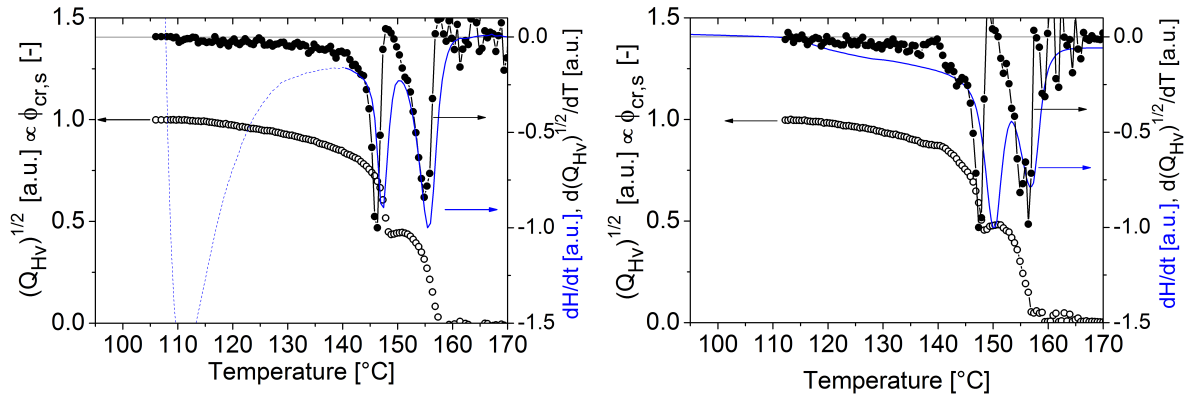


Figure B.10: Normalized square root of the depolarized scattering invariant Q_{HV} (○) of coPLA and its first derivative (●) as a function of temperature in the analytical heating run at a rate of 10 K/min after isothermal crystallization at 105 °C (left) and 110 °C (right) for 30 min. The DSC thermogram (—) was recorded at a rate of 10 K/min immediately after isothermal crystallization (left, $T_c = 105$ °C) and at a rate of 20 K/min after quenching to room temperature (right, $T_c = 110$ °C), respectively (compare FIGURE B.5, see discussion in SUBSECTION 4.5). Exothermic heat flow is in positive ordinate direction.

B. SUPPORTING INFORMATION

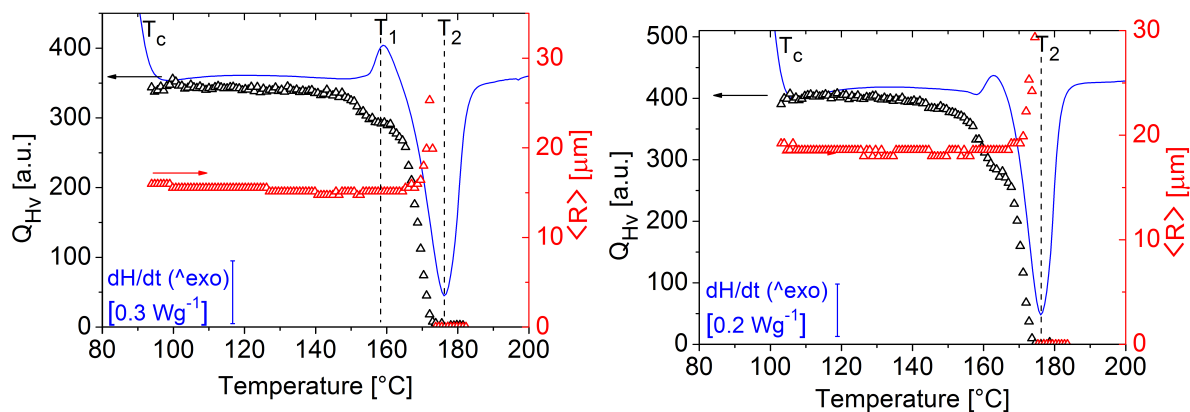


Figure B.11: Average spherulite size (Δ) and depolarized scattering invariant Q_{HV} (Δ) of PDLA as a function of temperature in the analytical heating run at a rate of 10 K/min after isothermal crystallization for 30 min at $T_c = 90^\circ\text{C}$ (left) and $T_c = 100^\circ\text{C}$ (right). The DSC thermogram ($—$) was recorded at a rate of 10 K/min. Exothermic heat flow is in positive ordinate direction.

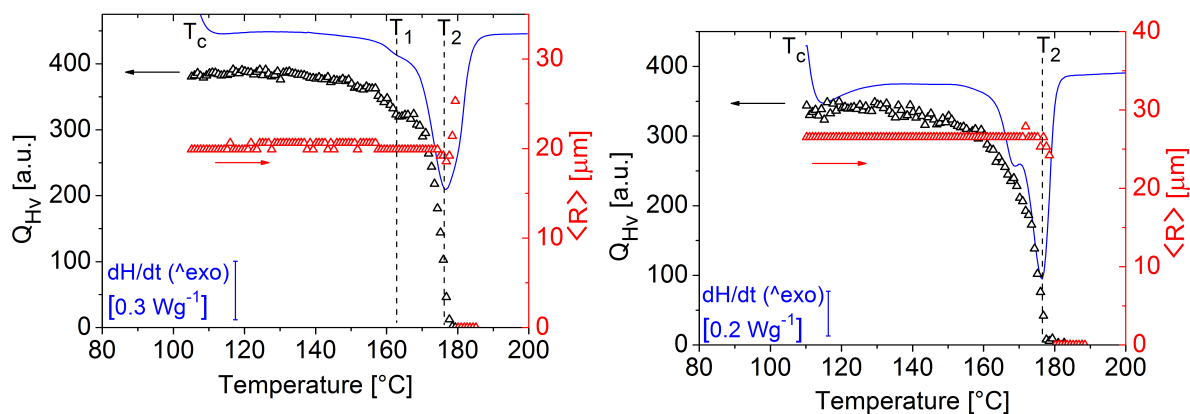


Figure B.12: Average spherulite size (Δ) and depolarized scattering invariant Q_{HV} (Δ) of PDLA as a function of temperature in the analytical heating run at a rate of 10 K/min after isothermal crystallization for 30 min at $T_c = 105^\circ\text{C}$ (left) and $T_c = 110^\circ\text{C}$ (right). The DSC thermogram ($—$) was recorded at a rate of 10 K/min. Exothermic heat flow is in positive ordinate direction.

B. SUPPORTING INFORMATION

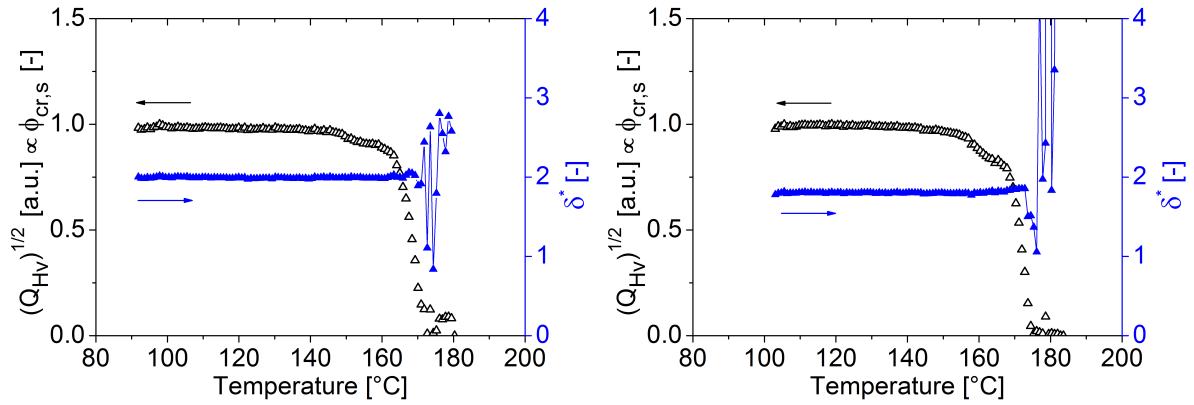


Figure B.13: Normalized square root of the depolarized scattering invariant Q_{HV} (Δ) and relative disorder δ^* (\blacktriangle) of PDLA as a function of temperature in the analytical heating run at a rate of 10 K/min after isothermal crystallization at 90 °C (left) and 100 °C (right) for 30 min.

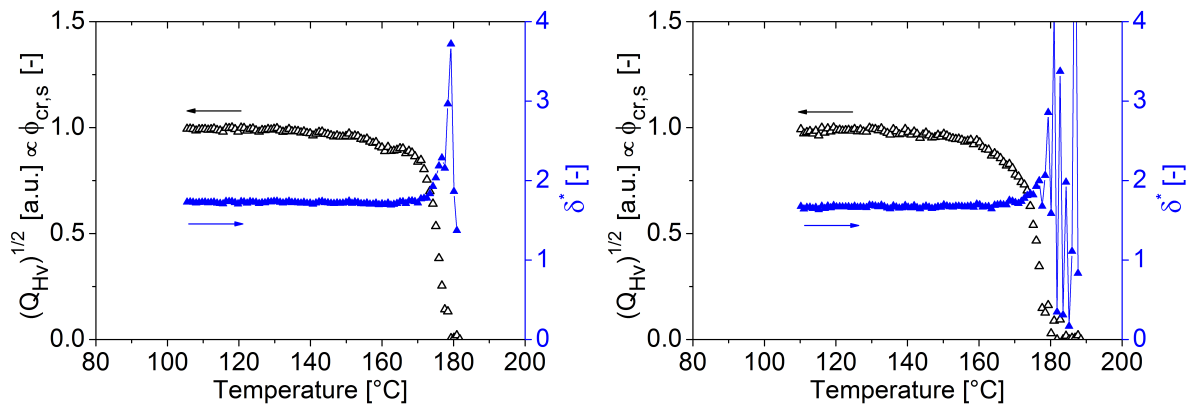


Figure B.14: Normalized square root of the depolarized scattering invariant Q_{HV} (Δ) and relative disorder δ^* (\blacktriangle) of PDLA as a function of temperature in the analytical heating run at a rate of 10 K/min after isothermal crystallization at 105 °C (left) and 110 °C (right) for 30 min.

B. SUPPORTING INFORMATION

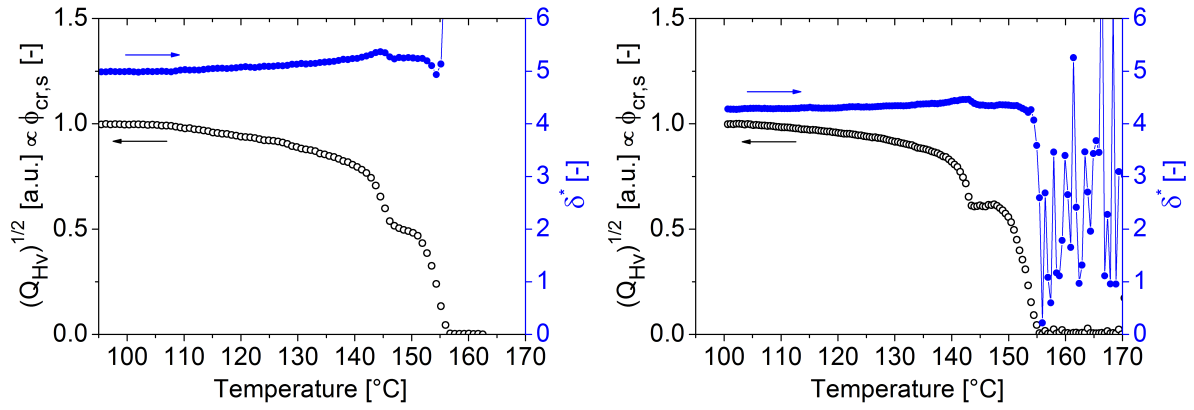


Figure B.15: Normalized square root of the depolarized scattering invariant Q_{HV} (○) and relative disorder δ^* (●) of coPLA as a function of temperature in the analytical heating run at a rate of 10 K/min after isothermal crystallization at 95 °C (left) and 100 °C (right) for 30 min.

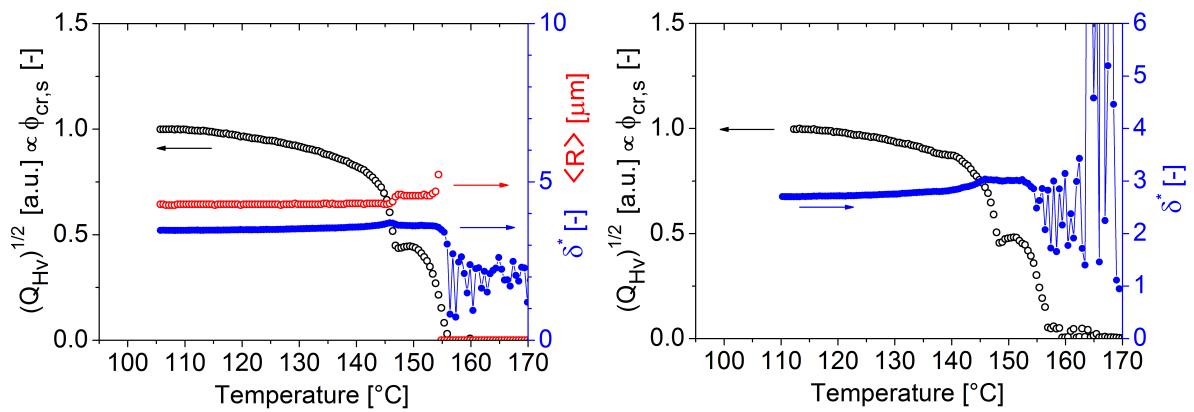


Figure B.16: Normalized square root of the depolarized scattering invariant Q_{HV} (○) and relative disorder δ^* (●) of coPLA as a function of temperature in the analytical heating run at a rate of 10 K/min after isothermal crystallization at 105 °C (left) and 110 °C (right) for 30 min.

C Calculating corrected sums of squares

Welford [210] presents a precise and stable online algorithm for the numerical computation of the unbiased sample variance

$$s_k^2 = \frac{1}{k-1} \sum_{i=1}^k (x_i - \bar{x}_k)^2 \quad (\text{C.1})$$

which is given by the sum of squares of elements x_i corrected by the sample mean \bar{x}_k , where

$$\bar{x}_k = \frac{1}{k} \sum_{i=1}^k x_i = \bar{x}_{k-1} + \frac{x_k - \bar{x}_{k-1}}{k}. \quad (\text{C.2})$$

A recurrence relation for the variance is readily obtained as

$$S_k = (k-1)s_k^2 \quad (\text{C.3})$$

$$= \sum_{i=1}^k (x_i - \bar{x}_k)^2 \quad (\text{C.4})$$

$$= \left(\sum_{i=1}^{k-1} (x_i - \bar{x}_k)^2 \right) + (x_k - \bar{x}_k)^2 \quad (\text{C.5})$$

$$= \left(\sum_{i=1}^{k-1} (x_i - \bar{x}_{k-1} + \bar{x}_{k-1} - \bar{x}_k)^2 \right) + (x_k - \bar{x}_k)^2 \quad (\text{C.6})$$

$$= \left(\sum_{i=1}^{k-1} (x_i - \bar{x}_{k-1})^2 + 2(x_i - \bar{x}_{k-1})(\bar{x}_{k-1} - \bar{x}_k) + (\bar{x}_{k-1} - \bar{x}_k)^2 \right) + (x_k - \bar{x}_k)^2 \quad (\text{C.7})$$

$$= S_{k-1} + (k-1)(\bar{x}_k - \bar{x}_{k-1})^2 + (x_k - \bar{x}_k)^2. \quad (\text{C.8})$$

It is further simplified, i. e. computational steps are reduced, by introducing the auxiliary variables

$$\gamma = \bar{x}_k - \bar{x}_{k-1} \quad (\text{C.9})$$

and (by applying the recurrence relation for the mean EQUATION (C.2))

$$\delta = k\gamma = x_k - \bar{x}_{k-1} \quad (\text{C.10})$$

such that

$$\delta - \gamma = (k-1)\gamma = x_k - \bar{x}_k \quad (\text{C.11})$$

yielding

$$S_k = S_{k-1} + (k-1)\gamma^2 + (k-1)^2\gamma^2 \quad (\text{C.12})$$

$$= S_{k-1} + (x_k - \bar{x}_{k-1})(x_k - \bar{x}_k). \quad (\text{C.13})$$

D List of Figures

2.1	Characteristic structure size L normalized by the wavelength λ applied by light scattering as a function of the scattering angle θ	6
2.2	Basic geometry of a small angle light scattering experiment. Reproduced from [107].	7
2.3	Common optical designs for SALS instruments. Adapted from [112].	8
2.4	Routes for synthesis of PLA from the stereoisomers of lactic acid. With amendments reproduced from [9].	10
2.5	Glass transition temperature T_g of linear PLA as a function of molecular weight and isomer composition and melting temperature T_m of linear PLA with low D-LA content as a function of molecular weight. Reproduced from [3].	12
2.6	Lattice spacing and crystal size based on XRD measurements, and crystalline volume fractions of α' -phases and α -phases. Changes in crystalline morphology of PLLA upon heating simultaneously monitored via DSC and WAXD. Reproduced from [39].	13
2.7	Effect of the heating rate on the melting of α' -crystals and reorganization into α -crystals of PLA with varying D-lactide fraction. Reproduced from [162]. Kinetics of melt-recrystallization of α' -crystals into α -crystals of PLLA. Reproduced from [163].	14
2.8	Primary crystal nuclei density as assessed from spherulite density as a function of the isothermal crystallization temperature for PLA. POM images of isothermally crystallized PLLA. Reproduced from [169].	15
2.9	Dependence of the onset time of isothermal nuclei formation in PLA on temperature and stereo-regularity. Lower critical cooling rates from the PLA melt to below T_g for suppression of crystal growth or of nuclei formation. Reproduced from [170].	16
2.10	Linear radial growth rate $G(T_c)$ of spherulites of PLLA as a function of crystallization temperature T_c . Time of maximum endothermic heat flux during isothermal crystallization as a function of the crystallization temperature. Reproduced from [32].	17
2.11	Spherulite linear radial growth rates as a function of the crystallization temperature. Effect of chain stereoregularity and molecular weight. Reproduced from [33, 34].	18
2.12	Temperature-dependent crystal polymorphism of PLA as a function of the optical purity (i. e. stereoregularity or isotactic sequence length L_L of the chain). Reproduced from [48]	19
2.13	Depolarized SALS scattering patterns and corresponding polarized light microscopy images of isothermally crystallized PLA samples. Modified reproduction from [62].	20
2.14	Evolution of spherulite size and overall relative crystallinity in PLLA crystallized at 90 °C after quenching from the melt as determined by SALS and DRS. Reproduced from [63].	21
2.15	Spherulite size determined by depolarized SALS versus time for neat and plasticized PLA isothermally crystallized at 130 °C after quenching from the melt. Reproduced from [64].	22

2.16	Average spherulite radius as a function of isothermal crystallization time of a PLLA / 1%PDLA mixture crystallized at 100 °C. Radial spherulite growth rates as a function of crystallization temperature T_c determined from SALS and POM. Reproduced from [65].	23
2.17	Depolarized SALS patterns of crystallized racemic PLLA/PDLA blends after prior annealing. Reproduced from [184].	24
2.18	Depolarized SALS patterns of films annealed at various temperatures under high-pressure CO ₂ treatment and annealed under ambient conditions. Reproduced from [185].	25
3.1	Geometry of the scattering problem. Reproduced from [187].	27
3.2	Polar diagram of the angular intensity distribution in the scattering plane for Rayleigh scattering.	30
3.3	Overview of the home-built small angle light scattering instrument.	31
3.4	Overview of the home-built colloidal sample stage for SALS measurements of liquid systems.	33
3.5	Overview of the home-built high temperature sample stage for SALS measurements of polymer melts.	34
3.6	Sketch of the polymer melt stage and the components involved in the temperature-control of the device.	35
3.7	Temperature scale verification of the home-built hotstage.	36
3.8	Temperature dynamics of the home-built polymer melt hotstage ($K_p = 10$, $K_I = 0.1$).	37
3.9	Fourier lens-type detection optics of the SALS instrument.	40
3.10	Image of the test target placed in the Fourier plane of L1 for adjusting magnification and focus of the detector.	41
3.11	Graphical user interface (GUI) of the Basler Pylon camera software suite.	43
3.12	Solid angle $\Delta\Omega$ subtended by a pixel of a two-dimensional detector with respect to the sample position.	45
3.13	Visualization of the averaging process of scattered intensity in azimuthal direction.	46
3.14	Average dark current and background signals of the detector for various exposure times.	48
3.15	Chart depicting data processing.	49
3.16	False-colour image of the pattern generated by the primary beam on the detector imaged at high attenuation and short exposure time with removed beam stop.	51
3.17	Holder for positioning the apertures in the laser beam. Light microscopy of the 50 μm aperture.	52
3.18	False-colour image of the diffraction pattern of the 50 μm aperture and processed diffraction pattern.	52
3.19	Calibration of scattering angles θ . Measured intensity distribution of the aperture with $R = 50 \mu\text{m}$ as a function of diffraction angle compared to the theoretical curve.	53
3.20	The two different lens-cell configurations of the Mastersizer S.	55
3.21	SEM micrograph and particle size distribution determined by measurements with the Malvern Mastersizer S of 5 μm standard latex beads.	57
3.22	SEM micrograph and particle size distribution determined by measurements with the Malvern Mastersizer S of 2 μm standard latex beads.	57

3.23	SEM micrograph and particle size distribution determined by measurements with the Malvern Mastersizer S of 500 nm standard latex beads.	58
3.24	SALS scattering curve of 5 μm standard latex beads dispersed in water compared to theoretical scattering curves based on Lorenz-Mie theory.	59
3.25	SALS scattering curve of 2 μm standard latex beads dispersed in water compared to theoretical scattering curves based on Lorenz-Mie theory.	60
3.26	Polar diagram of the intensities scattered by the standard particles based on Lorenz-Mie theory. Numerical calculations were carried out with MATLAB algorithms from [188].	61
3.27	SALS scattering curve of 500 nm standard latex beads dispersed in water compared to theoretical scattering curves based on Lorenz-Mie theory.	62
3.28	Uncorrected SALS intensities of particle suspensions compared to the respective background signal and typical SALS signals of all three standard suspensions normalized to exposure times.	62
4.1	Temperature-time protocols for SALS measurements of the isothermal spherulite growth rate and SALS characterization of the melting behaviour of PLA after isothermal crystallization.	65
4.2	Sketch of the internal structure of polymeric spherulites. After Boyd <i>et al.</i> in [227].	67
4.3	Two possible orientations of the indicatrix with respect to the spherulite radius direction giving rise to the Maltese cross when viewed under crossed polarizers. Reproduced from [224].	68
4.4	Typical four-lobed H_V pattern from an optically anisotropic spherulite in a depolarized SALS experiment.	69
4.5	Typical four-lobed H_V scattering pattern of spherulites during isothermal crystallization experiments and processed scattering curves (PLLA1).	72
4.6	Exemplary average spherulite radii $\langle R \rangle$ as a function of time and isothermal crystallization temperature. Data-sets are from PLLA2.	73
4.7	Temperature dependent linear radial growth rates $G(T_c)$ of PLLA1 spherulites determined by SALS and POM.	75
4.8	Spherulite linear radial growth rate curves of PLLA1, PLLA2, PDLA and coPLA.	76
4.9	Lauritzen-Hoffman analysis of the spherulite growth rate data of PLLA2.	77
4.10	DSC thermograms of the isothermal crystallization of nPLLA1 and nPLLA2 in comparison to the neat polymers PLLA1 and PLLA2, respectively.	78
4.11	Crystallization peak times during isothermal crystallization of nPLLA1 and nPLLA2 in comparison to the neat polymers PLLA1 and PLLA2, respectively, as a function of crystallization temperature.	79
4.12	Temperature dependent linear radial growth rates of PLLA1 spherulites, stereocomplex nucleated nPLLA1, PLLA2 and stereocomplex nucleated nPLLA2.	80
4.13	Average spherulite size of coPLA and PDLA, and total integrated scattering intensity (invariant Q_{H_V}) during isothermal crystallization at 105 $^{\circ}\text{C}$. Final average spherulite size as a function of isothermal crystallization temperature.	81
4.14	Radial H_V scattering intensity profiles of coPLA during the analytical heating run after isothermal crystallization at $T_c = 105^{\circ}\text{C}$	81

4.15	Average spherulite size, depolarized scattering invariant Q_{HV} and corresponding DSC signal of coPLA during the analytical heating run after isothermal crystallization at $T_c = 105^\circ\text{C}$	83
4.16	Normalized square root of the depolarized scattering invariant Q_{HV} of coPLA, its first derivative and DSC trace during the analytical heating run after isothermal crystallization at $T_c = 105^\circ\text{C}$	85
4.17	Average spherulite size, depolarized scattering invariant Q_{HV} and DSC trace of coPLA during the analytical heating run after isothermal crystallization at $T_c = 105^\circ\text{C}$ and during annealing at 145°C	86
4.18	Average spherulite size, depolarized scattering invariant Q_{HV} and corresponding DSC thermogram of PDLA as a function of temperature in the analytical heating run after isothermal crystallization at (A) $T_c = 105^\circ\text{C}$ and (B) $T_c = 80^\circ\text{C}$ for 30 min.	87
4.19	Average spherulite size, depolarized scattering invariant Q_{HV} and relative disorder parameter δ^* of PDLA as a function of temperature and time in the analytical heating run after isothermal crystallization at $T_c = 80^\circ\text{C}$ and during annealing at 155°C	88
4.20	Average spherulite size, depolarized scattering invariant Q_{HV} and DSC trace of PDLA during the analytical heating run after isothermal crystallization at 80°C and during an analogous experiment with added annealing segment at 155°C	89
4.21	Effect of annealing at 155°C on crystallinity of PDLA after isothermal crystallization at 80°C	90
4.22	Depolarized SALS patterns of nPLLA2 after isothermal crystallization at $T_c = 85^\circ\text{C}$, $T_c = 90^\circ\text{C}$, $T_c = 95^\circ\text{C}$ and $T_c = 100^\circ\text{C}$	92
4.23	Evolution of spherulite radius, integrated scattering intensities and scattering profiles of nPLLA2 during isothermal crystallization at $T_c = 95^\circ\text{C}$	93
4.24	Depolarized scattering invariant Q_+ of nPLLA2 as a function of temperature in the analytical heating run after isothermal crystallization at $T_c = 85^\circ\text{C}$	94
A.1	^{13}C NMR spectra of the methine region and carbonyl region of the polylactide samples.	108
A.2	DSC thermograms of PLLA1 of the analytical heating run after isothermal crystallization at various T_c . Determination of the equilibrium melting temperature T_m^0 of PLLA1 via Hoffman-Weeks analysis.	110
A.3	DSC thermograms of PLLA2 of the analytical heating run after isothermal crystallization at various T_c . Determination of the equilibrium melting temperature T_m^0 of PLLA2 via Hoffman-Weeks analysis.	110
A.4	DSC thermograms of PDLA of the analytical heating run after isothermal crystallization at various T_c . Determination of the equilibrium melting temperature T_m^0 of PDLA via Hoffman-Weeks analysis.	111
A.5	DSC thermograms of coPLA of the analytical heating run after isothermal crystallization at various T_c . Determination of the equilibrium melting temperature T_m^0 of coPLA via Hoffman-Weeks analysis.	111
A.6	Non-isothermal TGA in argon at a heating rate of 5 K/min. Isothermal TGA in synthetic air at various temperatures.	112
B.1	Alignment procedure of the optical components of the home-built SALS instrument.	113

B.2	DSC thermograms of scPLA in the film-casted blends of poly(L-lactide) and poly(D-lactide).	114
B.3	DSC thermograms of nPLLA1 of the analytical heating run after isothermal crystallization at various T_c . Determination of the equilibrium melting temperature T_m^0 of nPLLA1 via Hoffman-Weeks analysis.	115
B.4	DSC thermograms of nPLLA2 of the analytical heating run after isothermal crystallization at various T_c . Determination of the equilibrium melting temperature T_m^0 of nPLLA2 via Hoffman-Weeks analysis.	115
B.5	Effect of the temperature-time protocol on the thermograms of the DSC analytical heating runs after isothermal crystallization of coPLA and PDLA.	116
B.6	Melting peak temperatures T_1 and T_2 of coPLA and PDLA, respectively.	116
B.7	Average spherulite size, depolarized scattering invariant Q_{H_V} and DSC trace of coPLA as a function of temperature in the analytical heating run after isothermal crystallization at $T_c = 95^\circ\text{C}$ and $T_c = 100^\circ\text{C}$	117
B.8	Average spherulite size, depolarized scattering invariant Q_{H_V} and DSC trace of coPLA as a function of temperature in the analytical heating run after isothermal crystallization at $T_c = 105^\circ\text{C}$ and $T_c = 110^\circ\text{C}$	117
B.9	Change in crystallinity of coPLA during analytical heating determined by SALS and DSC isothermally crystallized at 95°C and 100°C	118
B.10	Change in crystallinity of coPLA during analytical heating determined by SALS and DSC isothermally crystallized at 105°C and 110°C	118
B.11	Average spherulite size and depolarized scattering invariant Q_{H_V} of PDLA as a function of temperature in the analytical heating run after isothermal crystallization at $T_c = 90^\circ\text{C}$ and $T_c = 100^\circ\text{C}$	119
B.12	Average spherulite size and depolarized scattering invariant Q_{H_V} of PDLA as a function of temperature in the analytical heating run after isothermal crystallization at $T_c = 105^\circ\text{C}$ and $T_c = 110^\circ\text{C}$	119
B.13	Normalized square root of the depolarized scattering invariant and relative disorder of PDLA during heating after isothermal crystallization at 90°C and 100°C	120
B.14	Normalized square root of the depolarized scattering invariant and relative disorder of PDLA during heating after isothermal crystallization at 105°C and 110°C	120
B.15	Normalized square root of the depolarized scattering invariant and relative disorder of coPLA during heating after isothermal crystallization at 95°C and 100°C	121
B.16	Normalized square root of the depolarized scattering invariant and relative disorder of coPLA during heating after isothermal crystallization at 105°C and 110°C	121

E List of Tables

3.1	Thermal properties of materials used for temperature-dependent experiments.	38
3.2	Particle size values of the standard latex beads utilized for benchmarking the home-built SALS instrument as verified by various methods.	58
4.1	Properties of the polylactide samples used in the studies of the phase transformation behaviour of PLA.	64
A.1	Polymer properties of the polylactide samples used in this work.	105
A.2	Stereo-isomer composition of the polylactide samples as determined by polarimetry. . .	107
A.3	Stereo-isomer composition of the polylactide samples as determined by NMR spectroscopy.	109

F Bibliography

- [1] Rafael Auras, Loong-Tak Lim, Susan E. M. Selke, and Hideto Tsuji. *Poly(Lactic Acid)*. John Wiley & Sons, Inc, Hoboken, NJ, USA, 2010.
- [2] Hideto Tsuji, Ryota Ozawa, and Nobutsugu Matsumura. Effect of incorporated star-shaped four-armed stereo diblock poly(lactide) on the crystallization behavior of linear one-armed poly(l-lactide) or poly(d-lactide). *Polymer Journal*, 48(2):209–213, 2015.
- [3] Sajjad Saeidlou, Michel A. Huneault, Hongbo Li, and Chul B. Park. Poly(lactic acid) crystallization. *Progress in Polymer Science*, 37(12):1657–1677, 2012.
- [4] Cornelis A. P. Joziassse, Harm Veenstra, Dirk W. Grijpma, and Albert J. Pennings. On the chain stiffness of poly(lactide)s. *Macromolecular Chemistry and Physics*, 197(7):2219–2229, 1996.
- [5] Kelly S. Anderson and Marc A. Hillmyer. Melt chain dimensions of polylactide. *Macromolecules*, 37(5):1857–1862, 2004.
- [6] A. P. Gupta and Vimal Kumar. New emerging trends in synthetic biodegradable polymers – polylactide: A critique. *European Polymer Journal*, 43(10):4053–4074, 2007.
- [7] Md. Hafezur Rahaman and Hideto Tsuji. Isothermal crystallization and spherulite growth behavior of stereo multiblock poly(lactic acid)s: Effects of block length. *Journal of Applied Polymer Science*, 129(5):2502–2517, 2013.
- [8] Love-Ese Chile, Parisa Mehrkhodavandi, and Savvas G. Hatzikiriakos. A comparison of the rheological and mechanical properties of isotactic, syndiotactic, and heterotactic poly(lactide). *Macromolecules*, 49(3):909–919, 2016.
- [9] E. Castro-Aguirre, F. Iniguez-Franco, H. Samsudin, X. Fang, and R. Auras. Poly(lactic acid) - mass production, processing, industrial applications, and end of life. *Advanced Drug Delivery Reviews*, 107:333–366, 2016.
- [10] Lidong Feng, Xinchao Bian, Zhiming Chen, Sheng Xiang, Yanlong Liu, Bin Sun, Gao Li, and Xuesi Chen. Determination of d-lactide content in lactide stereoisomeric mixture using gas chromatography-polarimetry. *Talanta*, 164:268–274, 2017.
- [11] Nanou Peelman, Peter Ragaert, Kim Ragaert, Bruno de Meulenaer, Frank Devlieghere, and Ludwig Cardon. Heat resistance of new biobased polymeric materials, focusing on starch, cellulose, pla, and pha. *Journal of Applied Polymer Science*, 132(48):42305, 2015.
- [12] Felice de Santis, Valentina Volpe, and Roberto Pantani. Effect of molding conditions on crystallization kinetics and mechanical properties of poly(lactic acid). *Polymer Engineering & Science*, 57(3):306–311, 2017.
- [13] Longfei Yi, Junrong Zhang, Jiyu Yang, Furong Sun, Huan Zhang, and Lijuan Zhao. Effect of annealing induced crystalline evolution on the scratch resistance of polylactide. *Tribology International*, 128:328–336, 2018.
- [14] Dongyu Bai, Huili Liu, Hongwei Bai, Qin Zhang, and Qiang Fu. Powder metallurgy inspired low-temperature fabrication of high-performance stereocomplexed polylactide products with good optical transparency. *Scientific reports*, 6:20260, 2016.
- [15] Naruki Kurokawa and Atsushi Hotta. Thermomechanical properties of highly transparent self-reinforced polylactide composites with electrospun stereocomplex polylactide nanofibers. *Polymer*, 153:214–222, 2018.
- [16] B. Kalb and A. J. Pennings. General crystallization behaviour of poly(l-lactic acid). *Polymer*, 21(6):607–612, 1980.
- [17] Jeffrey J. Kolstad. Crystallization kinetics of poly(l-lactide-co-meso-lactide). *Journal of Applied Polymer Science*, 62(7):1079–1091, 1996.
- [18] Hideto Tsuji and Yoshito Ikada. Crystallization from the melt of poly(lactide)s with different optical purities and their blends. *Macromolecular Chemistry and Physics*, 197(10):3483–3499, 1996.
- [19] Jiang Huang, Melissa S. Lisowski, James Runt, Eric S. Hall, Robert T. Kean, Nancy Buehler, and J. S. Lin. Crystallization and microstructure of poly(l-lactide-co-meso-lactide) copolymers. *Macromolecules*, 31(8):2593–2599, 1998.

F. BIBLIOGRAPHY

- [20] Tadakazu Miyata and Toru Masuko. Crystallization behaviour of poly(l-lactide). *Polymer*, 39(22):5515–5521, 1998.
- [21] Jose-Ramon Sarasua, Robert E. Prud'homme, Muriel Wisniewski, Alain Le Borgne, and Nicolas Spassky. Crystallization and melting behavior of polylactides. *Macromolecules*, 31(12):3895–3905, 1998.
- [22] S. Baratian, E. S. Hall, J. S. Lin, R. Xu, and J. Runt. Crystallization and solid-state structure of random polylactide copolymers: Poly(l-lactide-co-d-lactide)s. *Macromolecules*, 34(14):4857–4864, 2001.
- [23] Maria Laura Di Lorenzo and Rene Androsch, editors. *Synthesis, Structure and Properties of Poly(lactic acid)*. Advances in Polymer Science. Springer International Publishing, Cham, 1st edition 2018 edition, 2018.
- [24] W. Hoogsteen, A. R. Postema, A. J. Pennings, Gerrit ten Brinke, and P. Zugenmaier. Crystal structure, conformation and morphology of solution-spun poly(l-lactide) fibers. *Macromolecules*, 23(2):634–642, 1990.
- [25] L. Cartier, T. Okihara, Y. Ikada, H. Tsuji, J. Puiggali, and B. Lotz. Epitaxial crystallization and crystalline polymorphism of polylactides. *Polymer*, 41(25):8909–8919, 2000.
- [26] Bernard Lotz, Gao Li, Xuesi Chen, and Jordi Puiggali. Crystal polymorphism of polylactides and poly(pro-alt-co): The metastable beta and gamma phases. formation of homochiral plla phases in the plla/pdla blends. *Polymer*, 115:204–210, 2017.
- [27] Yoshito Ikada, Khosrow Jamshidi, Hideto Tsuji, and Suong Hyu Hyon. Stereocomplex formation between enantiomeric poly(lactides). *Macromolecules*, 20(4):904–906, 1987.
- [28] R. Vasanthakumari and A. J. Pennings. Crystallization kinetics of poly(l-lactic acid). *Polymer*, 24(2):175–178, 1983.
- [29] René Androsch, H. NaeemM. Iqbal, and Christoph Schick. Non-isothermal crystal nucleation of poly (l-lactic acid). *Polymer*, 81:151–158, 2015.
- [30] Maria Laura Di Lorenzo. Determination of spherulite growth rates of poly(l-lactic acid) using combined isothermal and non-isothermal procedures. *Polymer*, 42(23):9441–9446, 2001.
- [31] Maria Laura Di Lorenzo. Crystallization behavior of poly(l-lactic acid). *European Polymer Journal*, 41(3):569–575, 2005.
- [32] Munehisa Yasuniwa, Shinsuke Tsubakihara, Koji Iura, Yoshinori Ono, Yusuke Dan, and Kazuhisa Takahashi. Crystallization behavior of poly(l-lactic acid). *Polymer*, 47(21):7554–7563, 2006.
- [33] Maria Laura Di Lorenzo, Paolo Rubino, Romain Luijkx, and Marion Hérou. Influence of chain structure on crystal polymorphism of poly(lactic acid). part 1: Effect of optical purity of the monomer. *Colloid & Polymer Science*, 292(2):399–409, 2014.
- [34] Maria Laura Di Lorenzo, Paolo Rubino, Barbara Immirzi, Romain Luijkx, Marion Hérou, and René Androsch. Influence of chain structure on crystal polymorphism of poly(lactic acid). part 2. effect of molecular mass on the crystal growth rate and semicrystalline morphology. *Colloid & Polymer Science*, 293(9):2459–2467, 2015.
- [35] Munehisa Yasuniwa, Koji Iura, and Yusuke Dan. Melting behavior of poly(l-lactic acid): Effects of crystallization temperature and time. *Polymer*, 48(18):5398–5407, 2007.
- [36] Yong He, Zhongyong Fan, Yanfei Hu, Tong Wu, Jia Wei, and Suming Li. Dsc analysis of isothermal melt-crystallization, glass transition and melting behavior of poly(l-lactide) with different molecular weights. *European Polymer Journal*, 43(10):4431–4439, 2007.
- [37] Tai-Yon Cho and Gert Strobl. Temperature dependent variations in the lamellar structure of poly(l-lactide). *Polymer*, 47(4):1036–1043, 2006.
- [38] Pengju Pan, Weihua Kai, Bo Zhu, Tungalag Dong, and Yoshio Inoue. Polymorphous crystallization and multiple melting behavior of poly(l-lactide): Molecular weight dependence. *Macromolecules*, 40(19):6898–6905, 2007.
- [39] Jianming Zhang, Kohji Tashiro, Hideto Tsuji, and Abraham J. Domb. Disorder-to-order phase transition and multiple melting behavior of poly(l-lactide) investigated by simultaneous measurements of waxd and dsc. *Macromolecules*, 41(4):1352–1357, 2008.

F. BIBLIOGRAPHY

- [40] G. Hauser, J. Schmidtke, and G. Strobl. The role of co-units in polymer crystallization and melting: New insights from studies on syndiotactic poly(propene-co-octene). *Macromolecules*, 31(18):6250–6258, 1998.
- [41] Zhi-Gang Wang, Xue-Hui Wang, Benjamin S. Hsiao, Roger A. Phillips, Francisco J. Medellin-Rodriguez, Srivatsan Srinivas, Howard Wang, and Charles C. Han. Structure and morphology development in syndiotactic polypropylene during isothermal crystallization and subsequent melting. *Journal of Polymer Science Part B: Polymer Physics*, 39(23):2982–2995, 2001.
- [42] Barbara Heck, Silvia Siegenführ, Gert Strobl, and Ralf Thomann. A law controlling polymer recrystallization showing up in experiments on s-polypropylene. *Polymer*, 48(5):1352–1359, 2007.
- [43] M. Al-Hussein and G. Strobl. The mechanisms of recrystallization after melting in syndiotactic polypropylene and isotactic polystyrene. *The European Physical Journal E*, 6(4):305–314, 2001.
- [44] Ying Lu, Yaotao Wang, Ran Chen, and Yongfeng Men. Crystallization and melting of isotactic polypropylene crystallized from quiescent melt and stress-induced localized melt. *Journal of Polymer Science Part B: Polymer Physics*, 55(12):957–963, 2017.
- [45] Zhenzhen Zhou, Le Ma, Weiwei Zhen, Xiaoli Sun, Zhongjie Ren, Huihui Li, and Shouke Yan. An abnormal melting behavior of isotactic polypropylene spherulites grown at low temperatures. *Polymer*, 111:183–191, 2017.
- [46] J. Schmidtke, G. Strobl, and T. Thurn-Albrecht. A four-state scheme for treating polymer crystallization and melting suggested by calorimetric and small angle x-ray scattering experiments on syndiotactic polypropylene. *Macromolecules*, 30(19):5804–5821, 1997.
- [47] Jianming Zhang, Yongxin Duan, Harumi Sato, Hideto Tsuji, Isao Noda, Shouke Yan, and Yukihiro Ozaki. Crystal modifications and thermal behavior of poly(l-lactic acid) revealed by infrared spectroscopy. *Macromolecules*, 38(19):8012–8021, 2005.
- [48] Ping Song, Lin Sang, Chenhao Jin, and Zhiyong Wei. Temperature-dependent polymorphic crystallization of poly(l-lactide)s on the basis of optical purity and microstructure. *Polymer*, 134:163–174, 2018.
- [49] Takahiko Kawai, Nelly Rahman, Go Matsuba, Koji Nishida, Toshiji Kanaya, Mitsuru Nakano, Hirotaka Okamoto, Jumpei Kawada, Arimitsu Usuki, Nobutaka Honma, Katsuhiko Nakajima, and Masatoshi Matsuda. Crystallization and melting behavior of poly(l-lactic acid). *Macromolecules*, 40(26):9463–9469, 2007.
- [50] Jian Hu, Jiping Wang, E. Bhoje Gowd, Yuan Yuan, Tongping Zhang, Yongxin Duan, Wenbing Hu, and Jianming Zhang. Small- and wide-angle x-ray scattering study on α' -to- α transition of poly(l-lactide acid) crystals. *Polymer*, 167:122–129, 2019.
- [51] K. Kishore, R. Vasanthakumari, and A. J. Pennings. Isothermal melting behavior of poly(l-lactic acid). *Journal of Polymer Science: Polymer Physics Edition*, 22(4):537–542, 1984.
- [52] Richard S. Stein and Marion B. Rhodes. Photographic light scattering by polyethylene films. *Journal of Applied Physics*, 31(11):1873–1884, 1960.
- [53] R. J. Tabar, P. Leite-James, and R. S. Stein. Quantitative small-angle light scattering studies of the melting of poly(ethylene terephthalate). *Journal of Polymer Science: Polymer Physics Edition*, 23(10):2085–2107, 1985.
- [54] Peter Erhardt, K. Sasaguri, and R. S. Stein. Studies of rates of spherulite deformation by low-angle light scattering. *Journal of Polymer Science Part C: Polymer Symposia*, 5(1):179–190, 1964.
- [55] Even Lemieux and Robert E. Prud'homme. Crystallization and morphology of isotactic poly(methyl methacrylates). *Polymer Bulletin*, 21(6):621–626, 1989.
- [56] Wayne T. Culberson and Martin R. Tant. A device for study of polymer crystallization kinetics via real-time image analysis of small angle light scattering. *Journal of Applied Polymer Science*, 47(3):395–405, 1993.
- [57] G. Schlatter, C. Serra, M. Bouquey, R. Muller, and J. Terrisse. Online light scattering measurements: A method to assess morphology development of polymer blends in a twin-screw extruder. *Polymer Engineering & Science*, 42(10):1965–1975, 2002.

F. BIBLIOGRAPHY

- [58] Yvonne A. Akpalu and Youyu Lin. Multivariable structural characterization of semicrystalline polymer blends by small-angle light scattering. *Journal of Polymer Science Part B: Polymer Physics*, 40(23):2714–2727, 2002.
- [59] B. Yalcin and M. Cakmak. Superstructural hierarchy developed in coupled high shear/high thermal gradient conditions of injection molding in nylon 6 nanocomposites. *Polymer*, 45(8):2691–2710, 2004.
- [60] Karin Bernland, J. G. P. Goossens, Paul Smith, and Theo A. Tervoort. On clarification of haze in polypropylene. *Journal of Polymer Science Part B: Polymer Physics*, 54(9):865–874, 2016.
- [61] Nan Chen, Xuerong Yao, Cui Zheng, Yujing Tang, Minqiao Ren, Yi Ren, Meifang Guo, Shijun Zhang, and Li-Zhi Liu. Study on the miscibility, crystallization and crystalline morphology of polyamide-6/polyvinylidene fluoride blends. *Polymer*, 124:30–40, 2017.
- [62] Miroslaw Pluta and Andrzej Galeski. Crystalline and supermolecular structure of polylactide in relation to the crystallization method. *Journal of Applied Polymer Science*, 86(6):1386–1395, 2002.
- [63] Benjamin D. Fitz and Saša Andjelić. Real-time monitoring of segmental dynamics during crystallization of poly(l(-)-lactide) by simultaneous drs/sals technique. *Polymer*, 44(10):3031–3036, 2003.
- [64] Z. Kulinski and E. Piorkowska. Crystallization, structure and properties of plasticized poly(l-lactide). *Polymer*, 46(23):10290–10300, 2005.
- [65] P. J. A. Lohmeijer, J. G. P. Goossens, and G. W. M. Peters. Quiescent crystallization of poly(lactic acid) studied by optical microscopy and light-scattering techniques. *Journal of Applied Polymer Science*, 134(10):37, 2017.
- [66] Bruce J. Berne and Robert Pecora. *Dynamic Light Scattering: With Applications to Chemistry, Biology, and Physics*. Dover Books on Physics. Dover Publications, Newburyport, 2013.
- [67] John Tyndall. On the blue color of the sky, the polarization of sky light, and on the polarization of light by cloudy matter generally. *Phil. Mag.*, 37:384–394, 1869.
- [68] John Tyndall. Notes on the formation and phenomena of clouds. *Phil. Mag.*, 38:156–158, 1869.
- [69] J. W. Rayleigh. On the scattering of light by small particles. *Phil. Mag.*, 41(275):447–454, 1871.
- [70] J. W. Rayleigh. On the transmission of light through an atmosphere containing small particles in suspension, and on the origin of the blue of the sky. *Phil. Mag.*, 47(287):375, 1899.
- [71] L. Rayleigh. On the scattering of light by spherical shells, and by complete spheres of periodic structure, when the refractivity is small. *Proceedings of the Royal Society A: Mathematical, Physical and Engineering Sciences*, 94(660):296–300, 1918.
- [72] P. Debye. Der lichtdruck auf kugeln von beliebigem material. *Annalen der Physik*, 335(11):57–136, 1909.
- [73] P. Debye. Zerstreung von röntgenstrahlen. *Annalen der Physik*, 351(6):809–823, 1915.
- [74] Richard Gans. Die molekulare lichtzerstreuung in festen isotropen körpern und flüssigkeiten. *Annalen der Physik*, 382(11):317–324, 1925.
- [75] Gustav Mie. Beiträge zur optik trüber medien, speziell kolloidaler metallösungen. *Annalen der Physik*, 330(3):377–445, 1908.
- [76] Ludvig Lorenz. Lysbevaegelsen i og uden for en af plane lysbolger belyst kugle. *Videnskab. Selskab. Skrifter.*, 6(6):1–62, 1890.
- [77] M. v. Smoluchowski. Molekular-kinetische theorie der opaleszenz von gasen im kritischen zustande, sowie einiger verwandter erscheinungen. *Annalen der Physik*, 330(2):205–226, 1908.
- [78] A. Einstein. Theorie der opaleszenz von homogenen flüssigkeiten und flüssigkeitsgemischen in der nähe des kritischen zustandes. *Annalen der Physik*, 338(16):1275–1298, 1910.
- [79] Bruno H. Zimm. Apparatus and methods for measurement and interpretation of the angular variation of light scattering; preliminary results on polystyrene solutions. *The Journal of Chemical Physics*, 16(12):1099–1116, 1948.
- [80] Paul J. Flory. The configuration of real polymer chains. *The Journal of Chemical Physics*, 17(3):303–310, 1949.

F. BIBLIOGRAPHY

- [81] Eric J. Roth, Michael E. Mont-Eton, Benjamin Gilbert, Tim C. Lei, and David C. Mays. Measurement of colloidal phenomena during flow through refractive index matched porous media. *The Review of scientific instruments*, 86(11):113103, 2015.
- [82] S. Tang. Prediction of fractal properties of polystyrene aggregates. *Colloids and Surfaces A: Physicochemical and Engineering Aspects*, 157(1-3):185–192, 1999.
- [83] Jürgen Schmidtke, Werner Stille, and Gert Strobl. Static and dynamic light scattering of a nematic side-group polysiloxane. *Macromolecules*, 33(8):2922–2928, 2000.
- [84] Franz J. T. Huber, Michael Altenhoff, and Stefan Will. A mobile system for a comprehensive online-characterization of nanoparticle aggregates based on wide-angle light scattering and laser-induced incandescence. *The Review of scientific instruments*, 87(5):053102, 2016.
- [85] Andreas Aschinger and Jörg Winter. The application of dynamic light scattering to complex plasmas. *New Journal of Physics*, 14(9):093035, 2012.
- [86] John Gilmer, Niel Goldstein, and Richard S. Stein. Light-scattering studies of phase-demixing of polystyrene/poly(o-chlorostyrene) blends. *Journal of Polymer Science: Polymer Physics Edition*, 20(12):2219–2227, 1982.
- [87] Takeji Hashimoto, Jiro Kumaki, and Hiromichi Kawai. Time-resolved light scattering studies on kinetics of phase separation and phase dissolution of polymer blends. 1. kinetics of phase separation of a binary mixture of polystyrene and poly(vinyl methyl ether). *Macromolecules*, 16(4):641–648, 1983.
- [88] P. Guenoun, R. Gastaud, F. Perrot, and D. Beysens. Spinodal decomposition patterns in an iso-density critical binary fluid: Direct-visualization and light-scattering analyses. *Physical Review A*, 36(10):4876–4890, 1987.
- [89] Z.-Y. Wang, M. Konno, and S. Saito. Small-angle light scattering of phase separation structures in polymer blends. *The Journal of Chemical Physics*, 90(2):1281–1284, 1989.
- [90] J. T. Cabral, J. S. Higgins, T. C. B. McLeish, S. Strausser, and S. N. Magonov. Bulk spinodal decomposition studied by atomic force microscopy and light scattering. *Macromolecules*, 34(11):3748–3756, 2001.
- [91] Yvonne A. Akpalu and Ping Peng. Probing the melt miscibility of a commercial polyethylene blend by small-angle light scattering. *Materials and Manufacturing Processes*, 23(3):269–276, 2008.
- [92] Juan Sabin, Arthur E. Bailey, and Barbara J. Frisken. Exploring the dynamics of phase separation in colloid-polymer mixtures with long range attraction. *Soft matter*, 12(24):5325–5333, 2016.
- [93] Jaroslav Holoubek. Some applications of light scattering in materials science. *Journal of Quantitative Spectroscopy and Radiative Transfer*, 106(1-3):104–121, 2007.
- [94] Xiao Liu, Xianming Dong, Ying Xiong, Ping Yi, Yikun Ren, and Shaoyun Guo. Light scattering materials with tunable optical properties by controlling refractive index of the dispersed phase. *Journal of Applied Polymer Science*, 133(43):2927, 2016.
- [95] Benjamin Chu. *Laser light scattering: Basic principles and practice*. Academic Press, Boston, 2nd ed. edition, 1991.
- [96] Milton Kerker and Ernest M. Loeb. *The Scattering of Light and Other Electromagnetic Radiation: Physical Chemistry: A Series of Monographs*. Elsevier Science, Burlington, 1969.
- [97] Y. Akpalu, L. Kielhorn, B. S. Hsiao, R. S. Stein, T. P. Russell, J. van Egmond, and M. Muthukumar. Structure development during crystallization of homogeneous copolymers of ethene and 1-octene: Time-resolved synchrotron x-ray and sals measurements. *Macromolecules*, 32(3):765–770, 1999.
- [98] Manabu Tsuburaya and Hiromu Saito. Crystallization of polycarbonate induced by spinodal decomposition in polymer blends. *Polymer*, 45(3):1027–1032, 2004.
- [99] H. Fukushima, Y. Ogino, G. Matsuba, K. Nishida, and T. Kanaya. Crystallization of polyethylene under shear flow as studied by time resolved depolarized light scattering. effects of shear rate and shear strain. *Polymer*, 46(6):1878–1885, 2005.
- [100] C. Picot, R. S. Stein, M. Motegi, and H. Kawai. Small-angle light scattering by random assemblies of incomplete spherulites. i. sheaflike textures. *Journal of Polymer Science Part A-2: Polymer Physics*, 8(12):2115–2126, 1970.

F. BIBLIOGRAPHY

- [101] R. E. Prud'homme, D. Yoon, and R. S. Stein. Scattering of light from spherulitic polymers: Effect of internal structure. *Journal of Polymer Science Part A-2: Polymer Physics*, 11(6):1047–1054, 1973.
- [102] Takeji Hashimoto, Akira Todo, and Hiromichi Kawai. Light scattering from tilted two-dimensional spherulites. *Journal of Polymer Science Part A-2: Polymer Physics*, 11(1):149–173, 1973.
- [103] Do Yeung Yoon and Richard S. Stein. Effect of interference between anisotropic scattering entities on light scattering from polymer films. ii. the correlation function approach. *Journal of Polymer Science: Polymer Physics Edition*, 12(4):735–761, 1974.
- [104] Robert J. Samuels. Small-angle light scattering and crystallization processes in solid polymer films. *Journal of Polymer Science: Polymer Physics Edition*, 12(7):1417–1439, 1974.
- [105] Masaru Matsuo, Shunji Nomura, Takeji Hashimoto, and Hiromichi Kawai. Light scattering from a random assembly of anisotropic plates in two- and three-dimensional space. *Polymer Journal*, 6(2):151–164, 1974.
- [106] R. S. Stein and John J. Keane. The scattering of light from thin polymer films. i. experimental procedure. *Journal of Polymer Science*, 17(83):21–44, 1955.
- [107] J. Koberstein, T. P. Russell, and R. S. Stein. Total integrated light-scattering intensity from polymeric solids. *Journal of Polymer Science: Polymer Physics Edition*, 17(10):1719–1730, 1979.
- [108] Masahiko Motegi, Takashi Oda, Masahiko Moritani, and Hiromichi Kawai. Light-scattering patterns from polyethylene films in relation to spherulitic crystalline texture. *Polymer Journal*, 1(2):209–221, 1970.
- [109] V. G. Baranov. Small angle light scattering by ordered polymer solutions. *Discussions of the Faraday Society*, 49:137, 1970.
- [110] Takeji Hashimoto, Kouji Sasaki, and Hiromichi Kawai. Time-resolved light scattering studies on the kinetics of phase separation and phase dissolution of polymer blends. 2. phase separation of ternary mixtures of polymer a, polymer b, and solvent. *Macromolecules*, 17(12):2812–2818, 1984.
- [111] S. Li, K. B. Migler, E. K. Hobbie, H. Kramer, C. C. Han, and E. J. Amis. Light-scattering photometer with optical microscope for the in-line study of polymer extrusion. *Journal of Polymer Science Part B: Polymer Physics*, 35(17):2935–2943, 1997.
- [112] E. Tamborini and L. Cipelletti. Multiangle static and dynamic light scattering in the intermediate scattering angle range. *The Review of scientific instruments*, 83(9):093106, 2012.
- [113] Richard S. Stein, Jens Cronauer, and H. G. Zachmann. Real time scattering measurements of the crystallization of polymers and their blends. *Journal of Molecular Structure*, 383(1-3):19–22, 1996.
- [114] Brian Richard Pauw. Everything saxs: Small-angle scattering pattern collection and correction. *Journal of physics. Condensed matter : an Institute of Physics journal*, 25(38):383201, 2013.
- [115] Howard G. Barth. *Modern methods of particle size analysis*, volume 13 of *Chemical analysis*. Wiley, New York usw., 1984.
- [116] Tatsuo Igushi and Yoshiaki Togawa. Apparatus for measuring a particle size distribution, 1991.
- [117] Takeshi Niwa. Device and method for determining the particle size distribution, 1993.
- [118] Ananth Annapragada and Akwete Adjei. An analysis of the fraunhofer diffraction method for particle size distribution analysis and its application to aerosolized sprays. *International Journal of Pharmaceutics*, 127(2):219–227, 1996.
- [119] R. J. Tabar, R. S. Stein, and M. B. Long. A two-dimensional position-sensitive detector for small-angle light scattering. *Journal of Polymer Science: Polymer Physics Edition*, 20(11):2041–2049, 1982.
- [120] Moonhor Ree, Thein Kyu, and Richard S. Stein. Quantitative small-angle light-scattering studies of the melting and crystallization of lldpe/ldpe blends. *Journal of Polymer Science Part B: Polymer Physics*, 25(1):105–126, 1987.
- [121] Tetsuo Okada, Hiromu Saito, and Takashi Inoue. Time-resolved light scattering studies on the early stage of crystallization in isotactic polypropylene. *Macromolecules*, 25(7):1908–1911, 1992.
- [122] Koji Nishida, Hiroki Ogawa, Go Matsuba, Takashi Konishi, and Toshiji Kanaya. A high-resolution small-angle light scattering instrument for soft matter studies. *Journal of applied crystallography*, 41(4):723–728, 2008.

F. BIBLIOGRAPHY

- [123] Marcela Alexander and F. Ross Hallett. Small-angle light scattering: Instrumental design and application to particle sizing. *Applied optics*, 38(19):4158, 1999.
- [124] Fabio Ferri. Use of a charge coupled device camera for low-angle elastic light scattering. *Review of Scientific Instruments*, 68(6):2265–2274, 1997.
- [125] T. Kawai and G. Strobl. Crystallization mechanism of syndiotactic polypropylene analyzed by time-dependent light scattering. *Macromolecules*, 37(6):2249–2255, 2004.
- [126] David Lee, Iris A. Gutowski, Arthur E. Bailey, Laurent Rubatat, John R. de Bruyn, and Barbara J. Frisken. Investigating the microstructure of a yield-stress fluid by light scattering. *Physical review. E, Statistical, nonlinear, and soft matter physics*, 83(3 Pt 1):031401, 2011.
- [127] Luca Cipelletti and D. A. Weitz. Ultralow-angle dynamic light scattering with a charge coupled device camera based multispeckle, multitau correlator. *Review of Scientific Instruments*, 70(8):3214–3221, 1999.
- [128] L.-T. Lim, R. Auras, and M. Rubino. Processing technologies for poly(lactic acid). *Progress in Polymer Science*, 33(8):820–852, 2008.
- [129] Majid Jamshidian, Elmira Arab Tehrani, Muhammad Imran, Muriel Jacquot, and Stéphane Desobry. Poly-lactic acid: Production, applications, nanocomposites, and release studies. *Comprehensive Reviews in Food Science and Food Safety*, 9(5):552–571, 2010.
- [130] Shady Farah, Daniel G. Anderson, and Robert Langer. Physical and mechanical properties of pla, and their functions in widespread applications - a comprehensive review. *Advanced Drug Delivery Reviews*, 107:367–392, 2016.
- [131] Rafael Auras, Bruce Harte, and Susan Selke. An overview of polylactides as packaging materials. *Macromolecular bioscience*, 4(9):835–864, 2004.
- [132] Hans-Josef Endres and Andrea Siebert-Raths. *Engineering biopolymers: Markets, manufacturing, properties and applications*. Hanser, Munich and Cincinnati, Ohio, 2011.
- [133] Maria Laura Di Lorenzo and René Androsch. *Industrial Applications of Poly(lactic acid)*, volume 282. Springer International Publishing, Cham, 2018.
- [134] M. J. Pelouze. Mémoire sur l'acide lactique. *Ann. de Chim. et de Phys.*, 3(13):257–268, 1845.
- [135] Patrick Gruber and Micheal O'Brien. Polylactides "natureworks® pla". In Alexander Steinbüchel, editor, *Biopolymers Online*. Wiley-VCH Verlag GmbH & Co. KGaA, Weinheim, Germany, 2005.
- [136] Wim J. Groot and Tobias Borén. Life cycle assessment of the manufacture of lactide and pla biopolymers from sugarcane in thailand. *The International Journal of Life Cycle Assessment*, 15(9):970–984, 2010.
- [137] Wallace H. Carothers, G. L. Dorough, and F. J. van Natta. Studies of polymerization and ring formation. x. the reversible polymerization of six-membered cyclic esters. *Journal of the American Chemical Society*, 54(2):761–772, 1932.
- [138] Janna Börner, Sonja Herres-Pawlis, Ulrich Flörke, and Klaus Huber. [bis(guanidine)]zinc complexes and their application in lactide polymerisation. *European Journal of Inorganic Chemistry*, 2007(36):5645–5651, 2007.
- [139] Hiroshi Urayama, Takeshi Kanamori, and Yoshiharu Kimura. Properties and biodegradability of polymer blends of poly(l-lactide)s with different optical purity of the lactate units. *Macromolecular Materials and Engineering*, 287(2):116–121, 2002.
- [140] Rahul M. Rasal, Amol V. Janorkar, and Douglas E. Hirt. Poly(lactic acid) modifications. *Progress in Polymer Science*, 35(3):338–356, 2010.
- [141] Kotiba Hamad, Mosab Kaseem, Muhammad Ayyoob, Jinho Joo, and Fawaz Deri. Polylactic acid blends: The future of green, light and tough. *Progress in Polymer Science*, 85:83–127, 2018.
- [142] Weiyang Zhang, Zongyan Gui, Chong Lu, Shujun Cheng, Dianxiong Cai, and Yun Gao. Improving transparency of incompatible polymer blends by reactive compatibilization. *Materials Letters*, 92:68–70, 2013.
- [143] Bing Meng, Jingjing Deng, Qing Liu, Zhihua Wu, and Wei Yang. Transparent and ductile poly(lactic acid)/poly(butyl acrylate) (pba) blends: Structure and properties. *European Polymer Journal*, 48(1):127–135, 2012.

F. BIBLIOGRAPHY

- [144] Jon Anakabe, Ane Miren Zaldua Huici, Arantxa Eceiza, and Aitor Arbelaiz. Melt blending of polylactide and poly(methyl methacrylate): Thermal and mechanical properties and phase morphology characterization. *Journal of Applied Polymer Science*, 132(42), 2015.
- [145] Cedric Samuel, Jean-Marie Raquez, and Philippe Dubois. Plla/pmma blends: A shear-induced miscibility with tunable morphologies and properties? *Polymer*, 54(15):3931–3939, 2013.
- [146] Tomoko Shirahase, Yoichi Komatsu, Yoichi Tominaga, Shigeo Asai, and Masao Sumita. Miscibility and hydrolytic degradation in alkaline solution of poly(l-lactide) and poly(methyl methacrylate) blends. *Polymer*, 47(13):4839–4844, 2006.
- [147] Vu Thanh Phuong, Maria-Beatrice Coltelli, Patrizia Cinelli, Mario Cifelli, Steven Verstichel, and Andrea Lazzeri. Compatibilization and property enhancement of poly(lactic acid)/polycarbonate blends through triacetin-mediated interchange reactions in the melt. *Polymer*, 55(17):4498–4513, 2014.
- [148] Guoming Liu, Xiuqin Zhang, and Dujin Wang. Tailoring crystallization: Towards high-performance poly(lactic acid). *Advanced materials (Deerfield Beach, Fla.)*, 26(40):6905–6911, 2014.
- [149] René Androsch, Christoph Schick, and Maria Laura Di Lorenzo. Kinetics of nucleation and growth of crystals of poly(l-lactic acid). In Maria Laura Di Lorenzo and René Androsch, editors, *Synthesis, Structure and Properties of Poly(lactic acid)*, pages 235–272. Springer International Publishing, Cham, 2018.
- [150] Maria Laura Di Lorenzo, Mariacristina Cocca, and Mario Malinconico. Crystal polymorphism of poly(l-lactic acid) and its influence on thermal properties. *Thermochimica Acta*, 522(1-2):110–117, 2011.
- [151] Gabriele Perego, Gian Domenico Cella, and Catia Bastioli. Effect of molecular weight and crystallinity on poly(lactic acid) mechanical properties. *Journal of Applied Polymer Science*, 59(1):37–43, 1996.
- [152] Mariacristina Cocca, Maria Laura Di Lorenzo, Mario Malinconico, and Vincenzo Frezza. Influence of crystal polymorphism on mechanical and barrier properties of poly(l-lactic acid). *European Polymer Journal*, 47(5):1073–1080, 2011.
- [153] Erlantz Lizundia, Susana Petisco, and Jose-Ramon Sarasua. Phase-structure and mechanical properties of isothermally melt-and cold-crystallized poly (l-lactide). *Journal of the mechanical behavior of biomedical materials*, 17:242–251, 2013.
- [154] Mariacristina Cocca, René Androsch, Maria Cristina Righetti, Mario Malinconico, and Maria Laura Di Lorenzo. Conformationally disordered crystals and their influence on material properties: The cases of isotactic polypropylene, isotactic poly(1-butene), and poly(l-lactic acid). *Journal of Molecular Structure*, 1078:114–132, 2014.
- [155] Joram Slager and Abraham J. Domb. Biopolymer stereocomplexes. *Advanced Drug Delivery Reviews*, 55(4):549–583, 2003.
- [156] Hideto Tsuji. Poly(lactide) stereocomplexes: Formation, structure, properties, degradation, and applications. *Macromolecular bioscience*, 5(7):569–597, 2005.
- [157] B. Eling, S. Gogolewski, and A. J. Pennings. Biodegradable materials of poly(l-lactic acid): 1. melt-spun and solution-spun fibres. *Polymer*, 23(11):1587–1593, 1982.
- [158] Jia-Feng Ru, Shu-Gui Yang, Dong Zhou, Hua-Mo Yin, Jun Lei, and Zhong-Ming Li. Dominant beta-form of poly(l-lactic acid) obtained directly from melt under shear and pressure fields. *Macromolecules*, 49(10):3826–3837, 2016.
- [159] J. Puiggali, Y. Ikada, H. Tsuji, L. Cartier, T. Okihara, and B. Lotz. The frustrated structure of poly(l-lactide). *Polymer*, 41(25):8921–8930, 2000.
- [160] Bernard A. Lotz. Single crystals of the frustrated beta-phase and genesis of the disordered alpha'-phase of poly(l-lactic acid). *ACS Macro Letters*, 4(5):602–605, 2015.
- [161] P. de Santis and A. J. Kovacs. Molecular conformation of poly(s-lactic acid). *Biopolymers*, 6(3):299–306, 1968.
- [162] Maria Laura Di Lorenzo and René Androsch. Stability and reorganization of a'-crystals in random l/d-lactide copolymers. *Macromolecular Chemistry and Physics*, 217(13):1534–1538, 2016.

F. BIBLIOGRAPHY

- [163] René Androsch, Christoph Schick, and Maria Laura Di Lorenzo. Melting of conformationally disordered crystals (α' -phase) of poly(l-lactic acid). *Macromolecular Chemistry and Physics*, 215(11):1134–1139, 2014.
- [164] Maria Cristina Righetti, Massimo Gazzano, Maria Laura Di Lorenzo, and René Androsch. Enthalpy of melting of α' - and α -crystals of poly(l-lactic acid). *European Polymer Journal*, 70:215–220, 2015.
- [165] Pengju Pan, Bo Zhu, and Yoshio Inoue. Enthalpy relaxation and embrittlement of poly(l-lactide) during physical aging. *Macromolecules*, 40(26):9664–9671, 2007.
- [166] René Androsch, Evgeny Zhuravlev, and Christoph Schick. Solid-state reorganization, melting and melt-recrystallization of conformationally disordered crystals (α' -phase) of poly (l-lactic acid). *Polymer*, 55(19):4932–4941, 2014.
- [167] René Androsch and Maria Laura Di Lorenzo. Effect of molar mass on the α'/α -transition in poly (l-lactic acid). *Polymer*, 114:144–148, 2017.
- [168] Maria Laura Di Lorenzo. Calorimetric analysis of the multiple melting behavior of poly(l-lactic acid). *Journal of Applied Polymer Science*, 100(4):3145–3151, 2006.
- [169] Finizia Auriemma, Giovanni Carlo Alfonso, and Claudio de Rosa. *Polymer Crystallization I*, volume 276. Springer International Publishing, Cham, 2017.
- [170] René Androsch, Maria Laura Di Lorenzo, and Christoph Schick. Crystal nucleation in random l/d-lactide copolymers. *European Polymer Journal*, 75:474–485, 2016.
- [171] René Androsch and Maria Laura Di Lorenzo. Kinetics of crystal nucleation of poly(l-lactic acid). *Polymer*, 54(26):6882–6885, 2013.
- [172] René Androsch and Maria Laura Di Lorenzo. Crystal nucleation in glassy poly(l-lactic acid). *Macromolecules*, 46(15):6048–6056, 2013.
- [173] René Androsch, Christoph Schick, and Alicyn Marie Rhoades. Application of tammann’s two-stage crystal nuclei development method for analysis of the thermal stability of homogeneous crystal nuclei of poly(ethylene terephthalate). *Macromolecules*, 48(22):8082–8089, 2015.
- [174] John I. Lauritzen and John D. Hoffman. Theory of formation of polymer crystals with folded chains in dilute solution. *J. Res. Natl. Bur. Stand.*, (64A):73–102, 1960.
- [175] John D. Hoffman and John I. Lauritzen. Crystallization of bulk polymers with chain folding: Theory of growth of lamellar spherulites. *J. Res. Natl. Bur. Stand.*, (65A):297–336, 1961.
- [176] John I. Lauritzen and John D. Hoffman. Extension of theory of growth of chain-folded polymer crystals to large undercoolings. *Journal of Applied Physics*, 44(10):4340–4352, 1973.
- [177] Xiuqin Zhang, Lingyan Meng, Gen Li, Ningning Liang, Jing Zhang, Zhiguo Zhu, and Rui Wang. Effect of nucleating agents on the crystallization behavior and heat resistance of poly(l-lactide). *Journal of Applied Polymer Science*, 133(8):n/a–n/a, 2016.
- [178] Hongbo Li and Michel A. Huneault. Effect of nucleation and plasticization on the crystallization of poly(lactic acid). *Polymer*, 48(23):6855–6866, 2007.
- [179] Mohammadreza Nofar, Alireza Tabatabaei, and Chul B. Park. Effects of nano-/micro-sized additives on the crystallization behaviors of pla and pla/co2 mixtures. *Polymer*, 54(9):2382–2391, 2013.
- [180] Jia-Zhuang Xu, Zi-Jing Zhang, Huan Xu, Jing-Bin Chen, Rong Ran, and Zhong-Ming Li. Highly enhanced crystallization kinetics of poly(l-lactic acid) by poly(ethylene glycol) grafted graphene oxide simultaneously as heterogeneous nucleation agent and chain mobility promoter. *Macromolecules*, 48(14):4891–4900, 2015.
- [181] Hideto Tsuji and Yasufumi Tezuka. Stereocomplex formation between enantiomeric poly(lactic acid)s. 12. spherulite growth of low-molecular-weight poly(lactic acid)s from the melt. *Biomacromolecules*, 5(4):1181–1186, 2004.
- [182] H. Yamane and K. Sasai. Effect of the addition of poly(d-lactic acid) on the thermal property of poly(l-lactic acid). *Polymer*, 44(8):2569–2575, 2003.
- [183] Nelly Rahman, Takahiko Kawai, Go Matsuba, Koji Nishida, Toshiji Kanaya, Hiroshi Watanabe, Hirotaka Okamoto, Makoto Kato, Arimitsu Usuki, Masatoshi Matsuda, Katsuhiko Nakajima, and

F. BIBLIOGRAPHY

- Nobutaka Honma. Effect of polylactide stereocomplex on the crystallization behavior of poly(l -lactic acid). *Macromolecules*, 42(13):4739–4745, 2009.
- [184] Bing Na, Jie Zhu, Ruihua Lv, Yunhui Ju, Renping Tian, and Bibo Chen. Stereocomplex formation in enantiomeric polylactides by melting recrystallization of homocrystals: Crystallization kinetics and crystal morphology. *Macromolecules*, 47(1):347–352, 2013.
- [185] Hironori Marubayashi, Satoshi Akaishi, Shuichi Akasaka, Shigeo Asai, and Masao Sumita. Crystalline structure and morphology of poly(l -lactide) formed under high-pressure co 2. *Macromolecules*, 41(23):9192–9203, 2008.
- [186] H. C. van de Hulst. *Light Scattering by Small Particles*. Dover Books on Physics. Dover Publications, Newburyport, 2012.
- [187] Craig F. Bohren and Donald R. Huffman. *Absorption and Scattering of Light by Small Particles*. Wiley-VCH Verlag GmbH, Weinheim, Germany, 1998.
- [188] Christian Mätzler. Matlab functions for mie scattering and absorption: Iap res. rep. 2002-08.
- [189] W. J. Wiscombe. Improved mie scattering algorithms. *Applied optics*, 19(9):1505–1509, 1980.
- [190] Rainer Dohlus. *Photonik: Physikalisch-technische Grundlagen der Lichtquellen, der Optik und des Lasers*. Oldenbourg, München, 2010.
- [191] Kjell J. Gåsvik. *Optical metrology*. Wiley, Chichester, 3. ed., repr edition, 2003.
- [192] Hans Domininghaus, Peter Elsner, Peter Eyerer, and Thomas Hirth. *Kunststoffe*. Springer Berlin Heidelberg, Berlin, Heidelberg, 2012.
- [193] Karl J. Aström and Tore Hägglund. *PID controllers: [theory, design, and tuning]*. Instrument Society of America, Research Triangle Park, NC, 2. ed. edition, 1995.
- [194] Erich Hahne. *Technische Thermodynamik: Einführung und Anwendung*. Oldenbourg, München, 5. völlig überarb. aufl. edition, 2010.
- [195] François Cardarelli. *Materials handbook: A concise desktop reference*. Springer, London, 2. ed. edition, 2008.
- [196] International Organization for Standardization. Borosilicate glass 3.3 - properties, 1998-06.
- [197] Helmut Naumann, Gottfried Schröder, and Martin Löffler-Mang. *Handbuch Bauelemente der Optik: Grundlagen, Werkstoffe, Geräte, Messtechnik*. Hanser, München and Wien, 7., vollst. überarb. und erw. aufl. edition, 2014.
- [198] Thorlabs Inc. Protected silver mirrors, 2018.
- [199] Basler ace user’s manual for usb 3.0 cameras, 2015.
- [200] Universal serial bus revision 3.2 specification, 2017.
- [201] Gernot Wilhelm Buth. *Untersuchung der Mikrostruktur magnetooptischer Speicherschichten mit Röntgenkleinwinkelstreuung unter Anwendung der Kontrastvariationsmethode*. Phd thesis, 1992.
- [202] B. R. Pauw, A. J. Smith, T. Snow, N. J. Terrill, and A. F. Thünemann. The modular small-angle x-ray scattering data correction sequence. *Journal of applied crystallography*, 50(Pt 6):1800–1811, 2017.
- [203] Tiff 6.0 specification, June 3rd, 1992.
- [204] P. Bösecke and O. Diat. Small-angle x-ray scattering at the esrf high-brilliance beamline. *Journal of applied crystallography*, 30(5):867–871, 1997.
- [205] Max Reiss. The \cos^4 law of illumination. *Journal of the Optical Society of America*, 35(4):283, 1945.
- [206] Irvine C. Gardner. Validity of the cosine-fourth-power law of illumination. *Journal of Research of the National Bureau of Standards*, 39(3):213, 1947.
- [207] Eustace L. Dereniak and Teresa D. Dereniak. *Geometrical and trigonometric optics*. Cambridge University Press, Cambridge, UK and New York, 2008.
- [208] Peter B. Catrysse and Brian A. Wandell. Optical efficiency of image sensor pixels. *Journal of the Optical Society of America A*, 19(8):1610, 2002.
- [209] Donald Ervin Knuth. *Seminumerical algorithms*, volume / Donald E. Knuth ; Vol. 2 of *The art of computer programming*. Addison-Wesley, Upper Saddle River, NJ, 3. ed., 33. printing edition, 2016.
- [210] B. P. Welford. Note on a method for calculating corrected sums of squares and products. *Technometrics*, 4(3):419–420, 1962.

F. BIBLIOGRAPHY

- [211] Tony F. Chan, Gene H. Golub, and Randall J. LeVeque. Algorithms for computing the sample variance: Analysis and recommendations. *The American Statistician*, 37(3):242, 1983.
- [212] Robert F. Ling. Comparison of several algorithms for computing sample means and variances. *Journal of the American Statistical Association*, 69(348):859, 1974.
- [213] Edward A. Youngs and Elliot M. Cramer. Some results relevant to choice of sum and sum-of-product algorithms. *Technometrics*, 13(3):657, 1971.
- [214] Curtis L. Beattie. Table of first 700 zeros of Bessel functions - $J_1(x)$ and $J'_1(x)$. *Bell System Technical Journal*, 37(3):689–697, 1958.
- [215] Hideto Tsuji, Suong Hyu Hyon, and Yoshito Ikada. Stereocomplex formation between enantiomeric poly(lactic acid)s. 3. calorimetric studies on blend films cast from dilute solution. *Macromolecules*, 24(20):5651–5656, 1991.
- [216] G. Tammann. Über die abhängigkeit der zahl der kerne, welche sich in verschiedenen unterkühlten flüssigkeiten bilden, von der temperatur. *Zeitschrift für Physikalische Chemie*, 25U(1):441–479, 1898.
- [217] Graecia Lugito and Eamor M. Woo. Three types of banded structures in highly birefringent poly(trimethylene terephthalate) spherulites. *Journal of Polymer Science Part B: Polymer Physics*, 54(13):1207–1216, 2016.
- [218] Shijun Wang, Shichen Yuan, Kun Wang, Wei Chen, Koji Yamada, Deborah Barkley, Tadanori Koga, You-lee Hong, and Toshikazu Miyoshi. Intramolecular and intermolecular packing in polymer crystallization. *Macromolecules*, 52(12):4739–4748, 2019.
- [219] James E. Mark. *Physical properties of polymers*. Cambridge University Press, Cambridge, third edition, 2004.
- [220] Bernhard Wunderlich. *Macromolecular Physics 1: Crystal structure, morphology, defects*. Elsevier, 1973.
- [221] Gert Strobl. *The Physics of Polymers: Concepts for understanding their structures and behavior*. Springer Berlin Heidelberg, Berlin, Heidelberg, 2007.
- [222] Masayuki Imai and Keisuke Kaji. Polymer crystallization from the metastable melt: The formation mechanism of spherulites. *Polymer*, 47(15):5544–5554, 2006.
- [223] Alexander G. Shtukenberg, Yuri O. Punin, Erica Gunn, and Bart Kahr. Spherulites. *Chemical reviews*, 112(3):1805–1838, 2012.
- [224] Buckley Crist and Jerold M. Schultz. Polymer spherulites: A critical review. *Progress in Polymer Science*, 56:1–63, 2016.
- [225] C. W. Bunn and T. C. Alcock. The texture of polythene. *Transactions of the Faraday Society*, 41:317, 1945.
- [226] W. M. D. Bryant. Polythene fine structure. *Journal of Polymer Science*, 2(6):547–564, 1947.
- [227] James P. Runt. *Dielectric spectroscopy of polymeric materials: Fundamentals and applications*. Washington, DC, 1997.
- [228] Bernard Lotz, Toshikazu Miyoshi, and Stephen Z. D. Cheng. 50th anniversary perspective: Polymer crystals and crystallization: Personal journeys in a challenging research field. *Macromolecules*, 50(16):5995–6025, 2017.
- [229] R. S. Stein, A. Misra, T. Yuasa, and F. Khambatta. Recent studies of light scattering from polymer films. *Pure and Applied Chemistry*, 49(7):915–928, 1977.
- [230] J. V. Champion, A. Killey, and G. H. Meeten. Small-angle polarized light scattering by spherulites. *Journal of Polymer Science: Polymer Physics Edition*, 23(7):1467–1476, 1985.
- [231] Matthew H. Hutchinson, John R. Dorgan, Daniel M. Knauss, and Sukhendu B. Hait. Optical properties of polylactides. *Journal of Polymers and the Environment*, 14(2):119–124, 2006.
- [232] Robert E. Prud'homme and Richard S. Stein. Scattering from truncated spherulites. *Journal of Polymer Science Part A-2: Polymer Physics*, 11(9):1683–1701, 1973.
- [233] R. J. Tabar, A. Wasiak, S. D. Hong, T. Yuasa, and R. S. Stein. Small-angle light scattering by random assemblies of incomplete spherulites. systems with partial degree of volume filling. *Journal of Polymer Science: Polymer Physics Edition*, 19(1):49–58, 1981.

F. BIBLIOGRAPHY

- [234] G. E. Wissler and B. Crist. Small-angle light scattering from a distribution of spherulite sizes. *Journal of Polymer Science: Polymer Physics Edition*, 23(11):2395–2406, 1985.
- [235] Z. Bartczak and A. Galeski. Homogeneous nucleation in polypropylene and its blends by small-angle light scattering. *Polymer*, 31(11):2027–2038, 1990.
- [236] Claude Picot, Richard S. Stein, R. H. Marchessault, Jens Borch, and A. Sarko. Interparticle interference in light scattering from spherulitic systems. *Macromolecules*, 4(4):467–470, 1971.
- [237] Ivanka Moneva and Marin Michailov. Average speckle size in small-angle light scattering from polymer films. *Die Makromolekulare Chemie, Rapid Communications*, 2(4):267–271, 1981.
- [238] Jaroslave Holoubek and Blahoslav Sedláček. Speckle patterns in small angle light scattering: A random phase screen approach. *Die Makromolekulare Chemie*, 185(9):2021–2031, 1984.
- [239] R. J. Tabar, R. S. Stein, and D. E. Rose. The effect of spherulitic truncation on small-angle light scattering. *Journal of Polymer Science: Polymer Physics Edition*, 23(10):2059–2084, 1985.
- [240] H. Tsuji. Properties and morphologies of poly(l-lactide): 1. annealing condition effects on properties and morphologies of poly(l-lactide). *Polymer*, 36(14):2709–2716, 1995.
- [241] John D. Hoffman and James J. Weeks. Melting process and equilibrium melting temperature of poly(chlorotrifluoroethylene). *J. Res. Natl. Bur. Stand. Sect. A*, (66):13–28, 1962.
- [242] Stephen Z.D. Cheng and Bernard Lotz. Enthalpic and entropic origins of nucleation barriers during polymer crystallization: The hoffman–lauritzen theory and beyond. *Polymer*, 46(20):8662–8681, 2005.
- [243] G. Porod. Die röntgenkleinwinkelstreuung von dichtgepackten kolloiden systemen. *Kolloid-Zeitschrift*, 124(2):83–114, 1951.
- [244] James L. White and Joseph E. Spruiell. Specification of biaxial orientation in amorphous and crystalline polymers. *Polymer Engineering & Science*, 21(13):859–868, 1981.
- [245] Yukiko Furuhashi, Yoshiharu Kimura, and Hideki Yamane. Higher order structural analysis of stereocomplex-type poly(lactic acid) melt-spun fibers. *Journal of Polymer Science Part B: Polymer Physics*, 45(2):218–228, 2007.
- [246] Sara A. Arvidson, Ka C. Wong, Russell E. Gorga, and Saad A. Khan. Structure, molecular orientation, and resultant mechanical properties in core / sheath poly(lactic acid)/polypropylene composites. *Polymer*, 53(3):791–800, 2012.
- [247] M. Radjabian, M. H. Kish, and N. Mohammadi. Structure–property relationship for poly(lactic acid) (pla) filaments: Physical, thermomechanical and shape memory characterization. *Journal of Polymer Research*, 19(6):63, 2012.
- [248] M. Al-Hussein and G. Strobl. The melting line, the crystallization line, and the equilibrium melting temperature of isotactic polystyrene. *Macromolecules*, 35(5):1672–1676, 2002.
- [249] Yoshitomo Furushima, Christoph Schick, and Akihiko Toda. Crystallization, recrystallization, and melting of polymer crystals on heating and cooling examined with fast scanning calorimetry. *Polymer Crystallization*, 1(2):e10005, 2018.
- [250] Masahiro Fujita, Tomoharu Sawayanagi, Hideki Abe, Toshihisa Tanaka, Tadahisa Iwata, Kazuki Ito, Tetsuro Fujisawa, and Mizuo Maeda. Stereocomplex formation through reorganization of poly(l-lactic acid) and poly(d-lactic acid) crystals. *Macromolecules*, 41(8):2852–2858, 2008.
- [251] Xiaohong Wang and Robert E. Prud'homme. Differences between stereocomplex spherulites obtained in equimolar and non-equimolar poly(l-lactide)/poly(d-lactide) blends. *Macromolecular Chemistry and Physics*, 212(7):691–698, 2011.
- [252] Jian Hu, Jiping Wang, Mengfan Wang, Yukihiko Ozaki, Harumi Sato, and Jianming Zhang. Investigation of crystallization behavior of asymmetric plla/pdla blend using raman imaging measurement. *Polymer*, 172:1–6, 2019.
- [253] Sajjad Saeidlou, Michel A. Huneault, Hongbo Li, Pierre Sammut, and Chul B. Park. Evidence of a dual network/spherulitic crystalline morphology in pla stereocomplexes. *Polymer*, 53(25):5816–5824, 2012.

F. BIBLIOGRAPHY

- [254] Mahmoud Al-Hussein and Gert Strobl. On the mechanisms of recrystallization after melting in semicrystalline polymers: The effect of the initial melt state. *Journal of Macromolecular Science, Part B*, 42(3-4):677–685, 2007.
- [255] C. Wutz, M. Bark, J. Cronauer, R. Döhrmann, and H. G. Zachmann. Simultaneous measurements of small angle x-ray scattering, wide angle x-ray scattering, and light scattering during phase transitions in polymers (invited). *Review of Scientific Instruments*, 66(2):1303–1307, 1995.
- [256] Sahar Nouri, Charles Dubois, and Pierre G. Lafleur. Synthesis and characterization of polylactides with different branched architectures. *Journal of Polymer Science Part B: Polymer Physics*, 53(7):522–531, 2015.
- [257] Hideto Tsuji and Yuki Arakawa. Synthesis, properties, and crystallization of the alternating stereocopolymer poly(l-lactic acid-alt-d-lactic acid) [syndiotactic poly(lactic acid)] and its blend with isotactic poly(lactic acid). *Polymer Chemistry*, 9(18):2446–2457, 2018.
- [258] Hironori Marubayashi, Ryo Mizukami, Yuji Hamada, and Shuichi Nojima. Crystallizability of substituted poly(lactic acid)s: Effects of alkyl side-chain structure. *Polymer Degradation and Stability*, 153:318–324, 2018.
- [259] Chantiga Choochottiros, Eunha Park, and In-Joo Chin. Synthesis and characterization of polylactide–poly(methyl methacrylate) copolymer by combining of rop and aget atrp. *Journal of Industrial and Engineering Chemistry*, 18(3):993–1000, 2012.
- [260] Bonnie O. Leung, Adam P. Hitchcock, John L. Brash, Andreas Scholl, and Andrew Doran. Phase segregation in polystyrene–polylactide blends. *Macromolecules*, 42(5):1679–1684, 2009.
- [261] Go Sato, Shotaro Nishitsuji, and Jiro Kumaki. Two-dimensional phase separation of a poly(methyl methacrylate)/poly(l-lactide) mixed langmuir monolayer via a spinodal decomposition mechanism. *The journal of physical chemistry. B*, 117(30):9067–9072, 2013.
- [262] M. C. Gupta and V. G. Deshmukh. Thermal oxidative degradation of poly-lactic acid: Part i: Activation energy of thermal degradation in air. *Colloid and Polymer Science*, 260(3):308–311, 1982.
- [263] M. C. Gupta and V. G. Deshmukh. Thermal oxidative degradation of poly-lactic acid: Part ii: molecular weight and electronic spectra during isothermal heating. *Colloid & Polymer Science*, 260(5):514–517, 1982.
- [264] D. Rasselet, A. Ruellan, A. Guinault, G. Miquelard-Garnier, C. Sollogoub, and B. Fayolle. Oxidative degradation of polylactide (pla) and its effects on physical and mechanical properties. *European Polymer Journal*, 50:109–116, 2014.
- [265] V. Speranza, A. de Meo, and R. Pantani. Thermal and hydrolytic degradation kinetics of pla in the molten state. *Polymer Degradation and Stability*, 100:37–41, 2014.
- [266] Amol V. Janorkar, Andrew T. Metters, and Douglas E. Hirt. Degradation of poly(l-lactide) films under ultraviolet-induced photografting and sterilization conditions. *Journal of Applied Polymer Science*, 106(2):1042–1047, 2007.
- [267] Nobuhiko Yasuda, Yan Wang, Takayuki Tsukegi, Yoshihito Shirai, and Haruo Nishida. Quantitative evaluation of photodegradation and racemization of poly(l-lactic acid) under uv-c irradiation. *Polymer Degradation and Stability*, 95(7):1238–1243, 2010.
- [268] Yabin Li, Akiko Hayashi, Mizuho Saito, Martin Vacha, Shigemitsu Murase, and Hisaya Sato. Degradation of aliphatic polyesters by vacuum ultraviolet irradiation. *Polymer Journal*, 38(4):395–399, 2006.
- [269] Hideto Tsuji, Yoshihisa Echizen, and Yoshiro Nishimura. Photodegradation of biodegradable polyesters: A comprehensive study on poly(l-lactide) and poly(ϵ -caprolactone). *Polymer Degradation and Stability*, 91(5):1128–1137, 2006.
- [270] Maciej Bero, Janusz Kasperczyk, and Zbigniew J. Jedlinski. Coordination polymerization of lactides, 1 structure determination of obtained polymers. *Die Makromolekulare Chemie*, 191(10):2287–2296, 1990.
- [271] K. A. Thakur, R. T. Kean, E. S. Hall, M. A. Doscotch, and E. J. Munson. A quantitative method for determination of lactide composition in poly(lactide) using (1)h nmr. *Analytical chemistry*, 69(21):4303–4309, 1997.

F. BIBLIOGRAPHY

- [272] Mark T. Zell, Brian E. Padden, Amanda J. Paterick, Khalid A. M. Thakur, Robert T. Kean, Marc A. Hillmyer, and Eric J. Munson. Unambiguous determination of the ¹³C and ¹H NMR stereosequence assignments of polylactide using high-resolution solution NMR spectroscopy. *Macromolecules*, 35(20):7700–7707, 2002.
- [273] James Lunt. Large-scale production, properties and commercial applications of polylactic acid polymers. *Polymer Degradation and Stability*, 59(1-3):145–152, 1998.
- [274] F. Carrasco, P. Pagès, J. Gámez-Pérez, O. O. Santana, and M. L. Maspocho. Kinetics of the thermal decomposition of processed poly(lactic acid). *Polymer Degradation and Stability*, 95(12):2508–2514, 2010.

